NET-SHAPE HOT ISOSTATIC PRESSING OF A NICKEL-BASED POWDER SUPERALLOY

by

CHUNLEI QIU

A thesis submitted to The University of Birmingham for the degree of

DOCTOR OF PHILOSOPHY

Department of Metallurgy and Materials
College of Engineering and Physical Sciences
The University of Birmingham
November 2010

Synopsis

Microstructural analysis and mechanical property assessment have been carried out on hot isostatically pressed (HIPped) and heat treated samples of RR 1000 powder to assess Net Shape HIPping as a process-route for aero engine components. HIPping led to (Hf,Zr)-rich oxides and carbides on prior particle boundaries (PPBs) which could be coarsened, but not eliminated by changing the HIP procedure. HIPping above the γ′ solvus resulted in coarser grains with serrated boundaries and in the formation of irregular-shaped secondary γ′ and fan-type γ-γ′ structures. Factors which influence the growth and morphology of γ′ particles are considered and it is shown that particle impingement dominates in the formation of irregular γ′ during continuous cooling from supersolvus. Solution treatment near the HIPping temperature led to thermally induced pores (TIP) but lower temperatures avoided TIP and changed the γ′ size, distribution and morphology giving a large volume fraction of finer cuboidal secondary γ′ and medium-sized spherical tertiary γ′.

The 0.2% proof stress decreased with increase of HIP temperature in room temperature and 700℃ tensile tests but HIPping at lower temperature resulted in particle debonding and very poor properties. Solution treatment at 1120℃ and ageing improved yield strength at both room temperature and 700℃. Deformation at room temperature occurred mainly by dislocations cutting through γ′; most of the medium-sized tertiary γ′ precipitates in solution-treated samples were not cut through. HIPped and aged samples showed the best four-point bending fatigue limit. Tension-tension fatigue tests showed an improved fatigue limit as compared with four-point bending fatigue tests. Fatigue failure was mainly associated with the presence of large inclusion clusters. Solution treatment improved creep performance

especially at elevated temperatures and stress levels. Samples HIPped at higher temperature (1180℃) and then heat treated all showed better creep rate than those HIPped at lower temperature (1107℃) and thermomechanically processed samples.

HIPping at 1180℃/150MPa/4h followed by post-HIP heat treatments of (i)1120℃/2h plus air cooling and (ii) an ageing treatment at 760℃/16h plus air cooling produces the optimal combination of properties. Samples processed in this way showed better mechanical properties than those defined for an engine casing component and Net Shape HIPping thus offers a process-route for a casing manufactured from RR1000 powder. Future work should focus on control of inclusion sizes and densities by compositional changes and by improved process control.

To my dear wife

Acknowledgements

The work presented in this thesis has been carried out with the financial support of the School of Metallurgy and Materials in the University of Birmingham and ORS Committee. The provision of essential research facilities by the Department of Metallurgy and Materials and the IRC is gratefully acknowledged.

I'm deeply grateful for my supervisors Professor Xinhua Wu and Dr. Junfa Mei for their guidance, suggestions and strong support in research. I especially appreciate them for encouraging me and for creating many opportunities for me to exercise and improve many necessary skills for this study.

A special thank must go to Professor Michael. H. Loretto for his continual and generous help, his inspiring suggestions, guidance and encouragement. He is not only a great scientist but also a wonderful teacher. I greatly appreciate his patience and efforts to explain many fundamental and practical aspects of transmission electron microscopy in a very simple and clear way, which led me to touch the beauty and magic of this technique. His excellent teaching and tremendous help in thesis writing and modification are also gratefully acknowledged.

I would like to thank Dr P. Andrews, Dr W. Voice, Dr M. Hardy and Dr M. Roberts in Rolls-Royce plc for very helpful discussions and suggestions. It's a great pleasure to acknowledge the considerable number of people who have generously provided technical help during this study: Mr. J. Shurvinton for his continual assistance and help in HIPping and many other things; Dr D. Hu for assistance in sorting out problems in tensile testing and EDM machining; Mr P. Stanley and Dr. M. Chu for training on several electron microscopes; Dr. T. Doel, Mr. D. Price and Dr. H. Li for mechanical testing; and Mr J. Singh for metallographic preparation. Thanks are also extended to many colleagues and friends.

Special thanks are also due to my family especially my parents and parents-in-law for their constant support, encouragement and understanding. Last but not least, a very special thank to my wife Liping Lu for her love and support. Thank you for always being here.

CONTENTS

Chapter One-The Gas Turbine Engine

1.1 Introduction

The past decades have witnessed significant advances in the performance of gas turbine engines and the concurrent, associated development of engine materials. The components in a gas turbine engine are exposed to a variety of service conditions, including high temperatures and thermal gradients, corrosive gases, vibratory and constant stresses [1,2]. Therefore, the materials used need to possess both good elevated temperature properties and adequate low temperature properties (for fabrication and engine maintenance). The demand for improved gas turbine engine efficiency, which is highly dependent on turbine inlet temperature, stimulates the continued development and application of higher performance materials.

1.2 The turbine engines

1.2.1 History of the gas turbine

The earliest form of jet reaction could be traced back to around 100.B.C and was called the aelophile of Heron (often called “Hero” of Alexandria) [3]. It operated with a plenum chamber filled with water, which was heated to a boiling condition. The steam was fed through tubes to a sphere mounted on a hollow shaft. Two exhaust nozzles located on opposite sides of the sphere and pointing in opposite directions were used to direct the steam with high velocity and rotate the sphere with torque (from the moment of momentum) around an axis.

In 1891 the first steam turbine was developed by Charles Parsons. It had two separate components: the steam generator-combustor and the turbine. This device can be considered as a predecessor to the modern gas turbine.

Developments in the 1930s resulted in the construction of the first gas turbine successfully operated expressly for power generation in 1939, being accomplished by Brown Boveri [4]. Simultaneously, extensive and strictly independent research and development were performed in Great Britain and Germany on gas turbines to propel an airplane. In 1930, Frank Whittle (Great Britain) patented the first modern propulsion gas turbine and the first prototype was completed in April 1937. The engine rotated at almost 18,000rpm and developed a thrust of 1000 1bf (4450N). It had a centrifugal flow compressor and a reverse-flow combustion chamber; that is, the flow in the burner was opposite in direction to the new flow of air in the engine- a concept still used for small engines to conserve space. This gas turbine was first installed on an aircraft in May 1941 after several years of development. The first flight using a gas turbine took place on August 27, 1939 in Germany. Hans von Ohain patented the engine for this aircraft in 1936, which developed a combination of axial flow and centrifugal compressor stages and a resulting thrust of 1100 1bf (4890N). A few years later the German Junkers Jumo004, designed by Anselm Franz, was the first engine to be mass produced. Today both Whittle and von Ohain are credited equally with the invention of the jet engine.

In the past decades, dramatic advances have been made for the turbine engines. Nowadays, General Electric, Pratt and Whitney and Rolls-Royce dominate the global commercial aero-engine market. All of these manufacturers can produce engines that develop thrusts in excess of 100,000 1bf (445,000 N) and have a turbine entry temperature of around 1500°C, considerably above the material′s melting point. Figure 1.1 illustrates the Rolls-Royce's most advanced Trent 900 high bypass ratio turbofan engine. With the increasing demand for aircraft, the gas turbine engine industry shows an immense marketing potential and will definitely move forward over a long period. However, the continued improvement of turbine

engine efficiency and performance will inevitably depend on the development and application of more advanced materials.

1.2.2 Operation of a Modern Aero Gas Turbine Engine

A typical turbine engine consists of three main sections: the compressor, combustion chamber and the turbine section, see Figure 1.1. The pressure and temperature variations in different sections are shown in Figure 1.2. The compressor is a multi-stage unit employing alternate rows of rotating blades and stationary vanes, called rotors and stators, respectively, to accelerate and diffuse the incoming air until the required pressure rise is obtained and then deliver the air to the combustion chamber. The rotor blades are rotated at high speed by the engine in order to accelerate the air and achieve high pressure ratio and thus will inevitably experience high centrifugal stresses. Therefore, high specific tensile strength is a dominant material requirement for these components. Fatigue strength is also required to resist the additional cyclic stresses arising from forced excitation due to irregularities in the air flow distribution around the annulus. The stators play a role in diffusing the incoming high speed air to minimize the flow variation and turbulence and directing the air at the correct angle to the next stage of rotor blades. In this case, the stators experience high cyclic stresses and vibrational stresses caused by flow variation and thus high fatigue strength is required. As the air velocity and pressure increase, the air temperature increases progressively as well. At the end of the compression section the air pressure could be increased up to 40 atmospheres and the temperature up to approximately 600°C. Increasing the temperature and pressure of the inlet air increases the efficiency of the engine. Basically, titanium alloys with their high specific tensile strength are the preferred materials for rotor blades and stator vanes in the low pressure area while nickel based superalloys, such as In718 and 901, are used for the blades and discs in the rear of the compression system where high pressure and temperature are encountered.

The combustion system heats the air from the compressor to the required turbine inlet temperature with minimum loss of pressure and maximum heat release, and must maintain stable and efficient combustion over a wide range of engine operating conditions. To ensure efficient combustion, only approximately 20% of the air flow is taken in by the snout or entry section to the combustion chamber consisting of primary zone and dilution zone. The air not picked up by the snout flows into the annular space between the combustion chamber and the air casing. The air entering the combustion chamber must be diffused to prevent the extinction of flame and provide efficient burning and this is achieved by using swirl vanes to disrupt the axial air flow. Around a further 20% air is fed through the sides of the combustion chamber into the primary combustion zone to create a low velocity recirculation region into which the fuel is injected. Extensive combustion then takes place in the primary zone of the combustion chamber and releases a gas flow whose peak temperature could reach around 2000°C. In the dilution zone, half of the remaining compressor air is introduced progressively into the flame tube to lower the gas temperature before it enters the turbine assembly, while the other half is used to cool the walls of the flame tube. The combustion liner walls experience peak temperatures around 2000°C with mean temperatures around 1000°C. Oxidation resistance is thus a major requirement together with thermal fatigue resistance because of rapid temperature changes which are experienced at various points in the flight cycle. Moderate creep and proof strengths are necessary to avoid buckling. Early combustion chambers were fabricated in simple solid solution strengthened alloys such as Nimonic 75. These alloys were found to have inadequate strength in later designs and stronger alloys were introduced, albeit with some sacrifice in the high temperature oxidation resistance.

The turbine takes the responsibility for providing power to drive the compressor and accessories by extracting energy from the hot gases released from the combustion system and

expanding them to a lower pressure and temperature. To produce the driving torque, the turbine may consist of several stages each employing one row of stationary nozzle guide vanes and one row of moving blades. The nozzles take advantage of their convergent shape to rapidly accelerate the gas and the nozzle guide vanes produce a 'spin' or 'whirl' to the gas flow in the direction of rotation of the turbine blades, causing the turbine blades to rotate at high speed. Since the spinning turbine blades are connected to the shafts which drive the compressor, the higher spinning speed will yield more power to drive compressor and thus more air could be drawn in and compressed. The turbine blades, designed to be twisted, also play a role in ensuring a uniform axial velocity of the gas flow for the exhaust system, which reduces gas whirl and thus improves the efficiency. The gases are finally expelled out of the rear of the engine at high velocity and produce thrust to propel the aircraft. The high pressure turbine blades operate under the most hostile condition of temperature and stress of any component in the engine. Not only does the blade experience high temperature and direct stress, it also experiences rapid temperature transients at various points in the flight cycle [5]. The hot gases which surround the blade are highly oxidising, may contain contaminants such as chlorides and sulphates, which can lead to hot corrosion. The combination of direct stress and temperature gives rise to creep while the temperature transients can cause thermal fatigue. Therefore, the turbine blades must possess superior high temperature tensile strength and creep property, high thermal fatigue property and excellent hot corrosion and oxidation resistance. For stationary vanes, due to their static condition, they do not endure the same rotational stresses as the turbine blades, the heat resistance and thermal fatigue property together with the high oxidation resistance are the important requirements. Turbine discs, operating in a relatively cool environment, are responsible for holding the turbine blades in place and are subjected to centrifugal force associated with rotation. There also exists a temperature gradient from the bore to the rim of the disc. High tensile strength, fatigue

property (especially damage tolerance) and creep resistance are all required in varying degrees, dependent on location within the component. In the bore of the disc there exist high stresses in the order of 1000MPa and relatively low temperatures. Here it is desirable to achieve good tensile strength. The rim experiences lower rotational forces but much higher temperatures, so good creep properties are needed. Although austenitic steels were used in Whittle's first engine, later nickel-based superalloys replaced them and are currently the only materials possessing the properties required for modern turbine discs and blades. The efficiency of the gas turbine increases with an increase of turbine inlet temperature. Figures 1.3 and 1.4 show how increased turbine inlet temperatures decrease both specific fuel and air consumption while increasing efficiency [6]. An incentive to go to the higher temperature in gas turbine is so great that the development and use of high performance new materials continue at an increasing rate.

1.3 Gas Turbine Engine Materials

Since the efficiency of the gas turbine is highly dependent on the turbine gas temperature and thus on the temperature capability of materials, many advances in gas turbine engine performance can be largely attributed to the introduction of an improved material.

1.3.1 Steels

In the early stage of gas turbine engine development, back to 1930s and 1940s, the major material choice for the gas turbine engine was steels. Almost all the main engine components, such as discs, shafts, bearings, gears, blades, and casings were made from either austenitic steels or martensitic steels. By the mid 1950s, steel still accounted for over 60% by weight of all engine components [7]. However, these materials generally suffered from inadequate creep strength, fatigue and limited oxidation resistance at high temperature and consequently very short service life [2, 7]. Eventually, the use of steels in gas turbine engine was very

significantly reduced with the introduction of higher performance materials, such as nickel-based superalloys and titanium alloys.

1.3.2 Titanium alloys

Although the development of titanium alloys only commenced in the late 1940s, their uniquely high strength:weight ratios led to their introduction in aircraft gas turbines as early as 1952 when they were used for compressor blades and discs in the famous Pratt and Whitney J57 engine. Immediate weight savings of approximately 200kg were achieved [8]. Since then, aircraft gas turbines have continued to provide the major application for titanium alloys which now make up 25-30% of the weight of most modern engines. In particular, titanium alloys like the α/β-alloy Ti-6Al-4V have played a major role in by-pass (fan-jet) engines for which a large front fan is required. In addition to the fan, titanium alloys are used for most of the blades and discs in the low and intermediate sections of the compressors of modern jet engines. However, lack of high temperature strength, oxidation and creep resistance has limited the use of titanium alloys to components operating in general below a temperature of 550℃ [9].

1.3.3 Nickel-based superalloys

The family of nickel-based superalloys in gas turbines have played a vital role in the development of the aircraft. Nickel-based superalloys have been extensively developed during the past 50 years, which leads to tremendous improvements in engine efficiency. Nickel-based superalloys exhibit outstanding room temperature strength and retain reasonable strength to a temperature of approximately 1000℃. They also have high oxidation and corrosion resistance and creep resistance over the required temperature range. They are used at temperatures in excess of well over 550℃ in components including the hotter parts of compressors, turbine blades, discs and combustion chambers. Despite their age, nickel-based

superalloys still look as if they will provide the basis of materials selection for the turbine section for some years. Improvements in processing, heat treatments, alloy chemistry and surface modification are all being studied with the aim of further maximizing their operating temperature.

In general, many factors have to been taken into account to select appropriate materials for turbine engine use, among which temperature capability and high strength/weight ratio are the most important. Decreasing engine weight could reduce engine operation stresses and thus increases the service life of engine components [6, 9]. Figure 1.5 shows the rough temperature dependence of specific strength for different engine materials. It is clear that titanium alloys show the highest specific strength at low and intermediate temperatures while nickel-based superalloys show superior capability and specific strength at even higher temperatures. According to the property requirements and operation conditions in different parts of a turbine engine, different materials are usually used in different parts of a modern engine, see Figure 1.6. Basically, nickel-based superalloys are used in hotter part of an engine while the cooler parts are mainly made of titanium alloys. Steels like maraging steels are still used to make components like shafts where high tensile strength and good creep properties at temperatures upto 500℃ are required. Some fibre composite materials are used in the containment system due to their light weight and low cost.

References

[1] Sahm PR, Seidel MO. High-temperature materials in gas turbine. Swizerland: Brown, Boveri & Company Limited, Swizerland, 1974.

[2] Rolls-Royce plc. The engine jet, 5th edition. Birmingham: Renault Printing Co Ltd; 1996. p.19-57.

[3] Flack RD. Fundamentals of jet propulsion with applications. New York: Cambridge University Press; 2005.p.3-10.

[4] Bathie WW. Fundamentals of gas turbines, 2nd edition. New York: John Wiley & Sons, Inc.; 1996. p.4.

[5] Driver D, Hall DW, Meetham GW. The gas turbine engine. In: Meetham GW, editor. The development of gas turbine materials. London: Applied Science Publishers Ltd; 1981. p.17-30.

[6] Boyce MP. Gas turbine engineering handbook, 3rd edition. Oxford: Elsevier Inc; 2006. p.430.

[7] Oaks G, Barraclough KC. Steels. In: Meetham GW, editor. The development of gas turbine materials. London: Applied Science Publishers Ltd; 1981. p.31-61.

[8] Polmear IJ. Light alloys, 4th edition. Oxford: Butterworth-Heinemann of Elsevier; 2006.p.354.

[9] Wu X. Microstructural effects on fatigue crack propagation in a high strength titanium aluminde, PhD thesis, 1996.

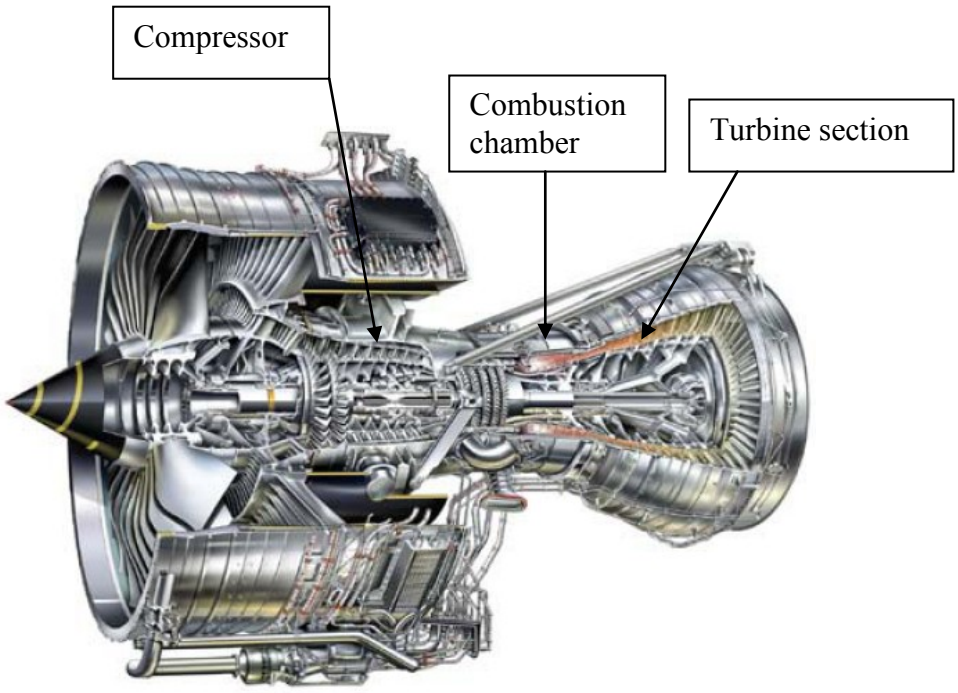

Figure 1.1 Rolls-Royce Trent 900 High bypass ratio turbofan engine to be used on the Airbus A380 (courtesy of Rolls-Royce Plc)

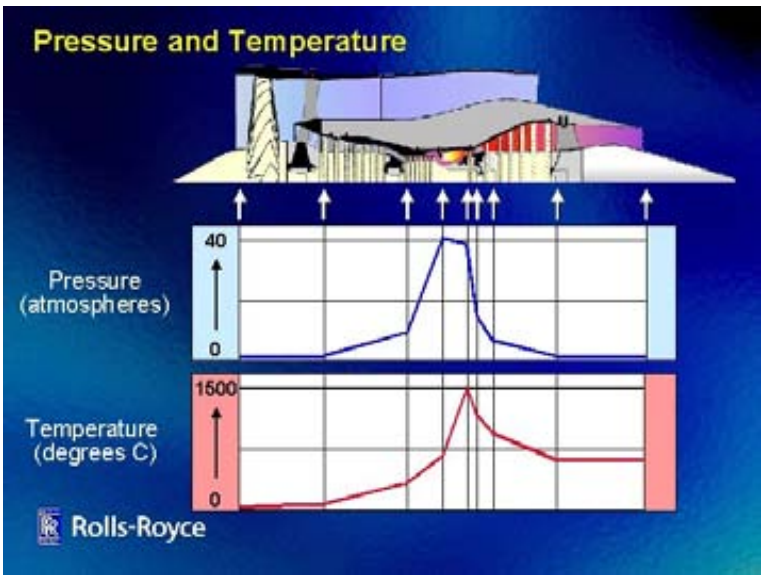

Figure 1.2 Variation in temperature and pressure through the core of a modern turbofan engine (courtesy of Rolls-Royce Plc).

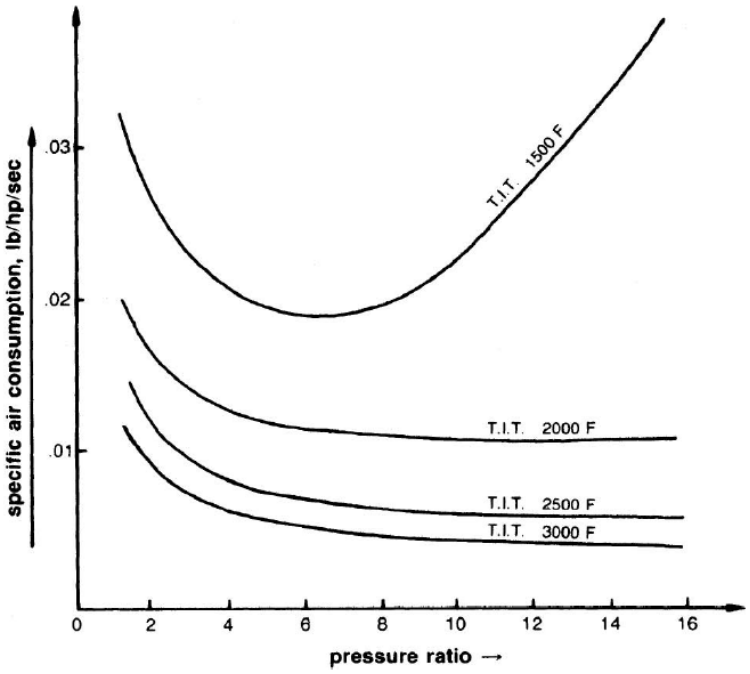

Figure 1.3 the relationship between specific air combustion and pressure ratio and turbine inlet temperature [6]

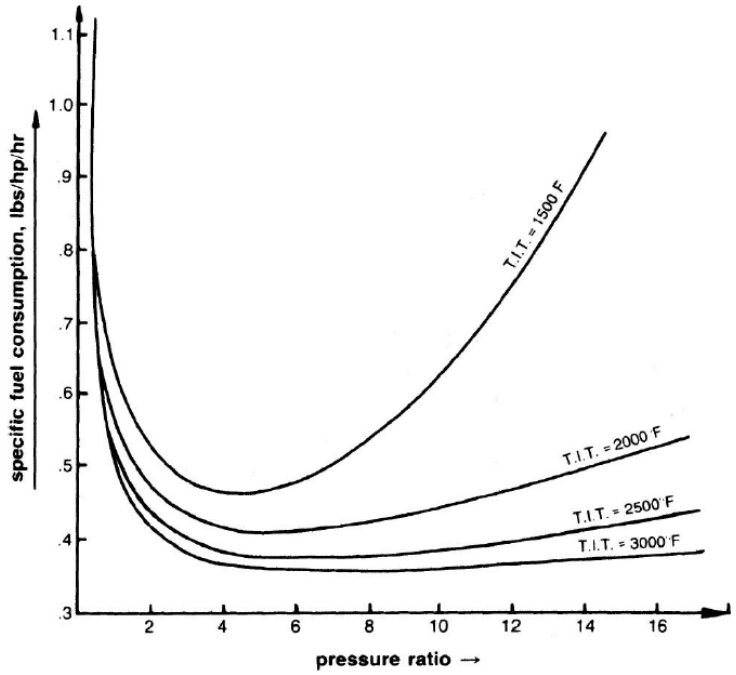

Figure 1.4 the relationship between specific fuel consumption and pressure ratio and turbine inlet temperature [6]

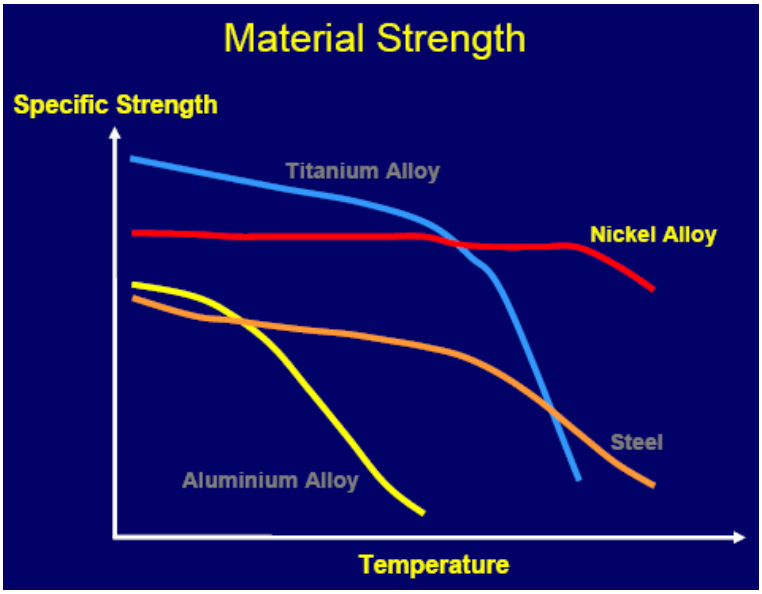

Figure 1.5 Comparison of temperature dependence of specific strength between engine materials (courtesy of Rolls-Royce Plc)

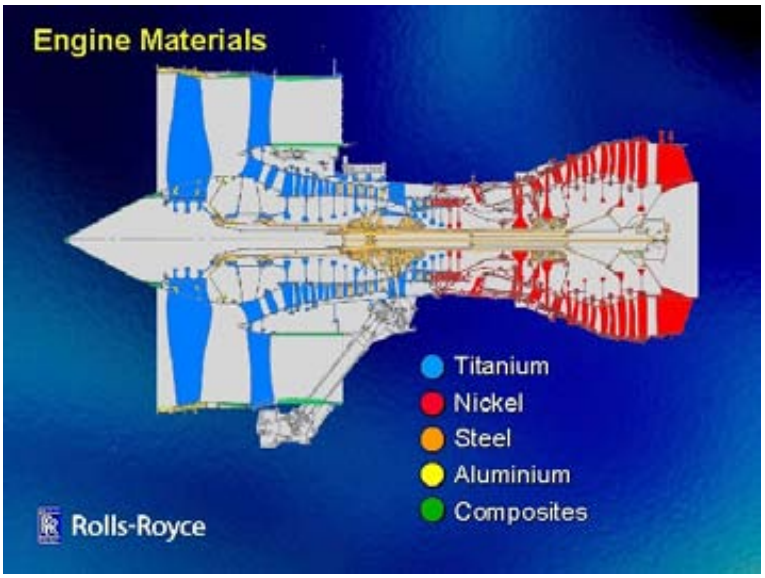

Figure 1.6 A broad classification of the types of materials used in the construction of Rolls-Royce Trent Engine (courtesy of Rolls-Royce Plc)

Chapter Two- Processing Technologies and Alloy Development for Nickel-based Superalloys

2.1 Introduction

So far, most of the components used in hot parts of a gas turbine engine, such as discs and casings, have been predominantly fabricated by machining of superalloy forgings. Two distinct approaches are available for the preparation of billets for subsequent forging or extrusion use. The first route is conventional ingot metallurgy, which involves thermomechanical working of materials produced by vacuum induction melting, electro-slag remelting and vacuum arc remelting [1]. The second route is called powder metallurgy (P/M), which involves production and consolidation of alloy powder to produce billets [2-3]. The choice of route depends on a number of factors, but is largely dictated by the chemistry of the chosen superalloy [1-3]. The conventional ingot metallurgy route is basically used for production of relatively less alloyed materials, such as Waspaloy and IN 718, which contain a low level of strengthening elements Al, Ti and Nb. However, as for the heavily alloyed grades, such as Rene 95 and RR 1000, which have been developed as high strength superalloys to meet the demand for improved efficiency for gas turbine engine, significantly increased addition of strengthening elements such as Al, Ti, Nb, Ta, and Mo, W, is usually involved. When using ingot metallurgy, the heavy alloying addition results in extensive segregation in cast ingots and thus considerable reduction in hot workability. Cracking becomes a common issue for these cast ingots during thermomechanical working [1]. Therefore, in this case, powder processing is preferred. However, the billet-based powder processing approach results in significant cost increase because powder is more expensive than the ingot and the fly-to-buy ratio is equally bad for this powder-route as for the ingot-route. Net Shape HIPping offers a possible solution to this high cost of producing

components from powder since this would lead to the reduction in forging and machining operations and thus to considerable cost reduction [1-5]. The interest in this technology has been further spurred by the remarkable achievement in dimensional accuracy in recent years through modeling [6-12].

In this chapter, the development of manufacturing processes and P/M nickel-based superalloys will be reviewed and the background and aim of this project will be introduced.

2.2 Ingot metallurgy

Figure 2.1 illustrates the sequence of processes used for production of superalloy forgings by ingot metallurgy. Vacuum induction melting (VIM) is followed by electro-slag refining and vacuum arc remelting; after annealing to improve the compositional homogeneity, the billet is thermomechanically worked before undergoing a series of forging operations [1,13].

During VIM processing, the vacuum conditions used lead to substantial reductions in the concentrations of nitrogen and oxygen of the melt through degassing, which helps to prevent the oxidation of reactive elements such as Al, Ti, Zr and Hf. Low-melting-point contaminants such as Pb, Bi are removed from the melt by volatilisation on account of their substantial vapour pressures [1,14]. Desulphurisation of the melt could be achieved by adding lime (CaO) and fluxing agents.

Further secondary melting processes such as vacuum arc melting (VAR) and possibly also electro-slag remelting (ESR) are used to reduce the significant level of segregation, casting defects (such as solidification pipe, cracks and porosity) and refractory particles of ceramic introduced from the VIM process. These could particularly reduce ingot pipe and improve the yield and forgeability of the large ingots.

The ingots produced by the remelting processes must undergo thermomechanical working in order to break down the as-cast structure and to reduce the grain size to acceptable levels, i.e. from a few tens of millimetres to a few tens of microns. This is known as ingot-to-billet

conversion and it is usually achieved by a process known as cogging, during which the diameter of the cylindrical ingot is reduced in size by a factor of approximately 2, so that its length increases four-fold. The conversion is achieved in a series of alternate stages of deformation processes and heats. The deformation applied to the ingot causes substantial re-crystallisation to a finer grain structure while the heating temperatures are carefully selected to inhibit grain growth.

Having achieved a fine-grained uniform structure through the conversion process, the obtained billets are then ready for forging. Forgings achieved will be subjected to suitable heat treatments to obtain the desired microstructure and properties. Finally, the forgings will be machined into components.

2.3 Powder metallurgy

The need for powder metallurgy (P/M) for the production of superalloy-made critical turbine components, like turbine discs, became apparent in the 1970s due to the development of alloys such as Rene 95, Astroloy and MERL 76 (with strength levels higher than earlier alloys such as IN 718 and Waspaloy), which were found to be not amenable to processing via the ingot-route [15]. Initially, the use of P/M product was limited to gas turbines for military purposes, for example, the Pratt & Whitney F 100 engine for the F-15 Eagle fighter, which entered service in 1974 [16], but commercial applications such as General Electric's CF6-80 engine for the Boeing 747-400 and the GE 90 for the Boeing 777 have emerged as experience has been accumulated. Nowadays, the use of powder metallurgy in producing turbine engine components has become widespread.

Figure 2.2 illustrates the sequence of processes used for the production of superalloy forgings by conventional powder metallurgy. Vacuum induction melting (VIM) is used as well, followed by remelting and inert gas atomisation to produce powder, which is then sieved to remove any large non-metallic inclusions inherited from the processing. This step is

important since it improves, in principle, the cleanliness of the product. To prepare a billet for forging, the powder is consolidated by loading it into a can, which is then degassed and sealed, and finally subjected to hot isostatic pressing and/or extrusion.

One of the most important steps in the production of P/M products is inert gas atomisation from master melts produced by VIM processing. In this process, the cleanliness is highly important since any contamination will be inherited by the powder. A typical arrangement is shown in Figure 2.3. Molten metal is poured into a tundish, which contains a carefully designed ceramic nozzle surrounded by one or more inert gas jets; usually argon is preferred. A continuous stream of gas at high pressure is delivered to the stream of molten metal arriving at the nozzle, the action of which causes its disintegration into spherical particles of diameter 30 to 300μm. The atomisation chamber is designed to be long enough to allow solidification of the particles before they reach the outlet of the chamber. Cooling rates are typically in excess of 100ºC/s, being greater for finer particles.

Strict screening of the powder obtained from gas atomisation is required before being subjected to consolidation, due to the possible presence of ceramic inclusions in the powder, which are caused by erosion of the melt crucible, tundish or nozzle. This screening process usually involves the passing of powder through filters of different mesh sizes, which removes the oversized particles, into which category the most damaging non-metallic inclusions fall.

Another important step involved in P/M route is the consolidation of powder. Usually, powder with the required size range is packed into a carefully cleaned and annealed steel container. This is then evacuated to encourage out-gassing, sealed and then compacted by hot isostatic pressing (HIP) or hot compaction. Hot isostatic pressing (HIPping) is a process involving the application of both high temperature and high pressure to achieve fully dense material.

After consolidation, a very high-tonnage press with specialized tooling is then used to extrude the material to the high reduction ratios necessary for fine-grained billet. A fine grain size that is typically smaller than ASTM 12 can be obtained. This process also plays an important role in dispersing any non-metallic inclusions and defects still present and in breaking down most of the prior particle boundaries (PPBs) in the billets [17]. This structure is not only ideal for inspection of the billet but also endows the material with superplasticity due to the fine grain size, which makes isothermal forging possible.

Whilst the hot die route can be used for some forging operations on powder alloys, the majority of the necessary hot work required to produce the desired finished shape and grain structure is accomplished by isothermal forging [17]. As lower strain rates are used during deformation, isothermal forging currently offers greater control of structure (such as recrystallization and controlled grain growth) and the ability to forge quite complex, 'near-net' shapes that enable significant reductions in material input weight and machining time [16,17].

2.4 Net-shape HIPping

Net-shape HIPping is a powder metallurgy processing technology which eliminates extrusion and forging procedures and massive machining work by using appropriate tooling for direct HIPping to produce near-shape or net-shape components. Figure 2.4 illustrates possible processing sequences for the compressor discs of the GE F-101 engine, which was one of the first applications of the Rene 95 P/M superalloy [16].

2.4.1 Advantages

As a special powder metallurgy process, net-shape HIPping inherits many strengths from the traditional P/M route, including elimination of macro-segregation and casting defects (such as freckles, white spots and laves phases), achievements of homogeneous

microstructure and fine grain size and thus uniform and superior mechanical properties. As a net-shape manufacturing technology, the elimination of extrusion and forging procedures together with massive reduction in input materials and machining leads to a significant decrease in cost and energy consumption, but a considerable enhancement in component production efficiency. Its environmental impact is remarkably less than current methods that use extensive machining and noxious chemicals. Moreover, this technology permits manufacture of graded component functionality or hybrid components for advanced high temperature and pressure designs that are critical to achieve significant reductions in fuel burn (CO_2) for future large civil aero gas turbines [5].

2.4.2 Issues associated with Net-shape HIPping

Despite considerable advantages to be expected, there are still some critical issues to be overcome before this technology could be widely used in producing components. From the microstructural point of view, these issues include non-metallic inclusions; prior particle boundaries (PPBs) decorated with carbides or oxides and thermally induced pores.

2.4.2.1 Non-metallic Inclusions

Non-metallic inclusions have been well recognized as one of the major defects that adversely affect the mechanical properties of P/M materials, especially low cycle fatigue property (LCF) [18-28]. These ceramic inclusions mostly originate from the melting crucible, pouring tundish or the atomizing nozzle and mainly contain Al and Si in the typical form of AlO_2 and SiO_2 with Zr, Mg or Ca also present in various amounts. The size range of this kind of defects is from several nanometers to several hundred micrometers. These inclusions act as origins for fatigue cracks, and decrease tensile properties and LCF capability of P/M superalloys. Many reports have indicated that the LCF life of a P/M superalloy is closely related to the size, location and number of inclusions [18-21, 24-25]. When the inclusion is at the surface of component (or specimen), it is easier to initiate a fatigue crack than if it is

internal. With the increase of inclusion size for both surface and internal inclusions, the LCF life of P/M superalloy decreases. The inclusion composition or type sometimes is not a significant factor.

Many efforts have been made to decrease inclusion amount or size. Organic seals were eliminated and progressively finer sieve sizes were used to screen out non-metallic inclusions. This has been made affordable by the development of nozzles for high yield and cleanliness powder production [28]. An alternative method called triboelectric separation was investigated to remove ceramic defects from superalloy powders [29]. With increasing cleanliness of alloy powders, the interest in powder-based manufacturing techniques will be further spurred.

2.4.2.2 Prior Particle Boundaries (PPBs)

PPB precipitation has been the major issue which largely limits the application of Net-shape HIPping of nickel-based superalloys. It is generally believed that PPBs are caused by atomic segregation and particle contamination [18, 30]. Both result in precipitation at PPBs, either as carbides [31], oxides [18, 32], oxy-carbides [33-34], or possibly as oxy-carbonitrides [35]. It was also reported that oxides such as ZrO_2, Al_2O_3, and TiO_2 could act as nuclei for the preferential precipitation of MC-type carbides along the PPBs [30,33,35]. These PPB precipitates could be formed on the powder particle surface during atomisation [34] or subsequent compaction [31, 33]. PPB precipitation is more likely with increased oxygen and carbon content [35-37]. The volume of PPBs is also dependent on many other things including the atomisation method, particle size, pre-consolidation handling and consolidation parameters [30]. The post-HIP heat treatment was also noted as a factor affecting PPB precipitates' amount and morphology [38-39].

The detrimental effects of PPBs on mechanical properties have been well documented [18, 30, 36-37, 40-41]. It was found that the presence of PPBs decorated with oxides or carbides

decreases the bonding between powder particles during HIPping and thus becomes the crack initiation and growth sites under load [18, 36, 40]. This becomes more apparent at elevated temperatures and leads to significant degradation of high temperature tensile ductility and stress creep rupture properties [36-37, 40-41]. LCF life could be impaired by the presence of PPB precipitates as well [18].

Massive efforts have been carried out to eliminate or decrease PPBs. Since PPBs were caused by oxygen and carbon contamination, reduction in O and C content of powder is one of the most commonly used methods to decrease PPBs and the results are usually positive. It was reported that decreasing either oxygen or carbon to a low level could significantly decrease or even eliminate PPBs [36-37]. Rotating electrode process, by electric-arc melting ingot as an electrode (anode) and by continuously feeding the consumable electrode, was reported to less disturb an inert atmosphere than gas atomisation and thus enables powders of less oxygen content to be obtained. This led to the reduced prior particle boundary decoration and gave longer smooth-bar creep lives and better impact strength, but also lower yield stresses [42]. Using high HIPping temperature is another commonly used method to reduce PPBs by promoting the grain boundaries to go beyond PPBs [43]. However, too high HIPping temperature may lead to grain boundary melting or formation of continuous grain boundary films and abnormal grain growth, which in turn seriously degrades mechanical properties [44]. Higher temperature solution treatment was tried to dissolve carbides at PPBs and thus to disrupt PPBs [39]. For some alloys where PPB precipitates in as-HIP materials are normally carbides, it was suggested that conducting heat treatment on un-pressed powder prior to HIPping was another way to decrease PPB precipitation by promoting carbide formation and coarsening in the interior of powder particles during heat treatment [34, 35]. Some suggested addition of strong carbide formers such as Ta or Hf to promote interior stable carbide precipitation and thus to reduce the carbide precipitation at PPBs [34-35, 45].

2.4.2.3 Thermally Induced Porosity

It is well known that for HIPping it is not difficult to achieve full densification of powder due to the use of both high temperature and pressure. Actually, under high temperature and high pressure conditions, any gas left in a sealed container or gas entrapped in powder particles during gas atomisation process could be compressed and dissolved into the powder particle surface or matrix. However, during subsequent high temperature heat treatment without pressure, swelling can occur as gas establishes an equilibrium pressure dependent on the surface energy and gas bubbles may re-open [46]. This thermally induced porosity (TIP) becomes another issue for net shape HIPped superalloys. It has been found that thermally induced pores could act as crack nucleation initiators and thus show negative impact on low cycle fatigue properties [18]. Extensive studies have been carried out on the influence of grain boundary elements such as B, C, Hf on porosity in P/M nickel-based superalloys [47-48]. Boron was found to be the most influential element in the study, with increased boron leading to increased grain boundary triple point void formation and tendency for thermally induced porosity. It was suggested that the higher boron caused increased amount of incipient melting, apparently promoting TIP formation by weakening of grain boundary triple points [47]. This resulted in shortened low cycle fatigue and creep life which was attributed to the pore initiation sites. Increased superheat was also found to promote TIP level in consolidated material [47].

It was suggested that to decrease TIP, it is important to minimize the gas in closed pores by degassing the compact and avoiding temperatures where one of the species can decompose or react to create a vapor [46]. This can be done by vacuum sintering to the closed-pore condition, prior to pressurization, to avoid trapped gas. Alloy chemistry should be also optimized and appropriate post-HIP solution treatment temperature selected to avoid TIP formation. Hyzak et al [21-22] found hafnium oxide inclusions and thermally induced

pores were the main fatigue crack origins for P/M alloy AF-115. By considerably reducing the carbon and hafnium contents from 0.155% and 2.02% to 0.043% and 0.85% (all in weight percentage), respectively, and slightly decreasing post-HIP solution treatment temperature from 1190℃ to 1182℃to reduce the thermal induced pore level from 0.42vol.% to 0.16 vol.%, the fatigue lifetimes were greatly improved by two to five times.

2.4.3 Densification Mechanisms during HIPping

It is well established that powder consolidation during HIPping involves several densification mechanisms [6,49], e.g. mechanical compacts, plastic yield, creep, and diffusion. When a pressure is applied to packed powder particles, it is transmitted through the powder bed as a set of forces acting across the particle contacts. The deformation at these contacts is at first elastic, but as the pressure rises, the contact stress increases, causing plastic yielding and expanding the points of contact into contact areas, e.g. necks. When the particles deform plastically, the contact area is increased, and for a constant applied pressure, the contact stress is reduced. When the contact stress falls below the yield stress, densification by plastic yielding will cease. In the end of plastic yielding process, voids surrounded by spherical thick shells would remain. Further densification involves power-law creep in the contact zones and diffusion of matter from a grain-boundary source or lattices to the void surface. During the final stage of power-law creep, densification is determined by the creep of the thick spherical shell surrounding each hole. When densification occurs by diffusion from interparticle boundaries, diffusion of material can take place across the contact areas between particles. As a result, the particles move closely together, and the void spaces between them are filled. The material becomes denser.

In reality, since P/M consolidates are made of a natural distribution of powder sizes below a given mesh size, inhomogeneous deformation for particles with different sizes may occur. As a result, some particles may be experiencing plastic yield while some others may be just

subject to creep or even remain undeformed. It is generally believed that the smaller particles undergo more extensive deformation in comparison with the larger particles [50], leaving behind undeformed boundaries of the large powder particles in the final consolidate. These undeformed boundaries, also known as prior particle boundaries (PPB), are sites for deleterious precipitation of carbide or oxide films as mentioned above. At high temperature, recrystallisation may occur in those powder particles with extensive deformation.

2.5 Nickel-based Powder Superalloy Development

The development of nickel-based superalloys is highly dependent on alloy chemistry. The function of various elements in nickel-based superalloys has been well understood [51], and is summarized in Table 2.1. Basically, the influence of elements on properties of nickel-based superalloys is realized by affecting the microstructure of the materials.

The early nickel-based powder metallurgy (P/M) alloys such as Waspaloy and Inconel 718 normally show relatively simple compositions characterized by a limited addition of gamma-prime-forming elements such as Al, Ti, Ta and so on (see Table 2.2). With the increasing demand for improved jet engine efficiency and performance, high strength alloys such as Rene 95, IN100, and Astroloy alloys were developed [18, 52-53]. The compositional designs for these alloys were characterized by considerably increased the level of gamma prime formers, Al and Ti and strong solid solution strengthening elements W and/or Mo. The concept of grain boundary strengthening was also exercised by addition of C, B and Zr. These alloys usually show much higher strength levels and high temperature capability than the earlier alloys such as Inconel 718 and Waspoloy. However, considerable addition of C was found to lead to carbide or oxide precipitation at PPBs, which adversely affected the LCF, intermediate temperature ductility and stress rupture properties. This resulted in the development of some derivative alloys such as LC Astroloy, MERL 76 which have much lower carbon content [54-55], as shown in Table 2.2.

With continued study, it was further noted that for many of the P/M alloys developed to that point, such as Rene 95, IN100, MERL 76 and Astroloy, crack growth rates scaled with the yield strength, as shown in Figure 2.5 [56]. The alloys such as Rene 95 and IN 100 with volume fractions of γ', as high as 50-60%, show high tensile strength but suffer from very fast rates of crack growth. As a result, a concept of damage tolerance for P/M superalloys was established, aiming at developing P/M superalloys with a combination of high yield strength and a low crack growth rate. The P/M superalloys of this kind include N18 [56], Rene 88DT [57], ME3 [58], Udimet 720Li [59], and RR 1000 [17], see Table 2.3. This type of superalloy usually shows a high Ti/Al ratio (≥ 1), high Cr and Co contents but a further reduced level of B, C and Zr. The significant effect of Ta in reducing dwell fatigue crack propagation (FCP) rates has been noted in the development of the alloy RR 1000 and ME3 [17, 58]. The beneficial effect of minor Hf addition (0.5wt.%) of both FCP and creep resistance was also recognized in the development of RR 1000 [17]. Also, in RR 1000, addition of Co has been maximized to produce a minimum value of stacking fault energy (SFE) to promote planar slip and to inhibit cross slip, which has a beneficial effect on both crack growth rates and creep behaviour [17]. In addition, microstructural stability was also taken into account in the synthesis of this new generation of superalloys. For example, although Cr was found to reduce the rate of FCP at elevated temperature, its concentration was limited to 15 wt% because it promotes the precipitation of the σ and μ phases, particularly above 700 ºC [59]. These phases are known to degrade the creep properties of nickel disc alloys [60-61].

In short, as compared with the previously developed P/M nickel-based superalloys, the new generation of P/M superalloys tend to put more emphasis on seeking a good combination of mechanical properties (such as high yield strength, desirable damage tolerance and creep properties), microstructural stability and HIPpability (lower C). The

gamma prime content is not the only factor that is taken into account and thus the content of gamma prime forming elements is not necessarily higher than in older comparable alloys.

As an advanced P/M superalloy, RR 1000 showed a good combination of high strength, good damage tolerance and creep resistance and therefore was selected as one of the principal materials for net-shape HIPping of turbine engine components such as turbine discs and combustion casings in this project.

2.6 Microstructure of Polycrystalline Nickel-based Superalloys

A nickel-based superalloy is basically composed of two main phases, namely gamma phase (γ) and gamma prime (γ') or gamma double prime (γ''). The γ-phase is a disordered solid solution with a face-centred cubic lattice and a random distribution of the different species of atoms. By contrast, γ' has a primitive cubic lattice in which the nickel atoms are at the face-centres and the aluminium or titanium atoms at the cube corners and thus is an ordered solid solution. In general the composition of γ' is Ni_3Al. In highly alloyed Ni-base superalloys many other elements can substitute for either nickel or aluminum or both so that the composition can be best expressed as $(Ni, Co)_3(Al, Ti, Ta)$. γ'' is based on a body-centred tetragonal lattice with an ordered arrangement of nickel and niobium atoms, see Figure 2.6(c). The composition of the γ'' is then Ni_3Nb or Ni_3V. The typical γ''-strengthened alloy is Inconel 718. However, most of the precipitate-strengthened nickel-based superalloys are γ' strengthened. The influence of alloy chemistry on the microstructure of nickel-based superalloys has been briefly summarized in Table 2.1. The strength of polycrystalline nickel-based superalloys is achieved through a combination of solid solution strengthening of the disordered γ matrix and γ' precipitates, precipitate hardening of the ordered γ' phase with multiple size ranges and grain size control. Therefore, there are different mechanisms that contribute to the strengthening of a polycrystalline nickel-based superalloy.

In addition to these basic microstructural features, net-shape HIPped nickel-based superalloys usually show some unique microstructural characteristics including the presence of PPBs and PPB precipitates such as carbides or oxides, thermally induced pores, non-metallic inclusions, and so on, all of which show significant influence on fatigue and fracture behaviours.

2.7. The Role of Heat Treatment

Polycrystalline nickel-based superalloys used for turbine casings or disc applications typically undergo a two-stage heat treatment aimed at optimising the γ′ size, morphology and distribution. The first stage is the solution treatment (ST) at a temperature near or above the γ′ solvus, which is typically for 2-6 hours. The main purpose of this is to dissolve the precipitate phases, principally γ′ and in some instances carbides, prior to their controlled precipitation during cooling or ageing. The second stage is an ageing stage, typically in the range of 650-800℃ for 1-24 hours. The aim of this stage is to refine the γ′ precipitate morphology, in particular the tertiary γ′, and to relieve residual stresses in the material which may exist as a result of rapid cooling after solution treatment.

2.7.1 The Solution Treatment Stage

Since grain growth is highly dependent on solution treatment temperature, this temperature should be considered carefully to obtain the desired grain size according to mechanical properties requirement. The finer the grain size, the better the low temperature tensile and fatigue properties - hence a low solution temperature would be preferred. Elevated temperature creep rupture properties are improved by having coarser grains, produced by a higher solution temperature.

Basically, grain growth is controlled by grain boundary precipitates such as primary γ′, carbides or oxides and even borides. If the solution treatment is kept under the γ′ solvus

temperature, grain boundary migration will be strongly pinned by primary γ′ and grain growth will be difficult. When the solution stage is performed above the γ′ solvus, then those elements that make up the γ′ phase are in solid solution and homogeneously distributed throughout the disordered γ matrix and other phases, such as carbides or oxides, are relied upon to limit grain growth. Using the super-solvus solution treatment temperature usually sees a pronounced grain growth probably due to the weak pinning effect of carbides or oxides at grain boundaries given their small volume fraction and size.

Increasing the subsolvus solution temperature decreases the volume fraction of γ′. At the solution temperature there is unlikely to be any tertiary γ′ present, as this typically has a much lower solvus temperature, due to its different composition [63].

For powder net-shape HIPped materials, increased solution treatment temperature would increase the formation propensity of thermally induced porosity (TIP), as reviewed in Chapter 2. Also, the solidus of the alloy should be taken into account since solution temperatures above the solidus would lead to local melting, especially at grain boundaries. This would increase the risk of inter-granular fracture. Therefore, in terms of suppression of TIP and avoidance of local melting, extremely high solution temperature should be avoided.

Following the solution treatment, an appropriate cooling rate is chosen to provide a specific distribution of intragranular γ′. The rate of cooling from solution temperature determines the initial size, distribution, morphology and volume fraction of γ′. Very often, a tri-modal γ′ distribution (defined by the different size ranges of γ′) would be observed in a polycrystalline nickel-based superalloy after a solution treatment. This usually consists of coarse primary γ′ with sizes from several hundred nanometers (like 500nm) up to microns, secondary γ′ with sizes of 150nm-500nm and tertiary γ′ with sizes smaller than 150nm (usually around 50nm). Increased cooling rate from solution treatment decreases the γ′ size. Quenching in oil is usually used to maximize the cooling rate and thus minimize the size of

secondary γ' precipitates to achieve highest strength. However, rapid quenching in oil from solution treatment can cause quench cracking in thin sections or at corners of complex forging shapes [17]. Significant internal residual stresses also develop from cooling rate gradients that can occur in forgings due to differences in section size. These have been found to produce distortion during machining, which increases the time and cost for component manufacture. In addition, there is some evidence to suggest that fast quenching leaves grain boundary regions free of secondary and tertiary γ', which increases the propensity for inter-granular cracking [64-65]. Using slower rates of cooling, such as air-cooling (AC) could produce a reasonable distribution of γ' precipitates without significant internal residual stresses and consequently, a desirable tensile strength and superior resistance to elevated crack growth.

However, a very slow cooling rate from a high temperature usually leads to formation of an irregular microstructure such as irregular-shaped γ′, fan-type γ-γ′ structure and serrated grain boundaries [66-72]. Formation of serrated grain boundaries is believed to be beneficial for both creep and fatigue crack propagation rates because they could impede grain boundary sliding and crack growth [66-68]. Coarse irregular-shaped γ′ and fan-type γ-γ′ structure usually need to be optimised into fine cuboidal γ′ through proper heat treatment to achieve optimum strength. Also, it is noted that there is considerable debate about the formation mechanism of these irregular microstructures. In terms of the formation mechanism of fan-type γ-γ′ structure, Danflou et al's model [69] suggested that the formation of fan-type structure was a result of discontinuous precipitation and growth due to solute diffusion. Mitchell et al. [71] suggested that the finger-shaped γ′ nucleated at the sites of Hf-enriched particles (carbides or oxides) and assumed that their growth was controlled by a composition gradient.

As for the formation of irregular-shaped γ′, there is extensive evidence that large cuboidal γ′ particles formed during isothermal ageing, break up to form dendritic γ′ or even clusters of smaller γ′ during extended ageing of Ni superalloys [72-74]. It is generally believed that this break up is driven by increased mismatch with coarsening of γ′ particles and consequent instability [73-76]. The detailed splitting mechanism thus involves coarsening to produce a large cuboidal γ′ particle, which with further growth could extend from the corners of the cuboid and then splits into an octet or dendritic γ′. However, the work so far has been mainly focused on elevated temperature isothermal ageing. The microstructural evolution process during continuous slow cooling from supersaturated solid solution is not fully understood. Mitchell et al. [72] conducted study on the samples that were slowly cooled from high temperature to room temperature and suggested the formation of irregular-shaped γ′ during continuous cooling may be attributed to the increased elastic misfit strain as well. Mao et al. [78] studied several interrupted microstructures of a Ni superalloy which corresponded to several temperatures during continuous cooling and suggested the formation of of irregular-shaped γ′ during continuous slow cooling may be due to coarsening or coalescence of the precipitates.

As far as serrated grain boundaries are concerned, Koul et al. [79-80] suggested the formation of grain boundary serrations were due to the movement of primary γ′ particles in the direction of grain boundaries, which was believed to be driven by the strain energy difference between the matrix side and the boundary side of γ′ particle-matrix interface. Henry et al. [69], Danflou [70] and Mitchell et al. [71] argued that the grain boundary serrations were caused by accelerated coarsening of grain boundary γ′ particles or the preferential growth of dendrite arms of the coarsened γ′ particles which gave rise to protuberances along grain boundaries.

2.7.2 The Ageing Treatment Stage

The cooling rate from solution treatment fixes the initial distribution of γ′. The ageing treatment has the effect of causing further nucleation of tertiary γ′ and growth through particle coarsening [63,78]. Therefore, the major objective of the ageing treatment is to maximize γ′ precipitation from still saturated γ matrix caused by the high cooling rate from solution treatment. However, there are many reports suggesting that if the ageing treatment temperature is too high, secondary γ′ could even coarsen and morphology change with ageing progress [63, 78]. Also, if the ageing time is too long, the size of the fine γ′ precipitates could grow beyond the critical value, and overageing and softening occur [63, 78].

2.8 Deformation and Strengthening Mechanisms of Polycrystalline Nickel-based Superalloys

Basically, work hardening of a material is highly dependent on deformation. In polycrystalline nickel-based superalloys, however, the factors which could contribute to strengthening are so considerable that the strengthening mechanisms are far more complicated than deformation mechanisms.

2.8.1 Deformation Mechanisms

It has been shown that at lower temperatures up to 600℃, deformation is dominated by anti-phase boundary (APB) coupled a/2<110> unit dislocations shearing the γ′ in polycrystalline alloys [81-83]. At much higher temperatures (around 800℃), climb by-pass of γ′ precipitates by individual, unpaired a/2<110> dislocations is dominant and the dislocation activity is restricted to the γ channels between the γ′ particles [84]. With respect to casings and disk applications however, this climb by-pass regime appears to be well beyond the practical service temperatures. In the intermediate temperature range between APB shearing and climb by-pass processes, i.e. 650-800°C (depending on the alloy),

deformation can be extremely planar and complex. It is generally believed that deformation in the intermediate temperature range is associated with the formation of a/3<112> stacking fault ribbons through γ′ [85-86]. There has been considerable debate about the mechanism of formation of the a/3<112> dislocation ribbons in polycrystalline nickel-based superalloys. Zhang, et al [85] have suggested that a unit matrix dislocation of a/2<110> dissociated into two partials of a/3<112> and a/6<112>. Stacking faults were created in both γ and γ′ phases, presumably being created by the movement of the leading a/3<112> partial, while the movement of the a/6<112> partial eliminates the stacking fault in the matrix, but leaves a partial dislocation loop around the faulted γ′ precipitates. Viswanathan, et al [86-87] suggested that a/2<110> unit dislocation initiates the shearing process in the matrix. Shearing in γ′ (especially large secondary γ′ precipitates) is accomplished by a/3<112> Shockley dislocations which are the product of the interaction between a/2<110> unit dislocation and a/6<112>. Recently, a rather novel deformation mechanism has been proposed based on the experimental work by Viswanathan [86-88] and Kovarik et al [89]. This mechanism involves the formation of microtwinning in γ′ with twins on the order of 4-50 atomic planes. To be noted, in the immediate temperature range, cross-slip processes may operate. It is emphasized that this temperature regime appears to correspond to the onset of more strongly thermally-activated deformation, and it is therefore essential to understand this with respect to improving the temperature capability of the polycrystalline superalloys.

2.8.2 Strengthening Mechanisms

2.8.2.1. Solid Solution Strengthening

The principal mechanism of strengthening in the disordered γ phase is the introduction of solute atoms of different sizes, which create elastic strains in the crystal. These strains are either tensile or compressive, depending on the size difference between the solute atom and

the parameter of the host lattice. In order to achieve the maximum degree of solid solution strengthening the alloying elements are chosen to provide the largest amount of strain, without precipitation of a new phase. Elements that are commonly used in nickel-base superalloys, which provide varying degrees of solid solution strengthening, are tungsten, molybdenum, chromium and cobalt.

2.8.2.2 Precipitate Hardening by γ′

The contribution to strength by the γ' phase arises due to the precipitates impeding the motion of dislocations, through a variety of mechanisms dependent on factors that may affect the hardening by coherent precipitates. The suggested factors include:

1. Coherency strains,
2. Existence of order in the particles,
3. Differences in elastic moduli between particle and matrix,
4. Difference in stacking fault energy of particle and matrix
5. Energy to create additional particle-matrix interface, and
6. Increases in lattice resistance of particles with temperature.

Among these factors, it now appears that the coherency strains and the presence of order in the particles are the major factors that contribute to strengthening by γ' in nickel-based superalloys [90]. Correspondingly, the coherency strains and anti-phase boundary energies associated with the movement of dislocations through the intermetallic precipitates will be discussed here.

A. Order Strengthening

The presence of coherent precipitates causes dislocations to cut through or bow around them. If a $\frac{a}{2}<1\bar{1}0>\{111\}$ dislocation cuts through the ordered γ', atomic displacements will occur, which leaves behind a surface of disorder, i.e, APB. Order may be restored, by a

second $\frac{a}{2}<1\bar{1}0>\{111\}$ dislocation to remove the APB introduced by the first. Therefore, the dislocations must travel through the γ/γ′ structure in pairs, which has been supported by TEM evidence [81-83]. The associated anti-phase boundary energy represents a barrier which must be overcome if particle cutting is to occur. Actually, it is the energy required to generate the APB that determines the activation energy responsible for γ' shearing and thus caused substantial order strengthening, which is believed to make the largest contribution to the strengthening of nickel-based superalloys [1, 91].

Depending upon the size of the precipitates and the APB energy (and, thus, the equilibrium spacing of paired dislocations), there are several mechanisms that can dictate the dislocation interaction when a pair of dislocations shears a precipitate [92-93]. For small precipitates (less than approximately 20 nm), the pair of dislocations may not lie within an individual precipitate (Figure 2.7 (a)). This case is referred to as weak pair coupling. When the precipitates are larger, the trailing dislocation enters a precipitate before the leading dislocation exits (Figure 2.7 (b)).This situation is referred to as strong pair coupling. Figure 2.7 (c) schematically compares the stress required to push a pair of dislocations though a precipitate for each mechanism as a function of precipitate size. The active mechanism changes from weak pair coupling to strong pair coupling as the γ′ size increases. For small particles, the critical resolved shear stress (CRSS) $\Delta\tau_0$, is determined by the stress necessary to move weakly coupled dislocation pairs, according to [92]

$$\Delta\tau_0 = \frac{1}{2}\left(\frac{\Gamma}{\boldsymbol{b}}\right)^{3/2}\left(\frac{\boldsymbol{b}df}{T}\right)^{1/2}A - \frac{1}{2}\left(\frac{\Gamma}{\boldsymbol{b}}\right)f \qquad \text{Equation 2.1}$$

where Γ is the APB energy of the γ′ in the {111} plane, $\boldsymbol{b}$ is the Burgers vector of the edge dislocation in the γ matrix, d the particle diameter, f the volume fraction of the γ′ precipitates, T the line tension of the dislocation and A a numerical factor depending on the morphology

of the particles. For larger spherical particles, where dislocations cut in strongly coupled pairs, the CRSS is given by [93]

$$\Delta\tau_0 = \left(\frac{1}{2}\right)1.72\,\frac{Tf^{1/2}w}{bd}\left(1.28\,\frac{d\Gamma}{wT}\right)^{1/2} \qquad \text{Equation 2.2}$$

$$T = \left(\frac{Gb^2}{2}\right)$$

where w is a constant which accounts for the elastic repulsion between the strongly paired dislocations, and which is of the order of unity [94]. According to Equations 2.1 and 2.2, weak pair coupling is approximately a function of $d^{1/2}$ and Γ while strong pair coupling is inversely proportional to $d^{1/2}$ but proportional to the square root of Γ. Optimum strength is achieved, for a given volume of γ', when the γ′ is of a size which maximizes the resistance to cutting by weakly coupled dislocation pairs, i.e. at a size which is large enough for cutting by strongly coupled pairs to become favoured [82, 93]. This critical size varies from alloy to alloy. For U720Li superalloy, it was reported to be 40nm [82], while for IN 100, it could be as small as 20nm [83]. If γ' particles are larger than this critical size, then the strength decreases with a further increase in their size whereas if γ' particles are smaller than the critical size, their strength increases with increase in their size prior to the critical size. This shearing mechanism forms the basis of maximizing cooling rate from solution treatment temperature to minimise the size of γ' to achieve maximum strength in practical applications.

However, when the γ' particle size is very big like hundreds of nanometers, the cutting of particles would become very difficult and Orowan bowing mechanism will take over and dislocations will find ways to pass around the particles and consequently an Orowan loop will be created [90]. This Orowan loop exerts a shear stress on the particle. If the particle is strong enough to withstand this stress, then it does not deform and the result is the generation

of an extra dislocation at the particle. The shear stress required for a dislocation to bypass particles is given by Equation 2.3.

$$\tau_{bow} \propto \frac{Gbf^{\frac{1}{2}}}{r} \qquad \text{Equation 2.3}$$

Where γ_0 is the APB energy, G is the shear modulus, b is Burgers vector of the dislocation, r is the particle radius and f is the volume fraction of γ'. To achieve optimum strength, for a given volume of γ', the particle size should be controlled to be small enough to prevent dislocations from bowing.

B. Development of Coherency Strains

The cube-cube orientation of the γ and γ' unit cells facilitates the development of coherency strains, due to the similarities in the lattice parameters of the two phases. Both the magnitude and sign of the mismatch are important in determining the microstructure and the interactions that occur between dislocations and the precipitates. The magnitude of the strengthening effect of γ' is influenced by the mismatch in lattice parameters between the γ' and the γ matrix, which is given by Equation 2.4.

$$\delta = \frac{2(a_{\gamma'} - a_{\gamma})}{a_{\gamma}} \qquad \text{Equation 2.4}$$

where δ is the mismatch and a is the lattice parameter of γ or γ', respectively. Small differences in the lattice parameters of either phase can have a large effect on the mismatch. The γ- γ' mismatch is mainly determined by the composition of the two phases.

The effect of the mismatch on flow stress exerted on dislocations is given by Equation 2.5 below [90].

$$\Delta\tau = AG\delta^{3/2}\left(\frac{rf}{b}\right)^{1/2} \qquad \text{Equation 2.5}$$

Where δ is the mismatch, A=3 for edge dislocations and A=1 for screw dislocations. This equation predicts that the flow stress should increase slightly more rapidly than δ because increasing misfit bends the dislocation more and makes it interact with more regions of adverse stress.

2.8.2.3 Grain Size Hardening

Metals and alloys tested at temperatures below about 0.5Tm (Tm= absolute melting temperature) are further strengthened by the resistance of grain boundaries to dislocation motion. The effect of average grain size on the mechanical strength of an alloy is often modelled using the Hall-Petch equation, which relates the yield strength of an alloy to the grain size.

$$\sigma_y = \sigma_o + \frac{k}{\sqrt{d}} \qquad \text{Equation 2.6}$$

where σ_y is yield stress, d is grain diameter, both σ_o and k are constants, representing a lattice friction stress and the grain boundary resistance, respectively. This equation shows that as the grain size decreases, alloy strength increases. For a fine grained microstructure the grain boundary surface area per unit volume is higher than that in a coarse grained one. The grain boundaries present an impediment to plastic deformation and therefore increase yield strength. However, for good creep resistance a large grain size is preferred [95-97], since grain boundary sliding and cavity formation would become aggravated with increased grain boundary areas, i.e. decreased grain size.

2.8.2.4 Cross-slip-induced hardening

Basically, dislocation slip in the γ and γ' phase occur on the {111} glide plane in the <110> direction. However, there is a tendency with increasing temperature for dislocations in the γ' phase to cross-slip on to the {100} planes where they have a lower anti-phase domain boundary energy. Situations arise where the extended dislocation is then partly on the close-

packed plane and partly on the cube plane. Such a dislocation becomes locked, leading to an increase in strength of materials at elevated temperatures [98].

In practice, the nucleation, growth, and coarsening of precipitates during a particular heat treatment process typically results in a characteristic precipitate distribution. Variation in precipitate size will inevitably lead to the operation of different mechanisms. Different strengthening mechanisms make their own contributions to the materials strengthening. Kazor et al established a comprehensive model by taking into account different factors, which offers a method for the prediction for the contribution of each strengthening mechanism to yield strength as well as the dominant strengthening mechanism [83].

2.9 Mechanical behaviours of nickel-based superalloys

2.9.1 Tensile Properties

For gas turbine applications, tensile properties are usually one of the major requirements for many components. Firstly, the yield stress of the materials must be sufficient to ensure that the stresses experienced do not exceed this value during operating conditions. Secondly, there must be sufficient ductility in the material to allow for some plastic deformation whilst not compromising critical tolerances. The microstructure of the material is responsible for all of these properties.

According to Kozar et al.'s modelling, which was established to assess the contribution of each specific feature of the microstructure to the overall strength of the material [83], it was suggested that Hall–Petch effects and precipitate shearing are the two most influential factors for the strength of a polycrystalline nickel-base superalloy. Apparently, the grain size and γ' size and distribution are two predominant microstructure features affecting the strength of a nickel-base superalloy.

For nickel-based superalloys, it was found that the yield and fracture properties are slightly temperature dependent. In the majority of materials like nickel, strength decreases and ductility increases with increasing temperature. However, the strength response of nickel-base superalloys containing a significant volume fraction of γ′, is anomalous in that the yield stress increases with temperature up to about 700℃, see Figure 2.8 [99-100]. This is believed to be due to the ease with which dislocations can cross-slip onto {001}. Cross-slip strengthens with increasing temperature up until a certain point. The overall result of cross-slip is increased hardening.

2.9.2 Creep behaviour

Creep is the time-dependent plastic deformation of a material, under the action of an applied load at elevated temperature. At the rear part of casings the material operating temperature may potentially be in excess of $0.5T_m$, where T_m is the melting temperature in Kelvin. This environment of relatively low mechanical loading and high temperature leads to thermally assisted movement of dislocations and results in creep deformation. Creep tests are conducted by subjecting a specimen of known geometry to a constant tensile or compression load and measuring the strain evolution as a function of time. A typical creep curve showing the macroscopic deformation response is shown in Figure 2.8. As soon as the load is applied, there is an instantaneous elastic response, followed by a period of primary transient creep (Stage I). Initially the rate is high, but it gradually decreases to a secondary steady state (Stage II). Finally the strain rate may increase again (Stage III), accelerating until failure occurs.

A. Primary Creep

As the load is applied to the specimen it experiences an initial strain, corresponding to ε_0 in Figure 2.9. This strain is elastic, but may extend marginally into the plastic range. Primary

creep is characterized by a period of decreasing creep rate during which the strain hardening is occurring more rapidly than softening due to the high temperature.

B. Secondary Creep

This region is characterized by a constant creep rate as strain hardening and recovery mechanisms operate simultaneously. Deformation results in strain hardening due to the generation and movement of dislocations. During steady state creep however, these mechanisms are balanced by dislocation recovery processes, such as climb and cross slip. This results in dislocations acquiring lower energy arrangements or annihilating one another. The gradient of this part of the creep curve is commonly used as the minimum creep rate for design purposes.

C. Tertiary Creep

Tertiary creep is characterized by an increase in strain rate. The rapid acceleration can be attributed to a number of various factors:

i. The microstructural instability from prolonged high temperature exposure
ii. Gradual increases in true stress levels due to the decrease in cross-sectional area (under constant strain (for tensile creep testing)
iii. Stress concentration at cracks or cavities developed in the grain boundaries

All of the damage mechanisms lead to complete fracture of the specimen when the remaining load bearing material is unable to support the applied load.

2.9.2.1 Creep mechanisms

The mechanisms which may operate in a given alloy system are dependent on the microstructure, in particular the structure and number of grain boundaries. This is because only a finite amount of strain is accommodated internally within the grain. Dominant creep mechanisms that operate are governed by temperature and strain rate [101].

A. Dislocation creep

Dislocation creep involves the movement of dislocations, which overcome barriers by thermally assisted mechanisms associated with the diffusion of vacancies or interstitials. This type of creep is a combination of dislocation glide and vacancy diffusion. A dislocation will move by action of the glide process until it encounters an obstacle, such as a γ′ precipitate or a solute atom. The γ′ precipitate will pin the dislocation until the external stress and any thermally activated diffusion process, can cause the dislocation to overcome it. At high temperature the predominant mechanism for overcoming obstacles is dislocation climb, which requires diffusion of vacancies to the dislocation [102]. With climb, the creep rate is not dependent on the grain size, but the rate of climb does depend very strongly on the stress,

Equation 2.7

The value of m is approximately 5 for climb-controlled creep. Because climb depends on diffusion of vacancies, the constant A_s has the same temperature dependence as lattice diffusion. At lower temperatures, creep is not entirely climb-controlled and higher exponents are observed [103].

B. Diffusion-controlled creep

Diffusion creep involves the diffusion of atoms and vacancies within materials. A single grain within a polycrystalline material is subject to both a tensile and compressive stress. Tensile stress increases the separation of atoms on grain boundaries that are normal to the stress axis, and the Poisson contraction (compressive stress) decreases the separation of atoms on grain boundaries that are parallel to the stress axis. The result is a driving force for diffusion transport of atoms from grain boundaries parallel to the tensile stress to boundaries normal to the tensile stress. Correspondingly, there is a flow of vacancies in the opposite

direction. Such diffusion produces a plastic elongation as shown in Figure 2.10. The specimen elongates as atoms are added to grain boundaries perpendicular to the stress.

The atomic transport involving this process is accomplished by both bulk diffusion and grain boundary diffusion. Both kinds of diffusion are highly dependent on the grain size. Therefore, the creep rate is highly dependent on grain size and the magnitude of the external load.

If the creep occurs by diffusion through the crystal, it is called Nabarro-Herring creep. The strain rate can be expressed by

$$\dot{\varepsilon} = A_L(\sigma / d^2)D_L \qquad \text{Equation 2.8}$$

where A_L is a constant and D_L, the lattice diffusivity

On the other hand, if creep occurs by diffusion along the grain boundaries, it is called Coble creep and the creep rate is given by

$$\dot{\varepsilon} = A_G(\sigma / d^3)D_{gb} \qquad \text{Equation 2.9}$$

where D_{gb} is the diffusivity along grain boundaries, and A_G is a constant.

The ratio of lattice diffusion to grain boundary diffusion increases with temperature because the activation energy for grain boundary diffusion is always lower than that for lattice diffusion. Therefore Coble creep is more important at low temperatures and Nabarro-Herring creep at high temperatures.

Equations 2.7 through 2.9 predict creep rates that depend only on stress and temperature and not on strain. Thus, they apply only to secondary creep stage. Equation 2.8 and Equation 2.9 also revealed the significant dependence of creep rate on grain size, especially when diffusion-controlled creep is involved.

C. Grain boundary sliding

In polycrystalline materials, grain boundary sliding is a thermally activated viscous flow in nature. The strain rate attributable to grain boundary sliding can be written as

$$\dot{\varepsilon} \propto (1/d)\exp[(-Q_v/(RT)] \quad \text{Equation 2.10}$$

If grain boundary sliding were the only active mechanism, there would be an accumulation of material at one end of each boundary on which sliding occurred and a deficit at the other end, as sketched in Figure 2.11. This incompatibility must be relieved by another deformation mechanism, one involving dislocation motion, diffusion, or grain boundary migration. Otherwise, damage accumulates along the boundaries and finally leads to the initiation and growth of cavities or cracks at grain boundaries, which is blamed for the failure of most polycrystalline superalloys under creep conditions.

2.9.2.2 Creep deformation in Nickel-base Superalloys

Creep deformation is known to be highly sensitive to microstructure of a material, especially grain size, grain boundary structure and precipitates. It is generally believed that a microstructure with coarse grains is usually more creep resistant than fine grains [100]. This occurs because the prominent formation of creep damage in polycrystalline nickel alloys is creep cavitation at the γ grain boundaries due to grain boundary sliding and this becomes less influential as the grain size increases. Grain boundary structure has also been found to be important for creep properties. It was reported that the presence of carbides and/or borides and γ′ at grain boundaries acts to impede grain boundary sliding and cavity nucleation and thus lead to decrease of the secondary creep rate [101-103]. Development of grain boundary serrations was also found to impede grain boundary sliding and thus considerably reduced the creep rate [66-68, 104].

Precipitate hardening is also significant for creep deformation. This is mainly due to the complex interactions between dislocations and γ′ precipitates, which have been reviewed above.

2.10 The Aim of This Project

The aim of this project is to investigate the influence of HIPping processing conditions and the subsequent heat treatments on the resultant microstructure and mechanical properties of RR 1000 powder superalloy. Through the investigation, an optimum process-route which would lead to desirable combination of properties is expected to be developed for the net-shape HIPping of a turbine engine component, such as combustion casing or turbine engine disc. Given the service condition for the turbine engine components, good mechanical properties such as tensile, creep and fatigue properties are essential and thus will be extensively evaluated. A list including general property requirements for the materials used for future combustion casings is shown in Appendix A.

References

[1] Reed RC. The superalloys: fundamentals and applications. Cambridge: Cambridge University Press; 2006; p. 217-237.

[2] Moll JH, Conway JJ. Characteristics and properties of as-HIP P/M alloy 720. In: Pollock CM, Kissinger RD, Bowman RR, et al, editors. Superalloys 2000. Warrendale, PA: The Minerals, Metals and Materials Society (TMS); 2000. p. 135-142.

[3] Moll JH, Conway JJ, McTieman BJ. As-HIP P/M Superalloys: A Technical and Commercial Success. Advances in Powder Metallurgy and Particulate Materials 1999; 2: 4-75.

[4] Baccino R, Moret F, Fellerin F, Guichard D, Raisson G. High performance and high complexity net shape parts for gas turbines: the ISOPREC powder metallurgy process. Materials and Design 2000; 21: 345–350.

[5] Voice W, Hardy M, Rugg D. Development of Powder Consolidated Components for the Gas Turbine Engine. In: Powder Metallurgy World Congress & Exhibition (PM2004) 2004: p. 6-11.

[6] Arzt E, Ashby MF, Easterling KE. Practical application of hot isostatic pressing diagrams: four case studies. Metallurgical Transaction A 1983; 14: 211–221.

[7] Jinka AGK, Lewis RW. Finite element simulation of hot isostatic pressing of metal powders. Computer Methods in Applied Mechanics and Engineering 1994; 114: 249–272.

[8] Haggblad HA, Li WB. A micro mechanical based constitutive model for finite element simulation of hot isostatic pressing of powder. Computer Methods in Applied Mechanics and Engineering 1995; 128: 191-198.

[9] Svoboda A, Haggblad HA, Karlsson L, Simulation of hot isostatic pressing of a powder metal component with an internal core, Computer Methods in Applied Mechanics and Engineering 1997; 148: 299–314.

[10] Baccino R, Moret F. Numerical modeling of powder metallurgy processes. Materials and Design 2000; 21: 359-364.

[11] Konak A, Konak SK, Smith A, Nettleship I. Estimation of shrinkage for near net-shape using a neural network approach. Journal of Intelligent Manufacturing 2003; 14: 219-228.

[12] Yuan WX, Mei J, Samarov V, Seliverstov D, Wu X. Computer modelling and tooling design for near net shaped components using hot isostatic pressing. Journal of Materials Processing Technology 2007; 182: 39–49.

[13] Benz MG. Preparation of clean superalloys. In: Briant CL, editor. Impurities in Engineering Materials: Impact, Reliability and Control. New York: Marcer Dekker Inc.; 1999. p. 31-47.
[14] Turillon PP. Evaporation of elements from 80/20 nickel-chromium during vacuum induction melting. In: Transaction of the Sixth International Vacuum Metallurgy conference . New York: American Vacuum Society; 1963.p. 88-102.
[15] Borofka JC, Tien JK, Kissinger RD. Powder metallurgy and oxide dispersion processing of superalloys. In: Tien JK, Caulfield T, editors. Superalloys, Supercomposites and superceramics. San Diego: Academic Press; 1989. p. 237-284.
[16] Ferguson BL. Aerospace applications. In ASM Handbook Volume 7: Powder metallurgy, 6th Edition Materials Park, OH: ASM International; 1997. p. 646-656.
[17] Hardy MC, Zirbel B, Shen G, Shankar R. Developing damage tolerance and creep resistance in a high strength nickel alloy for disc applications. In: Green KA, Pollock TM, Harada H, editors: Superalloys 2004. Warrendale, PA: The Minerals, Metals and Materials Society (TMS); 2004. p. 83-90.
[18] Chang DR, Krueger DD, Sprague RA. Superalloy Powder Processing, Properties and Turbine Disk Applications. In: M. Gell, C.S. Kortovich, R.H. Bricknell, W.B. Kent, and J.F. Radavich, editors: Suneralloys 1984, Proceedings of the Fifth International Symposium on Superalloys. Warrendale, PA: TMS-AIME; 1984. p. 245-273.
[19] Bashir S, Taupin P, Antolovich SD. Low Cycle Fatigue of As-HIP and HIP+Forged Rene 95. Metallurgical Transactions A 1979; 10: 1481-1490.
[20] Jablonski DA. The Effect of Ceramic Inclusions on the Low Cycle Fatigue Life of Low Carbon Astroloy Subjected to Hot Isostatic Pressing. Materials Science & Engineering A 1981; 48: 189-198.
[21] Hyzak JM, Bernstein IM. The effect of defects on the fatigue crack initiation process in two P/M superalloys: Part1, Fatigue Origins. Metallurgical Transactions A 1982; 13: 33-43.
[22] Hyzak JM, Bernstein IM. The effect of defects on the fatigue crack initiation process in two P/M superalloys: Part2, surface-subsurface transition. Metallurgical Transactions A 1982; 13: 45-52.
[23] Shamblen CE et al. Effect of inclusions on LCF life of HIP Plus heat treated powder metal Rene95. Metallurgical Transactions B 1985;168: 775-784.
[24] Lautridou JC, Guedou JY, Honnorat Y. Effect of Inclusions on LCF life of PM Superalloys for Turboengine Discs. In: Bachelet E et al, editors. High Temperature Materials for Power Engineering. London, UK: Kluwer Academic Publishers; 1990.p.1163-1172.

[25] Roth PG, Murray JC, Morra JE, Hyzak JM. Heavy Liquid Separation: A Reliable Method to Characterize Inclusions in Metal Powder. In: Characterization, Testing and Quality Control, Advances in Powder Metallurgy and Particulate Materials. Princeton, NJ: Metal Powder Industries Federation; 1994;2: p.1-12.
[26] Huron ES, Roth PG. The Influence of Inclusion on Low Cycle Fatigue Life in a P/M Nickel-Base Disc Superalloy. In: Kissinger RD, Deye DJ, Anton DL, Nathal MV, Pollock TM, Woodford DA editors. Superalloys 1996. Warrendale, Pennsylvania, USA: The Minerals, Metals and Materials Society; 1996.p. 359-368.
[27] Xie XS, Zhang LN, Zhang MC, Dong JX, Bain K. Micro-mechanical behaviour study of non-metallic inclusions in P/M disc superalloy Rene 95. In: Green KA, Pollock TM, Harada H, editors. Superalloys 2004. Warrendale, Pennsylvania, USA: The Minerals, Metals and Materials Society; 2004.p. 451-458.
[28] Miller GA, Green KA, Banik A, Lemsky J, Richardson GY. Enhanced Powder Metallurgy (P/M) Processing of Udimet 720 AE1107C (T406) Turbine Disks. In: Chang KM, Srivastava SK, Furrer DU, Bain KR, editors. Advanced Technologies for Superalloy Affordability. Warrendale, Pennsylvania, USA: The Minerals, Metals and Materials Society; 2000. p. 37-48.
[29] Stence JM, Li TX, Neathery JK, Lherbie LW. Removal of ceramic defects from a superalloy powder using triboelectric processing. In: Pollock TM, Kissinger RD, Bowman RR, Green KA, et al, editors. Superalloys 2000. Warrendale, Pennsylvania, USA: The Minerals, Metals & Materials Society; 2000. p. 95-99.
[30] Thamburaj R, Kroul AK, Wallace W, Malherbe MC. Prior Particle Boundary Precipitation in P/M Superalloys. In: Aqua N, Charles L, editors. Modern Developments in Powder Metallurgy 1984. Princeton, New Jersey: Metal Powder Industries and the American Powder Metallurgy Institute; 1984.p. 635-674.
[31] Larson JM. Carbide Morphology in P/M IN-792. Metallurgical Transaction A 1976; 7: 1497-1502.
[32] Rao GA, Satyaprasad K, Kumar M, Srinivas M, Sarma DS. Characterization of hot isostatically pressed nickel base superalloy Inconel 718. Materials Science and Technology 2003; 19: 313–321.
[33] Menzies RG, Bricknell RH, Craven AJ. STEM microanalysis of precipitates and their nuclei in a nickel-base superalloy. Philosophy Magazine A 1980; 41: 493-508.

[34] Ingesten NG, Warren R, Winberg L. The nature and origin of previous particle boundary precipitates in P/M superalloys. Advanced materials, manufacturing, and testing information analysis center 1982:1013-1026.
[35] Dahlen M, Ingesten NG, Fishchmeister H. Parameters influencing particle boundary precipitation in superalloy powders. In: H.H. Hausner, H.W. Antes, G.D. Smith, editors. Modern Developments in Powder Metallurgy 1980. Washington, D.C: the Metal Powder Industries Federation and the American Powder Metallurgy Institute, 1981; 14: 3-14.
[36] Rao GA, Srinivas M, Sarma DS. Effect of oxygen content of powder on microstructure and mechanical properties of hot isostatically pressed superalloy Inconel 718. Materials Science and Engineering A 2006; 435-436: 84-89.
[37] Williams DL. Hot isostatically pressed alloy APK1, a nickel-based superalloy. Powder Metallurgy 1977; 2: 84-89
[38] Podob MT. Effect of heat treatment and slight chemistry variations on the physical metallurgy of hot isostatically pressed low carbon astrology powder. Modern Developments in Powder Metallurgy 1975; 11: 25-44
[39] Rao GA, Srinivas M, Sarma DS. Effect of solution treatment temperature on microstructure and mechanical properties of hot isostatically pressed superalloy Inconel 718. Materials Science and Technology 2004; 20: 1161-1170.
[40] Radavich J, Furrer D. Assessment of Russian P/M superalloy EP741NP. In: Green KA, Pollock TM, Harada H, editors. Superalloys 2004. Warrendale, Pennsylvania, USA: The Minerals, Metals and Materials Society; 2004.p. 381-390
[41] Rao GA, Kumar M, Srinivas M, Sarma DS. Effect of standard heat treatment on the microstructure and mechanical properties of hot isostatically pressed superalloy inconel 718. Materials Science and Engineering A 2003; 355: 114-125.
[42] Lu TC, Nguyen TT, Bienvenu Y, Davidson JH, Dugue O. The influence of powder processing variables on the structure and properties of HIPed low carbon Astroloy. In: Nihoul J, Ward J, editors. High temperature alloys: their exploitable potential. London and New York: Elsevier Applied Science; 1988. p. 297-305.
[43] Maurer GE, Castledine W, et al. Development of HIP consolidated P/M superalloys for conventional forging to gas turbine engine components. In: Kissinger RD, Deye DJ, Anton DL, Nathal MV, Pollock TM, Woodford DA editors. Superalloys 1996. Warrendale, Pennsylvania, USA: The Minerals, Metals and Materials Society;1996:p. 645-652.

[44] Hack GAJ, Eggar JW, Symonds CH. A comparison of APK- 1 consolidated at HIP temperatures above and below the boride solvus. In: Proceedings, Powder Metallurgy Superalloys; Zurich; 1980. p. 20.1-20.50.

[45] Gessinger GH. Mechanical properties of dispersoid-free P/M superalloys. In: Gessinger GH, editor. Powder Metallurgy of Superalloys. Cambridge: Cambridge University Press; 1984. p. 136-137.

[46] Atkinson HV, Davies S. Fundamental aspects of hot isostatic pressing: an overview Metallurgical and Materials Transactions A 2000;31:2981-3000.

[47] Huron ES, Casey RL, Henry MF, Mourer DP. The influence of alloy chemistry and powder production methods on porosity in a P/M nickel-base superalloy. In: Kissinger RD, Deye DJ, Anton DL, Nathal MV, Pollock TM, Woodford DA editors. Superalloys 1996. Warrendale, Pennsylvania, USA: The Minerals, Metals and Materials Society;1996. p. 645-652.

[48] Huron ES, Bain KR, Mourer DP, Schirra JJ, Reynolds PL, Montero EE. The influence of grain boundary elements on properties and microstructures of P/M nickel base superalloys. In: Green KA, Pollock TM, Harada H, editors: Superalloys 2004. Warrendale, PA: The Minerals, Metals and Materials Society (TMS); 2004. p. 381-390.

[49] Swinkels FB, Wilkinson DS, Arzt E, Ashby MF. Mechanisms of hot-isostatic pressing. Acta Metallurgica 1983; 31:1829-1840.

[50] Kissinger RD, Nair SV, Tien JK. Influence of powder particle size distribution and pressure on the kinetics of hot isostatic pressing (HIP) consolidation of P/M superalloy Rene 95. Materials Research Society Proceeding 1984; 28:285-294.

[51] Ross EW, Sims CT. Nickel-base Alloy. In: Sims CT, Stoloff NS, Hagel WC, editors. Superalloys, 2nd. New York, USA: John Wiley & Sons; 1987. p.98-122.

[52] Gessinger GH. Mechanical properties of dispersoid-free P/M superalloys. In: Gessinger GH, editor. Powder Metallurgy of Superalloys. Cambridge: Cambridge University Press; 1984. p. 157-161.

[53] Blackburn MJ, Sprague RA. Production of components by hot isostatic pressing of nickel-base superalloy powders. Metals Technology 1977;8: 388-395.

[54] Podop, MT. Effect of heat treatment and slight chemistry variations on the physical metallurgy of hot isostatically pressed low carbon astrology powder. In: Hausner HH, Taubenblat PV, editors. Modern Developments in Powder Metallurgy. Princeton, New Jersey: Metal powder industries federation and the American Powder Metallurgy Institute;1977;11: 25-44.

[55] Eng RD, Evans DJ. High strength HIP consolidation MERL 76 disks. In: Green KA, Pollock TM, Harada H, editors. Superalloys 1980. Warrendale, PA: The Minerals, Metals and Materials Society (TMS);1980. p. 491-500.
[56] Ducrocq C, Lasalmonie A, Honnorat Y. N18: a new damage tolerant P/M superalloy for high temperature turbine discs. In: Reichman S, Duhl D, Maurer G, Antolovich S, Lund C, editors. Superalloys 1988. Warrendale, PA: The Minerals, Metals and Materials Society (TMS); 1988. p. 63-72.
[57] Krueger DD, Kissinger RD, Menzies RG. Development and introduction of a damage tolerant high temperature nickel-base disk alloy Rene 88DT. In: Antolovich SD, Stusrud RW, Mackay RA, editors. Superalloys 1992. Warrendale, PA: The Minerals, Metals and Materials Society (TMS);1992. p. 277-286.
[58] Huron ES, Bain KR, Mourer DP. The influence of grain boundary elements and microstructures of P/M nickel-base superalloys. In: Green KA, Pollock TM, Harada H, editors: Superalloys 2004. Warrendale, PA: The Minerals, Metals and Materials Society (TMS); 2004. p. 73-82.
[59] Reed RC, Jackson MP, Na YS. Characterization and modeling of the precipitation of the sigma phase in Udimet 720 and Udimet 720Li. Metallurgical and Materials Transaction **A** 1999;30:521-533.
[60] Saunders N. Phase Diagram Calculations for Ni-Based Superalloys. In: Kissinger RD, Deye DJ, Anton DL, Nathal MV, Pollock TM, Woodford DA editors. Superalloys 1996. Warrendale, Pennsylvania, USA: The Minerals, Metals and Materials Society;1996:p. 101-110.
[61] Keefe PW, Mancuso SO, Maurer GE. Effects of Heat Treatment and Chemistry on the Long-Term Phase Stability of a High Strength Nickel-Based Superalloy. In: Antolovich SD, Stusrud RW, Mackay RA, Anton DL, Khan T, Kissinger RD, Klarstrom DL, editors. Superalloys 1992. Warrendale, PA: The Minerals, Metals and Materials Society (TMS);1992. p. 487–496.
[62] Bhadeshia HKDH. Nickel Based Superalloy [online]. [cited 2010 Feb 20]. Available from URL: http://www.msm.cam.ac.uk/phase-trans/2003/Superalloys/superalloys.html.
[63] Mitchell RJ. Development of a new powder processed Ni-base superalloy for rotor disc application, PhD thesis, 2004.
[64] Kane WM, Krupp U, Jacobs T, McMahon CJ. On the mechanism of quench cracking in Rene 95 nickel-based superalloy. Materials Science and Engineering A 2005;402: 42–46.

[65] Mao J, Chang KM, Furrer D. Quench cracking characterization of superalloys using fracture mechanics approach. In: Pollock TM, Kissinger RD, Bowman RR, Green KA, et al, editors. Superalloys 2000. Warrendale, Pennsylvania, USA: The Minerals, Metals & Materials Society; 2000:109-116.
[66] Larson JM, Floreen S. Metallurgical factors affecting the crack growth resistance of a superalloy. Metallurgical Transactions A 1977;8: 51-55.
[67] Koul AK, Au P, Bellinger N, Thamburaj R, Wallace W, Immarigeon JP. Development of a damage tolerant microstructure for Inconel 718 turbine disc material. Superalloys 1988, Ed. Duhl DN et al., TMS-AIME, 1988, 3-12.
[68] Zhiping M, Ruizeng Y, Lian G. Effect of zigzag grain boundary on creep and fracture behaviours of wrought γ′ strengthened superalloy. Materials Science and Technology 1988; 4:540-547.
[69] Henry MF, Yoo YS, Yoon DY, Choi J. The dendritic growth of γ' precipitates and grain boundary serration in a model nickel-base superalloy. Metallurgical Transaction A 1993; 24: 1733-1743.
[70] Danflou HL, Macia M, Sanders TH, Khan T. Mechanisms of formation of serrated grain boundaries in nickel base superalloys. In: Kissinger RD, Deye DJ, Anton DL, Nathal MV, Pollock TM, Woodford DA editors. Superalloys 1996. Warrendale, Pennsylvania, USA: The Minerals, Metals and Materials Society; 1996:p. 119-127.
[71] Mitchell RJ, Li HY, Huang ZW. On the formation of serrated grain boundaries and fan type structures in an advanced polycrystalline nickel-base superalloy. Journal of materials processing technology 2009; 209: 1011–1017
[72] Mitchell RJ, Hardy MC, Preuss M, Tin S. Influence of composition and cooling rate on constrained and unconstrained lattice parameters in advanced polycrystalline nickel–base superalloys. Materials Science and Engineering A 2006; 423: 282–291
[73] Doi M, Miyazaki T, Wakatsuki T. The effect of elastic interaction energy on the morphology of γ′ Precipitates in Nickel-based Alloys. Materials Science and Engineering A 1984; 67: 247-253
[74] Ricks RA, Porter AJ and Ecob RC. The growth of γ′ precipitates in nickel-base superalloys. Acta metallurgica 1983; 31:43-53.
[75] Khachaturyan AG, Semenovskaya SV, Morris JW. Theoretical analysis of strain-induced shape changes in cubic precipitates during coarsening. Acta metallurgica 1988; 36: 1563-1572

[76] Lee JK. Splitting of coherent precipitates caused by elastic non-equilibrium. Theoretical and Applied Fracture Mechanics 2000;33:207-217
[77] Cha PR, Yeon DH, Chung SH. Phase-field study for the splitting mechanism of coherent misfitting precipitates in anisotropic elastic media. Scripta Materialia 2005; 52: 1241–1245
[78] Mao J, Chang KM, Yang W, Ray K, Vaze SP, Furrer DU. Cooling precipitation and strengthening study in powder metallurgy superalloy U720LI. Metallurgical and Materials Transactions A 2001; 32:2441–2452.
[79] Koul AK, Thamburaj R. Serrated grain boundary formation potential of Ni-based superalloys and its implications. Metallurgical and Materials Transactions **A** 1985; 16: 17-26.
[80] Koul AK, Gessinger GH. On the mechanism of serrated grain boundary formation in Ni-based superalloys. Acta Metallurgica 1983;31: 1061–1069.
[81] Reppich B, Schepp P, Wehner G. Some new aspects concerning particle hardening mechanisms in γ′ precipitating Ni-base alloys-II Experiments. Acta Metallurgica 1982;30:95-104.
[82] Jackson MP, Reed RC. Heat treatment of UDIMET 720Li: the effect of microstructure on properties. Materials Science and Engineering A 1999;259:85–97
[83] Kozar RW, Suzuki A, Milligan WW, Schirra JJ, Savage MF, Pollock TM. Strengthening mechanisms in polycrystalline multimodal Nickel-Base superalloys. Metallurgical and Materials Transactions A 2009; 40:1588-1603
[84] Manonukul A, Dunne FPE, Knowles D. Physically based model for creep in Ni-base superalloy C263 both above and below the gamma solvus. Acta materialia 2002; 50: 2917-2931.
[85] Zhang YH, Chen QZ, Knowles DM. Mechanism of dislocation shearing of gamma in fine precipitate strengthened superalloy. Materials Science and Technology 2001;17: 1551-1555.
[86] Viswanathan GB, Sarosi PM, Henry MF, Whitis DD, Milligan WW, Mills MJ. Deformation mechanisms at intermediate creep temperatures in René 88 DT. In: Green KA, Pollock TM, Harada H, editors: Superalloys 2004. Warrendale, PA: The Minerals, Metals and Materials Society (TMS); 2004. p. 173-178.
[87] Viswanathan GB, Sarosi PM, Henry MF, Whitis DD, Milligan WW, Mills MJ. Investigation of creep deformation mechanisms at intermediate temperatures in René 88 DT. Acta Materialia 2005;53:3041-3057.

[88] Viswanathan GB, Karthikeyan S, Sarosi PM, Unocic RR, Mills MJ. Microtwinning during intermediate temperature creep of polycrystalline Ni-based superalloys: mechanisms and modelling. Philosophical Magazine 2006;86:4823-4840.
[89] Kovarik L, Unocic RR, Li J, Sarosi P, Shen C, Wang Y, Mills MJ. Microtwinning and other shearing mechanisms at intermediate temperatures in Ni-based superalloys. Progress in Materials Science 2009;54: 839–873
[90] Stoloff NS. Fundamentals of strengthening. In: Sims CT, Stoloff NS, Hagel WC, editors. Superalloys, 2nd. New York, USA: John Wiley & Sons; 1987. p.61-95.
[91] Stoloff NS. Ordered alloys-physical metallurgy and structural applications. International Metal Reviews 1984;29:123-135.
[92] Brown LM, Ham RK. Strengthening mechanisms in crystals. London: Applied Science; 1971.
[93] Huther W. Reppich B. Interaction of dislocations with coherent, stress-free ordered particles. Z. Metallkd 1978;69:628–634.
[94] Reppich B, Schepp P, Wehner G. Some new aspects concerning particle hardening mechanisms in γ′ precipitating Ni-base alloys-I Theoretical Experiments. Acta Metallurgica 1982;30:95-104.
[95] Krueger DD, Antolovich SD, Stone RHV. Effects of grain size and precipitate size on the fatigue crack growth behaviour of alloy 718 at 427℃. Metallurgical Transactions A 1987; 18:1431-1449.
[96] Gibbons TB, Hopkins BE. The influence of grain size and certain precipitate parameters on the creep properties of Ni-Cr-base alloys. Metal Science Journal 1971;5:233-240.
[97] Torster F, Baumeister G, Albrecht J, Lutjering G, Helm D, Daeubler MA. Influence of grain size and heat treatment on the microstructure and mechanical properties of the nickel-base superalloy U720Li. Materials Science and Engineering A 1997; 234-236:189-192.
[98] Takeuchi S, Kuramoto E. Temperature and orientation dependence of the Yield Stress in Ni_3Ga Single Crystals. Acta Metallurgica 1973;21: 415–425.
[99] Pope DP, Ezz SS. Mechanical properties of Ni3Al and nickel-base alloys with high volume fraction of gamma-prime. International metals review 1984; 29:136-167.
[100] Gibbons TB, Hopkins BE. Creep behaviour and microstructure of Ni-Cr base alloys. Metal Science 1984;18;273-280.
[101] Blum W, Reppich B. Creep of particle-strengthened alloys. In: Whilshire B, Evans RW. Creep behaviour of crystalline solids; 1985.p. 83-136.

[102] Koul AK, Wallace W. A note on the microstructural dependence of creep strength in Inconel 700. Metallurgical Transactions A 1982;13A: 673-675.
[103] Wu XJ, Koul AK. Grain boundary sliding in the presence of grain boundary precipitates during transient creep. Metallurgical and Materials Transactions A 1995; 26A: 905-914.
[104] Larson JM. Carbide Morphology in P/M IN-792. Metallurgical Transactions A 1976;7: 1497-1502

Table 2.1 Function of various elements in nickel-based superalloys

Effect		**Elements**
γ solid-solution elements		Co, Fe, Cr, Mo, W
γ′-forming elements		Al, Ti, Ta
γ′′-forming elements		Nb, V
Carbide-forming elements	MC type	Ti, Ta, Hf, Nb, Mo, W
	$M_{23}C_6$ type	Cr, Mo, W
	M_6C type	Ni, Co, Mo, W
Grain boundary strengthening elements		Zr, Hf, B, C
Topologically close-packed phase elments		Cr, Mo, W, Ni, Co
Elements good for oxidation resistance		Al, Cr

Table 2.2 Compositions of the early powder metallurgy alloys (wt%)

Alloys	Cr	Co	Mo	W	Nb	Hf	Al	Ti	Fe	V	C	B	Zr	Ni
Waspaloy	19.5	13.5	4.3	-	-	-	1.3	3.0	-	-	0.08	0.006	-	Bal.
Inconel 718	19.0	-	3.0	-	5.1	-	0.5	0.9	18.5	-	0.04	-	-	Bal.
Astroloy	15.0	17.0	5.3	-	-	-	4.0	3.5	-	-	0.06	0.03	-	Bal.
LC Astroloy	15.1	17.0	5.2	-	-	-	4.0	3.5	-	-	0.023	0.024	0.01	Bal.
IN 100	10.0	15.0	3.0	-	-	-	5.5	4.7	-	1.0	0.18	0.014	0.06	Bal.
modified IN 100	12.4	18.5	3.2	-	-	-	5.0	4.3	-	0.8	0.07	0.02	0.06	Bal.
MERL 6	11.9	18.0	2.8	-	1.2	0.3	4.9	4.2	-	-	0.015	0.016	0.04	Bal.
Rene 95	14.0	8.0	3.5	3.5	3.5	-	3.5	2.5	-	-	0.08	0.010	0.05	Bal.

Table 2.3 Chemical compositions in wt% of some advanced nickel-base P/M superalloys

Alloy	Cr	Co	Mo	W	Nb	Al	Ti	Ta	Hf	C	B	Zr	Ni
N18	11.5	15.7	6.5	0.6	-	4.35	4.35	-	0.45	0.015	0.015	0.03	Bal.
Rene 88DT	16.0	13.0	4.0	4.0	0.7	2.1	3.7	-	-	0.03	0.015	0.03	Bal.
Udimet 720	17.9	14.7	3.0	1.25	-	2.5	5.0	-	-	0.035	0.033	0.03	Bal.
Udimet 720LI	16.0	15.0	3.0	1.25	-	2.5	5.0	-	-	0.025	0.018	0.05	Bal.
ME3	13.1	18.2	3.8	1.9	1.4	3.5	3.5	2.7	-	0.03	0.03	0.05	Bal.
RR 1000	15.0	18.5	5.0	-	-	3.0	3.6	2.0	0.5	0.027	0.015	0.06	Bal.

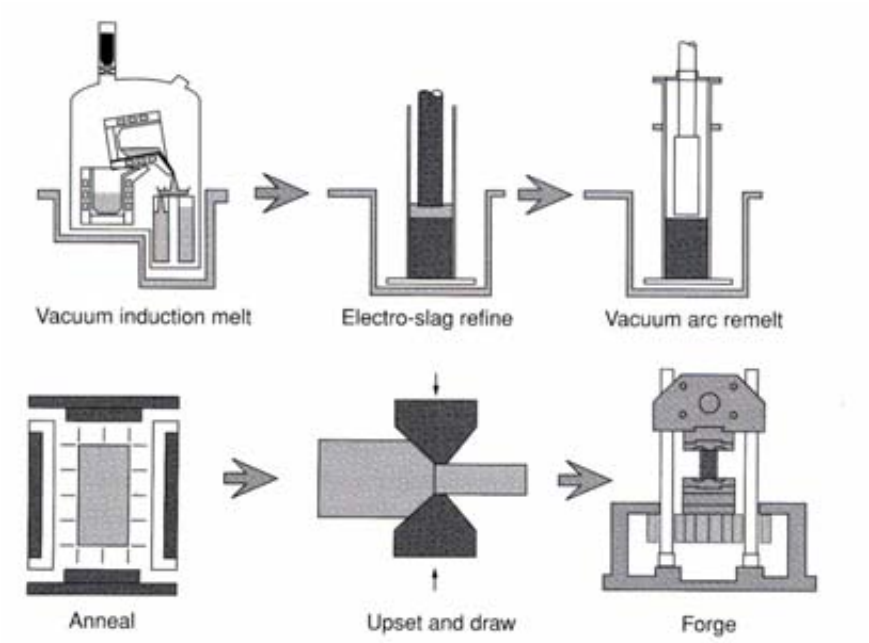

Figure 2.1 Diagram illustrating sequence of processes used for the production of a turbine disc alloy by ingot metallurgy [13].

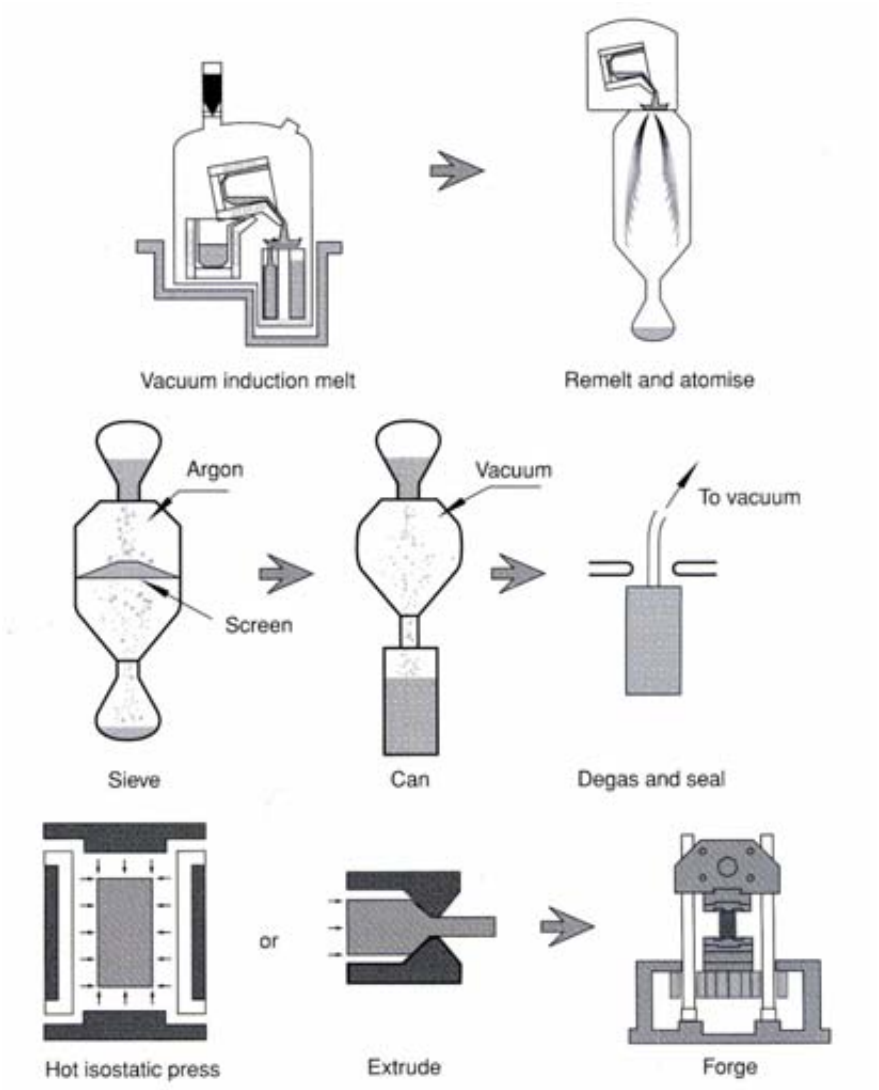

Figure 2.2 Diagram showing the sequence of processes used for the production of turbine disc alloys by conventional powder metallurgy [13].

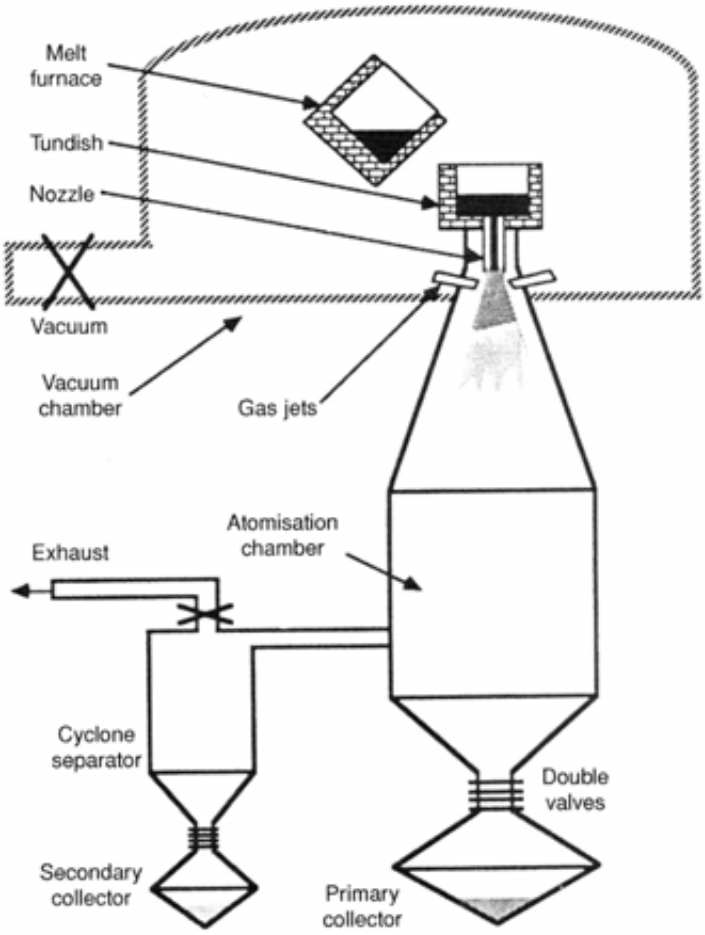

Figure 2.3 Diagram showing a typical arrangement for the Ar atomisation used for the production of superalloys by powder metallurgy [3].

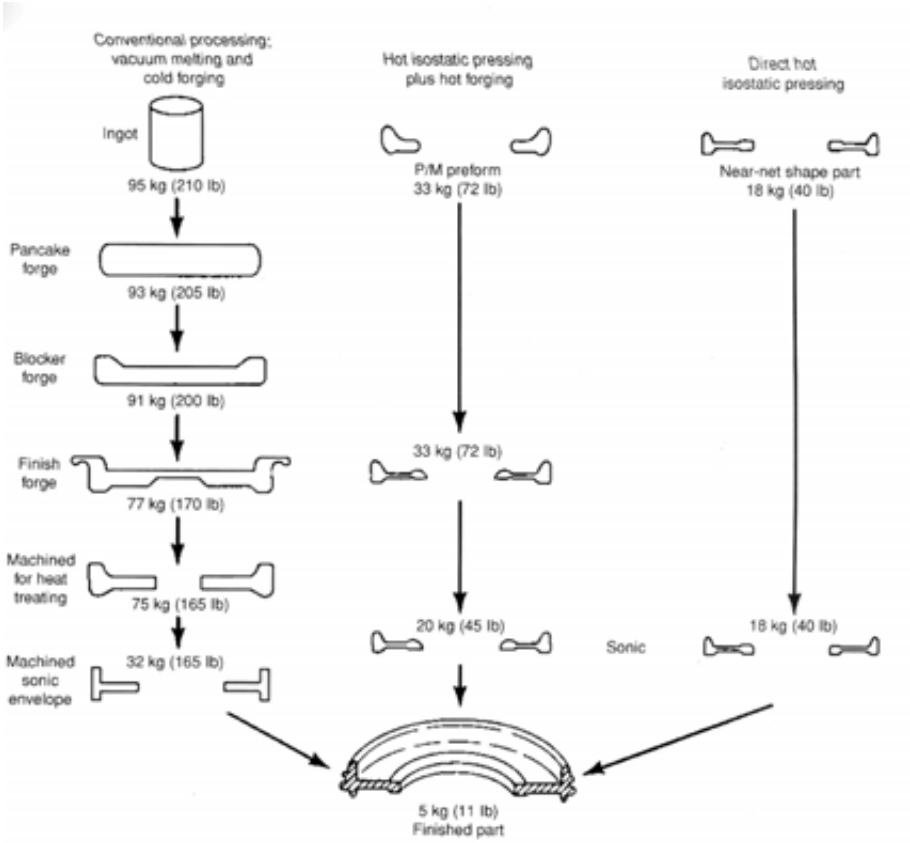

Figure 2.4 Processing sequences for the production of F-101 compressor discs [16]

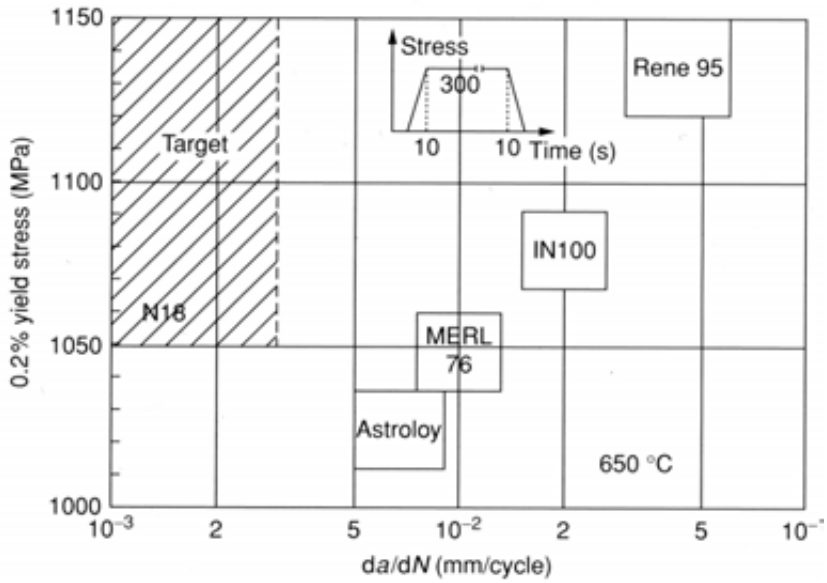

Figure 2.5 Variation of the yield stress with dwell fatigue crack growth (i.e. fatigue crack propagation during dwell period at peak load) rate for a number of P/M superalloys [56].

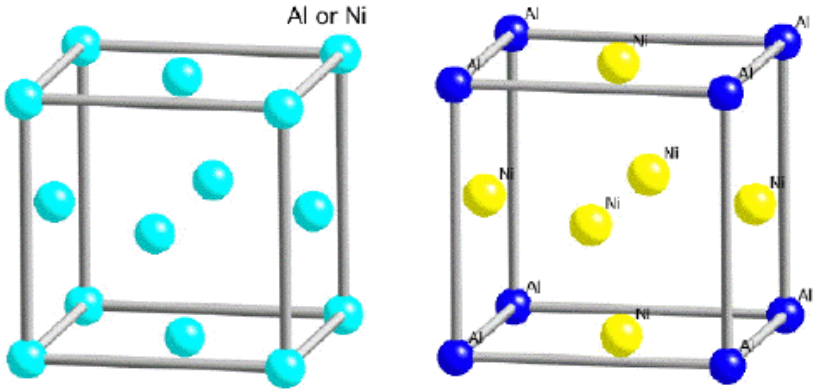

(a) Crystal structure of γ (b) Crystal structure of γ'

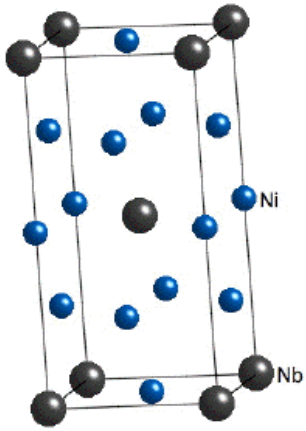

(c) Crystal structure of γ"

Figure 2.6 Diagrams showing the crystal structure of (a) γ; (b) γ′; (c)γ″ phases [62]

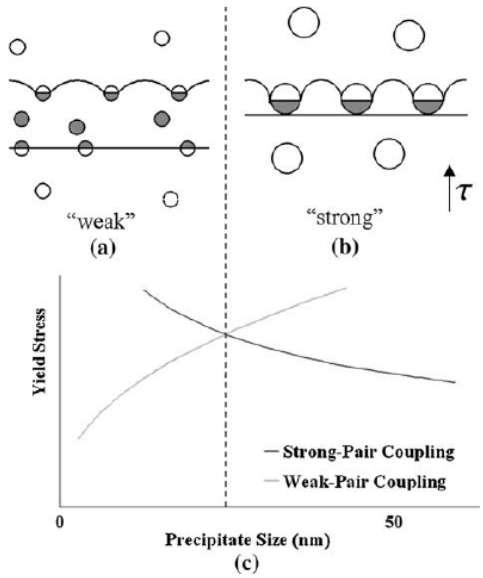

Figure 2.7. (a) Configuration of dislocations and precipitates during weak pair coupling, (b) configuration of dislocations and precipitates during strong pair coupling, and (c) relative strength due to each mechanism vs precipitate size. Duplicated from Huther et al. [93]

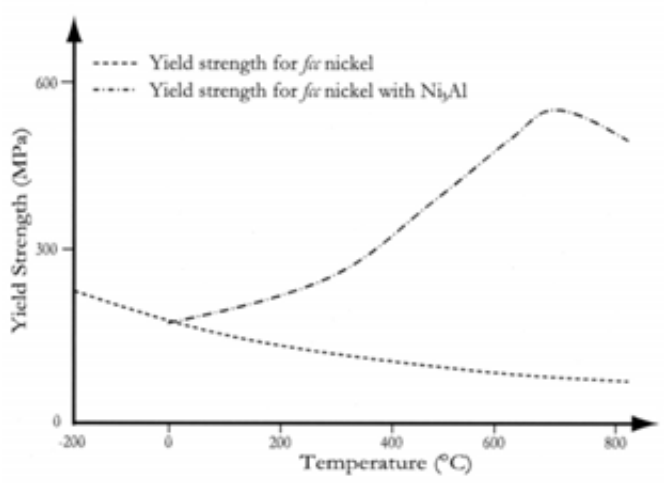

Figure 2.8 Effect of temperature on yield strength in fcc nickel and fcc nickel with γ′ [63, 99]

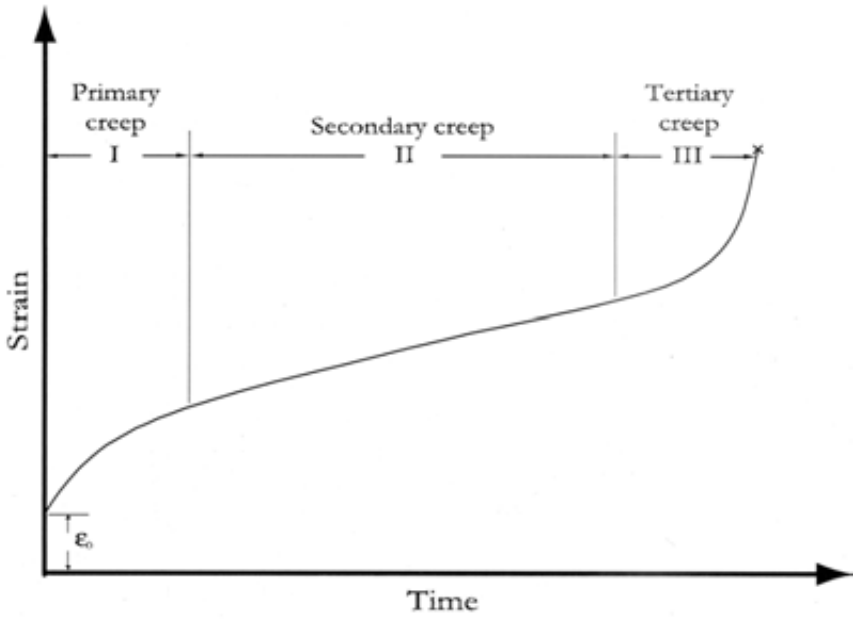

Figure 2.9. Typical creep curve showing three stages leading to creep failure

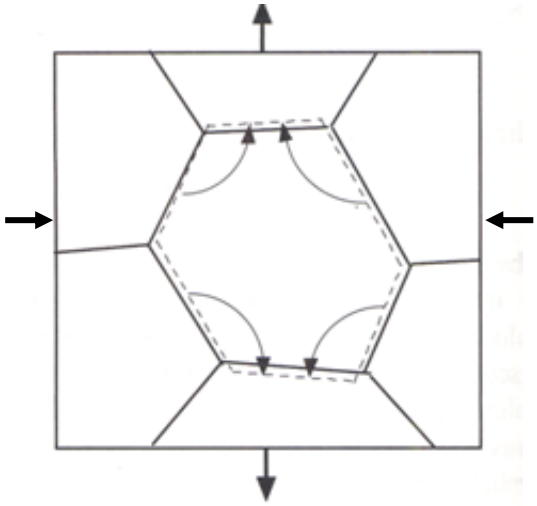

Figure 2.10 Diagram showing the diffusion-controlled creep process

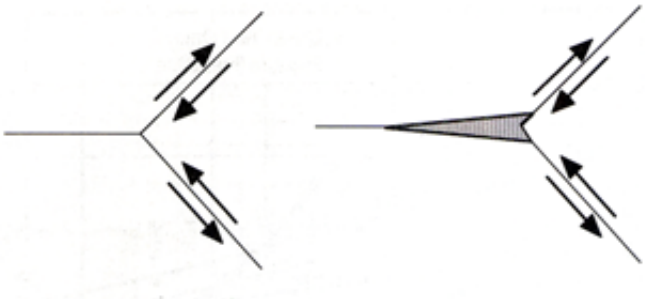

Figure 2.11 Diagram illustrating the grain boundary sliding during creep process

Chapter Three-Materials Characterization and Experimental Procedures

3.1 Materials and Processes

3.1.1 Materials

The material used in this project is a powder nickel-based superalloy called RR 1000, the norminal composition of which is listed in Table 3.1. The powder was prepared by Sandvik Osprey Ltd by atomisation of ingots they produced. It is important to note that Hf suffered great loss during primary and secondary meltings so that the Hf content of the ingots for atomisation was below specification. Thus, additional Hf was added by Sandvik during the remelting of the ingot prior to atomisation. As reviewed in Chapter 2, RR 1000 is an advanced nickel-based powder superalloy which usually contains 45-50% volume fraction of γ' after heat treatment to confer high strength.

Figure 3.1 shows the particle size distribution of the as-received RR 1000 powder, which was analyzed using a laser scattering particle size analyser. The maximum particle size was measured to be 53μm and the average particle size statistically determined to 17μm while the median particle size was 19μm.

To determine the γ' solvus of RR 1000, both Differential Scanning Calorimetry (DSC) analysis and water quench back method were used. For DSC analysis, bulk samples with weight of around 50mg were cut out from as-HIPped samples. Both heating and cooling rates for DSC were 10℃/min and the scanned temperature range was between 20℃ and 1300℃. For the quenching study, 12x12x8mm samples were cut out and held for 1h at different temperatures such as 1130℃, 1145℃, 1160℃ and 1180℃. The temperature control for the thermocouples in the furnace was +/−5℃. The samples were then taken out immediately

from each temperature for water quenching to freeze the high temperature microstructure. The cooled samples were sectioned, polished and etched for SEM observation. The metallographic sample preparation procedure is detailed in section 3.2.

Figure 3.2 (a) and (b) show the DSC analysis results for the thermal response of RR 1000 samples during heating and cooling at 10℃/min, respectively. The γ′ solvus is usually defined as the temperature at which all of the γ′ is dissolved, which according to figure 3.2 (a) is around 1170℃. The solidus was determined to be 1235℃. The onset γ′ nucleation temperature could be determined to 1132℃ according to Figure 3.2 (b).

Figure 3.3 shows the water-quenched microstructure of RR 1000 from different temperatures. It can be seen that in the sample quenched from 1145℃, quite a few γ′ precipitates with size of 150nm-300nm could still be observed at grain boundaries and at 1160℃ very few remained. At 1180℃, no γ′ precipitate could be observed at grain boundaries. This suggested that the γ′ solvus is between 1160℃and 1180℃.

3.1.2 Pre-HIP Heat Treatment

To study the influence of temperature on microstructure of powder particles and thus to better understand the microstructural evolution during HIPping, some heat treatments on powder particles prior to HIPping were conducted. For these experiments, powder was loaded into annealed stainless steel cans and then outgassed (to 10^{-4} mbar) and sealed, followed by being heat treated for 2 hours at 850℃, 900℃, 1107℃, and 1200℃, respectively. Some of these samples were also subjected to HIPping at 1107℃/100MPa/4h to study the influence of pre-HIP heat treatment of powder on the microstructure of as-HIPped samples. To study the effect of oxygen level on microstructure of powder particles, some powder samples were directly loaded in a crucible and then moved to a vacuum furnace for heat treatment. To be mentioned, the vacuum level for both outgassing system and vacuum

furnace can reach 10^{-4} mbar but given that the vacuum chamber with an inner diameter of 100mm and a length of 1m is much larger than a can (usually with an inner diameter of 6mm and a length of 20mm, the total oxygen level in the vacuum furnace is expected to be much higher than that in a small can. The particle surface and section of powder particles with different heat treatments were then studied using SEM. Compositional distribution on the particle surface and sub-surface areas was also studied using Auger Electron Spectroscopy (AES) in a Thermofisher MICROLAB 350 electron spectrometer equipped with a hemispherical sector energy analyzer. 10 KeV electrons were employed and the spot size of the electron beam was 10 nm. A depth profile was also obtained by etching the sample surface using a rastered Ar ion beam at 3KV. The etching rate under the conditions employed was 0.17nm/s.

To study the influence of outgassing condition on oxygen, nitrogen and hydrogen levels in RR 1000 samples, some powder samples were heat treated at 400℃ for 4 hours and 24 hours, respectively, during the outgassing process. Others were outgassed (to 10^{-4} mbar) at room temperature for 4hours, 19 hours and 67 hours, respectively. The outgassed and sealed powder samples were then HIPped at 1107℃/100MPa/4h and sent out for chemical analysis. The oxygen, nitrogen and hydrogen levels of the samples were determined using the Carrier Gas Extraction methods in IncoTest's LECO TC436AR ANALYSER and LECO RH404 ANALYSER, respectively. The sample was melted in an inert gas stream in a graphite crucible and the gases evolved were measured by thermal conductivity or infrared absorption techniques.

3.1.3 Hot Isostatic Pressing

Stainless steel 316 cans were used to contain powder for HIPping. Before use, the cans were leak tested and then annealed at 1100℃ for 2hours in order to remove any grease or

other impurities that might still be present. Powders were then loaded into the prepared cans in a vibrating system and out-gassed by slowly bringing them under vacuum for a period of around 24 hours, to ensure the outgassing pressure to be 10^{-4} mbar. While under vacuum, the cans were sealed by heating the closures with a blowtorch and then crimping using a hydraulic press.

The samples were then HIPped in an EPSI HIPping system (see Figure 3.4) with the required HIPping procedure or condition. The maximum operation pressure capability for this HIPping system is 200MPa and the maximum furnace operation temperature 1450℃. For a normal HIPping procedure, temperature is ramped up at 5℃/min and after HIPping furnace cooling (FC) was used with cooling rate of around 5℃/min, see Figure 3.5(a). In the following chapters wherever no particular HIPping procedure is mentioned, it means a normal HIPping procedure has been followed, e.g., ramping up temperature and pressure together to designated values. HIPping procedure could also be changed by ramping pressure first and then temperature, or temperature first and then pressure, see Figure 3.5(b) and (c), respectively. The influence of HIPping procedure on microstructure of as-HIPped materials was also investigated. In the following chapters, wherever the HIPping procedure is not particularly indicated, it means the HIPping process has followed a normal procedure mentioned above.

The cooling rate from the HIPping temperature could also be controlled by controlling the flow rate of room-temperature argon, which is used to cool the HIPped samples and chamber. With increased argon flow rate, the cooling rate would be increased. Since it is well known that cooling rate affects significantly the microstructure of nickel-based superalloys during heat treatment, the effect of cooling rate from HIPping on microstructure was also studied here. In the current study, two cooling rates of 5℃/min and 132℃/min were used.

3.1.4 Interrupted Cooling Tests

Interrupted cooling tests were designed to attain a better understanding of the development of γ′ precipitates and precipitation kinetics during cooling. The interrupted cooling test was comprised of several continuous cooling tests, each interrupted at a different intermediate temperature. Samples with a dimension of around 10×10×7mm were machined for each test. Specifically, the tests were carried out by heating the specimens to a supersolvus solution temperature of 1180℃, holding for 1 hour, and then cooling at 5℃/min. The cooling was interrupted at 1160℃, 1130℃, 1110℃, 1095℃, 1080℃, 1050℃, and 950℃, respectively, and the specimens were then immediately taken out and water quenched to freeze the high temperature structures. The water quenching was found to be able to drop the temperature of each sample from more than one thousand degrees down to room temperature within 5 seconds, e.g. the cooling rate could reach higher than 1.2×10^4℃/min, which suggests that γ′ nucleation actually might have been suppressed during water quench and that the as-quenched microstructure would exactly reflect the high temperature microstructure [1]. Type K mineral thermocouples were attached to sample surface to measure sample temperatures accurately for all heat treatments.

3.1.5 Heat Treatments

The as-HIPped samples were solution treated for 2 or 4 hours at 1120℃ or 1125℃, and 1160℃, respectively, followed by air cooling. Aging treatment was conducted at 760℃ for 16 hours followed by air cooling (AC).

3.2 Specimen Preparation and Microstructural Characterization

3.2.1 Sample Preparation

Metallographic specimens were cut using a low speed diamond cutting wheel and mounted in conductive Bakelite. Specimens were then ground on 240 grit, 400 grit, 800 grit, 1200 grit and 2500 grit silicon carbide waterproof papers in sequence and polished using Struers Dac cloth with 3 micron Kemet diamond suspension and then Struers Nap cloth with 1 micron Kemet diamond suspension in a DAP-7 automatic polishing machine. For observation of gamma prime, further electrolytic etching in 10% H_3PO_4 in H_2O at 25V for 2-5 seconds was carried out. For EBSD investigation, the mechanically polished samples were further subjected to a chemical polishing process using a Struers Chem disc with activated colloidal silica solution in order to remove the mechanically deformed surface layer into which work may be introduced during grinding and mechanical polishing process.

For TEM analysis, specimen blanks were cut using a low speed diamond cutting wheel into a thickness of 0.5mm. They were then punched into 3mm diameter discs by using a spark erosion cutting machine (EDM). These discs were ground further to a thickness of 150 μm -200 μm using 400-800 grade silicon carbide paper. The specimens were then electro-polished to perforation using a twin-jet electropolisher (StruersTenupol-5). A polishing solution containing 10% perchloric acid and 90% methanol was used operating at approximately -20℃ with an applied voltage of 25 to 30V and a current of around 100-200 mA.

The microstructures of as-polished or etched samples were then investigated using appropriate characterization techniques

3.2.2 Microstructural Characterization

3.2.2.1 Electron-sample interaction

This work involves considerable microstructural, deformation and fracture analysis, which all are heavily dependent on the use of electron microscopes. Selection of appropriate microscopes is therefore highly important to achieve useful information. It is well known that interaction between electrons and samples could produce quite a lot of electron and X-ray information which is used for different analysis, as can be seen in Figure 3.6 (a). The incident beam electrons encountering specimen atoms could be elastically (involving no energy loss) or inelastically scattered through all angles including being forward scattered see Figure 3.6 (b).

3.2.2.2 Secondary Electron Microscopy (SEM)

SEM takes advantage of either secondary electrons or backscattered electrons. Secondary electrons are those low energy electrons which are emitted or knocked out from the specimen while backscattered electrons are high energy electrons which have been scattered (elastically) through high angles by nuclei of atoms in specimen. The secondary electrons have low energy (≤50eV) and can therefore be easily attracted into the secondary detector so that they contain topological information. Backscattered electrons with higher energy contain topological information (but only a limited amount because only those travelling straight into a detector contribute to the signal) and also chemical or orientation information.

In this work, secondary electron SEM images were used extensively to study powder particle and gamma prime precipitate size, distribution and detailed morphology and microstructure together with fracture surfaces of mechanically tested samples. Back-scattered electron SEM images were mainly used to study the size and distribution of precipitates at PPBs or grain boundaries on as-polished samples. The imaging analysis was carried out on a JEOL 6060 SEM, or a Philips XL 30 SEM or a JEOL 7000 FEG-SEM. A 20 KV accelerating

voltage, probe size of 10 and a 10mm working distance were usually chosen for these analyses.

3.2.2.3 Electron Backscattered Diffraction (EBSD)

The elastically backscattered electrons could be further Bragg diffracted by appropriate oriented planes, which leads to the formation of electron backscattered diffraction patterns. These patterns are very useful to reveal crystallographic information of samples in the SEM and thus have been utilized to determine crystal structure, grain size and orientation of as-HIPped and heat treated RR 1000 samples. The EBSD analysis was conducted using a JEOL 7000 FEG-SEM with attached computer-algorithm EBSD software. Before analysis, samples were tilted by 70° against the sample holder stage. The layout for EBSD analysis is shown in Figure 3.7. The EBSD mapping was undertaken at a 20 KV accelerating voltage. Two main phases, gamma and gamma prime (Ni_3Al) in RR 1000 were used for the analysis.

3.2.2.4 Energy Dispersive (EDX) and Wavelength Dispersive (WDX) X-ray spectrometry

When electrons interact with matter X-rays will be generated. If the energy of the incident electrons is high enough to eject inner shell electrons then characteristic energy loss electrons will be generated and characteristic X-rays and Auger electrons will be emitted from the ionized atom as an outer shell electron falls into the inner shell vacancy. The mechanism of generation of characteristic X-rays have been detailed elsewhere [3]. The separation of the various X-rays could be achieved in a WDX system by using a crystal spectrometer and in an EDX system by using a silicon-lithium detector.

For a crystal of known lattice spacing d, X-rays of a specific wavelength λ will be diffracted at an angle θ given by the well-known Bragg equation,

$$N\lambda = 2d \sin\theta \qquad \text{Equation 3.1}$$

By changing θ, different wavelengths are selected and the desired elements could be analyzed. In a WDX system, X-rays are Bragg diffracted with the angle of diffraction defining their wavelength. In order to cover the necessary range of wavelengths several crystals of different *d* spacings are usually used successively in a spectrometer. Detectors used in WDX spectrometers are most commonly gas proportional counter types. Incoming X-rays enter the detector through a collimator (slit) and thin window and cause ionization of the gas atoms in the counter ejecting photoelectrons out. The electrons are then attracted to an anode wire in the counter where electronic pulses are produced and amplified. Electronic signal is proportional to the X-ray intensity so that quantification can be carried out.

In an EDX spectrometer, X-rays enter through the thin beryllium window and produce electron-hole pairs in the SiLi, which cause charging of the SiLi detector. By measuring and amplifying the charge caused by X-ray photons, an amplified shaped pulse would be obtained and the height of the pulse is then a measure of the energy of the incident X-ray photon. Given that the X-ray photons arrive with a sufficient time interval between them the energy of each incident photon can be measured and the output presented as an intensity versus energy display.

In comparison with EDX, WDX shows a much better energy resolution (down to 1 or 2eV) to unravel the peak overlaps that plague EDX (resolution of ~160eV at $Mn_{K\alpha}$). WDX also exhibits better peak-to-background capability to detect smaller amounts of elements and better detection of light elements. The main advantage of EDX detectors is that simultaneous collection of the whole range of X-rays is possible and an indication of all the elements can be obtained in a matter of seconds.

Both EDX and WDX measurements were carried out to analyze the precipitates at PPBs using a JEOL 7000 FEG SEM linked to Oxford Software (see Figure 3.8 (a)). For EDX

analysis, a 20KV accelerating voltage and a 10mm working distance were used while for WDX analysis, a 10KV accelerating voltage together with a beam current of more than 10nA was used.

3.2.2.5 Transmission Electron Microscopy (TEM)

If the sample is thin enough, electrons could transmit through the sample. The transmitted electrons are generally used to form either an image or a diffraction pattern of the specimen and schematic ray diagrams for these two modes of operation are shown in Figure 3.9(a) and (b). In the conventional imaging mode, an objective aperture is inserted in the back focal plane of the objective lens to select only one electron beam so that the the image plane of the objective lens acts as the object plane of the diffraction lens (e.g. the intermediate lens) to form images; a bright field image is formed if the directly transmitted beam is selected and a dark field image if a diffracted beam is selected. To form diffraction patterns, the selected area aperture is inserted to select the diffracted area so that the back focal plane of the objective lens acts as objective plane for the diffraction lens. The images obtained in electron microscopes are influenced to greater or lesser extents by the diffraction conditions which constitute the most important factors in influencing the contrast in TEM, especially for crystal defects such as dislocations and stacking faults. The detailed theories about diffraction contrast have been introduced elsewhere [3]. To analyze defects using TEM, a two-beam condition (one direct transmitted beam ***O*** and one diffracted beam) is usually required. Figure 3.10(a) shows a typical two-beam condition operation for bright-field imaging which involves tilting to move the Kikuchi lines (the broad full lines) to exactly pass through the transmitted and adjacent diffracted beams. The resolution of diffraction contrast images can be significantly improved by using weak beam technique, in which the deviation from the Bragg condition (s_g) is increased so that the width of the image is reduced. Figure 3.10(b) illustrates a typical operation for weak-beam imaging, which involves motion of

Kikuchi lines in between two high-index planes, that is, weaker diffracted beams. The intensity of weak beam images is low and thus dark field is used so that the background intensity is very low generating significant contrast for the weak images.

To identify PPB precipitates, TEM analysis was carried out by using an FEI TecnaiF20 FEG TEM microscope fitted with EDX facility (see Figure 3.8 (b)). An accelerating voltage of 200kV was usually employed for TEM analysis. TEM was also used to study the dislocation structure of deformed samples under two-beam condition or using weak beam techniques.

3.3 Mechanical Testing

3.3.1 Tensile Testing

Tensile tests were performed on specimens in as-HIPped or HIPped and then heat treated status using a computer controlled electric screw driven Zwick/Z100 tensile testing machine. Two types of specimens, that is, plain and notched tensile test pieces, were used in the tests. The geometry and surface finish of plain tensile specimens are shown in Figure 3.11. The notched samples showed a stress concentration factor K_t=3.1 and a notched root cross section area to be 7mm^2, see Figure 3.12. For plain tensile test pieces, the tests were conducted under strain control and the strain rate was $5x10^{-4}$ s^{-1}. For notched test pieces, the tests were position-controlled and the ramp rate is 0.6mm/min, which is equivalent to a strain rate at $5x10^{-4}$ s^{-1}. Tests were performed at room temperature, and at temperatures of 700℃ or 750℃. Prior to testing, the samples were held at these temperatures for at least half an hour.

After tensile testing, the fracture surface and longitudinal section of the tested samples were subject to SEM analysis. Discs were cut from the part close to fracture surface but normal to tensile testing direction and subsequently ground and electro-polished at -10°C and 25 V in 10% perchloric acid in methanol. The thin foils were then subject to TEM inspection.

The dislocation structure was studied under two-beam condition or using weak beam techniques.

3.3.2 Fatigue Testing

Both four-point bending fatigue test and tension-tension fatigue test were performed to evaluate the HCF properties of the materials in as-HIPped or HIPped and heat treated state. However, the purposes for these two types of tests are very different. The 4-point bending test is designed to assess the surface-sensitiveness of materials under cyclic stress condition while tension-tension tests are used to examine the fatigue behaviour of a volume of material as a whole. The HCF limit stress in the present investigation was defined as the fatigue strength corresponding to a fatigue life of 1.0×10^7 cycles.

Samples with dimension of $60\times10\times10mm^3$ were cut out using EDM for four-point bending fatigue test. Prior to the testing, the sharp edges of samples were ground to be round and the surface was gently polished using 800 grit silicon carbide papers to remove the surface deposits formed during EDM machining. The four-point bending fatigue test was performed on an Amsler Vibrophore electro-magnetic resonance machine (see Figure 3.13 (a)) at a stress ratio R ($R=\sigma_{min}/\sigma_{max}$) of 0.1 and at frequencies in the range of 110–120Hz. The 4-point bend arrangement and the position of sample's test surface during fatigue test are shown in Figure 3.13 (b).

Tension-tension fatigue tests were carried out at both room temperature and 700℃on an Amsler Vibrophore machine at frequencies in the range of 70–85Hz with a stress ratio R of 0.1. Two types of test pieces have been used, including plain specimens and notched samples, the drawings of which have been shown in Figure 3.14 and Figure 3.15, respectively. The notched samples were machined with an elastic stress concentration factor $K_t=2.26$ at the

notch root. For high temperature testing, a heating furnace was set up around the testpieces and before testing, samples were held at 700℃ for 0.5 hour.

Fracture surfaces after fatigue failure were ultrasonically cleaned in acetone for at least three minutes and then subjected to analysis using Scanning Electron Microscopy (SEM) for all tests.

3.3.3 Creep Testing

A quick creep testing was carried out on an alumina ceramic flexural creep apparatus in which all parts are made out of alumina. The testing configuration is shown in Figure 3.16. Samples with a dimension of 45×5×3mm were used for the creep testing and the 45×5mm faces were loaded. Temperature was ramped by setting up a furnace around the testing unit. The creep testing duration varied from several hours up to 25 hours depending on the temperature and stress level used. The creep strain is computed from the degree of central flexure using elastic bending equations. The detailed calculation of stress and strain has been described elsewhere [4]. The detection limit for creep strain for the current testing system was 10^{-7}.

References

[1] Mao J, Chang KM, Yang W, Ray K, Vaze SP, Furrer DU. Cooling precipitation and strengthening study in powder metallurgy superalloy U720LI. Metallurgical and Materials Transactions A 2001; 32:2441–2452.

[2] Williams DB, Carter CB. Transmission electron microscopy I, Basics. New York;London: Plenum, C;1996.

[3] Loretto MH. Electron beam analysis of materials. London: Chapman and Hall; 1984.

[4] Hollenberg GW, Terwilliger GR, Gordon RS. Calculation of stresses and strains in four-point bending creep tests. Journal of American Ceramic Society 1971; 54: 196-199.

Table 3.1 compositions of RR 1000 powder in wt.%

Alloy	Cr	Co	Mo	Al	Ti	Ta	Hf	C	B	Zr	Ni
RR1000	15.0	18.5	5.0	3.0	3.6	2.0	0.5	0.027	0.015	0.06	Bal.

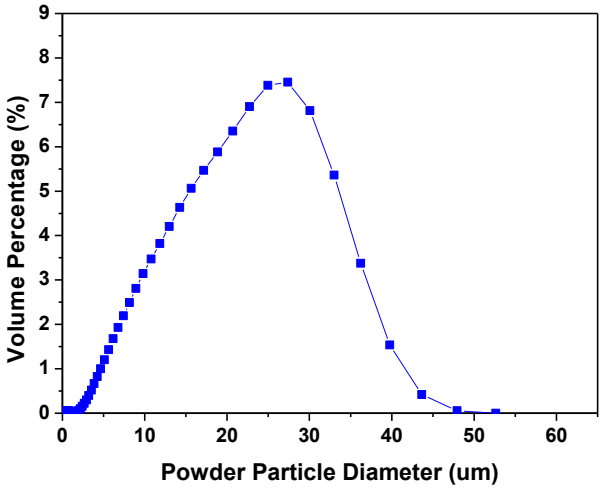

Figure 3.1 Particle size distribution of the as-received RR 1000 powder obtained by using a laser scattering particle size analyser

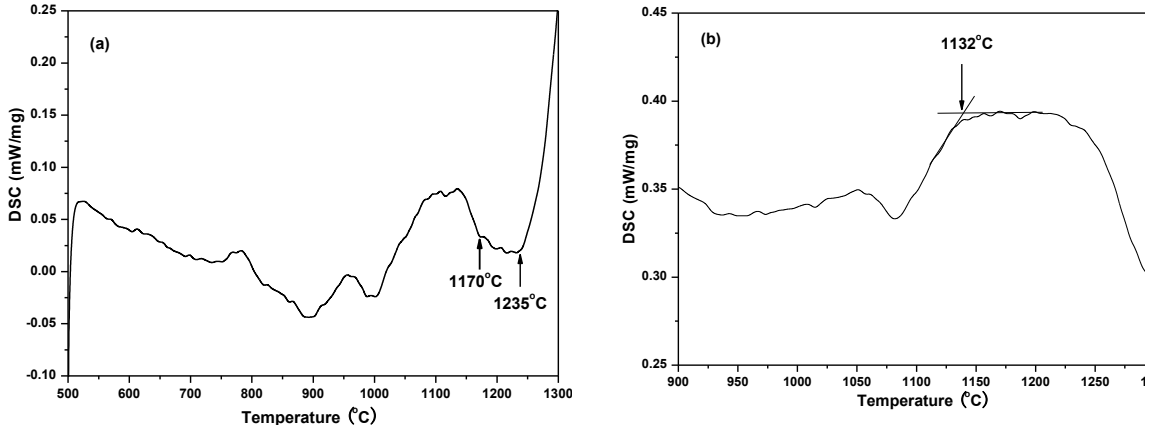

Figure 3.2 DSC curves showing the thermal response of RR 1000 when (a) heated at 10℃ /min from 500℃ to 1300℃; (b) cooled at 10℃/min from 1300℃ to 500℃.

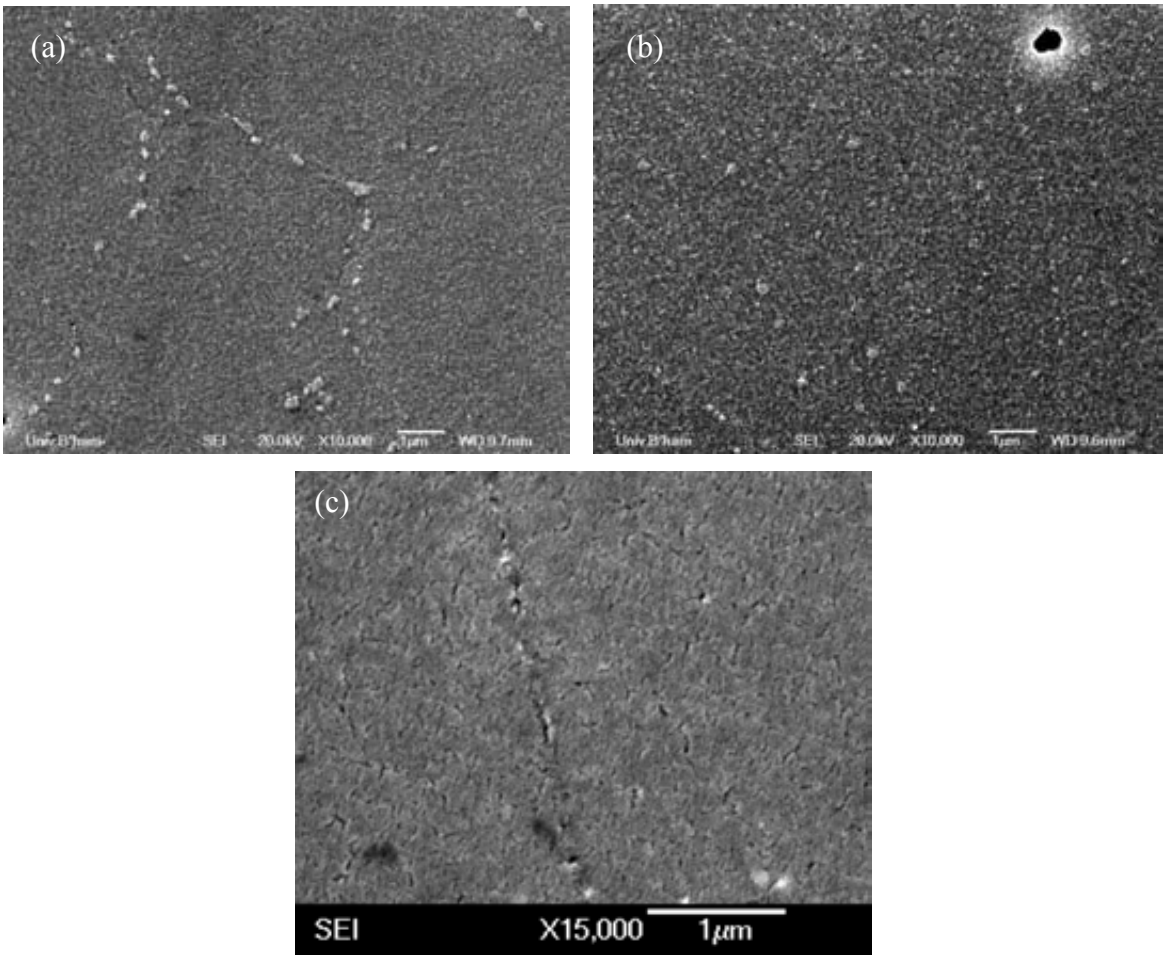

Figure 3.3 Secondary electron SEM micrographs showing the remained gamma prime in RR 1000 material after water quenching from (a) 1145℃; (b) 1160℃; (c)1180℃.

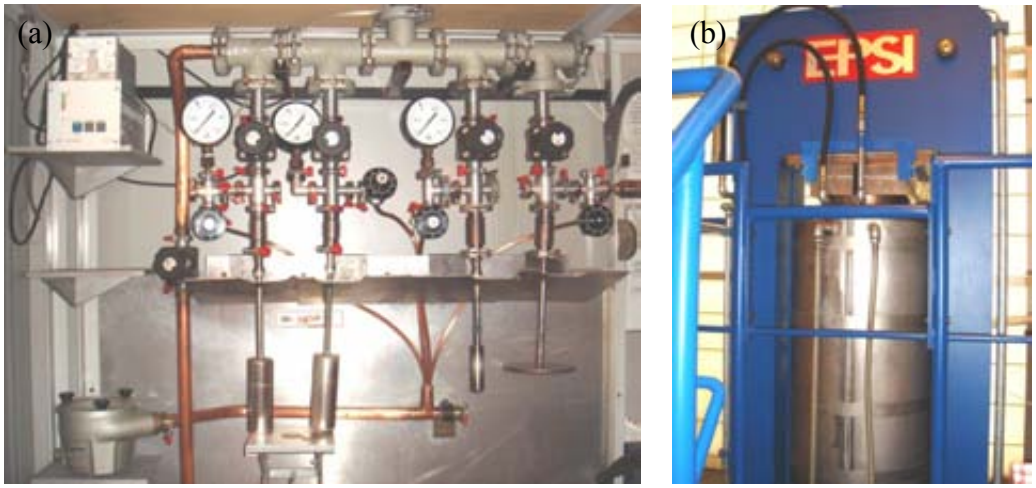

Figure 3.4 Photographs showing (a) the outgassing system (b) EPSI HIPping system used

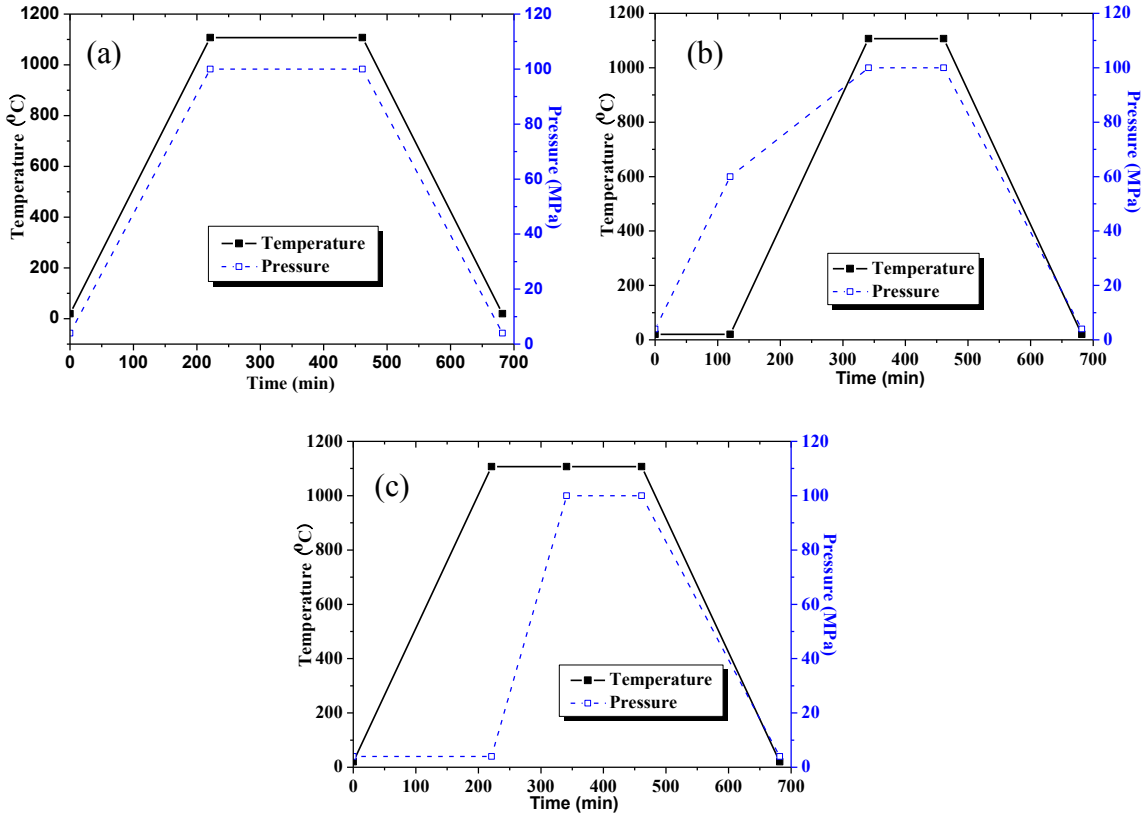

Figure 3.5 Diagrams illustrating the different HIPping procedures (a) temperature and pressure ramped together to 1107℃ and 100MPa (normal procedure); (b) pressure ramped to 60MPa at room temperature and then temperature and pressure to 1107℃ and 100MPa (e.g. ramping pressure first and then temperature); (c) temperature ramped to 1107℃ at 4MPa and then pressure to 100MPa (e.g. ramping temperature first and then pressure)

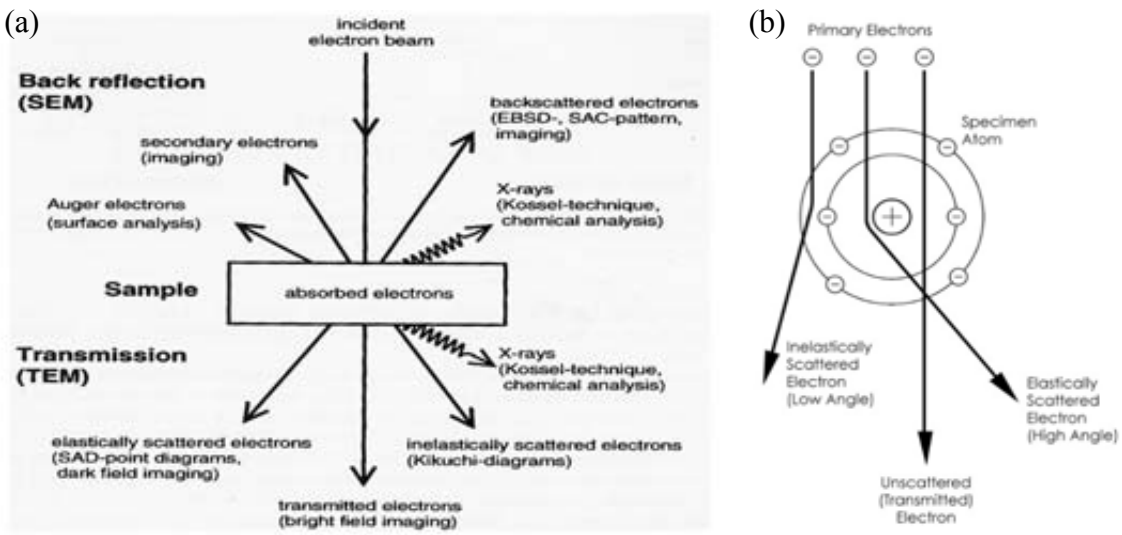

Figure 3.6 Schematic showing (a) electron-sample interaction and the electron and X-rays information obtained; (b) electron-atoms interaction, note that the forward scattered are not unscattered [2]

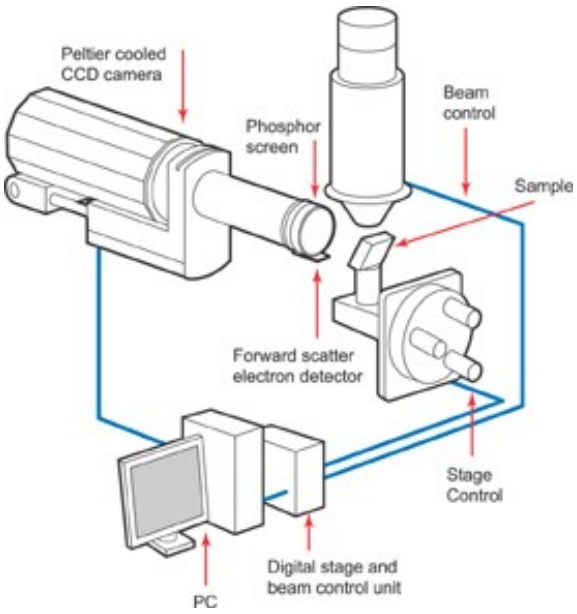

Figure 3.7 Diagram showing the sample layout for EBSD analysis

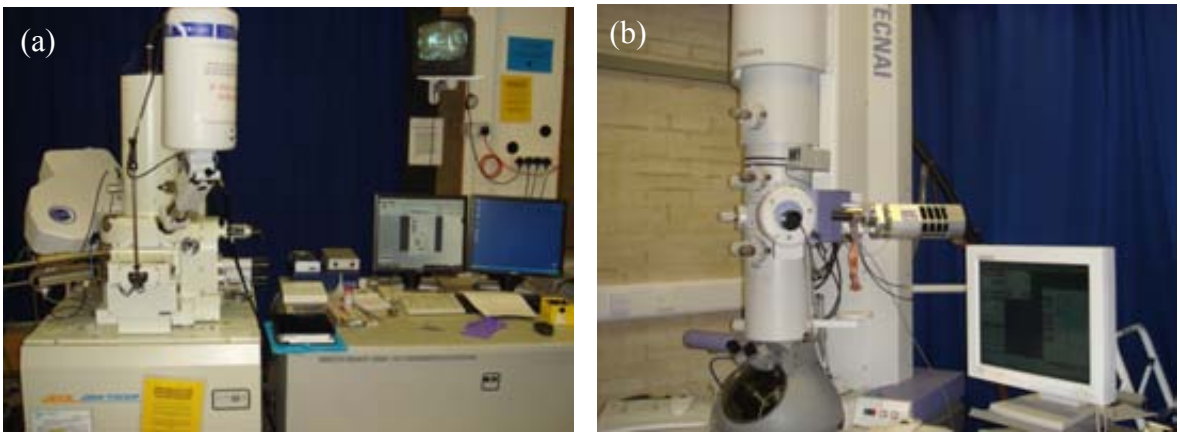

Figure 3.8 Photographs showing (a) JEOL 7000 FEG-SEM; (b) FEI TecnaiF20 FEG TEM

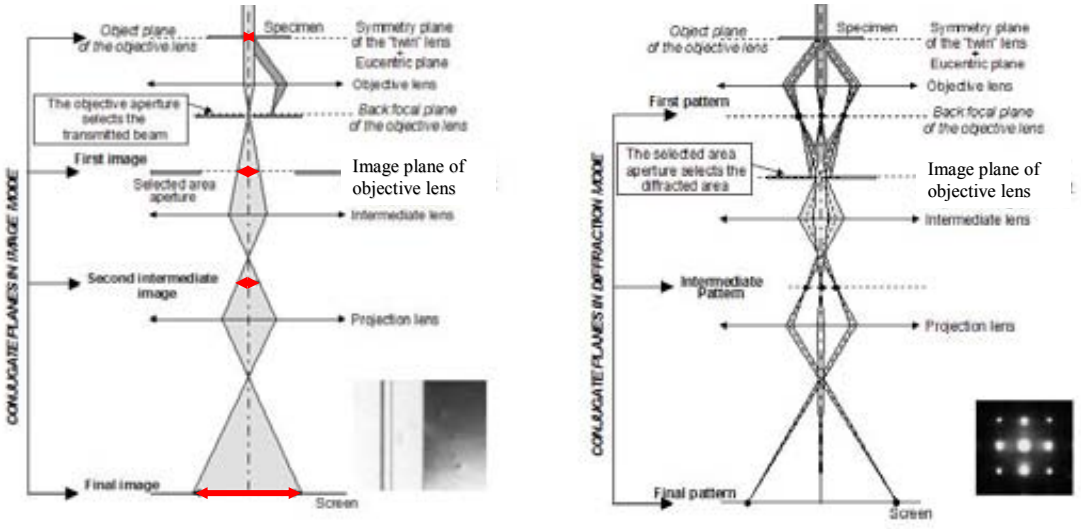

(a) TEM in imaging mode (b) TEM in diffraction mode

Figure 3.9 Schematic ray diagrams for a transmission electron microscopy showing (a) imaging formation and (b) diffraction pattern formation [2]. The intermediate lens refer to diffraction lens.

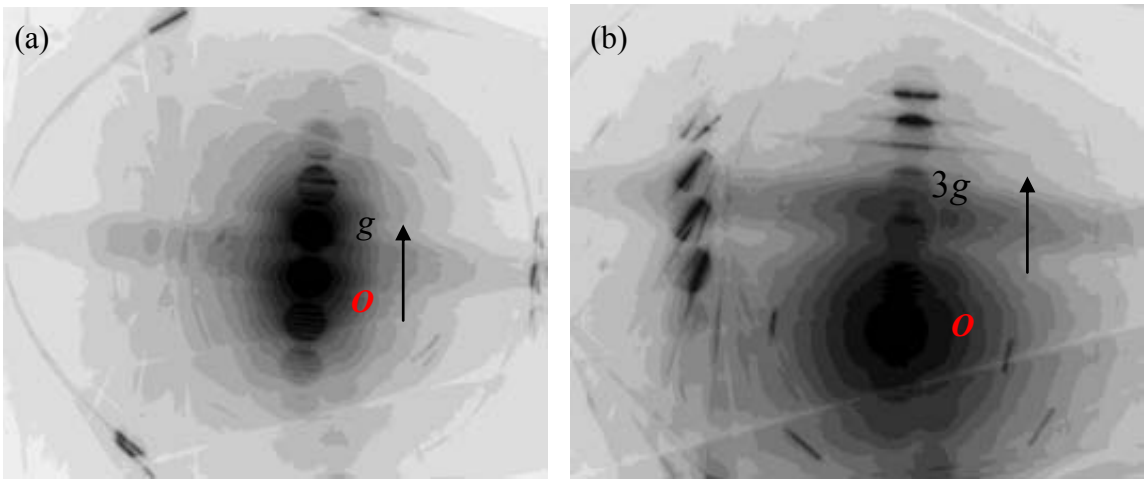

Figure 3.10 (a) a two-beam condition for bright-field imaging achieved by tilting the sample so that the Kikuchi line exactly goes through in between ***O*** (the directly transmitted beam) and g diffraction vector (the diffraction beam next to transmitted beam); (b) a diffraction condition for weak-beam imaging involves tilting to move the Kikuchi line to pass through high vectors such as $g-2g$, $2g-3g$, and so on.

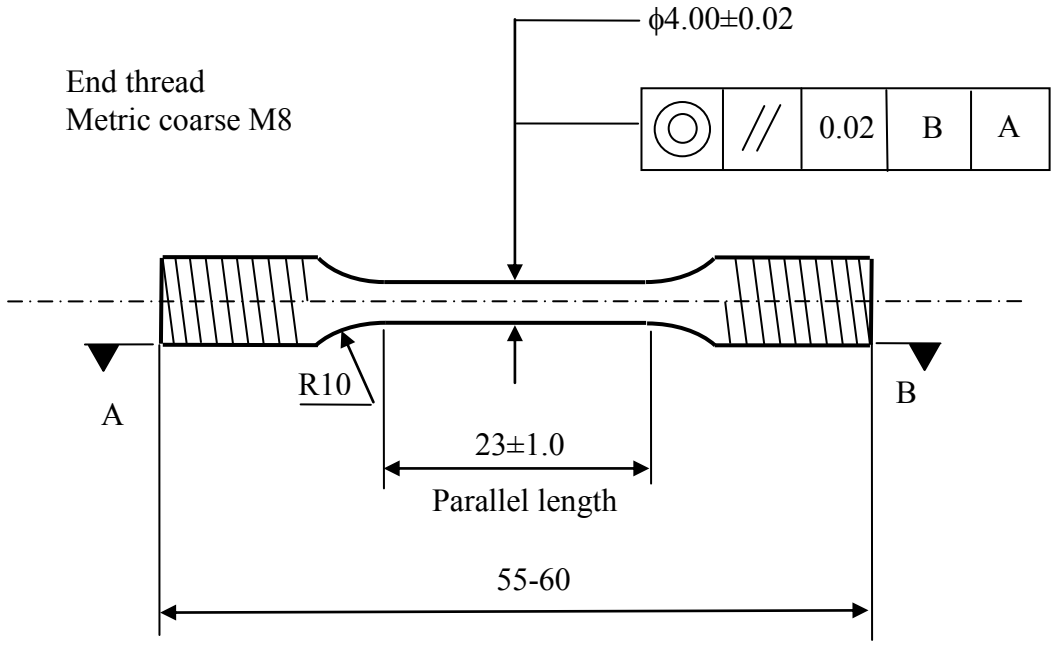

Figure 3.11 Drawing for plain tensile test pieces with roughness value for machined surfaces to be 1.6 micrometers and all dimensions and tolerances are in mm

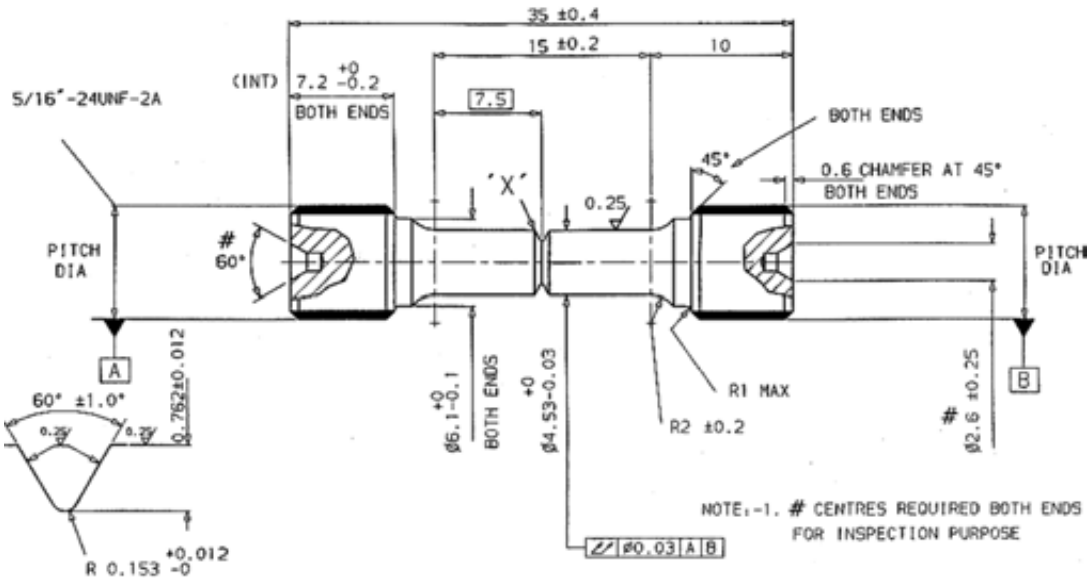

Figure 3.12 Diagram showing the geometry of notched tensile test pieces with Kt=3.1 and the notched cross section area to be 7mm^2.

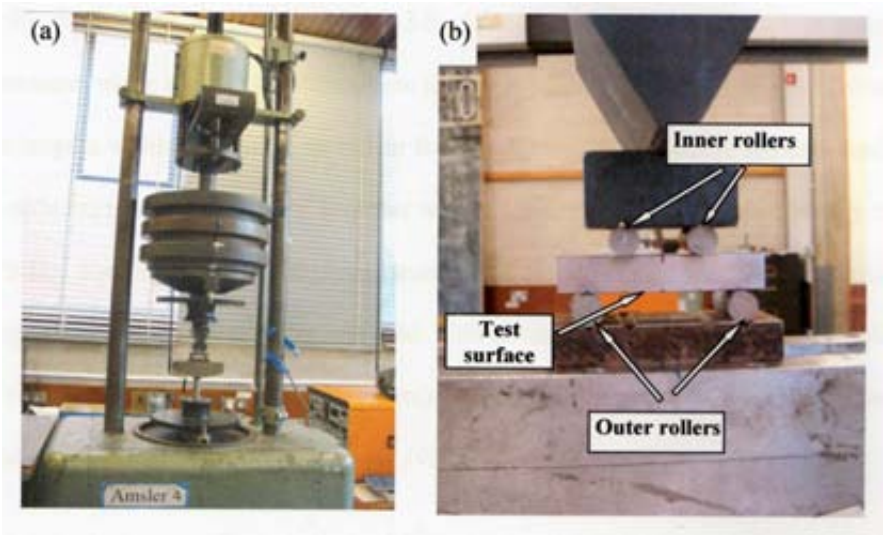

Figure 3.13 Photographs showing (a) Amsler Vibrophore electro-magnetic resonance testing machine for fatigue property assessment; (b) four point bending arrangement and the position of sample's test surface during fatigue test (courtesy of Dr. K. Zhang).

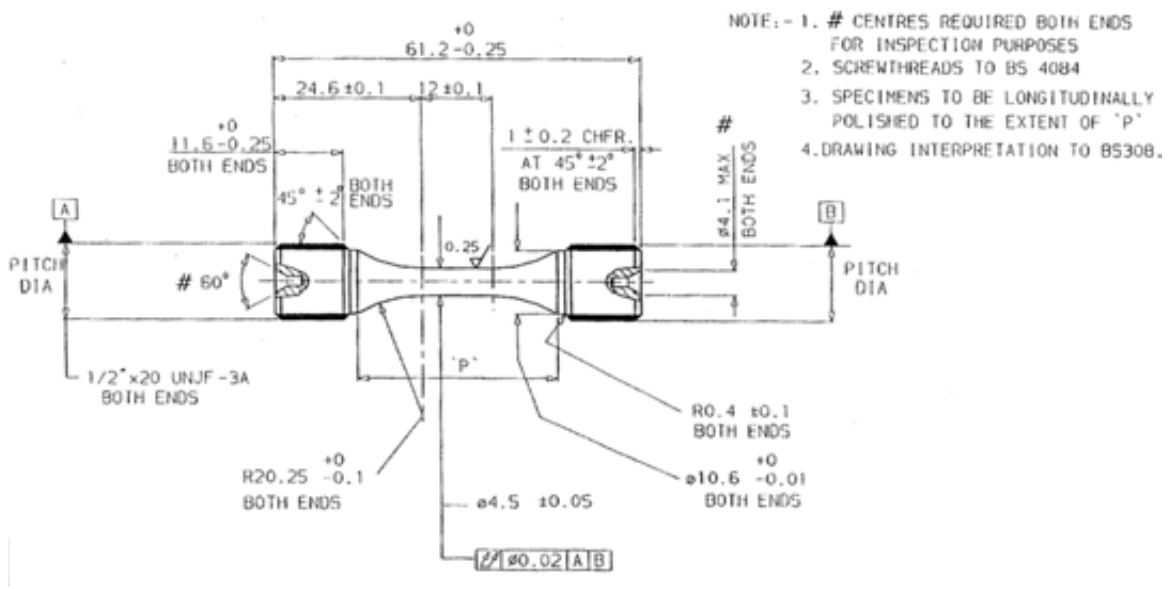

Figure 3.14 Diagram showing the geometry of un-notched tension-tension fatigue testpiece

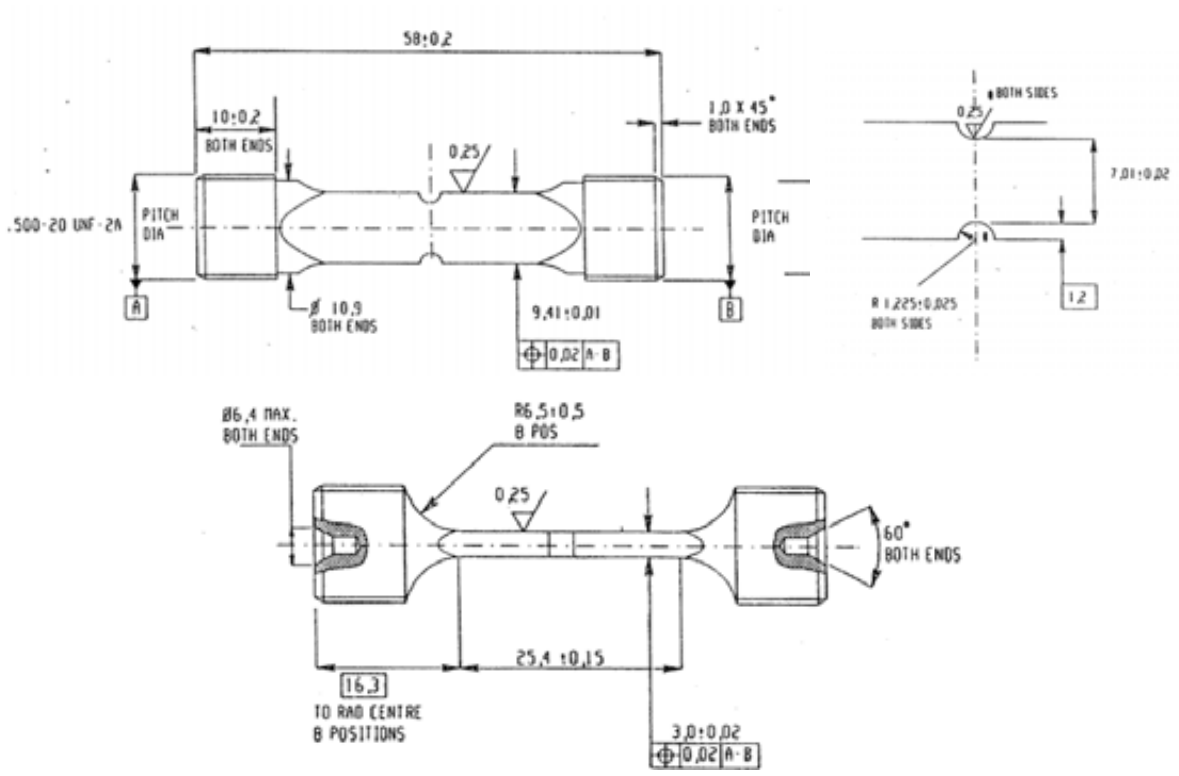

Figure 3.15 Three-view diagrams showing the geometry of notched tension-tension fatigue testpiece with K_t=2.26

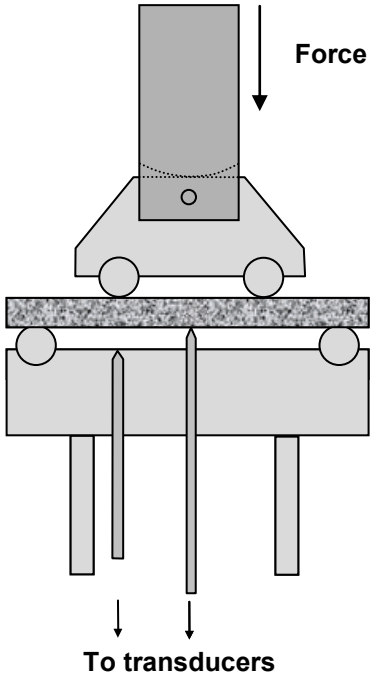

Figure 3.16 Diagram showing the flexural creep testing configuration

Chapter Four-Characterization of Powders

4.1. Introduction

As reviewed in Chapter 2, PPBs have been one of the critical issues for net-shape HIPping. The PPBs are usually found associated with the formation of precipitates which decorate them. Among the two major parameters that are involved in HIPping, e.g. pressure and temperature, the temperature generally shows a more significant influence than pressure on the microstructure such as grain size and precipitates in the as-HIPped samples. The use of pressure is mainly to promote consolidation and deformation, which together with temperature may lead to recrystallisation. To better understand the formation of precipitates at particle boundaries and identify the contribution of temperature or pressure to the formation of precipitates, some heat treatment experiments with or without pressure were designed and conducted to study the response of powder to temperature and/or pressure.

4.2. Results

4.2.1. The Particle Size, Distribution, and Microstructure of as-received Powder

Figure 4.1(a) shows a typical particle distribution of RR 1000 powder. It can be seen that particles with different sizes are uniformly distributed and many small particles tend to attach to bigger particles. Most of the particles show a dendritic surface with numerous boundaries (see Figure 4.1(b)), indicating a dendritic microstructure of the particles. Some of the particles seem to be enwrapped with a metallic layer, as shown in Figure 4.1(c). This is believed to be a coat of splat-cooled material, which is formed during gas atomization where solidified particles could be carried back by gas turbulence into the atomization zone and intercept liquid particles. The molten material spreads over the particle surface and solidifies rapidly with an entirely different solidification structure [1].

In some particles of the as-received powder, large inclusion clusters (>5μm) were observed, see Figure 4.1(d), which were believed to be hafnia according to EDX analysis. Some large precipitates which were generally bigger than 2 μm were also observed. These were usually located in the interior of powder particles, see Figure 4.1(e) (red arrow) and Figure 4.2 (a). These large precipitates usually showed strong Hf and O peaks in the EDX spectra, see Figure 4.2 (c), suggesting that they may be Hf-rich oxides. As noted in 3.1.1 Hf was added during melting prior to atomisation and it seems likely that these large particles may have been formed at this stage. The Hf would tend to getter the melt and it is reasonable to expect that large hafnia particles could then be formed which may not be broken down during melting and atomisation. In the cross section of powder particles, a typical dendritic microstructure could be observed, see Figure 4.1(e) and (f). The inter-dendritic regions of the as-received powder usually appear bright by virtue of atomic number contrast in the back scatter electron SEM image in Figure 4.1(e), which suggests the presence of high atomic number elements such as Hf and Zr. This was further verified by EDX analysis on the inter-dendritic and matrix areas (see Figure 4.3). A distinct Hf peak is present in the EDX trace of the inter-dendritic boundaries but is absent in that of the adjacent matrix, suggesting the inter-dendritic regions may be rich in Hf. The high atomic number contrast in the interdendritic regions is continuous suggesting that the Hf, which is giving rise to this contrast, is not present as discrete particles but may be in solution, having been rejected during the initial solidification. No significant oxygen or carbon-enrichment is seen in the EDX spectrum from these Hf-rich regions, which is consistent with the view that the Hf is in solution, but the sensitivity of EDX for these elements in such small regions would not be high and it cannot be concluded on this basis alone that the Hf is in solution rather than as thin oxide/carbide films.

Figure 4.4 shows the EBSD micrographs of the section of original RR 1000 powder particles. It can be seen that each particle contains several grains which are randomly distributed and which have an average diameter of around 6μm.

Figure 4.5 shows the presence of gas bubbles with diameters of 2μm~15μm inside some powder particles.

4.2.2. Influence of Heat Treatment on the Microstructure of RR1000 Powder

Given that HIPping involves a temperature ramping-up process, heat treatment of RR 1000 powder at different temperatures was carried out to better understand the microstructural evolution during heating history. Figure 4.6(a)-(e) show the SEM images of the particle surface of as-received powder and of out-gassed and sealed powders which have been subjected to heat treatments at different temperatures. It can be seen that no obvious change of the particle surface could be observed until the powder was heat treated to 900℃ and above, at which temperature very fine precipitates were formed on the particle surface (as in Figure 4.6 (c)). At increased temperatures the precipitates coarsened and became more discrete (Figure 4.6 (c)-(e)). The precipitates formed here due to heat treatment at high temperatures (up to 1200℃) are generally small (around or smaller than 1μm after a 1200°C treatment) and appear to have grown from the original size seen at 900°C. These particles thus appear to have a different origin from those large particles or clusters (>2μm) present in the as-received material which it has been suggested earlier originate from Hf addition before atomisation.

Figure 4.7(a)-(f) show the back-scatter electron SEM micrographs of sections of as-received and heat treated powders. As can be seen, the previously mentioned segregation of high atomic number elements such as Hf at interdendritic regions was not completely removed until the powders were heat treated to 1107℃ or above. As discussed below it may

be significant that this obvious dispersion from the interdendritic regions of the original segregation of Hf may be associated with the formation of the Hf particles on the surfaces of heat treated powders as shown in Figure 4.6.

EDX analysis shown in Figure 4.8 indicates that precipitates formed on the particle surface during heat treatment were rich in Hf, Zr and O, which may be assigned as (Hf, Zr) oxides. Due to beam spreading, some other detected elements in the spectra may come from the matrix. On the other hand, no Hf was found on the particle surface of as-received powders, as indicated in the EDX analysis on Figure 4.9. It seemed that the Hf which contributed to the formation of precipitates on particle surface during high temperature heat treatment may have come from the interior through diffusion, which finally led to the elimination of Hf segregation in the interior of particles as described above.

4.2.3. Influence of Oxygen Level on the Microstructure of RR1000 Powder during Heat Treatment

Figure 4.10 show the comparison of surface microstructure between out-gassed and then sealed powder and unsealed powder, both of which were heat treated at 1107℃ for 2h. For the unsealed powder, heat treatment was conducted in a dynamically pumped large vacuum furnace (100mm inner diameter and 1m length) where the total oxygen level is believed to be higher than the outgassed and sealed small can (6mm inner diameter and 20mm length) as indicated in Chapter 3. It can be seen that the un-encapsulated powder shows a significant increase in precipitate size and density as compared with those that were heat treated in sealed cans. A continuous precipitation has actually occurred along the boundaries on the surface of un-encapsulated powder after heat treatment. On the section of these unsealed powder particles, a continuous precipitate decoration was also observed around the particle periphery, see Figure 4.11. Obviously, increased O level would lead to an increased number

and size of precipitates on powder particle surface, if the precipitates are oxides and there is a supply of elements which are easily oxidised. The precipitates were also identified to be rich in Hf, O, and Zr as shown in Table 4.2.

Figure 4.12 shows the Auger electron depth profiles of the as-received powders and the powders that were heated treated in a vacuum furnace at 1107℃ for two hours, respectively. The as-received powders showed a very low level of O and Zr and showed no Hf on the particle surface. After heat treatment at 1107℃ for 2 hours in the vacuum furnace, the Hf, Zr and O contents all increased considerably on the very particle surfaces and subsurface areas. The accumulation of these elements on the particle surfaces obviously would promote (Hf, Zr) oxide precipitation. It is clear from figure 4.12 that an extremely high level of carbon was observed in the Auger electron depth profile, which is inconsistent with carbon content in this alloy (0.027wt%). This suggested the powders were contaminated. In the absence of other data the carbon signal has therefore been ignored and it has been assumed that the trends in concentration of all other elements are qualitatively correct and indicate changes of concentration with depth.

4.2.4. Influence of Pressure on the Microstructure of RR1000 Powder during HIPping

An actual HIPping process involves not only temperature history but also exertion of pressure and thus it is necessary to study the potential influence of pressure on the microstructure during HIPping. Figure 4.13 shows the SEM micrographs of the surfaces and sections of RR 1000 powders which were HIPped to 900℃/116 MPa, followed by immediate cooling at 5℃/min. In addition it can be seen that at this temperature and pressure, precipitates have already come out on the surfaces but seem to be less dense than those on the particle surfaces of powders that were heat treated in the absence of pressure. The lower

density of precipitates may be due to the influence of pressure or simply because no holding at 900℃ was implemented here. Besides, it can be seen that the Hf segregation at inter-dendritic regions and gas bubbles still remained under this condition, as shown in Figure 4.13(c). Powder particles tended to be connected to each other and especially those small particles were liable to be coalesced and integrated into big particles, see Figure 4.13(c)(d).

4.3. Discussion

The current experimental results have demonstrated that large Hf-rich particles and inclusion clusters were present in the as-received powder, which may remain in the samples even after HIPping and heat treatment, as further discussed in Chapters 7 and 8. These large particles and inclusion clusters are believed to be formed mainly due to the non-standard addition of Hf during atomisation melting in which Hf particles or clusters may be oxidized and remain in the powder particles during subsequent gas atomisation. In addition it is possible that some inclusion clusters may have been formed during conventional processing and gone through the preparation and secondary melting of ingots and finally remained in the atomized powders. This possibility is consistent with the many previous reports on the presence of large hafnium oxide inclusions in Hf-containing powder nickel superalloys even though a standard powder production procedure was followed [2, 3]. Further work is required to reduce the inclusions to as low a level as possible when following standard procedure.

In addition to the presence of inclusions, the as-received powder particles usually show a dendritic microstructure with high-atomic number elements such as Hf segregated at interdendrite regions. The Hf here seemed to be present in solid solution (given its continuous decoration at interdendritic regions) rather than as discrete Hf compound particles of the type shown in Figure 4.3 and Figure 4.6. This interpretation, that the continuous contrast arises from Hf in solution, is also supported by the fact that the interdendritic

enrichment of Hf was removed by high temperature heat treatment, which would not be expected if the Hf were in the form of oxides or carbides. As suggested from the data shown in figure 4.6 this interdendritic Hf seemed to have diffused from the interior to particle surfaces to form Hf-rich oxides. The thermodynamic driving force for this process is the high affinity of Hf (and Zr) for O which is usually rich on particle surfaces. Moreover, the inter-dendritic boundaries, where Hf was found to segregate, together with grain boundaries, would provide efficient routes for Hf to diffuse to particle surfaces at high temperature. With increased temperature, more Hf would diffuse to the particle surfaces to contribute to the growth of the precipitates. Ostwald ripening or coalescence of fine precipitates on the particle surface may also have occurred given the decreased density of precipitates and thus more discrete distribution of precipitates on the particle surfaces with increased temperature. Temperature would influence Ostwald ripening and thus is a potential method to control the particle size and distribution [4]. The data on changes in particle size with temperature is not detailed enough to confirm that Ostwald ripening is the mechanism responsible for particle growth in this case and no data was obtained for the time dependence at a fixed temperature. If much of the growth is associated with diffusion of the Hf, which it has been inferred is in solid solution, the kinetics would not be described by Ostwald ripening. Another key factor affecting the number and size of precipitates was found to be oxygen. With increased oxygen level, the precipitates became coarser and more continuously distributed, see Figure 4.10(b).

Since high temperature (like 1107℃) is usually required to consolidate powder into full density during HIPping, the formation of precipitates like (Hf, Zr)O_2 at PPBs seems to be unavoidable, which will be demonstrated in Chapter 5. In this sense, Hf, which is added as a grain boundary strengthening element may be harmful for net-shape HIPping of RR 1000 powder by forming precipitates decorating PPBs if they lead to poorer interparticle bonding.

4.4. Conclusions

The as-received and heat treated powders were studied using SEM and AES. For the as-received powder, a dendrite microstructure with segregation of high atomic number elements (such as Hf) at inter-dendrite regions was observed. These elements seemed to diffuse to particle surfaces at high temperatures (above 900℃) where (Hf, Zr)O_2 precipitates were formed. With increased temperature, precipitates became coarsened and more discrete. The Oxygen level was found to have a significant influence on the number, size and distribution of the precipitates. Increasing oxygen level led to increased size and number of precipitates.

References

[1] Dahlen M, Ingesten NG, Fischmeister H. Parameters influencing particle boundary precipitation in superalloy powders. Modern Developments in Powder Metallurgy 1981; 14: 3-14.

[2] Hardy MC, Zirbel B, Shen G, Shankar R. Developing damage tolerance and creep resistance in a high strength nickel alloy for disc applications. In: Green KA, Pollock TM, Harada H, editors: Superalloys 2004. Warrendale, PA: The Minerals, Metals and Materials Society (TMS); 2004. p. 83-90.

[3] Hyzak JM, Bernstein IM. The effect of defects on the fatigue crack initiation process in two P/M superalloys: Part2, surface-subsurface transition. Metallurgical Transactions A 1982; 13: 45-52.

[4] Porter PA, Easterling KE. Phase transformations in metals and alloys, second edition. London: Chapman & Hall; 1992, p.315-316.

Table 4.1 The compositions in at% of the precipitate and the adjacent matrix on the section of as-received RR1000 powder particle through EDX analysis

	C	O	Al	Ti	Cr	Co	Mo	Hf	Ni
particle	15.86	23.54	1.94	2.38	8.50	8.91	1.38	12.37	25.13
Matrix	18.64	-	3.84	2.37	13.53	15.87	2.12	0.39	43.26
matrix	17.63	-	3.68	2.51	13.95	16.19	2.16	0.32	43.56

Table 4.2 The composition in at. % of precipitates on the particle surface area of unsealed powder heat treated at 1107℃ for 2hours

	C	O	Al	Ti	Cr	Co	Zr	Hf	Ni
Particle 1	8.35	19.91	1.94	3.63	11.12	11.48	2.44	11.51	31.56
Particle 2	2.70	20.72	3.84	3.28	13.69	12.64	2.25	11.59	33.13
Particle 3	5.49	25.43	3.68	2.51	13.36	12.29	2.46	10.90	27.56

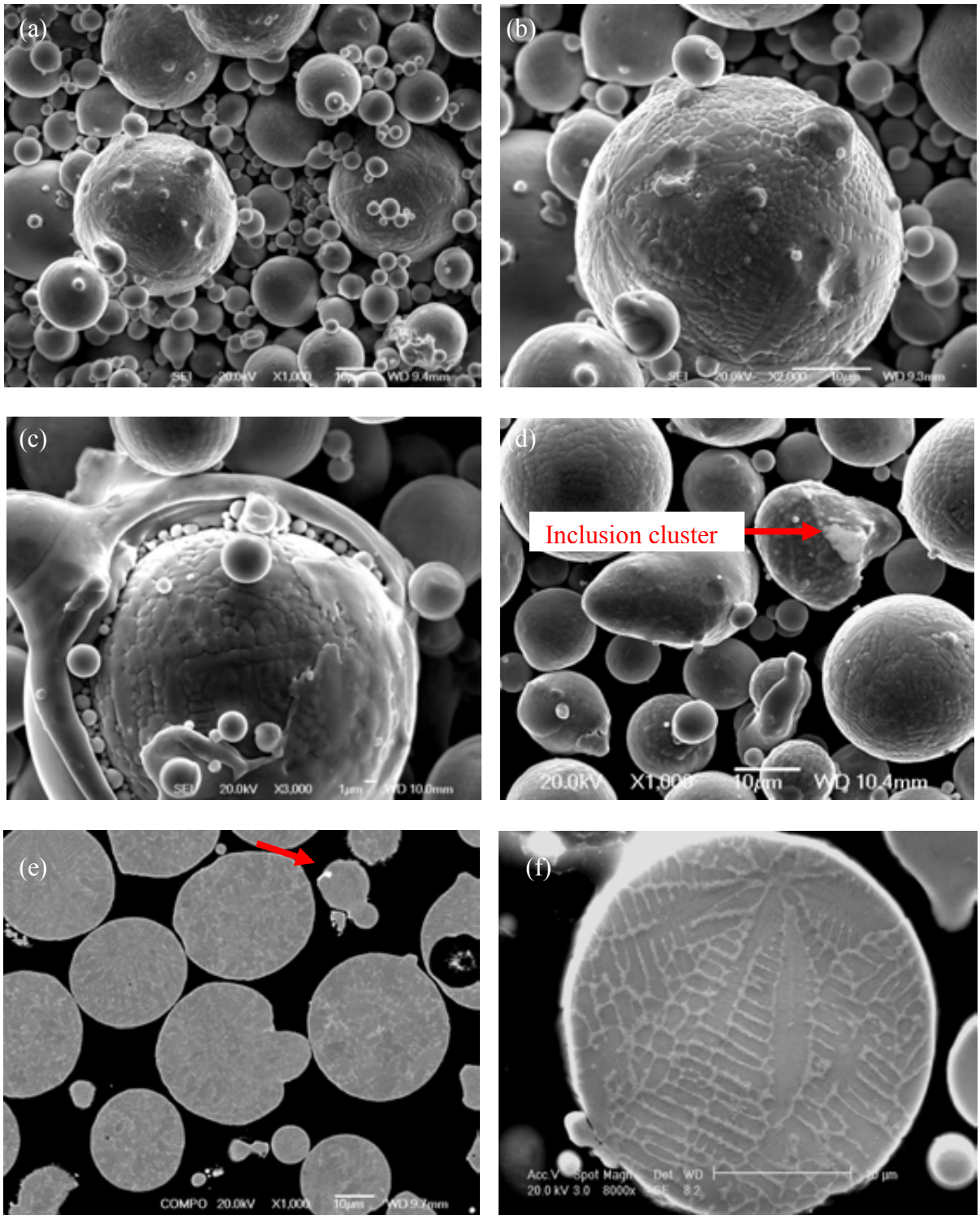

Figure 4.1. Secondary electron SEM micrographs showing (a) the powder particle size and distribution, (b) and (c) details of the particle surface structure and (d) the presence of inclusion clusters on particle surface of as-received RR 1000 powder; (e) back scattered SEM micrograph and (f) a secondary electron image showing the as-polished and etched sections of the as-received RR 1000 powder particles, respectively, showing the dendritic structure.

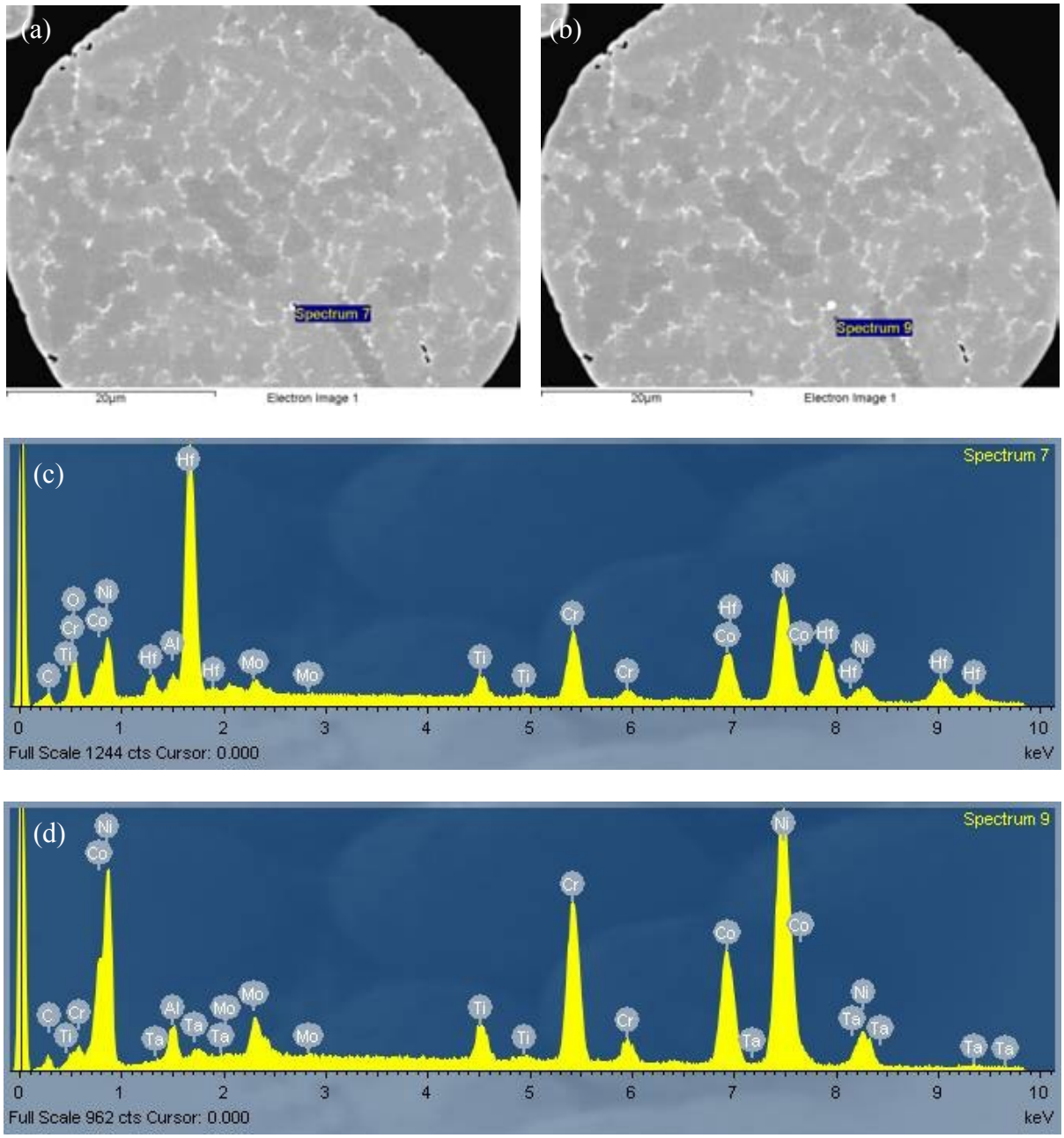

Figure 4.2 back scattered SEM images showing (a) an inclusion particle inside the powder particle, which was formed during melting for atomisation; (b) the matrix next to the inclusion; EDX analysis results showing the composition of (c) the inclusion particle and (d) the adjacent matrix, respectively.

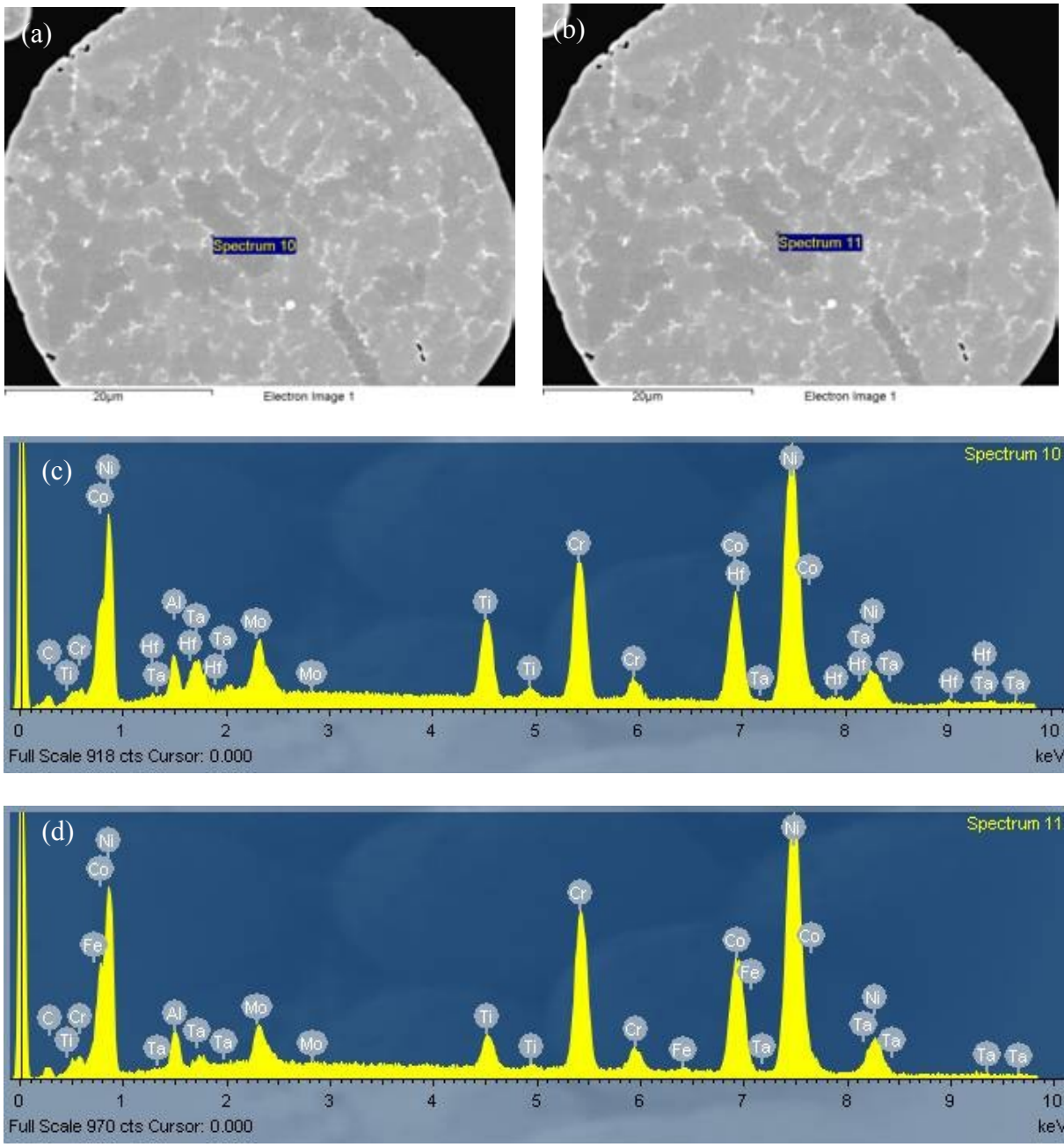

Figure 4.3 Back scattered SEM images showing (a) a interdendritc region and (b) the matrix next to the interdendritic region for EDX analysis; EDX analyses results showing the compositions of (c) the inter-dendritic region and (d) the adjacent matrix

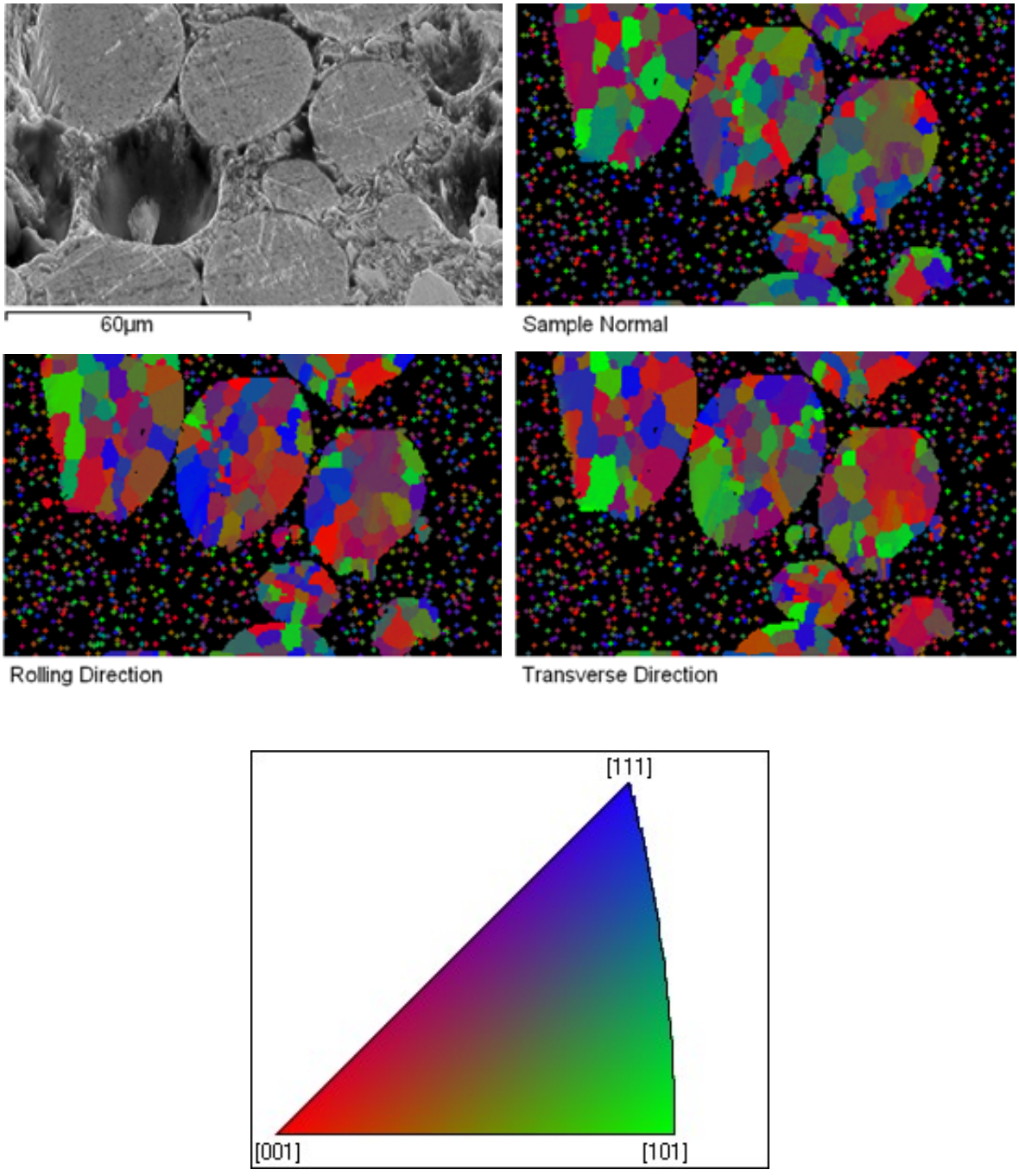

Figure 4.4 Electron back-scatter diffraction (EBSD) images showing the grain size and orientation of the as-received RR 1000 powder particles

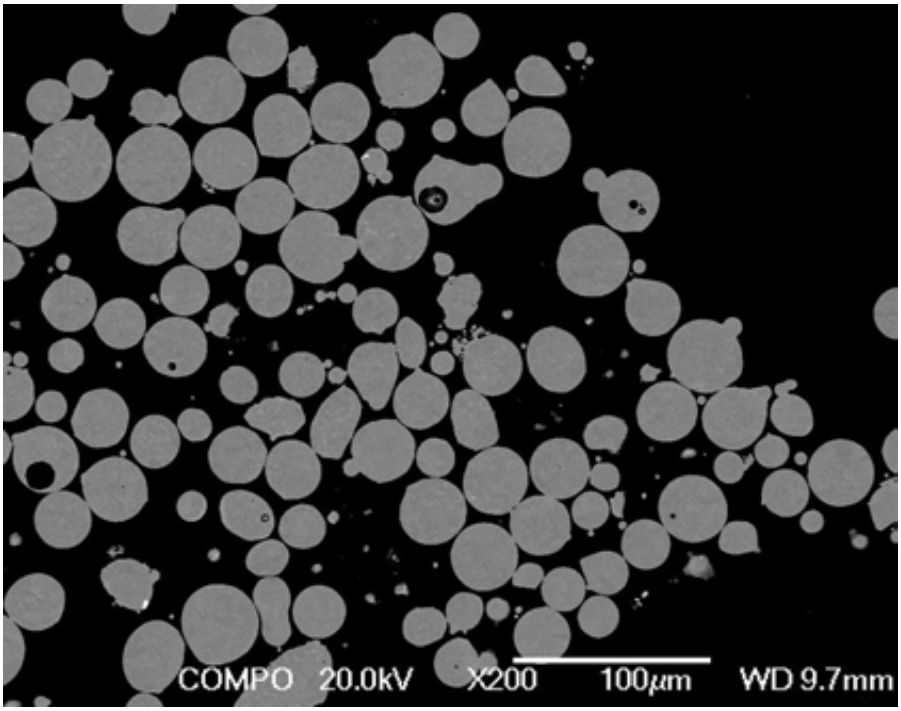

Figure 4.5 Back scattered SEM images showing gas bubbles in some as-received powder particles with sizes ranging from 2 μm to 15 μm.

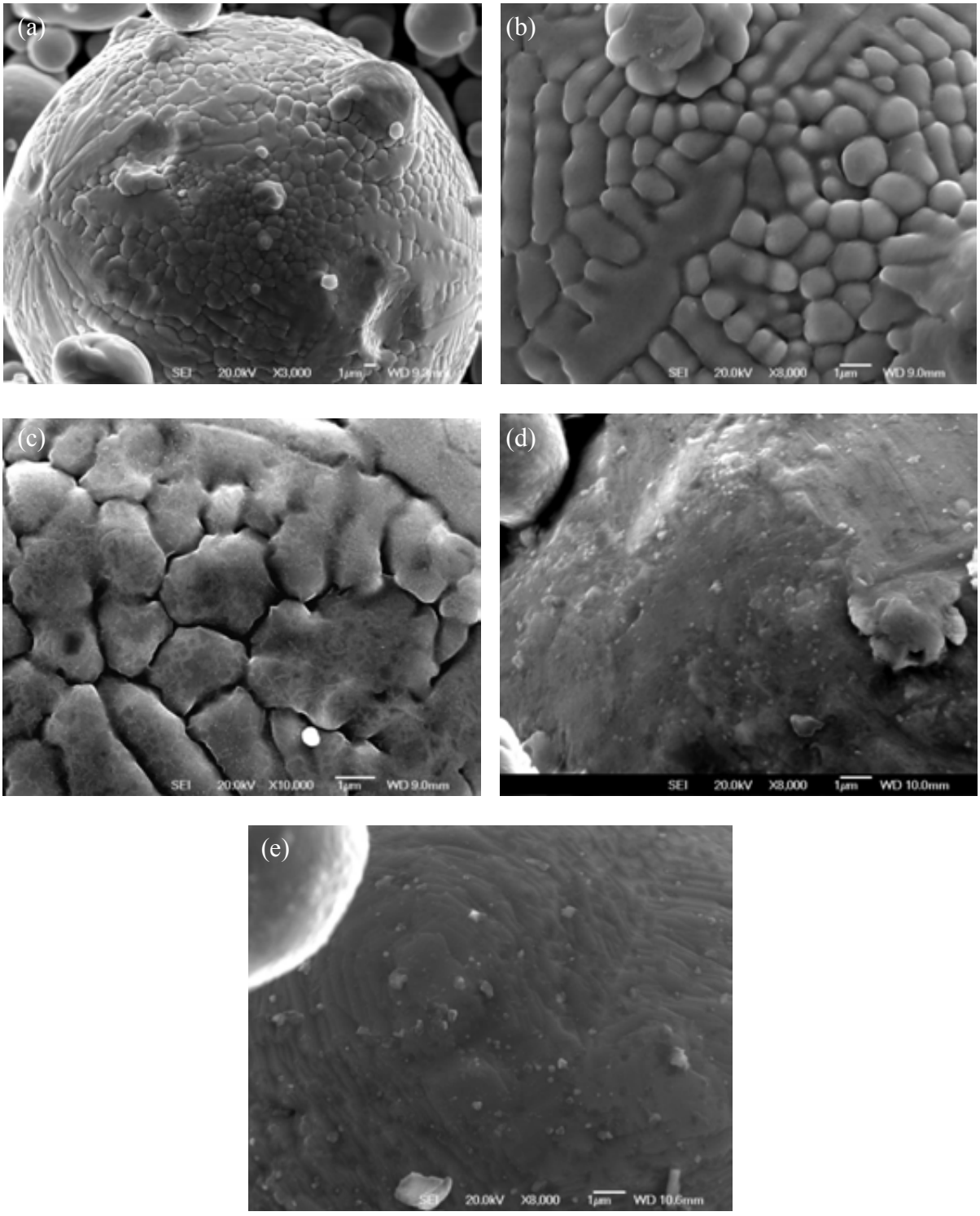

Figure 4.6 Secondary electron SEM micrographs showing the microstructural change on the RR 1000 powder particle surface with heat treatment, (a) without heat treatment; (b) out-gassed and sealed and heat treated at 850℃ for 2hours; (c) out-gassed, sealed and then heat treated at 900℃ for 2hours; (d) out-gassed, sealed and heat treated at 1107℃ for 2hours; (e) out-gassed, sealed and heat treated at 1200℃ for 2hours.

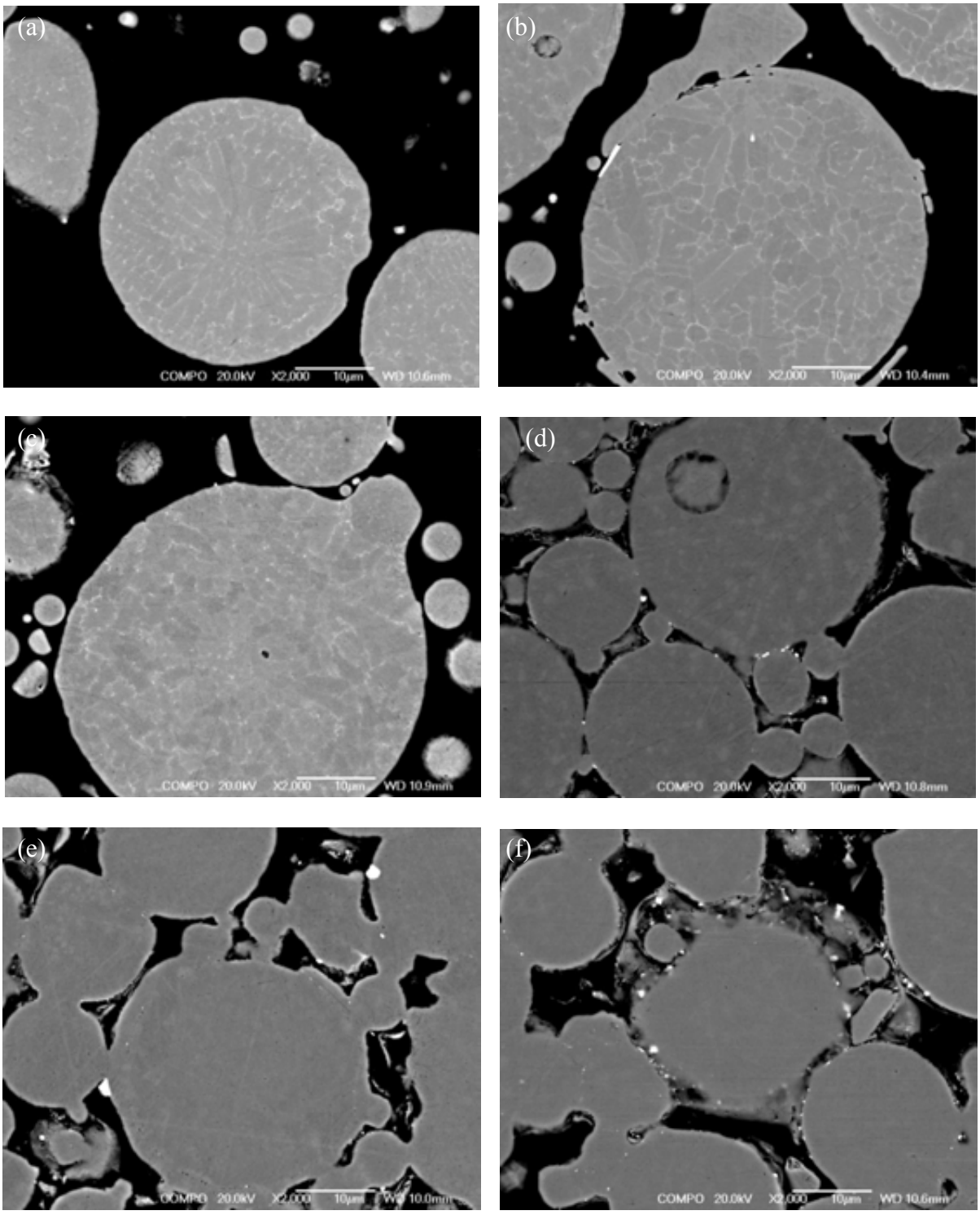

Figure 4.7 Back scattered SEM micrographs showing the microstructural change of the interior of RR1000 powder particles with heat treatment, (a)without heat treatment; (b) outgassed, sealed and heat treated at 850℃ for 2hours; (c)outgassed, sealed and heat treated at 900℃ for 2hours; (d)outgassed, sealed and heat treated at 1107 ℃ for 2hours; (e)(f)outgassed, sealed and heat treated at 1200 ℃ for 2hours. The 5μm white platelet at the periphery of the powder particle in Figure 4.7 (b) again is thought to have originated from the addition of Hf to the melt during atomisation.

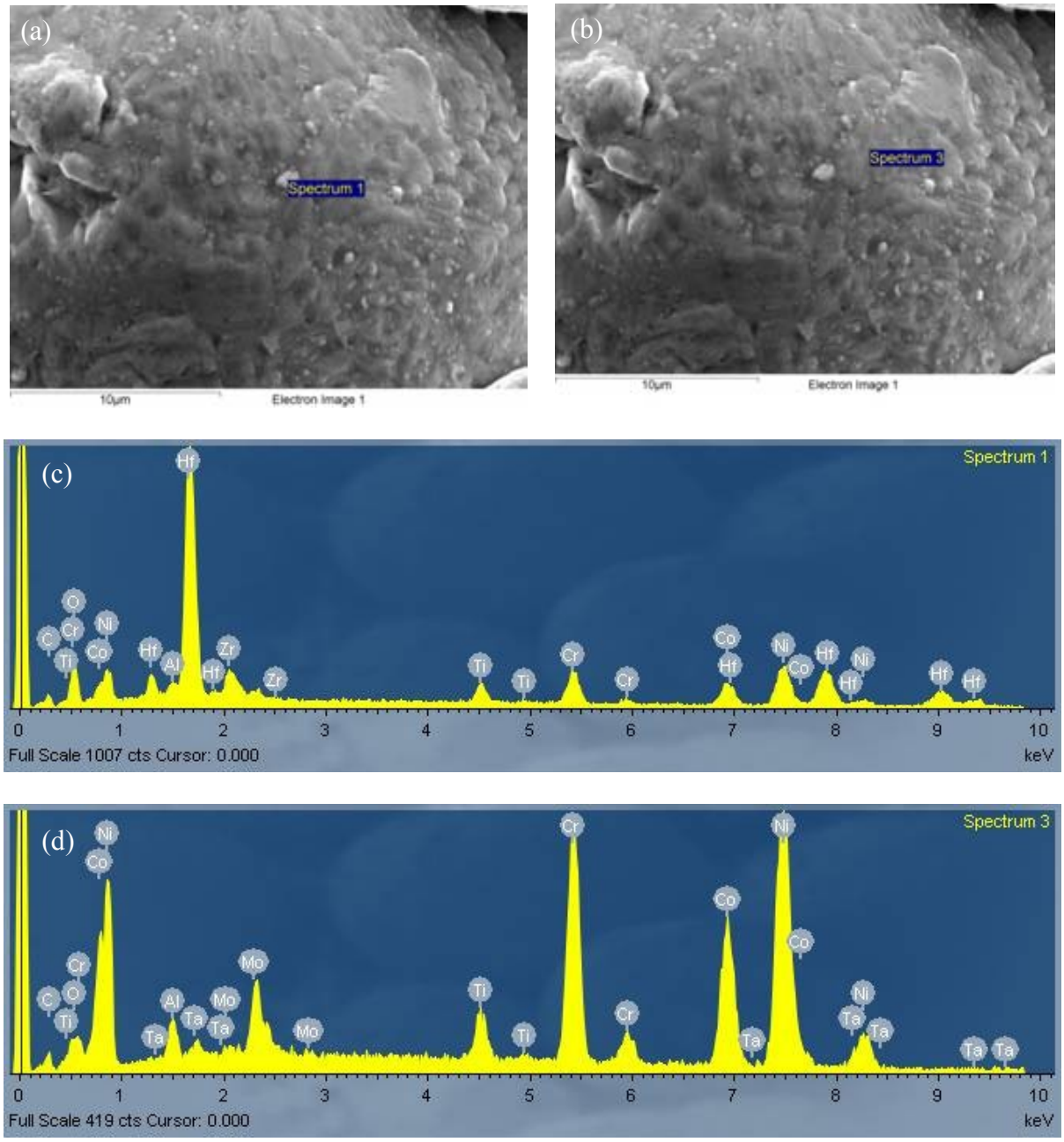

Figure 4.8 secondary electron SEM images showing (a) a precipitate for EDX analysis; (b) the matrix next to this precipitate; EDX results showing (c) the composition of the precipitate on the particle surface, and (d) the surface matrix next to the precipitate. The powders were outgassed, sealed and heat treated at 1107 ℃ for 2hours.

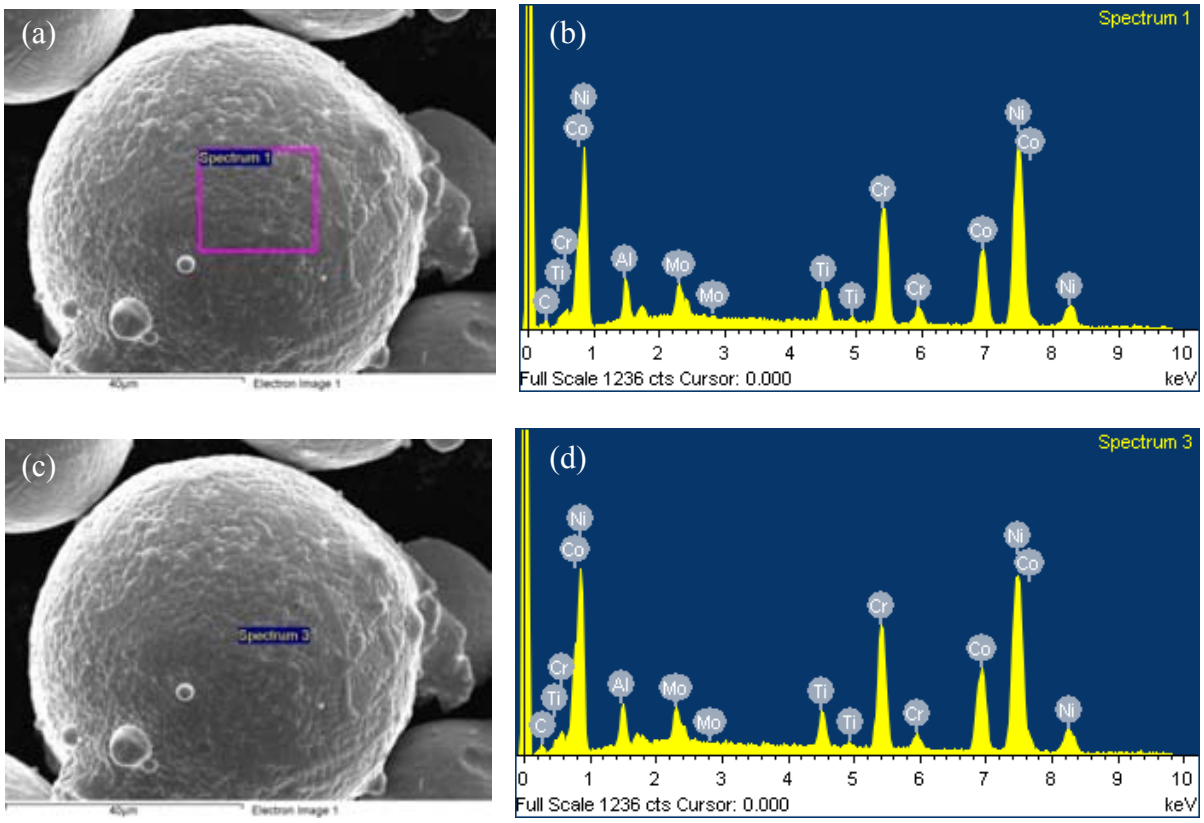

Figure 4.9 secondary electron SEM images showing (a) and (c) the regions for EDX analysis on the as-received powder particle surface; (b) and (d) EDX results showing the corresponding compositions of the regions in (a) and (c), respectively.

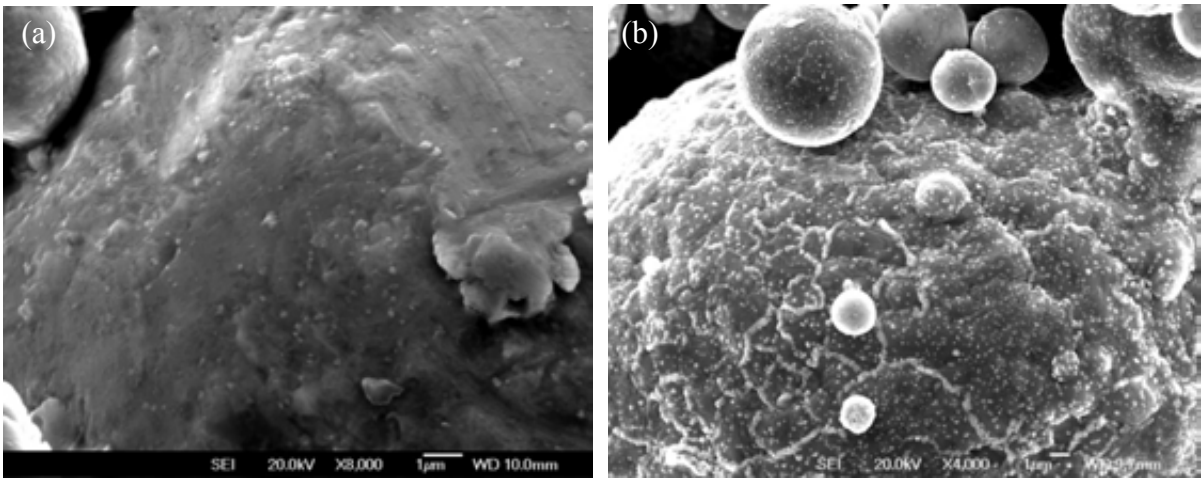

Figure 4.10 Secondary electron SEM micrographs showing the details of the RR 1000 powder particle surface after heat treatment under different conditions which had different oxygen level (a) heat treated in out-gassed and sealed cans at 1107 ℃ for 2hours; (b) un-sealed powder, heat treated in large vacuum furnace at 1107 ℃ for 2 hours (higher total oxygen level).

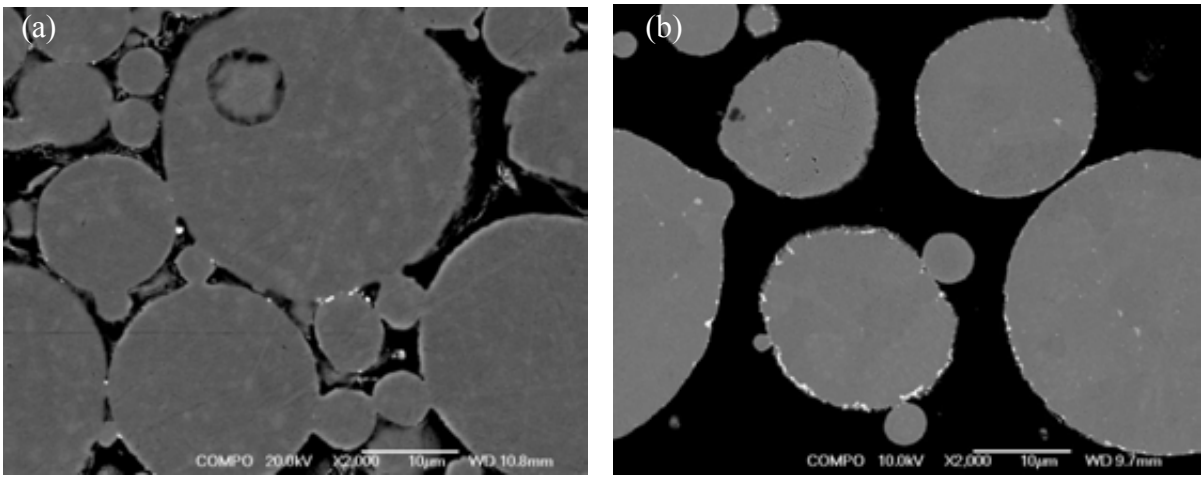

Figure 4.11 Back scattered SEM micrographs showing the section of RR1000 powder particles (a) heat treated in out-gassed and sealed cans at 1107 ℃ for 2 hours; (b) unsealed and heat treated in large vacuum furnace at 1107℃ for 2 hours (higher total oxygen level)

.

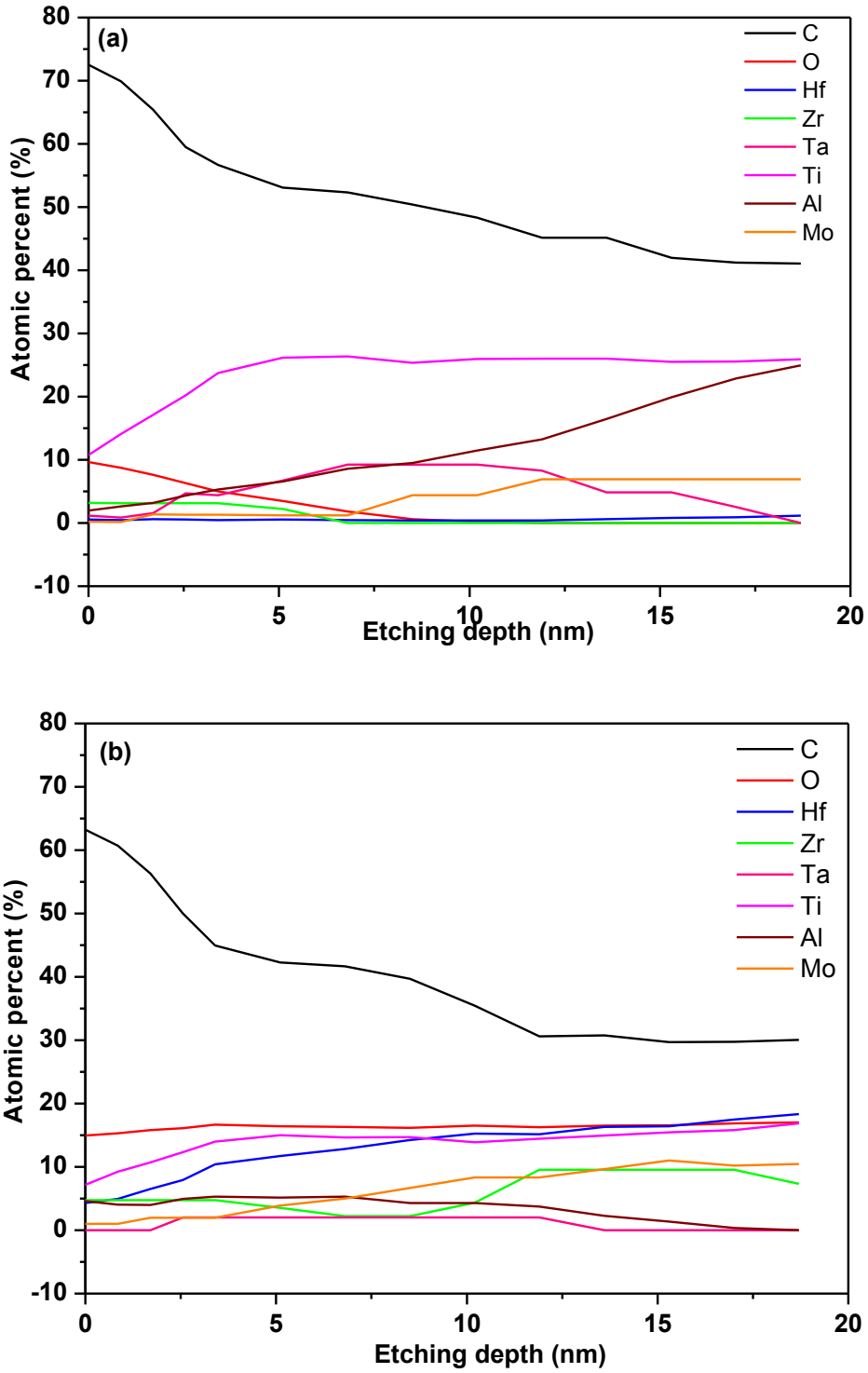

Figure 4.12 Auger electron depth profiles showing the compositional change in the very surface area with heat treatment (a)as-received powder; (b) unsealed powder which was heat treated in vacuum furnace at 1107℃ for 2 hours

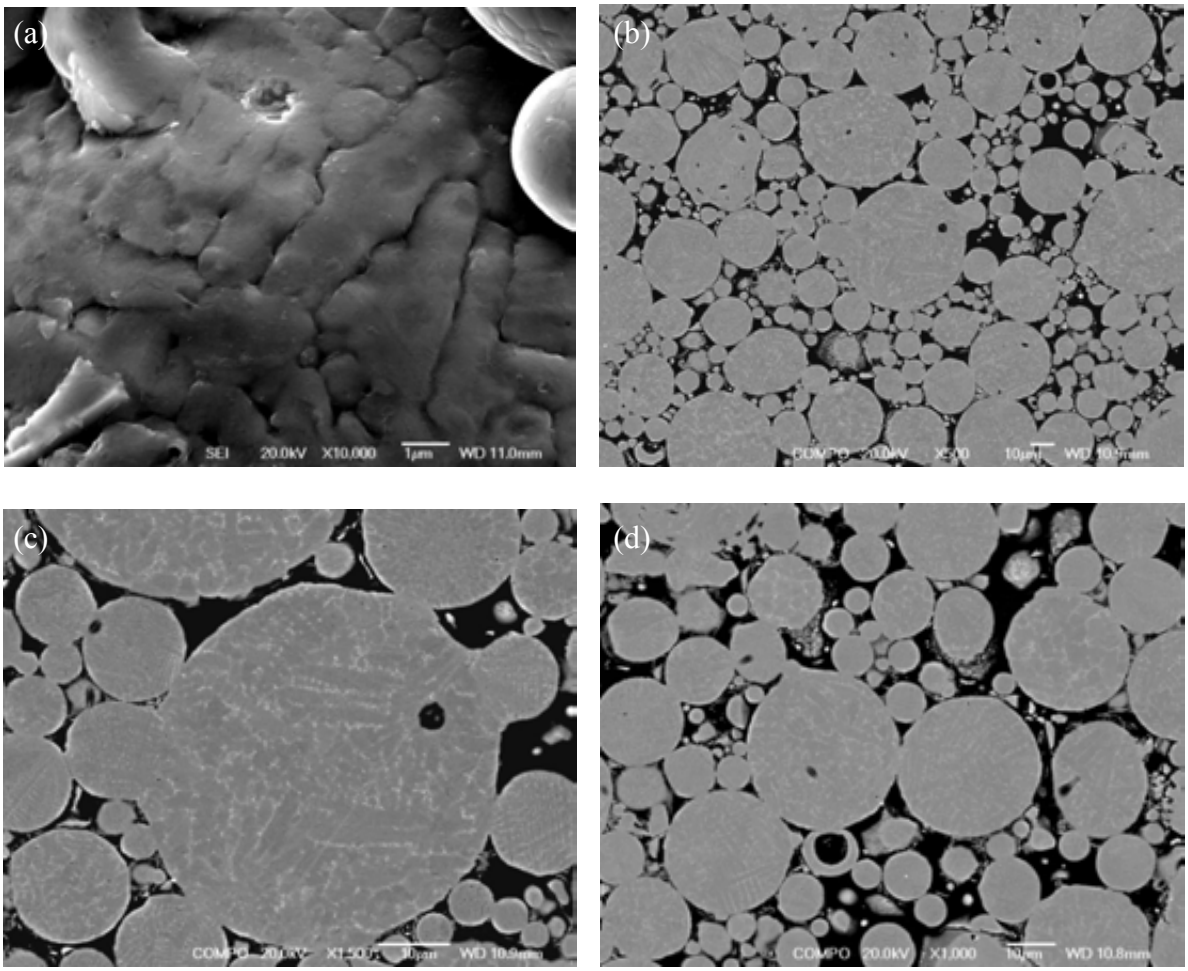

Figure 4.13(a) secondary electron SEM micrograph showing the powder particle surface and (b-d) back scattered SEM micrographs showing the section of RR1000 powder particles which were HIPped to 900℃/116MPa and then cooled at 5℃/min.

Chapter Five-Microstructure of as-HIPped RR 1000

5.1. Introduction

As reviewed in the second chapter, PPBs decorated with continuous precipitate films are extremely harmful for mechanical properties, especially high temperature tensile properties and low cycle fatigue properties. It was shown in chapter 4 that the number of precipitates formed on particle surfaces could be decreased through coarsening by increasing the temperature of heat treatment of powder prior to HIPping. This makes the precipitates more discretely distributed and thus prevents the formation of continuous precipitate film. Therefore, in this chapter, some heat treatment of powder prior to HIPping was conducted to study the effect of the heat treatment on PPB precipitate size and distribution in the as-HIPped RR1000 samples. The HIPping procedure was also changed to investigate potential change in PPB precipitation. On the other hand, it is generally believed that using super-solvus HIPping temperature could make grain boundaries grow beyond the PPBs and consequently leave the PPB precipitates inside the grain interior and thus reduce PPBs. Therefore, the influence of HIPping temperature on microstructure of as-HIPped RR1000 will be investigated as well. Besides, due to the necessity of using moulds to encapsulate powder for HIPping, the effect of mould material on the as-HIPped microstructure in the interface between the powder alloy and can materials was also investigated.

Moreover, in this chapter, the microstructural evolution during slow cooling from a supersolvus temperature was also studied in an attempt to reveal the formation mechanism of the irregular microstructures such as irregular-shaped γ′, fan-type γ-γ′ structure and serrated grain boundaries, as results of slow cooling from high temperature, which has been reviewed in Section 2.7.1.

5.2. Results

5.2.1. Interface between Can Materials and as-HIPped RR 1000

To find out the most suitable can material for encapsulating RR 1000 powder for HIPping, different can materials were tried. The so-called 'suitable can materials' here are interpreted as those that do not give rise to a significant diffusion layer (which may be very difficult to be removed via machining if hard precipitates are formed there) and better could produce a dense interface between the can and as-HIPped powder alloy. Figures 5.1 and 5.2 show the interfaces between the as-HIPped RR 1000 and different can materials after HIPping at 1107℃/100MPa/4h. It can be seen that using either mild steel or 1% Cr-bearing steel A4130 can material for consolidation of RR1000 powder leads to the formation of a diffusion zone extending around 300μm into the consolidated powder. In this zone, massive precipitates with a size of around 1.2μm were formed and basically distributed either along the prior particle boundaries or in the interior of the particles, see Figure 5.2. Meanwhile, a considerable number of voids were found at the can-RR1000 interface. When reducing carbon level by using ultra-low carbon steel can material, the depth of diffusion zone was reduced to less than 50μm. Using stainless steel 316L can material, where the carbon content is low while the alloying-elements (around 18wt.% Cr, 14wt.% Ni, 3wt.% Mo) are fairly high, seems to suppress the formation of diffusion zone in the interface, see Figure 5.1(d). The relationship between carbon levels of different can materials and the resultant depth of diffusion zone are shown in Table 5.1 and Figure 5.3. EDX analysis on these precipitates showed strong Hf, Ta and Ti and C peaks in the EDX trace (see Figure 5.4), indicating the precipitates should be Hf-, Ta- and Ti-rich carbides. A rough quantitative EDX analysis shown in Table 5.2 indicated that these carbides may be MC type carbides given the concentration ratio of (Hf, Ta, Ti) to C. Considering the significantly low carbon level in the

alloy matrix (around 0.027 wt.%) and the presence of Hf, Ta, and Ti in RR1000, it is apparent that C in the steel materials has diffused to the nickel alloy, which led to the formation of coarse carbides.

5.2.2 Influence of Outgassing Condition on O, N and H Levels of as-HIPped RR 1000

In chapter 4, it was found that increased O level led to the increased oxide precipitation. It is, therefore, highly necessary to avoid any oxygen pickup during powder handling before HIPping and better if oxygen level can be reduced. Here, the influence of outgassing condition on the O, N and H levels was investigated. Table 5.3 shows the H, N and O levels of the as-HIPped samples after outgassing under different conditions. In general, there is no significant difference in the H, N and O levels by using different conditions. Hot outgassing seemed to lead to marginal reduction in nitrogen and oxygen levels in the samples. Outgassing at 400℃ for 4 hours showed the lowest N (0.006 wt.%) and O (0.015 wt.%) levels.

5.2.3. Effect of Heat Treatment of Powder prior to HIPping on as-HIPped Microstructure

Figures 5.5 and 5.6 show the influence of heat treatment temperature or dwell duration (prior to HIPping) on the microstructures of RR 1000 after being HIPped at 1107℃ /100MPa/4h. PPBs were observed in all of the samples and the PPB precipitates seemed to generally coarsen marginally with increase of either heat treatment temperature or dwell duration. This is consistent with the previous observations on the particle surfaces of powder heat treated at different temperatures, see Figure 4.6.

5.2.4. Effect of HIPping Procedure

Figure 5.7 shows the precipitate distribution in the as-HIPped RR1000 samples which were HIPped with different procedures (see Figure 3.5). It can be seen that either ramping up temperature and pressure together or ramping up pressure first and then temperature led to the formation of PPBs with almost continuous precipitate decoration (see Figure 5.7 (a)-(c)) while ramping up temperature first and then pressure led to coarsened and more discretely distributed precipitates so that an intact spherical PPB could be hardly observed (see Figure 5.7(d) and (e)). This was further verified by TEM observation (see Figure 5.8) which revealed the precipitates obtained from the first two conditions to be 20-60nm in diameter and those from the latter condition to be 100-500nm in diameter. The effect of temperature ramp-up rate during HIPping on precipitate distribution was also studied, see Figure 5.9. No obvious change in PPB precipitate size and distribution can be distinguished by changing temperature ramp-up rate during HIPping.

To identify the precipitates formed in these as-HIPped samples, different analysis techniques have been used. Figure 5.10 shows TEM-EDX analysis of the precipitates of as-HIPped samples. The precipitates investigated for different HIPping procedures all showed strong Hf, Zr and O peaks. Quantitative results are shown in Table 5.4. It can be seen that these precipitates are all rich in Hf, Zr and O, indicating that they may have similar composition and the same structure. The ratio of Hf and Zr to O (around 1:2) indicates these precipitates may be (Hf, Zr)O_2 where the Hf content is much higher than Zr.

Figure 5.11 shows a TEM image of such a precipitate from which several diffraction patterns (b)-(e) were obtained. Detailed analysis and indexing procedure were described in Appendix B. The diffraction patterns along beam directions of [001] and [012] were obtained by tilting about a^* axis indicated by the white arrow in Figure 5.11 (c) while the diffraction patterns along zone $[\bar{1}11]$ obtained by tilting around b^* axis following a two-beam condition.

The interplanar spacings *d* for some particular crystal planes have been measured and calculated, which are shown in Table 5.5 in comparison with the theoretically calculated spacings by assuming the precipitates based on EDX and WDX analysis to be monoclinic HfO_2 with lattice parameters of a=5.1156Å, b=5.1722Å, c=5.2948Å, β=99.18° [1]. The equations for calculation of d-spacings are listed in Appendix B. It can be seen from Table 5.5 that the values of d-spacings obtained using two methods are very consistent with each other. The measured interplanar angles between some planes are also comparable to those calculated, see Table 5.6. Moreover, the measured angles between pole [011] and the other poles obtained are compared with those calculated, see Table 5.7, which also demonstrates highly consistent values. These suggest that the precipitates studied could be the monoclinic HfO_2. Given the observation of Zr in both EDX and WDX analysis and that Hf and Zr show unlimited solution to each other and that the monoclinic ZrO_2 and HfO_2 almost show the same lattice parameters (for ZrO_2, a=5.169 Å, b= 5.232Å, c=5.341Å, β=99.30°), the precipitates could be determined to be (Hf, Zr)O_2. The concentration ratio of Hf to Zr could vary from one precipitate to another but Hf seems to always dominate, as indicated by EDX and WDX analysis. For the precipitates studied in this work, the lattice parameters could also be determined by measurement of d-spacings for several crystal planes in combination of use of relevant equations but due to the complexity of those equations for monoclinic structure, it is very difficult to get precise lattice parameters. Roughly, the lattice parameters for the current precipitate were determined to be a≈4.977 Å, b=4.9 Å, and c≈5.376 Å.

Although the majority of precipitates analyzed in the current work were identified to be (Hf, Zr)O_2, there were also some other precipitates where Hf, Zr and C dominated, see the TEM-EDX analysis in Figure 5.12 (b). TEM diffraction patterns in Figures 5.12(c) and (d) for this precipitate correspond to the pole [101] and [001] for an fcc structure. The angle between the two poles was measured to be close to 45°. The measurement and calculation of

d-spacings for some crystal planes like (010) were also conducted. Specifically, $d_{(010)}$ (equals to lattice parameter *a*) was measured to be around 4.8 Å which is very close to the value of the typical $d_{(010)}$ or lattice parameter for fcc HfC that is 4.6395 Å according to [1]. Since Hf and Zr can substitute for each other in this structure, the precipitate could be identified as fcc (Hf, Zr)C in which Hf dominates. Some other diffraction patterns obtained from this precipitate were also analyzed but could not be fully identified in terms of the measured tilt angles, which was probably due to presence of polycrystals in the precipitate. The fact that both (Hf, Zr)O_2 and (Hf, Zr)C were present in the current as-HIPped materials may be due to that Hf is well known as not only a strong oxide former but also a strong carbide former.

In addition to the presence of PPB precipitates formed during HIPping, large inclusion particles or clusters which it has been suggested were inherited from the melting for atomisation could be observed in the as-HIPped samples as well, see Figures 5.13 (a) and (b). WDX analysis in SEM on these particles, as shown in Figures 5.13(c) and (d), suggests that these particles are rich in Hf, O and Zr. A small carbon peak was also noted in the WDX spectra. Table 5.8 shows the quantitative analysis of the concentrations of the detected elements in the particles in atomic percentage. It can be seen that there is no obvious compositional variation among the different particles except for the carbon content. The ratio of Hf and Zr to O suggests that these large particles could be (Hf, Zr)O_2, which is consistent with the EDX analysis in Chapter 4.

5.2.5. Influence of HIPping Temperature on Microstructure

5.2.5.1 PPB Precipitation

Figure 5.14-5.15 shows the PPB precipitate distribution of the samples after HIPping at different temperatures. It appears that no great difference could be distinguished in the precipitate size and distribution after HIPping at different temperatures. The PPB precipitates observed were always less than 100nm and seemingly decorated the PPBs continuously, see

Figure 5.14. Etching and high magnification observation revealed that these precipitates were actually not continuously distributed like a film but instead were discrete particles, see Figure 5.15.

Observation on slightly chemically etched samples revealed that increasing the HIPping temperature to super-solvus could make the grain boundaries grow across PPBs and leave the precipitates in the interior of coarsened grains, see Figure 5.16(c)(d). For samples HIPped at lower sub-solvus temperatures, grains tended to be confined by PPBs and thus precipitates were still present at PPBs, see Figure 5.16(a) and (b). It is also noted that pronounced grain boundary serrations were developed in the samples HIPped at 1180℃ followed by slow cooling (around 5℃/min), see Figure 5.16(d).

5.2.5.2 Grain Size and Distribution

Figure 5.17 shows the EBSD micrographs of the microstructure of as-HIPped samples. Irrespective of HIPping temperature, grains in all the samples studied were randomly orientated. However, with increased HIPping temperature, significant grain growth was observed. Correspondingly, the variation in grain size distribution (analyzed using EBSD analyzing software) of samples with different HIPping temperatures is shown in Figure 5.18. It can be seen that with increased HIPping temperature, the fraction of small grains decreased significantly while that of coarse grains increased steadily. The average grain sizes were statistically calculated to be 8.2 μm, 11.5 μm and 12.6 μm, for 1107℃, 1160℃ and 1180℃, respectively. At high temperatures, like 1160℃ and 1180℃, grain growth became less obvious with further increase of temperature. In the higher magnification EBSD images, irregular-shaped grains with serrated grain boundaries could be observed in the sample HIPped at higher temperature, see Figure 5.19(b).

5.2.5.3 Gamma Prime

Figure 5.20 shows the gamma prime distribution in as-HIPped RR 1000 samples that were cooled at 5℃/min from 1107℃, 1125℃, 1160℃ and 1180℃, respectively, to room temperature. A tri-modal gamma prime distribution, composed of primary, secondary and tertiary γ′ can be seen in all the samples. The coarse primary γ′ are usually formed at grain boundaries and show a big size range from 1μm-5μm and can exist in either a blocky morphology or script or dendritic morphology. As for secondary γ′, both the size and morphology change significantly with increasing HIPping temperature. When cooled from 1107℃, most of the secondary γ′ show a near-cuboidal morphology while others show a jagged morphology on one side and all show a size of 300nm~800nm. When cooled from 1125℃, the size of secondary γ′ does not change very much (around 300nm~1μm) but the morphology has become dendritic. Cooling from higher temperatures like 1160℃or 1180℃ led to even more irregular and complicated γ′ morphology with a much bigger size, basically in the range of 800nm~1.6μm. Tertiary γ′ basically show a very small size (<100nm) and a spherical morphology. Obviously, secondary γ′ show the greatest sensitivity in both size and morphology to the HIPping temperature from which slow cooling ensued.

In the samples that were HIPped at 1180℃or 1160℃ and then slowly cooled, fan-type γ-γ′ structures were observed, see Figure 5.21. They are usually composed of finger-shaped γ′ dendrites and the γ matrix in between and usually located in small grains or part of a large grain which is adjacent to grain boundary triple points. The size of this type of structure has been measured to be between 5μm to 15μm and the volume fraction of this structure in the samples is around 3%.

5.2.6 Evolution of Gamma Prime during Slow Cooling from Super-solvus

To study the evolution of gamma prime during slow cooling from super-solvus, interrupted cooling tests were carried out, which were designed to freeze (via water

quenching) the microstructure at several temperatures during slow cooling. All the samples were solution treated at a super-solvus temperature 1180℃ for 1hour first and then slowly cooled at 5℃/min to several temperatures of interest, from each of which the sample was immediately taken out for water quenching. The experimental details have been given in Chapter 3.

5.2.6.1 The formation of irregular-shaped γ′

Figure 5.22 shows the nucleation and morphological development of γ′ during slow cooling from 1180℃ which is above the γ′ solvus. It can be seen that on cooling to 1160℃ (i.e only 10℃ below the solvus) numerous γ′ precipitates were already developed and were homogeneously distributed throughout the sample, see Figure 5.22(a). The precipitates were so dense that a number of precipitates were very close to each other and many of them even contacted each other. These precipitates usually showed a spherical morphology and were all about 25nm in diameter. In the sample which had been cooled to 1130℃, intragranular γ′ had coarsened to around 50nm and it appeared that local aggregation of several adjacent γ′ precipitates with equivalent sizes may have occurred (see the red loops in Figure 5.22(b)). At grain boundaries some irregular-shaped γ′ of around 130nm were observed, see Figure 5.22(c). Slow cooling to 1110℃ resulted in significant coarsening of primary γ′ at grain boundaries to around 1 μm, which may be due to rapid diffusion at grain boundaries. Meanwhile, some irregular-shaped clusters of coarsened γ′ precipitates were found sporadically distributed in the interior of grains, see Figures 5.22(d)-(f). The diameter of these clusters was about 500~700nm and the size of individual coarsened γ′ particles in the clusters was typically 150~250nm. The coarsened γ′ in the clusters tended to contact and coalesce with each other. In the vast matrix area, the dominant precipitates were about 80-100nm in diameter and locally these precipitates were usually very close to each other with

the distance between two adjacent particles usually less than 100nm, see Figure 5.22(g); any further coarsening could lead to contact and coalescence of these 100nm particles. In between these precipitates many finer γ′ particles could be observed. When the sample was cooled further, down to 1095℃, irregular-shape γ′ clusters of about 500nm diameter were well developed and were widespread throughout grains, see Figures 5.22 (h) and (i). In addition to these irregular-shaped γ′, there were many colonies of contiguous γ′ particles with individual sizes around 80nm, see Figures 5.22 (i) and (j) (as indicated by the red loops). These loosely coalesced γ′ clusters were usually of a very similar diameter to those well developed irregular-shaped γ′. When the samples were cooled further to 1080℃, large irregular-shaped γ′ particles between 500nm and 800nm were dominant (see Figure 5.22(k)). With continued cooling, the irregular-shaped γ′ became coarser and more complex.

5.2.6.2 The formation of fan-type γ-γ′structure

Figure 5.23 shows the formation of fan-type γ-γ′ structure during slow cooling from above the solvus. It is noted that the fan-type γ-γ′ structure could be hardly observed until samples were slowly cooled (from 1180℃) to 1095℃ or lower temperatures. According to Figure 5.23(a), some γ′ rods in the structure were developed through contact and coalescence of γ′ particles ahead (see the red arrow). At temperatures below 1095℃, the fan-type γ-γ′ structures became well developed. Most of them were found as a part of a complete grain and usually caused pronounced indentations or serrations to the grain boundaries to which they were connected see Figures 5.23(b)-(d). The rest were found to spread through whole grains with γ′ rods radiating outward in every direction, see Figures 5.23(e)-(f).

5.2.6.3 The formation of serrated grain boundaries

Figure 5.24 shows the grain boundary (GB) morphological evolution during slow cooling at 5℃/min from a supersolvus, 1180℃. It can be seen that at high temperatures like 1130℃,

grain boundaries are basically straight with small γ′ present, see Figure 5.24 (a). When the samples were slowly cooled to 1110℃, it appeared that at sites of those fine spherical GB γ′ (see Figure 5.24 (b)), grain boundaries still remained straight but at many other sites where large and blocky GB primary γ′ (>1μm) were developed, pronounced grain boundary serrations were observed, see Figures 5.24 (c) and (d). It is noted that at the GBs around coarse primary γ′, the density of fine γ′ particles was much lower than those in the interior of grains or at straight GBs, see Figures 5.24 (b)-(d). With continued slow cooling, the grain boundary regions became more depleted of the fine precipitates and meanwhile more primary γ′ particles were developed, which made the grain boundary serrations even more pronounced, see Figures 5.24 (e)-(h). Besides, it is noted that wherever the GB primary γ′ were elongated and narrow in width, the grain boundaries kept fairly straight and no serration was observed, see Figure 5.24 (i). The formation of fan-type structure was also observed to cause pronounced grain boundary serrations, see Figure 5.23(b). But given the small number of fan-type structure, the development of pronounced grain boundary serrations could be mainly associated with the presence of large and blocky primary γ′ at grain boundaries.

5.2.7 Effect of Cooling Rate from HIPping Temperatures

Figures 5.25 and 5.26 show the γ′ distribution in the samples with different cooling rates after HIPping at 1107 ℃ and at 1125 ℃, respectively. It can be seen that the cooling rate from the HIPping temperature has a significant influence on the size, distribution and fraction of different kinds of γ′. Increased cooling rate led to significant reduction of secondary γ′ while producing considerable much finer tertiary γ′. The fraction and size of coarse primary γ′ also decreased slightly with increasing cooling rate, see Figure 5.25. The primary γ′ size range actually narrowed down from 1~1.8μm to 0.8μm~1.3μm when the cooling rate was increased from 5℃/min to 132℃/min. Moreover, it is noted that cooling at varied rates from

a HIPping temperature of 1125℃ resulted in significant morphological change for secondary γ′. A dendritic morphology is usually seen when cooled at 5℃/min whereas when cooled at 132℃/min a spherical or cuboidal morphology is observed, see Figure 5.26. The finer microstructure produced through rapid cooling from HIPping led to considerable increase in hardness which more or less reflects strength of a material, see Figure 5.27.

5.3 Discussion

5.3.1 Formation of Diffusion Layer between as-HIPped RR1000 and Can materials

Due to the necessity of using cans to encapsulate powder for net-shape HIPping and the necessity of removing cans after HIPping, the formation of diffusion layer at the interface between can material and powder alloy is of significant concern. The current experimental results clearly demonstrated a strong relationship between carbon level of a can material and the depth of diffusion layer formed at the boundary between the can material and RR 1000 alloy (see Figure 5.3). With increased carbon content in can materials, the depth of diffusion layer expanded. When using steel cans containing high level of carbon for powder HIPping, a diffusion layer of 300μm in depth and rich in (Hf, Ta, Ti)C carbides, was formed on the side of RR 1000 alloy, whereas on the side of can materials, voids were found. This happened obviously due to elemental diffusion and Kirkendall effect. The great difference in carbon content between these can materials and RR 1000 gave rise to a large chemical potential difference at the interface, which would drive carbon diffusion from can materials into the powder alloy during HIPping. The chemically active sites such as PPBs and grain boundaries in RR 1000 also provided a fast route for carbon diffusion and penetration and thus promoted the formation and growth of carbides. Using ultra-low carbon steel or stainless steel 316L can materials, which showed significantly low carbon content, could considerably

reduce or even eliminate a diffusion layer. Can materials (like stainless steel 316L) containing high level of alloying elements such as Cr, Ni and Mo , could further suppress carbon diffusion and thus avoid the formation of diffusion layer on the can-alloy interface. Obviously, a diffusion layer rich of hard (Hf, Ta, Ti)C carbides is a great challenge for machining and thus should be avoided. On the other hand, the ultra-low carbon steel can is apparently more easily removed than the stainless steel can. Therefore, the ultra-low carbon steel is preferred as a mould material for net-shape HIPping of RR 1000 powder.

5.3.2 Effect of Heat Treatment of Powder prior to HIPping or HIPping Procedure on as-HIPped Microstructure

The experimental results demonstrate that the precipitates that were formed on the surfaces of the powders that were heat treated at different temperatures were inherited in as-HIP samples as PPB precipitatates. The size of PPB precipitates also increased with increased powder heat treatment temperature prior to HIPping, consistent with the previous study on powder shown in Chapter 4. Obviously, heat treatment of powder prior to HIPping may be a route to modify PPB precipitate size and distribution.

In terms of the influence of HIPping procedure on PPB precipitate size and distribution, ramping temperature up first and then pressure led to the formation of coarser and more discrete precipitates as compared with those procedures like ramping pressure first or ramping pressure and temperature up together. It seemed that ramping up temperature at low pressure or without pressure (like heat treatment of powder prior to HIPping) promoted precipitate coarsening. Without high pressure, the powder consolidation process would be postponed and the free surfaces of powders may be more favourable for either surface elemental diffusion or coalescence of adjacent fine precipitates, which would promote precipitate coarsening. In other situations where pressure was ramped first and then temperature or pressure and temperature were ramped up together, powder consolidation

would occur much earlier, which may impede the contact and coalescence of adjacent precipitates or elemental diffusion and thus restrict the growth of precipitates.

5.3.3 The Formation of Irregular-shaped γ′

The interrupted cooling tests using water quenching after cooling at 5℃/min from 1180℃ to selected temperatures demonstrated that a high density of γ′ had been formed even in the very beginning of cooling. Thus on cooling to 1160℃ numerous γ′ precipitates with size about 25nm in diameter were already developed and homogeneously distributed throughout the sample. These precipitates further coarsened to around 50nm when the sample was cooled to 1130℃ before quenching. It is difficult to reconcile these observations with the interpretation of the DSC analysis (see Figure 3.3(b)) where it was suggested that the onset γ′ precipitation temperature was determined to be around 1130℃. On that basis the high densities of 25nm and 50nm diameter precipitates would have to have been formed during the water quench since both quenching temperatures are above or very close to the temperature at which it is inferred from the DSC curves that γ′ precipitation begins. The fact that the precipitates are larger when the samples were water quenched from the lower temperature is not consistent with this interpretation. Also in Figures 5.22 (a)-(b) some very fine precipitates with diameters smaller than 10nm are obvious between the larger precipitates. It is thus suggested that the 25nm and 50nm precipitates are formed during cooling at 5℃/min to 1160℃ and 1130℃ and that the fine precipitates between them may be formed during the water quench. The fact that there is a far lower density of the smaller precipitates in samples water-quenched from the lower temperatures (like 1080℃, see Figure 5.22(k)) is entirely consistent with this view since the supersaturation remaining when samples are further cooled before water quenching would be reduced and fewer small precipitates formed.

This interpretation of the observations summarised in Figures 5.22 is inconsistent with the interpretation of the DSC curves such as that shown in Figure 3.3(b). The usual definition of the temperature of the onset of nucleation in DSC analysis is a pronounced turning point in the DSC/DTA curve or by the point at which two tangential lines (like Figure 3.3(b)) cross. This approach is accepted in the literature, for example in references [2-4] but in fact this observation of a pronounced turning point cannot be the actual beginning of precipitation but corresponds to the situation (which is cooling-rate dependent) when precipitation is prolific enough to cause such an inflection. The actual onset of nucleation will be earlier than this temperature and quenching experiments are necessary to interpret these DSC curves. This interpretation of the observations made on these water quenched samples is important in understanding the observation of the large irregular-shaped precipitates as discussed in the following paragraphs.

The current experimental observations suggest that the formation of the irregular-shaped γ′ is associated with the coarsening and coalescing of γ′ precipitates. This conclusion is contrary to the widely accepted view, for which there is extensive evidence that large cuboidal particles of γ′ formed during ageing, break up to form dendrites or even clusters of smaller γ′ during extended ageing of Ni superalloys. This break up is driven by increased mismatch and consequent instability [4-6] and is illustrated in Figure 5.28. This mechanism thus involves coarsening to produce large cuboidal γ′ particles. Continued growth of the γ′ precipitates results in the extension of the corners of the cuboids, which then splits into an octet or dendritic γ′ and this process has been substantiated by observations where larger precursor particles are observed. In the present work where continuous cooling from the γ′ transus was used, no such large precursor precipitates were observed and it appears that under these conditions coarsening, followed by break-up may not be involved and that continuous growth occurs.

The present observations are not inconsistent with Doherty's [7] stress-directed diffusion coarsening model, which had been originally proposed to explain the formation of L-shaped γ′. In this model, he suggested two steps would be involved in bringing largest γ′ cuboids into contact, see Figure 5.29. Firstly, solute flux occurs from surrounding smaller precipitates to the largest γ′ cuboids; secondly, solute flux goes through the gap between the largest γ′ cuboids to remove elastically distorted matrix between cuboids. The difference of this model from the current experimental results is that in forming irregular-shaped γ′, several rather than two localized γ′ with comparable sizes need to be coarsened and coalesced by absorbing γ′-forming elements from surrounding matrix. The driving force for the coarsening and coalescing processes may be partly due to the trend for the system to reduce total interfacial energy and partly due to (as Doherty suggested) the removal of the elastically strained matrix lying between larger γ′ particles if the lattice parameter were different in the precipitates from the matrix, i.e. the process will partly depend on the precipitate/matrix misfit.

In addition the current experimental observations are also consistent with Mao et al's [2] study on continuous cooling precipitation in another advanced P/M superalloy (U720Li) with high volume fraction of γ′ (around 50% in volume which is also the case with RR1000.). In their work, the formation of irregular-shaped γ′ was also attributed to coarsening or coalescing of the precipitates.

On the basis of this discussion it appears that two mechanisms can lead to the formation of large irregular-shaped γ′ precipitates:

(i) coalescence as an inevitable consequence of continuous growth when coupled with extensive nucleation;

(ii) splitting, driven by increased mismatch and consequent instability.

The question that needs to be addressed is what conditions lead to which mechanism?

The answer to this question appears to be contained in reference [5] where it was shown that growth, followed by break-up is favoured under extended ageing and low supersaturation, because impingement is unlikely. In fact they state that the growth sequence giving rise to break-up "… may be interrupted by impingement effects when the γ′ is present in high number densities"; "…may be interrupted if sufficiently high γ′ nucleation densities cause overlap of the diffusion fields, as frequently observed in commercial heat treatments."

The ageing used in reference [5], where it is concluded that break-up is occurring, was for extended times just below (20℃) the γ′ transus, where super-saturation and nucleation density would be low so that γ′ could easily grow to several microns without impingement. In other work, where the ageing temperature was low, but the concentrations of γ′-forming elements are low (so that the density of γ′ nuclei would be low during ageing) [6] or the starting materials for ageing already contained very large γ′ cuboids (so that even a slight growth of γ′ during ageing would lead to splitting) [4,8], γ′ could easily grow to the critical sizes for break-up without encountering impingement. In the present work continuous cooling was used (at 5℃/min), leading to continuous increase of supersaturation and nucleation of a high density of γ′ particles (see Figures 5.22(a)-(b)). Simultaneous growth of adjacent γ′ precipitates with equivalent sizes would inevitably lead to mutual impingement so that the growth sequence giving rise to break-up would be suppressed before the γ′ was big enough for splitting. This view is supported by the absence of large cuboidal γ′ during the continuous cooling. The mutually impinged γ′ would tend to contact and coalesce to form the irregular-shaped γ′.

The above discussion has focused on the situation where samples were cooled from above the transus and it has been argued that coalescence is dominant because of the high density of γ′ particles formed during cooling to temperatures between 1160℃ and 1110℃ before water quenching as shown in figure 5.22. In contrast, the results shown in figure 5.20, obtained from powder which was HIPped without being taken above the γ′ solvus, show behaviour that indicates that under these conditions the behaviour may involve growth and splitting – as discussed below. Thus figure 5.20(a), which was taken from a sample HIPped at 1107℃ without being heated above the transus, shows an array of large γ′ particles; the small particles are clearly formed during post-HIP cooling since there are denuded zones around the large particles and it is the formation of these large particles which is significant. In order to clarify the situation additional experiments have been carried out by heating samples to 1107℃, holding them for only 1h before water quenching and a typical observation is shown in Figure 5.30. The aim of this experiment was to be able to see the early stages of growth of γ′ under conditions of low supersaturation and thus to compare with the behaviour when supersaturation was higher (as in figure 5.22 (d) – (g) where 1110℃ was used). It is clear that well-spaced irregular γ′ is formed at 1107℃ when powder is heated directly to that temperature, rather than cooled from above the transus. On that basis, in agreement with earlier suggestions [2, 5, 7] it is considered that the formation of irregular γ′ can occur by coalescence or by growth and splitting in the same alloy under different ageing conditions. In fact the situation is further clarified by comparing data obtained at a HIP temperature of 1180℃ (i.e. above the γ′ transus) when the γ′ particles in figure 5.20(d) could only have formed during cooling from the HIP temperature. Comparison of the γ′ formed in the HIPped sample with that formed when cooling from 1180℃ at 5℃/min (i.e. at the same rate as in the HIP) to the lowest temperature used in the present work of 1050℃ and then water quenching

(see figure 5.22(l)) shows that the γ′ is very similar in these two cases. This suggests that coalescence dominates when samples are cooled directly from above the γ′ transus, but this becomes clear only when interrupted cooling is used.

In summary, (i) impingement to form irregular γ′ will occur under conditions where high densities of γ′ are nucleated and (ii) break-up of large precipitates will occur where fewer nuclei are formed and these nuclei are able to grow independently.

5.3.4 The Formation Mechanism of Fan-type γ-γ′ Structure

The current experimental observations demonstrate the formation of fan-type γ-γ′ structure during slow cooling from either high temperatures (around the γ′ solvus) during HIPping or from supersolvus temperatures for solution treatment, see Figures 5.21 and 5.23. This is consistent with the previous work which indicated that fan-type γ-γ′ structure could be developed through slow cooling from supersolvus temperatures [9-12]. It is generally believed that the formation of fan-type γ-γ′ structure is due to discontinuous precipitation [11]. The growth of γ′ rods and the γ matrix between them could push the grain boundaries forward to develop a fan-type structure and cause indentations and serrations to the grain boundaries. Given that this type of structure could be developed during slow cooling from supersolvus solution treatment without pressure (e.g. deformation and thus recrystallisation could be considered not to happen), the formation of fan-type structure could be considered to occur because of local grain growth and discontinuous precipitation during slow cooling. The driving force may be the trend to reduce the total grain boundary energy and thus the total free energy in the system.

As for the formation of fan-type structures during HIPping, the plastic deformation of powder particles and thus recrystallisation involved in HIPping were suspected to have an influence on their formation. However, extensive plastic deformation of powder particles and

thus recrystallisation should have been completed before or during the HIPping holding process at high temperatures around the γ′ solvus where γ′ precipitates are believed not to nucleate. In this case, the formation of fan-type structure during HIPping may be still due to subsequent grain growth and discontinuous precipitation during slow cooling from super-solvus or near-solvus HIPping temperatures. In the early cooling stage where temperature and pressure were still high, creep may happen and may affect the grain boundary migration and discontinuous precipitation.

5.3.5 The Formation Mechanism of Serrated Grain Boundaries

The current experimental results indicated that the formation of grain boundary serrations was highly associated with the presence of large and blocky γ′ precipitates at grain boundaries. These precipitates due to their big size (＞1μm) and ellipsoidal or irregular morphology are usually considered to be incoherent with the matrix of the contacted grains. As Randle et al [13] suggested, for the case of incoherent particle dispersion, the particle/matrix interfacial energy is generally of the same order as the grain boundary energy. This means that the driving force for the movement of primary γ′, that is, as Koul et al suggested [14-15], the strain energy difference between the matrix side and the boundary side of γ′ particle-matrix interface, would be insignificant and thus very difficult to make the migration of primary γ′ in the direction of grain boundaries happen. On the other hand, it can be seen from the current experimental results that the magnitude of grain boundary serration was usually bigger than primary γ′ size (see Figure 5.24 (c)-(f)), suggesting that the protuberance caused by formation and coarsening of γ′ should not be the primary reason for the formation of serrated grain boundaries although this could promote grain boundary serrations to some extent. Instead, however, the pinning effect due to coarse precipitates on grain boundaries, known as Zener drag [13, 16-17], e.g. some points of grain bourdary are pinned by precipitates while the rest continues to grow, may account for the formation of

serrated grain boundaries. It is noted that the formation of large primary γ′ was accompanied by the decrease of fine γ′ precipitates along the parts of grain boundary near the primary γ′ (see Figure 5.24 (c)-(f)), which obviously increased the mobility of the grain boundary segments near or in between the coarse primary γ′ precipitates. The migration of these free parts of grain boundaries around or in between coarse primary γ′ precipitates may finally lead to the formation of grain boundary serrations. This is consistent with many models about the interactions of grain boundaries with precipitates during grain growth [16-18].

5.4 Conclusions

The can materials used for HIPping were found to have a significant influence on diffusion layers between as-HIPped RR 1000 alloy and can materials. With increased carbon content in can materials, the area of a diffusion layer rich in carbides expanded. Using ultra-low carbon steel can material or stainless steel 316L with extremely low carbon content led to significant reduction or even elimination of the carbide-rich diffusion layers.

The effect of processing condition on the microstructure of as-HIPped RR 1000 was investigated. Outgassing parameters such as temperature and outgassing duration showed no significant influence on O, N and H levels of the as- HIPped RR 1000. The PPB precipitates were identified to be mainly (Hf, Zr)O_2 in which Hf dominates but a certain number of Hf-rich carbides were also present. Pre-HIP heat treatment of powder, changing HIPping procedure or temperature was able to change the microstructure of as-HIPped samples to a greater or lesser extent. Heat treatment of powders prior to HIPping at high temperatures led to the coarsening of PPB precipitates and made the precipitates more discrete. Ramping up temperature first and then pressure during HIPping could make PPB precipitates coarsen and more discrete as well. Increasing HIPping temperature to a supersolvus not only made grain boundaries pass beyond PPB precipitates but also led to the formation of serrated grain

boundaries during the subsequent slow cooling. Increasing HIPping temperature also caused grain growth.

Slow cooling from a supersolvus led to the formation of large irregular-shaped secondary γ′, fan-type γ′-γ structure, and serrated grain boundaries. Study on microstructural evolution suggested that the formation of irregular-shaped γ′ precipitates during continuous cooling from a transus may be due to the growth, impingement and coalescence of γ′ particles when γ′ nucleated in high density. Fan-type γ′-γ structure was formed due to discontinuous precipitation and grain growth. Serrated grain boundaries were mainly associated with large blocky γ′ at grain boundaries.

Increasing cooling rate from HIPping temperature led to the formation of much finer cuboidal or spherical γ′.

References

[1] Pearson WB. A handbook of lattice spacings and structures of metals and alloys. Oxford : Pergamon, 1967

[2] Mao J, Chang KM, Yang W, Ray K, Vaze SP, Furrer DU. Cooling precipitation and strengthening study in powder metallurgy superalloy U720LI. Metallurgical and Materials Transactions A 2001; 32:2441–2452.

[3] Mao J, Chang KM, Yang W, Furrer DU, Ray K, Vaze SP. Cooling precipitation and strengthening study in powder metallurgy superalloy Rene88DT. Materials Science and Engineering A 2002; 332:318-329.

[4] Mitchell RJ. Development of a new powder processed Ni-base superalloy for rotor disc application, PhD thesis, Cambridge, 2004.

[5] Ricks RA, Porter AJ and Ecob RC. The growth of γ′ precipitates in nickel-base superalloys. Acta metallurgica 1983; 31:43-53.

[6] Doi M, Miyazaki T, Wakatsuki T. The effect of elastic interaction energy on the morphology of γ′ Precipitates in Nickel-based Alloys. Materials Science and Engineering A 1984; 67: 247-253

[7] Doherty RD. Role of interfaces in kinetics of internal shape changes. Metal Science 1982; 16: 1-16.

[8] Mitchell RJ, Preuss M, Tin S, Hardy MC. The influence of cooling rate from temperatures above the γ′ solvus on morphology, mismatch and hardness in advanced polycrystalline nickel-base superalloys. Materials Science and Engineering A 2008; 473: 158-165.

[9] Henry MF, Yoo YS, Yoon DY, Choi J. The dendritic growth of γ' precipitates and grain boundary serration in a model nickel-base superalloy. Metallurgical Transaction A 1993; 24: 1733-1743.

[10] Danflou HL, Macia M, Sanders TH, Khan T. Mechanisms of formation of serrated grain boundaries in nickel base superalloys. In: Kissinger RD, Deye DJ, Anton DL, Nathal MV, Pollock TM, Woodford DA editors. Superalloys 1996. Warrendale, Pennsylvania, USA: The Minerals, Metals and Materials Society; 1996:p. 119-127.

[11] Furrer DU, Fecht HJ. γ′ formation in superalloy U720Li. Scripta Materialia 1999; 40:1215-1220

[12] Mitchell RJ, Li HY, Huang ZW. On the formation of serrated grain boundaries and fan type structures in an advanced polycrystalline nickel-base superalloy. Journal of materials processing technology 2009; 209: 1011–1017.
[13] Randle V, Ralph B. Interactions of grain boundaries with coherent precipitates during grain growth. Acta Metallurgica 1986;34:891-898.
[14] Koul AK, Thamburaj R. Serrated grain boundary formation potential of Ni-based superalloys and its implications. Metallurgical and Materials Transactions **A** 1985; 16: 17-26.
[15] Koul AK, Gessinger GH. On the mechanism of serrated grain boundary formation in Ni-based superalloys. Acta Metallurgica 1983;31: 1061–1069.
[16] Smith CS. Grains, phases and interfaces: an interpretation of microstructure. Transactions of the Metallurgical Society of AIME 1948; 175: 15-51.
[17] Ashby MF, Harper J, Lewis J. The interaction of crystal boundaries with second-phase particles. Transactions of the Metallurgical Society of AIME 1969;245: 413-420.
[18] Nes E, Ryum N, Hundery O. On the Zener drag. Acta Metallurgica 1985; 33: 11-22

Table 5.1 Carbon content in wt.% of different can materials and the resultant depth of diffusion layer on the side of HIPped RR 1000 alloy

Can material	Mild steel	1wt.% Cr-containing Steel A4130	Ultra-low carbon steel	stainless steel 316L
C content (wt.%)	0.18	0.28-0.33	0.06	≤0.08
Depth of diffusion layer	300 μm	325 μm	40 μm	Un-observable

Table 5.2 EDX quantitative analysis on the composition of several precipitates in the diffusion layer when using mild steel can for HIPping (at.%)

Element	Particle 1	Particle 2	Particle 3	Particle 4	Average
C	49.72	49.02	48.77	48.34	48.96
Al	1.07	-	0.81	0.64	0.63
Ti	15.12	19.56	16.08	16.96	16.93
Cr	3.88	3.73	4.33	4.34	4.07
Co	4.14	3.70	4.34	4.21	4.10
Ni	12.99	8.35	12.17	11.03	11.13
Mo	1.39	1.30	1.52	1.56	1.44
Hf	1.27	1.67	1.39	1.48	1.45
Ta	10.41	12.67	10.60	11.44	11.28

Table 5.3 H, N and O level of the as-HIPped samples with different outgassing conditions

Outgassing condition*	H (ppm)	N (wt%)	O (wt%)
4h-cold outgassing	<10	0.010	0.020
4h-hot outgassing at 400℃	<10	0.006	0.015
19h-cold outgassing	<10	0.008	0.017
24h-hot outgassing at 400℃	<10	0.009	0.016
67h-cold outgassing	<10	0.010	0.020

＊cold outgassing refers to outgassing at room temperature while hot outgassing at increased temperature

Table 5.4 The compositions in at% of the precipitates in the as-HIPped RR1000 samples through EDX analysis carried out in TEM

particles	O	Hf	Zr	Ti	Ni	Cr
1	62.53	22.27	8.31	1.09	4.59	1.20
2	58.04	21.62	8.36	6.62	3.93	1.43

Table 5.5 measured and calculated d-spacings for some particular crystal planes

Crystal planes	Measured d-spacing	Calculated d-spacing
010	4.9000	5.1722
100	4.9495	5.0491
$01\bar{1}$	3.4300	3.6760
$02\bar{1}$	2.2273	2.3178

Table 5.6 measured and calculated interplanar angles ϕ

planes	(010) & (100)	$(01\bar{1})$ & (200)	$(02\bar{1})$ & (100)
Interplanar angles ϕ (measured)	90°	96°	96°
interplanar angles ϕ (calculated)	90°	96.44°	94.06°

Table 5.7 The orientations of the selected-area electron diffraction patterns shown in Figure 5.11. The tilt angle is the angle from the [011] axis as the sample was tilted about a^* axis to zones [001] and [012] or tilted about b^* axis to zone [001]. The measured angle ρ was obtained using α, β tilting readings and the expression $\cos\rho=\cos(\alpha_2-\alpha_1)\cos(\beta_2-\beta_1)$. The calculated angle was obtained by using equations shown in Appendix B.

Image label	(c)	(b)	(d)	(e)
Zone axis	[011]	[001]	$[\bar{1}11]$	[012]
Tilt angles ρ (measured)	0	44.73°	32.70°	17.47°
Tilt angles ρ (calculated)	0	44.33°	31.96°	18.30°

Table 5.8 The compositions in at% of the large inclusion particles in the as-HIPped RR1000 sample through WDX analysis in SEM

Precipitates / Elements	Part 1	Part 2	Part 3	Part 4	Part 5	Average
Zr	2.192	3.150	3.047	2.553	2.270	2.642
Hf	24.530	27.464	27.018	25.602	24.391	25.801
O	57.504	61.892	64.568	60.441	56.432	60.167
C	15.774	7.494	5.367	11.405	16.906	11.389
Totals	100	100	100	100	100	100

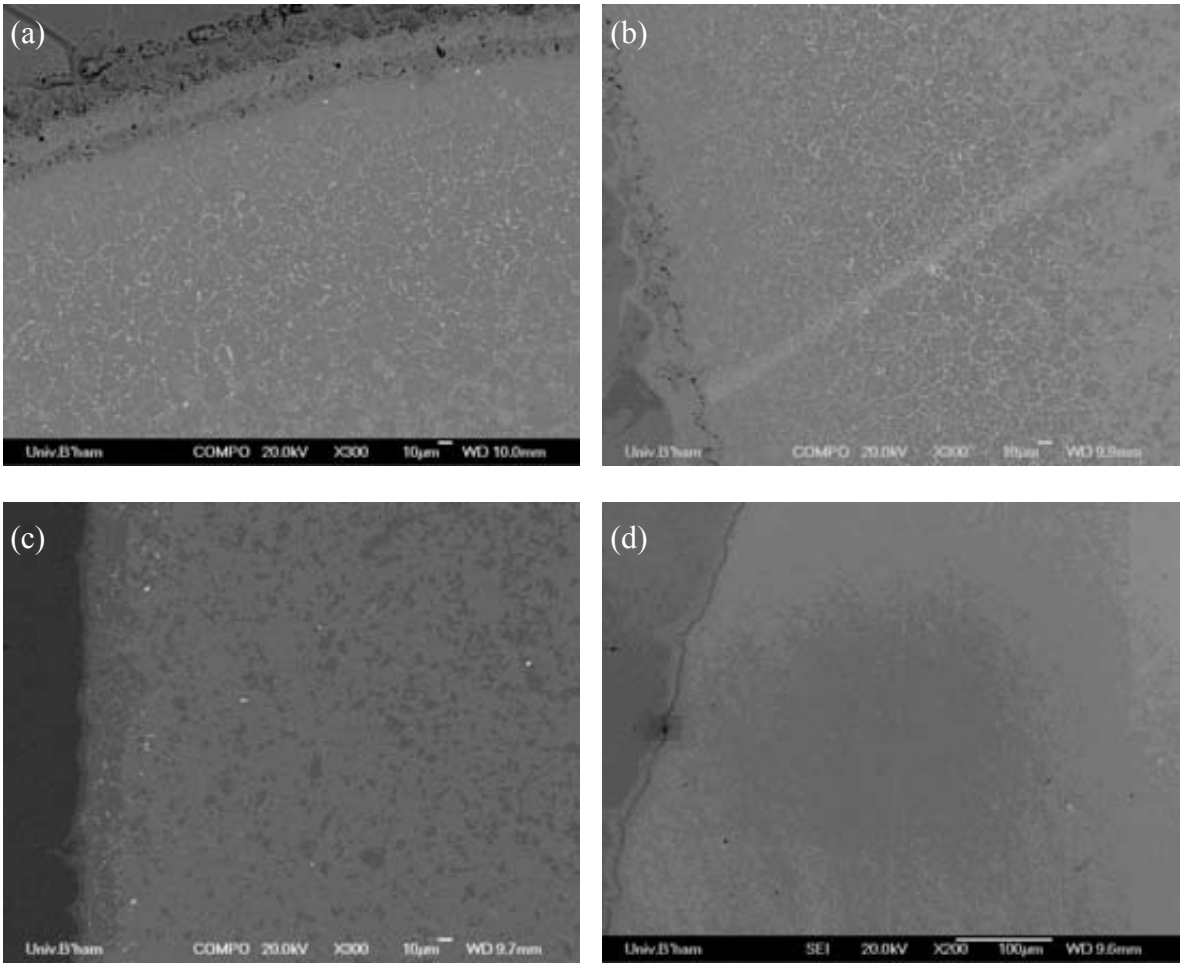

Figure 5.1 Back scattered SEM micrographs showing the microstructural change of can-powder interfaces with different can materials after HIPping at 1107℃/100MPa/4h (a) medium carbon steel; (b)1% Cr-bearing steel; (c) ultra-low carbon steel; (d) stainless steel 316L.

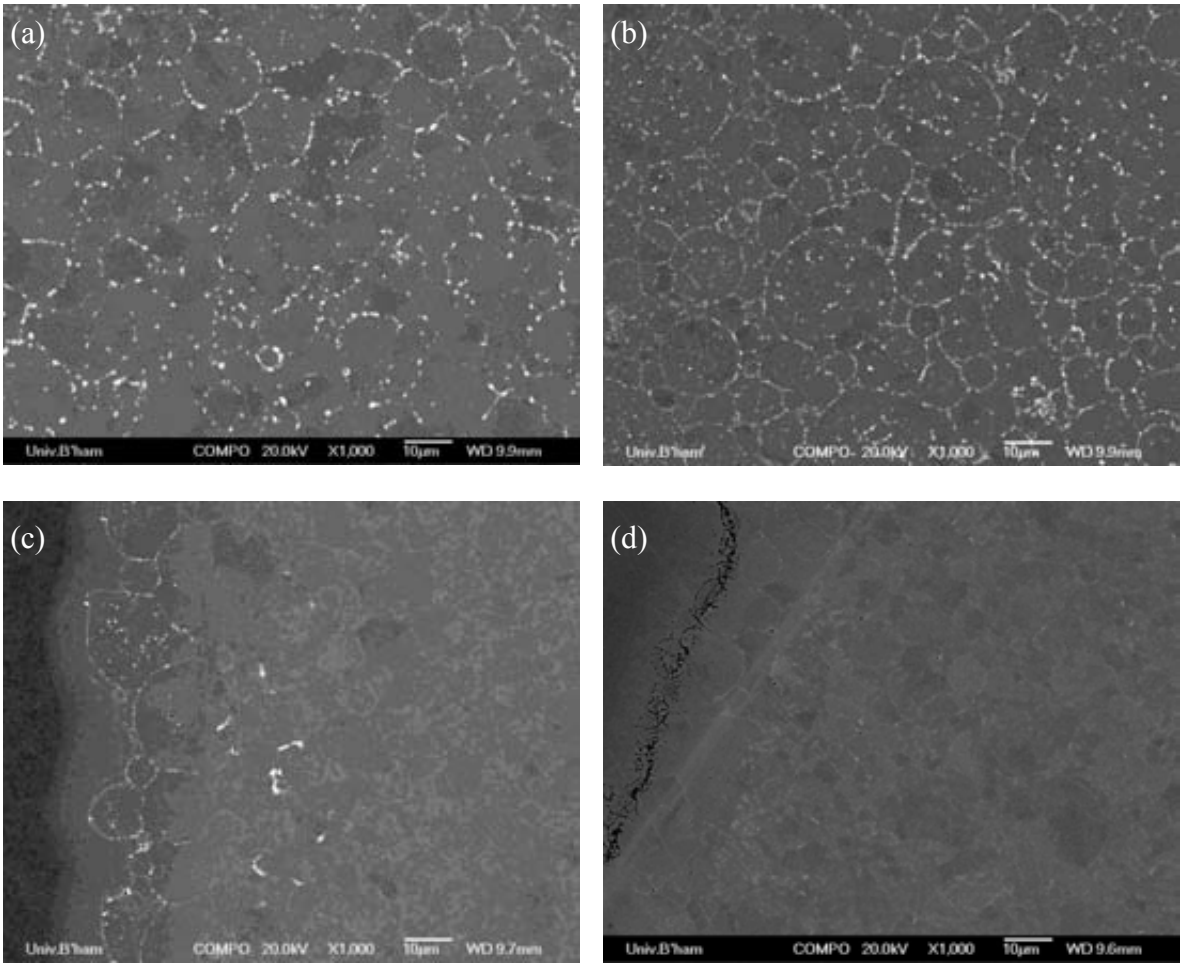

Figure 5.2 Back scattered SEM micrograph showing the can-powder interfaces with different can materials after HIPping at 1107℃/100MPa/4h (a) medium carbon steel; (b)1% Cr-bearing steel; (c) ultra-low carbon steel; (d) Stainless steel 316L, under high magnification.

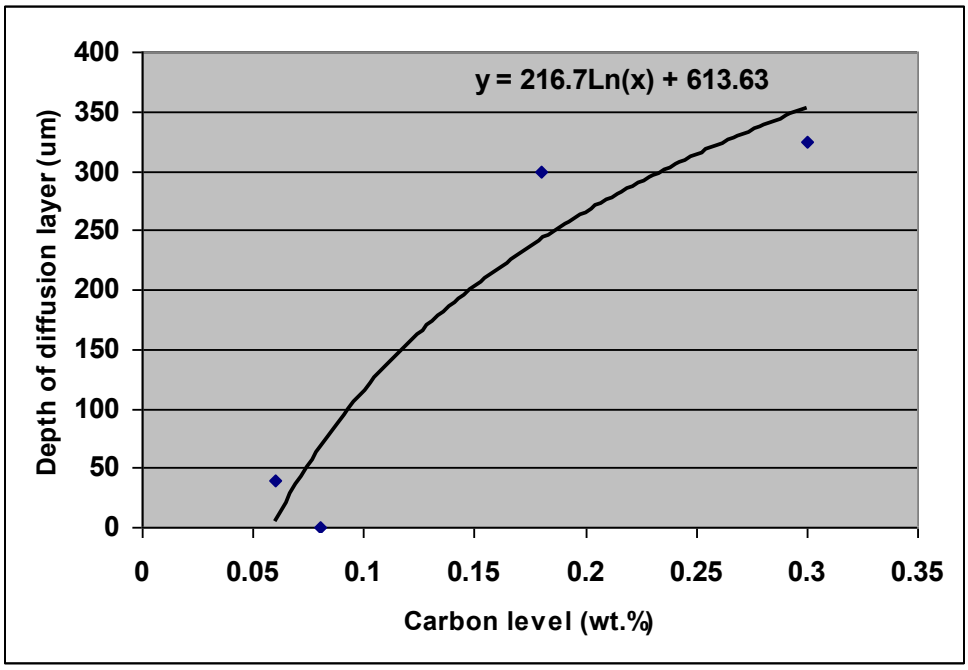

Figure 5.3 Diagram showing the dependence of the depth of diffusion zone on the carbon content of the can materials, after HIPping at 1107℃/100MPa/4h.

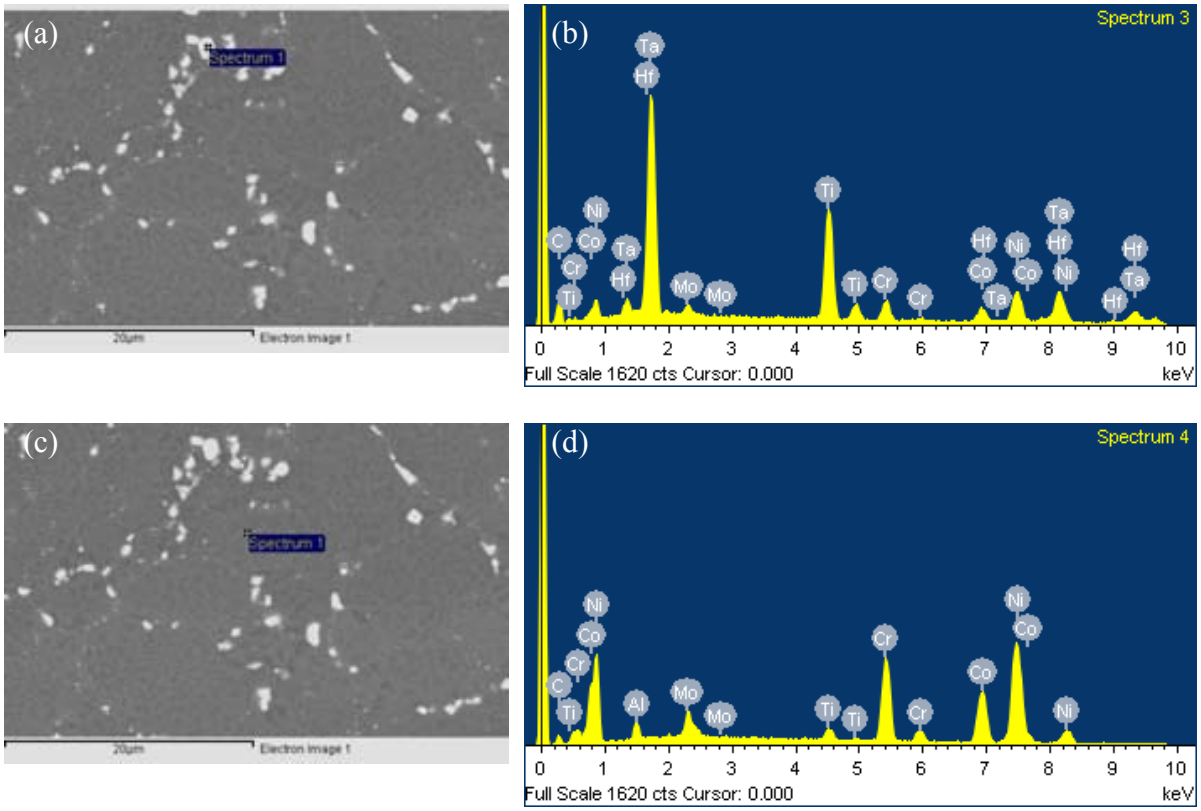

Figure 5.4 Back scattered SEM images showing (a) a precipitate in the mild steel can-powder interface after HIPping at 1107℃/100MPa/4h with EDX analysis in (b); (c) a matrix area next to the precipitate with EDX analysis on the matrix in (d).

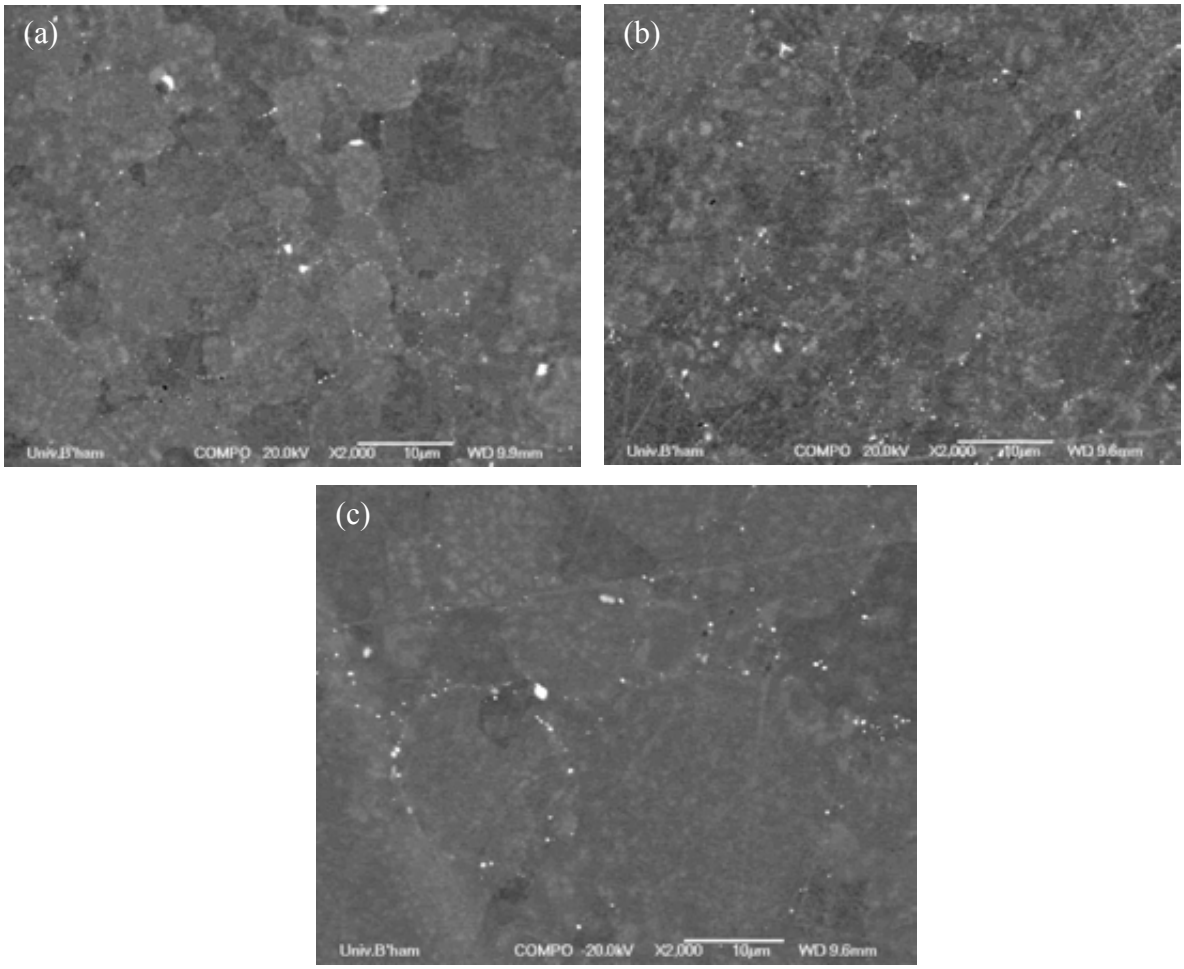

Figure 5.5 Back scattered SEM micrographs showing the PPB precipitate distribution in the RR 1000 samples after HIPping (at 1107℃/100MPa/4h) of powders which were previously heat treated in outgassed and sealed cans at (a) 960℃ for 4h; (b) 1107℃ for 4h; (c) 1200℃ for 4h, respectively.

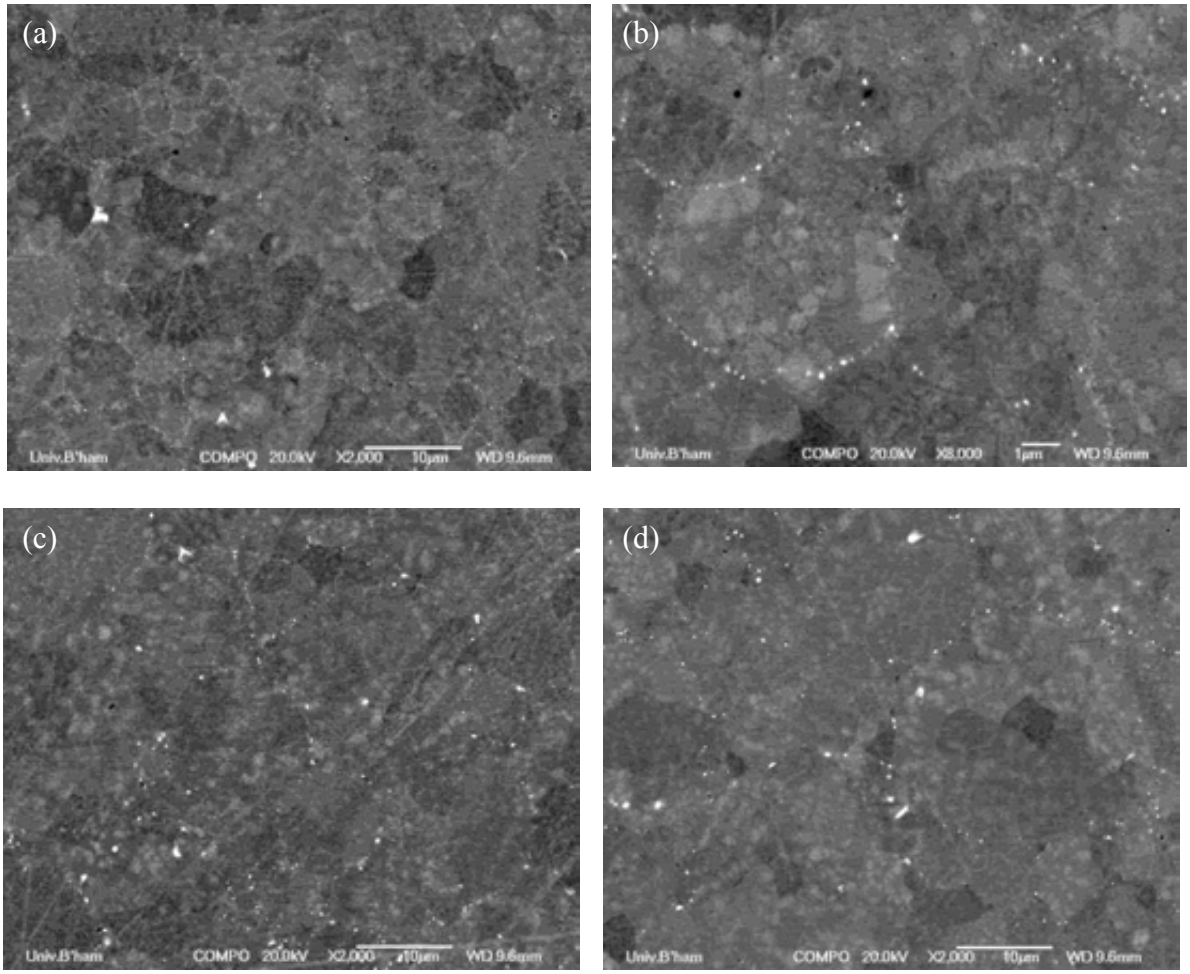

Figure 5.6 Back scattered SEM micrographs showing the PPB precipitate distribution in the RR 1000 samples after HIPping (at 1107℃/100MPa/4h) powders which were previously heat treated at 1107℃with dwell durations for (a)(b) 1 hour, the PPB precipitates in (a) were too fine to be observed in low magnification and could only be observed under higher magnification like (b); (c) 4hours; (d) 8hours.

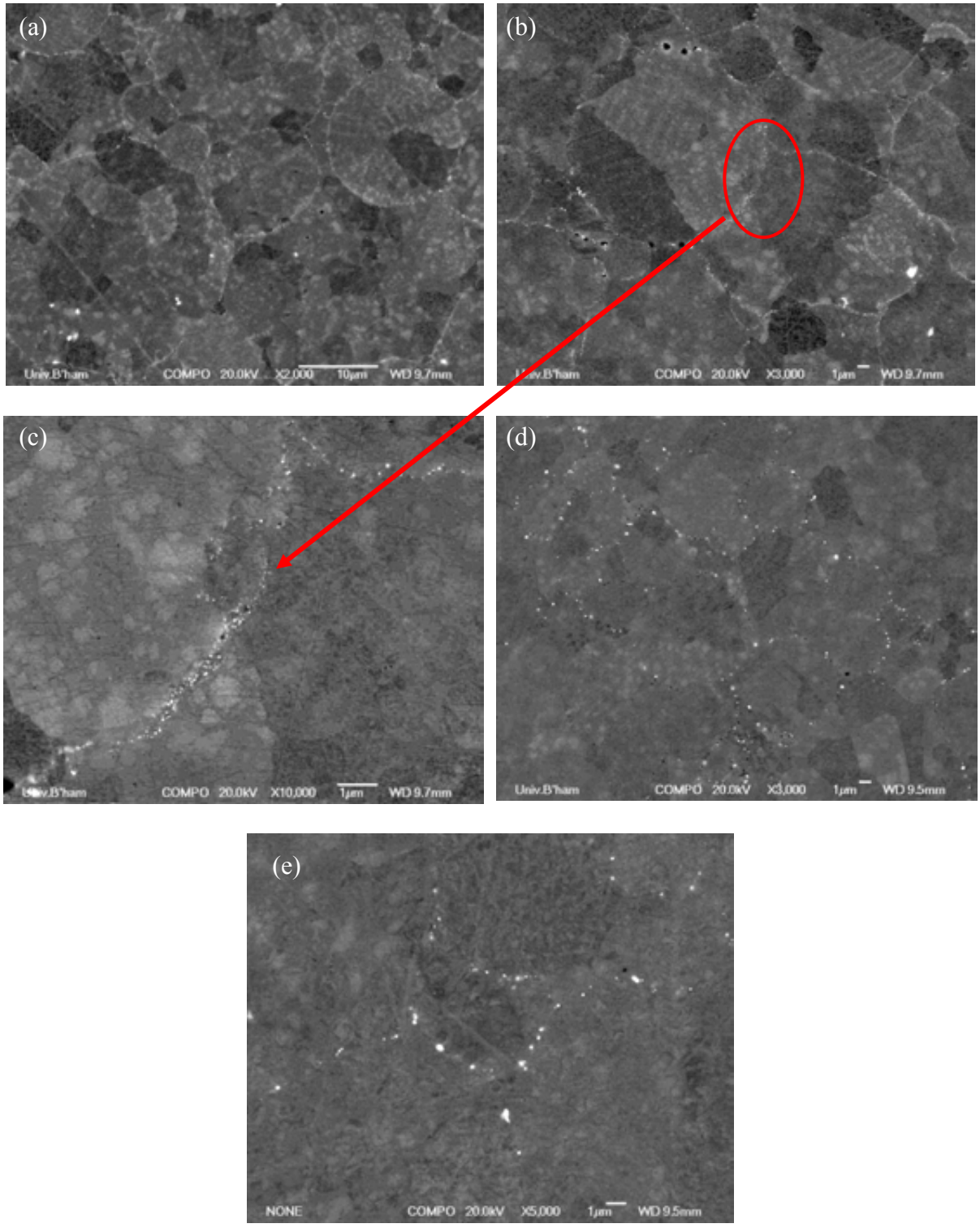

Figure 5.7 Back scattered SEM micrographs showing the PPB precipitate distribution of the as-HIPped RR 1000 samples with different HIPping procedures (a) ramping up temperature and pressure together; (b) ramping up pressure first and then temperature, the PPB precipitates in (a) and (b) were so fine that they could only be observed clearly in much higher magnification like (c); (d)(e) ramping up temperature first and then pressure

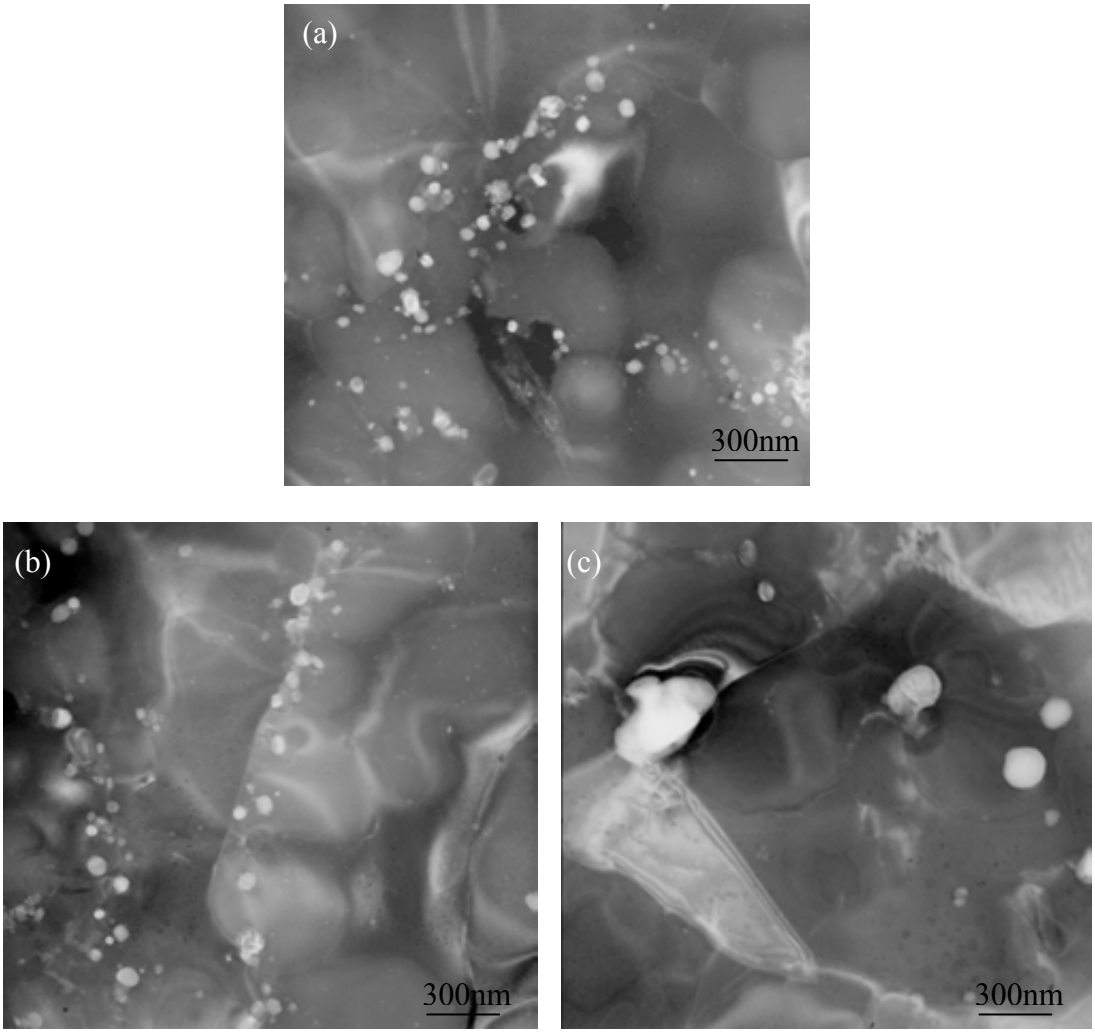

Figure 5.8 Many beam bright field TEM micrographs showing the PPB precipitate size and distribution of as-HIPped RR 1000 samples experiencing (a) ramping temperature and pressure together; (b) ramping pressure first and then temperature; (c) ramping up temperature first and then pressure, to 1107℃/100MPa/4h.

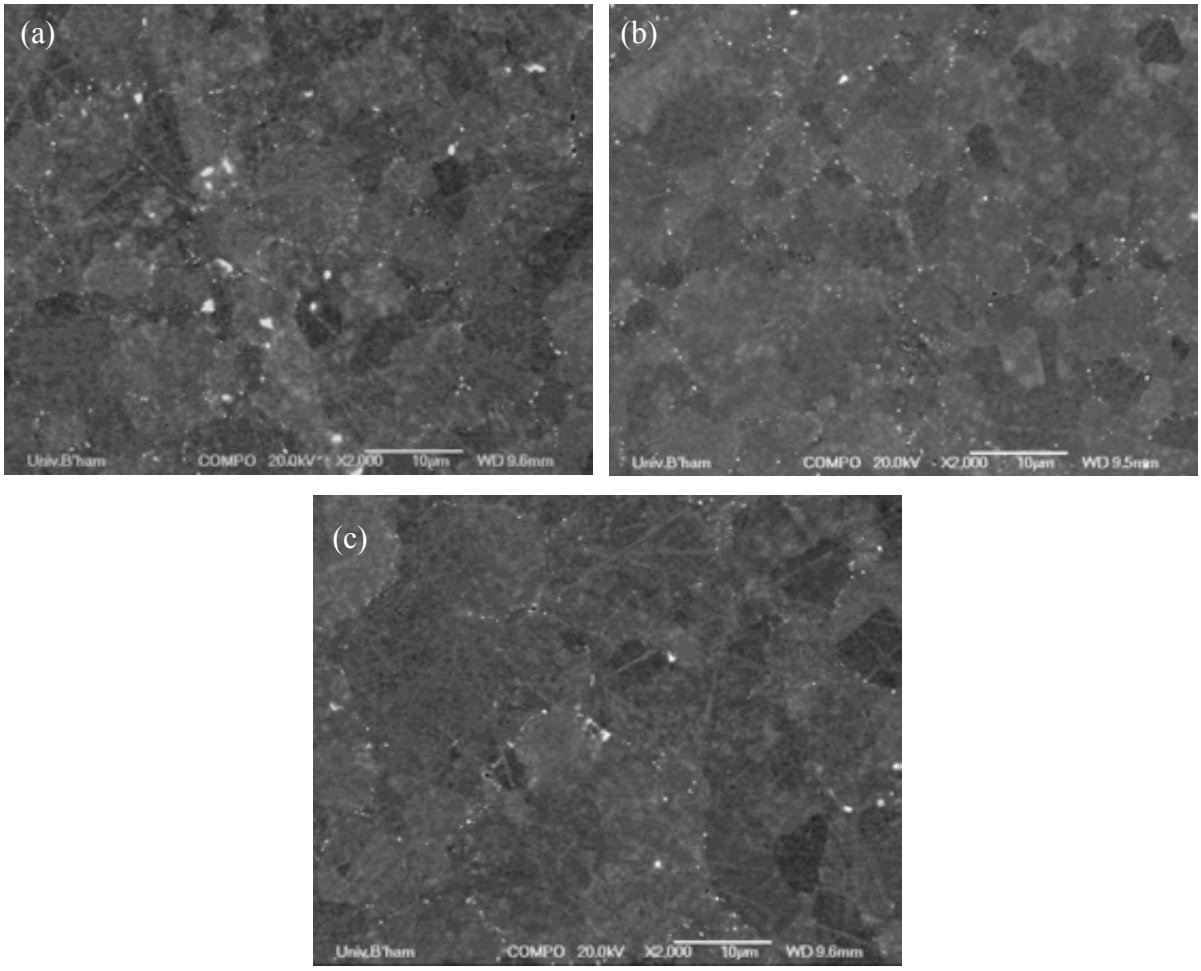

Figure 5.9 Back scattered SEM micrographs showing the PPB precipitate distribution of the as-HIPped RR 1000 samples with different temperature ramp-up rates during HIPping (a) 2.5 ℃/min; (b) 5 ℃/min; (c) 10 ℃/min, to 1107℃/100MPa/4h.

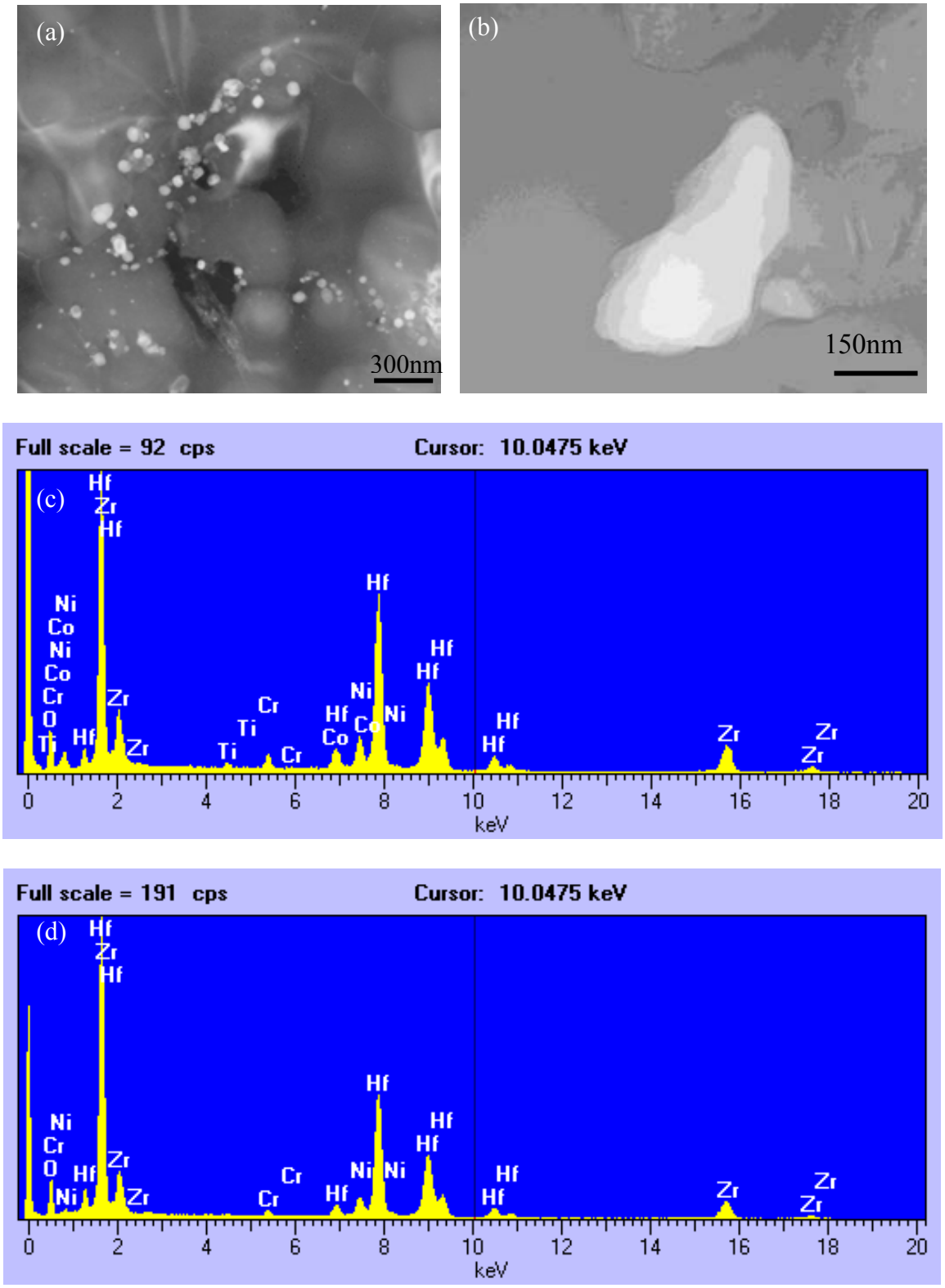

Figure 5.10 Many beam bright field TEM images and TEM-EDX spectra of the precipitates in the as-HIPped RR 1000 samples, (a)(c) ramping temperature and pressure together, to 1107℃/100MPa/4h; (b)(d) ramping up temperature first and then pressure, to 1107℃ /100MPa/2h

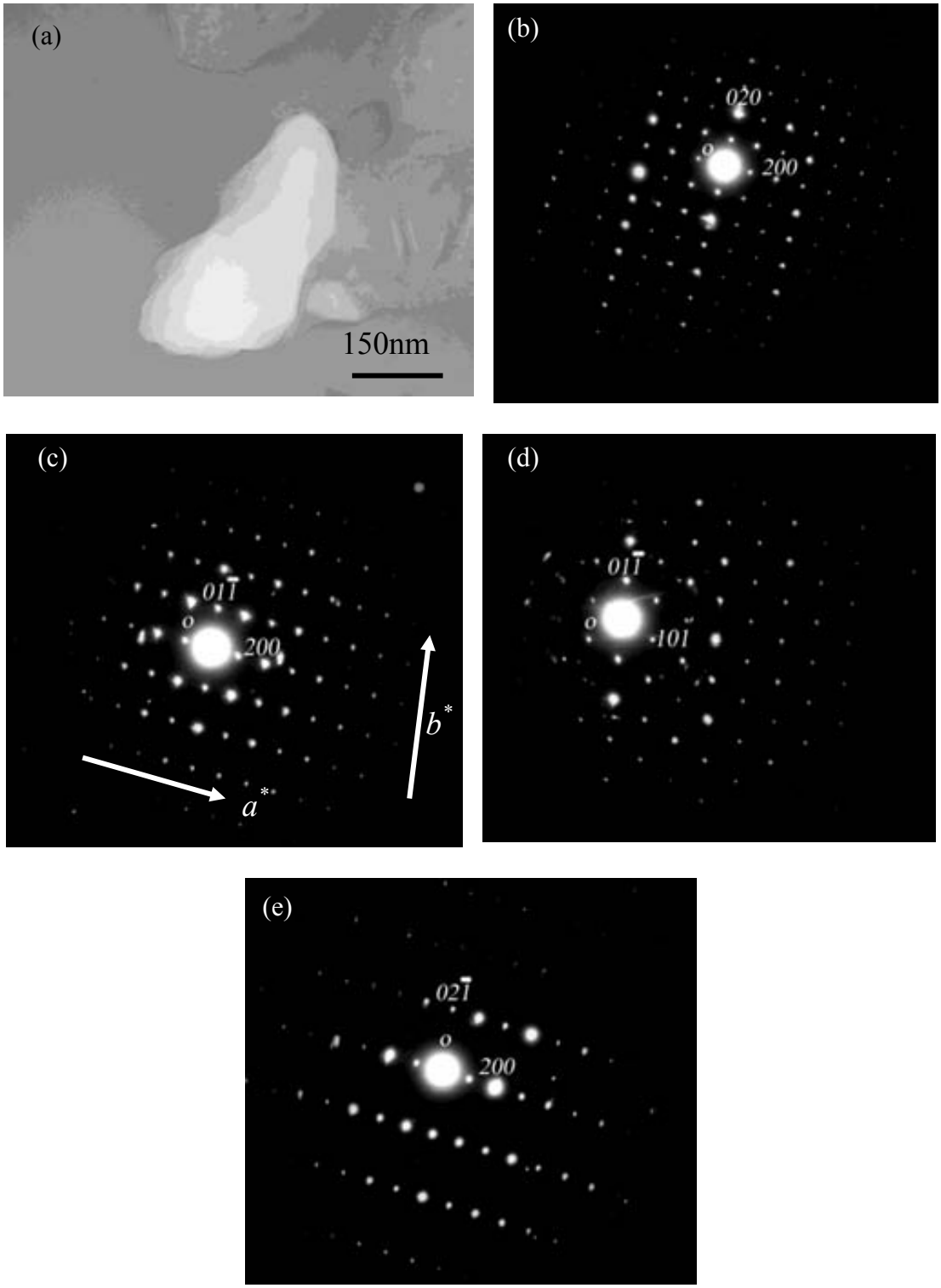

Figure 5.11 (a) many beam bright field TEM image showing the precipitate at which subsequent diffraction patterns were obtained; TEM diffraction patterns (b) and (e) obtained by tilting about a^* axis and diffraction pattern (d) by tilting about b^* axis, as indicated by the white arrows in Figure 5.11 (c). (b) zone [001]; (c) zone [011]; (d) zone $[\bar{1}11]$; (e) zone [012].

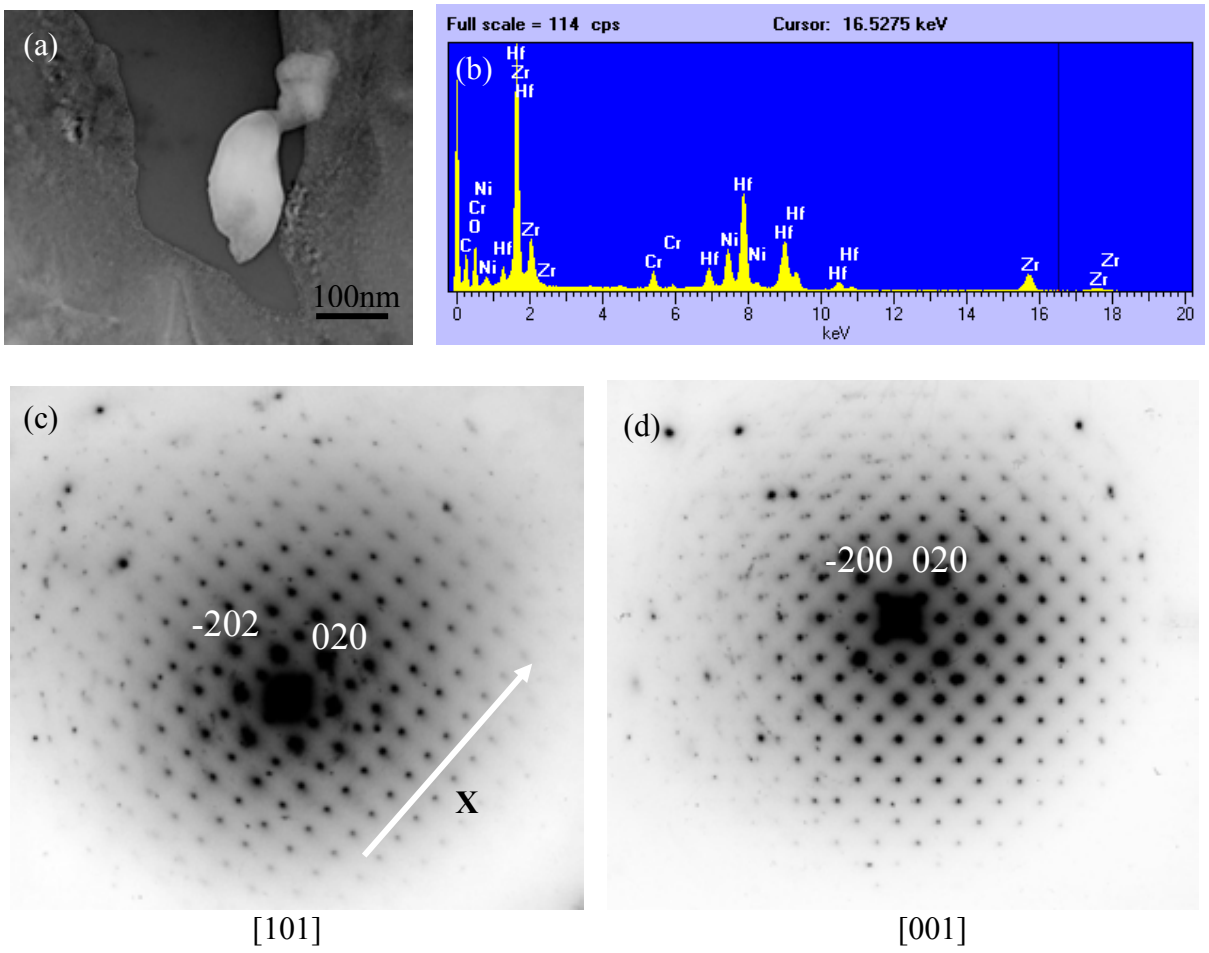

[101] [001]

Figure 5.12 (a) Bright field TEM micrograph showing the precipitate for EDX and diffraction analysis; (b) TEM-EDX spectra for the precipitate analyzed; (c)-(d) TEM diffraction patterns obtained from the precipitate in Figure 5.12 (a). Diffraction pattern in Figure 5.12 (d) was obtained by tilting the specimen around X axis in Figure 5.12 (c). (c) zone [101]; (d) zone [001].

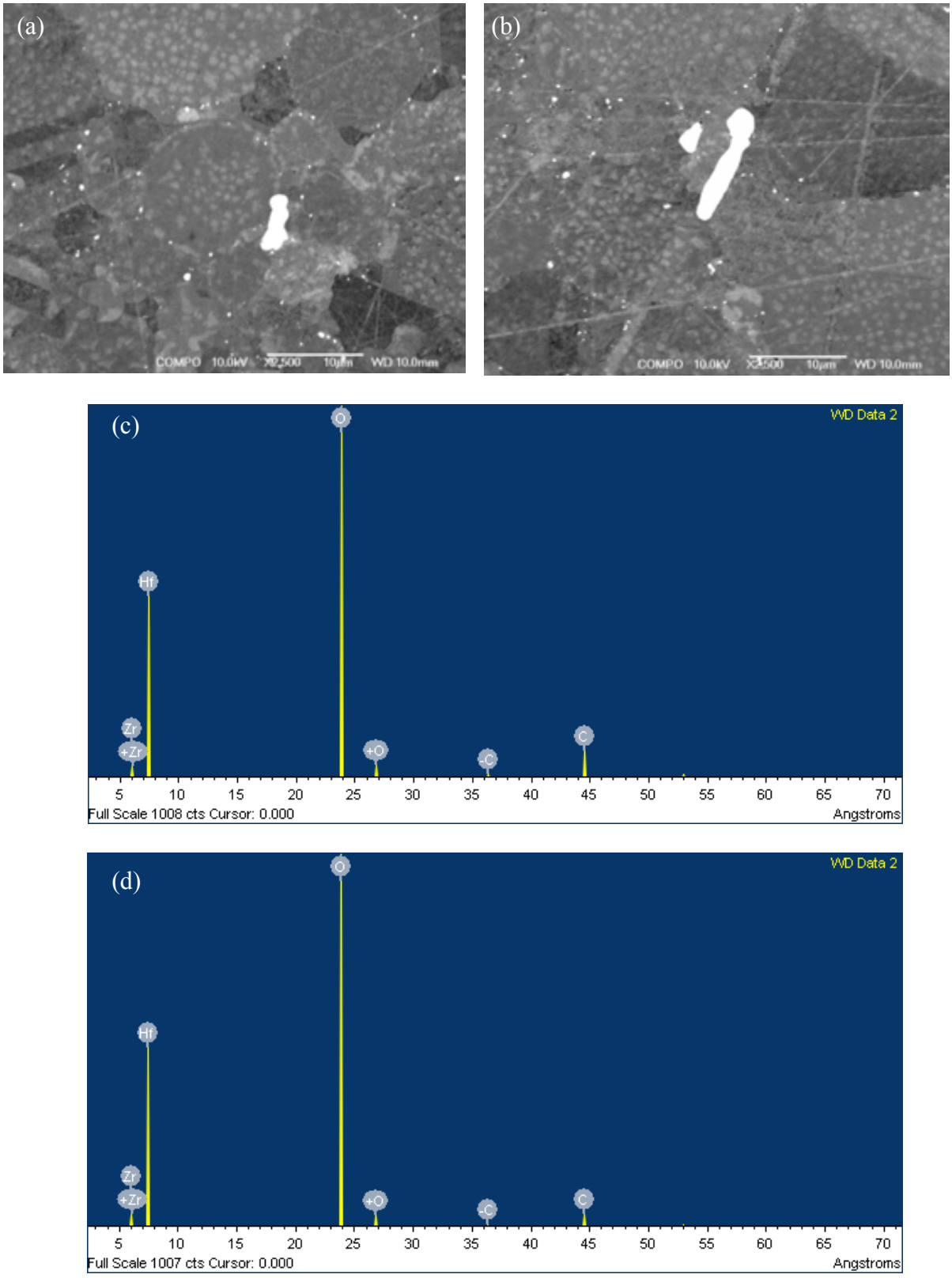

Figure 5.13 (a-b) Back scattered SEM micrographs showing the presence of large inclusion particles in as-HIPped samples and (c-d) WDX spectra showing the compositions for large inclusion particles remained in the as-HIPped RR 1000 samples

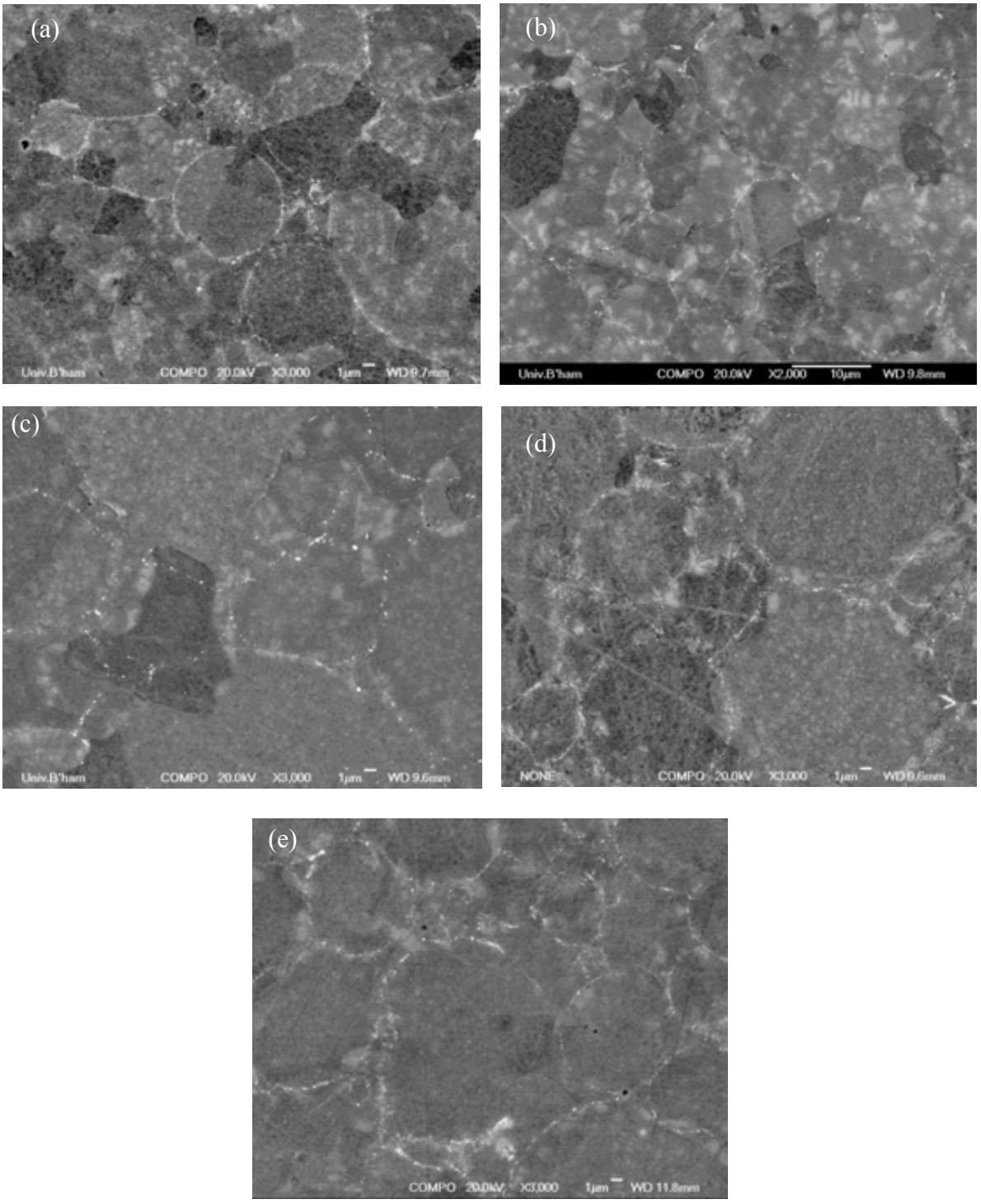

Figure 5.14 Back Scattered SEM micrographs showing the PPB precipitate distribution in the as-polished RR 1000 samples after being HIPped at (a)1107℃; (b)1130 ℃; (c)1160 ℃; (d)1180 ℃; (e)1200 ℃, respectively.

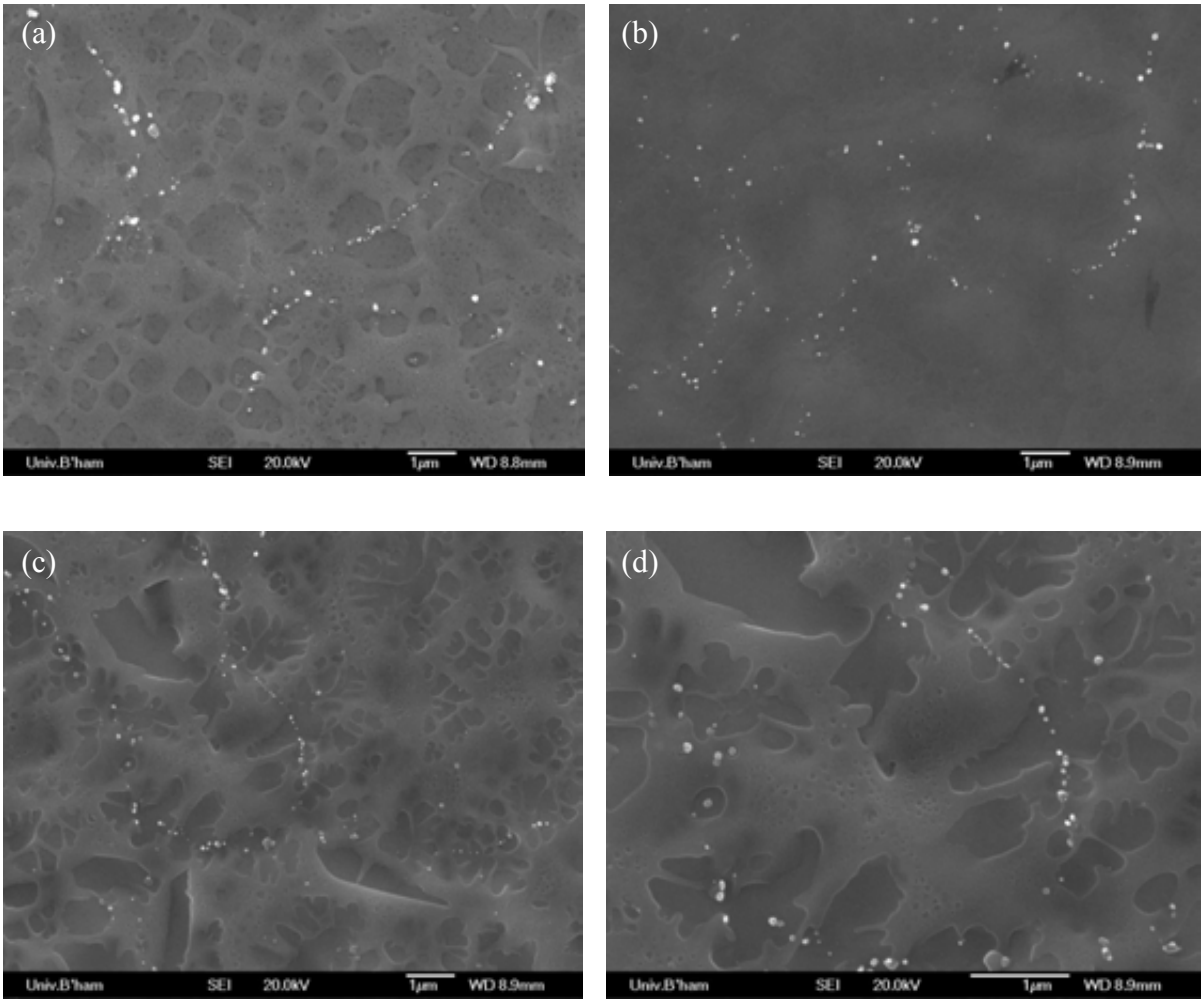

Figure 5.15 Secondary electron SEM micrographs showing the PPB precipitate distribution of RR 1000 samples after HIPping at (a)1107℃; (b)-(d)1130℃.

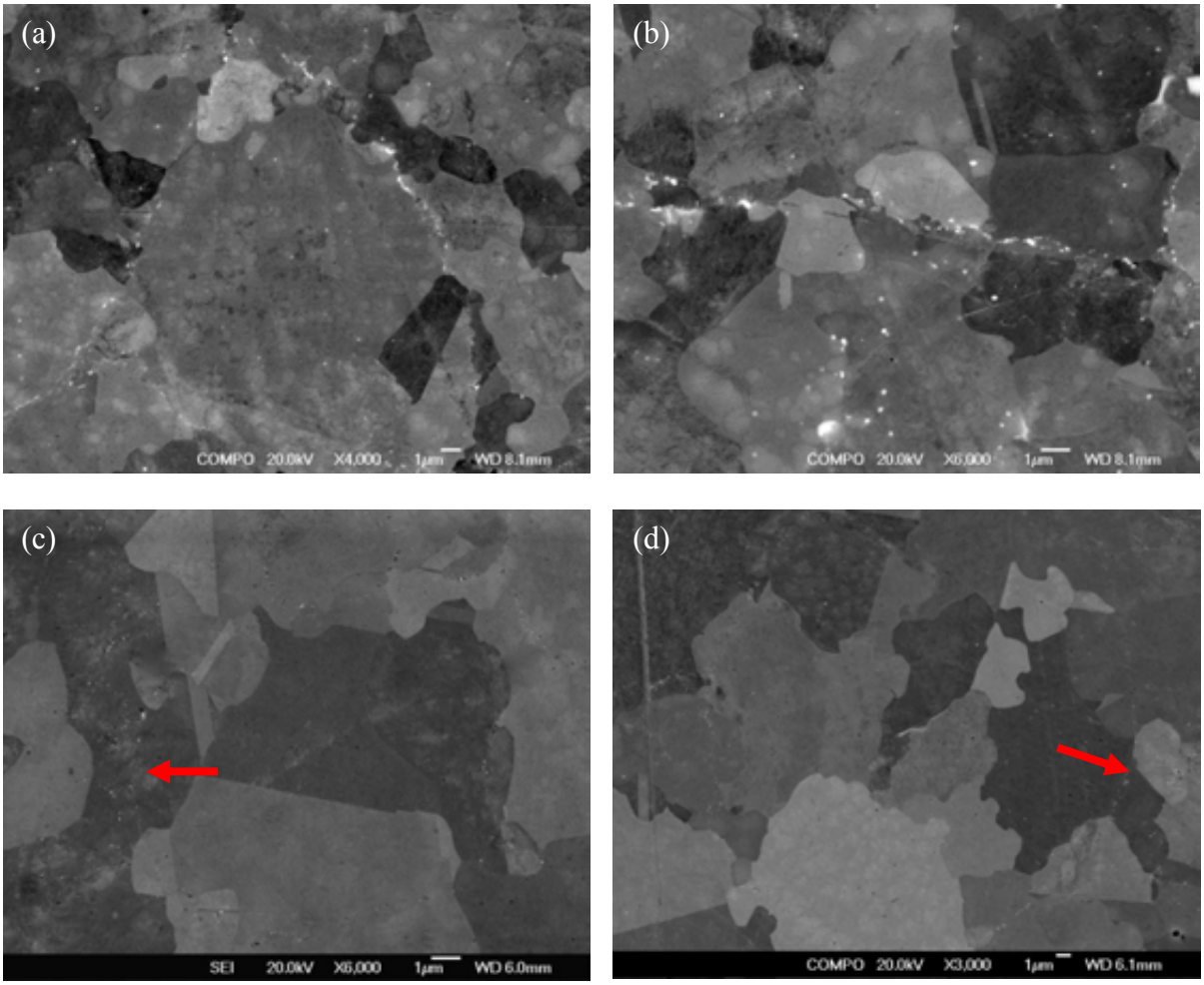

Figure 5.16 (a, b)back scattered SEM micrographs showing the PPB precipitates and grain structure of samples HIPped at 1107℃, many grains being confined within the PPBs; (c) and (d) secondary electron and back scattered SEM micrographs showing that grains grow beyond the PPBs and leave the PPB precipitates inside the grain interior when the samples were HIPped at 1180℃, see arrows.

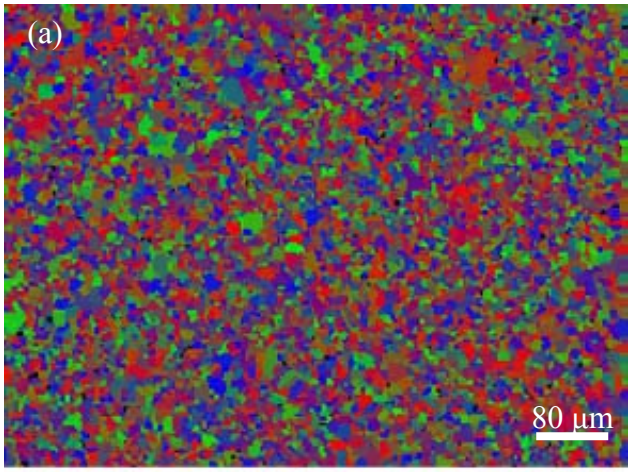
(a)
80 µm

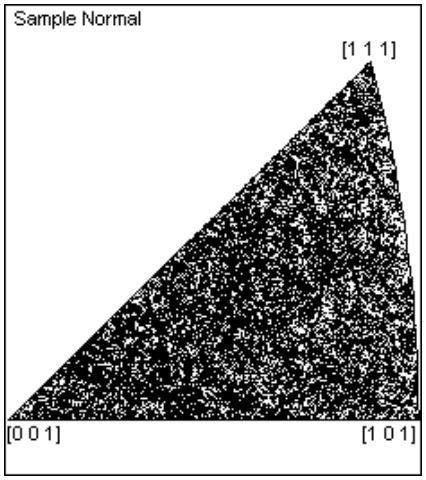
Sample Normal
[1 1 1]
[0 0 1]
[1 0 1]

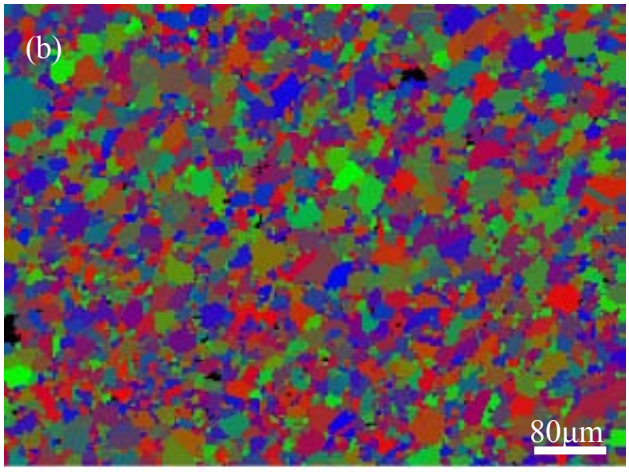
(b)
80µm

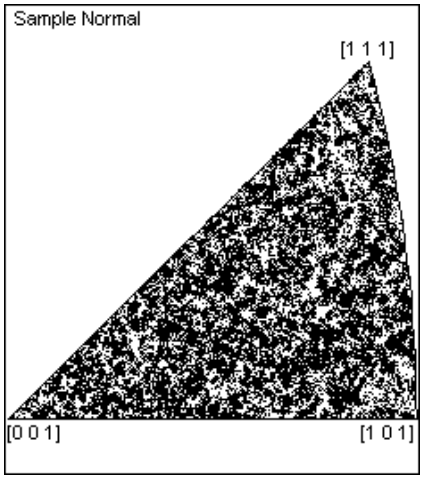
Sample Normal
[1 1 1]
[0 0 1]
[1 0 1]

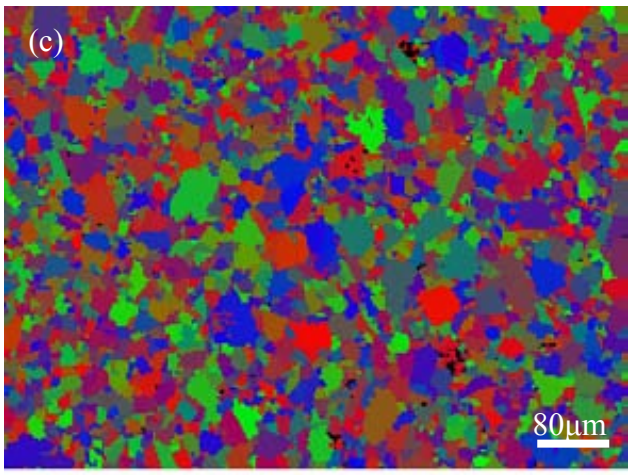
(c)
80µm

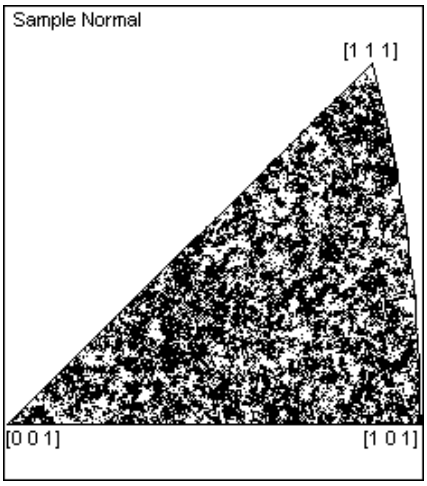
Sample Normal
[1 1 1]
[0 0 1]
[1 0 1]

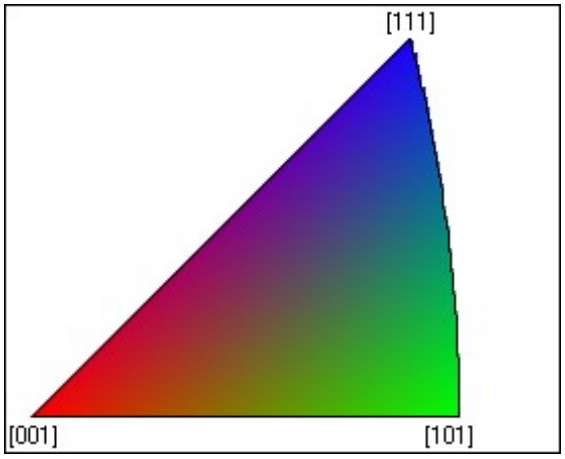

Figure 5.17 Electron back-scatter diffraction (EBSD) images showing the grain growth with increase of HIPping temperature and showing the grain orientation distribution, (a) 1107℃ /100MPa/4h; (b) 1160℃/150MPa/4h; (c) 1180℃/150MPa/4h.

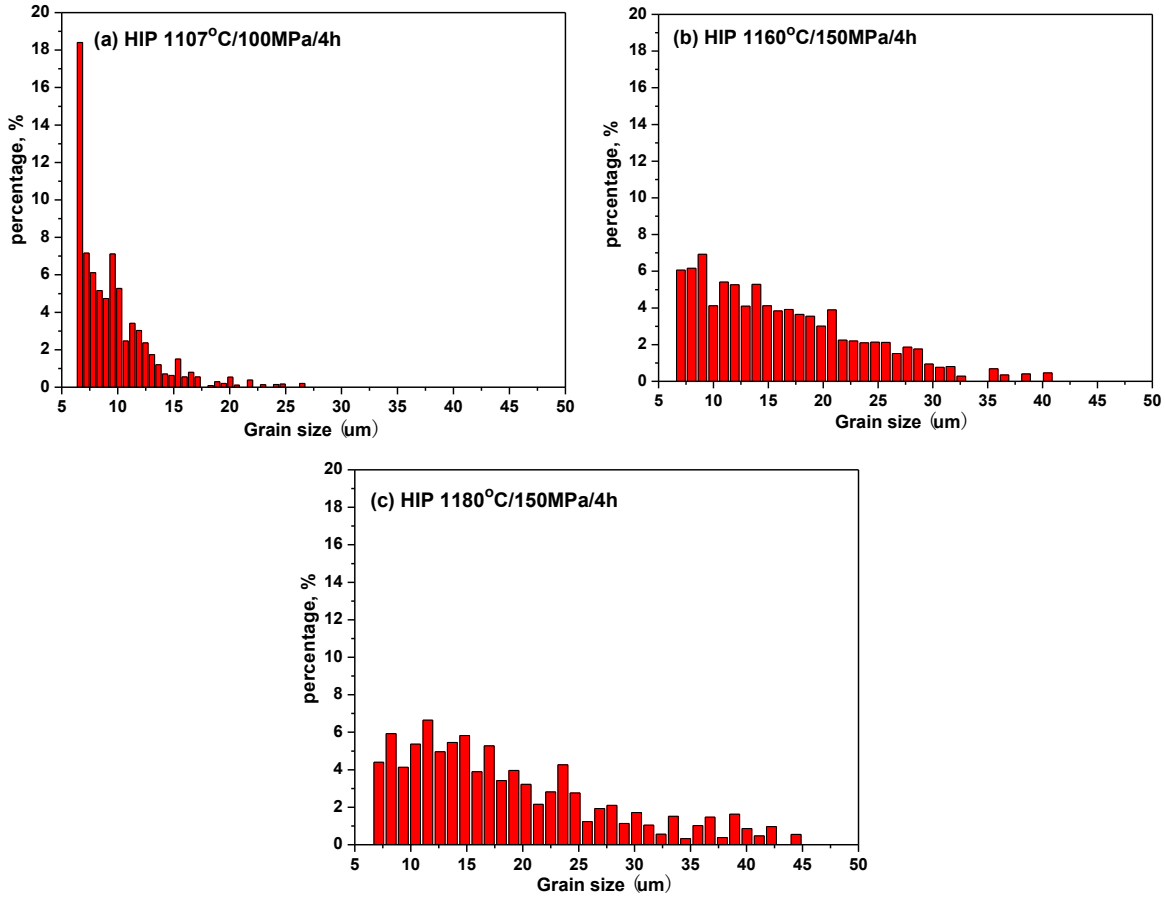

Figure 5.18 Figures showing the grain size distribution of RR 1000 samples HIPped at (a) 1107℃/100MPa/4h; (b) 1160℃/150MPa/4h; (c) 1180℃/150MPa/4h.

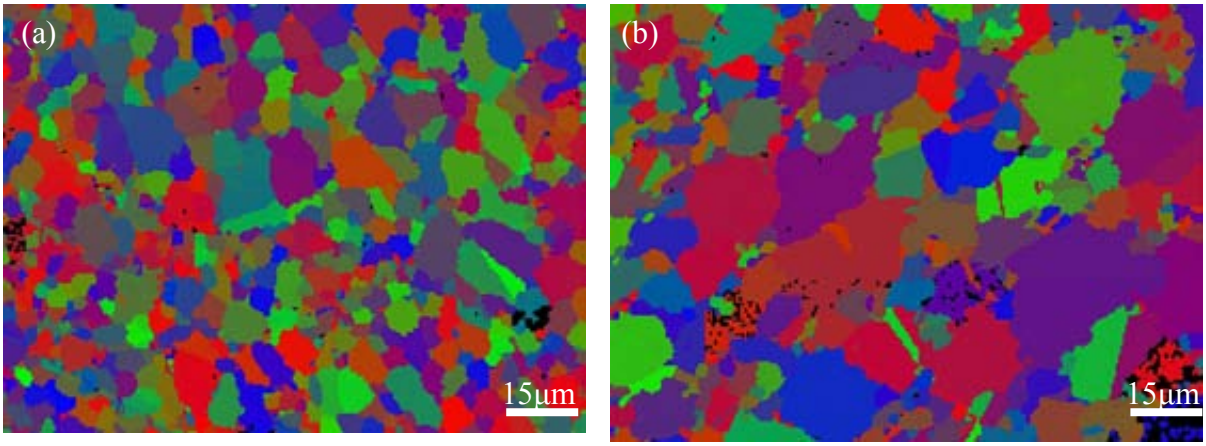

Figure 5.19 EBSD micrographs showing the grain growth and grain boundary morphological change of RR 1000 with increased HIPping temperature, (a) 1107℃/100MPa/4h; (b) 1180℃/150MPa/4h, pronounced serrated grain boundaries could be observed.

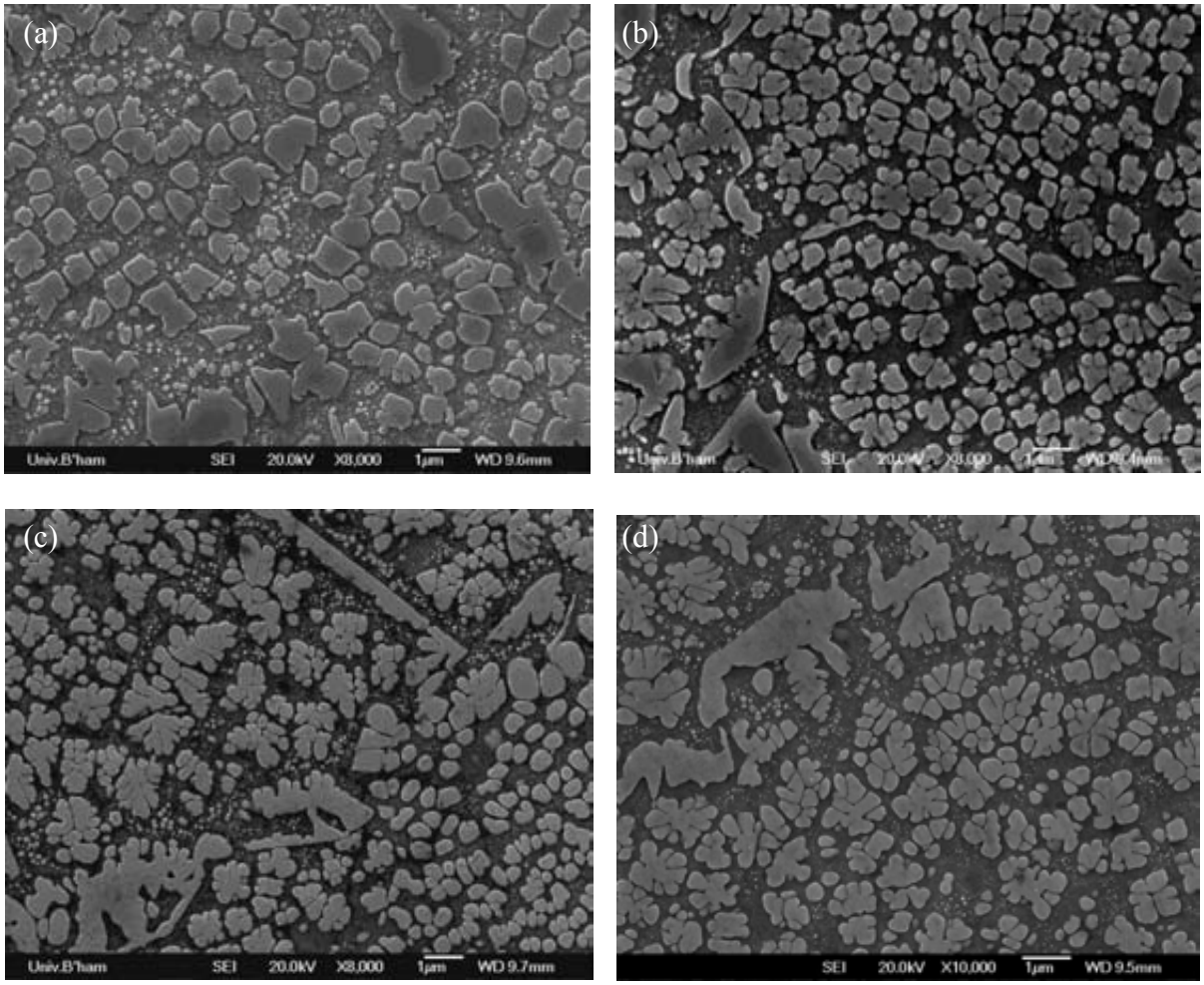

Figure 5.20 Secondary electron SEM micrographs showing the gamma prime distribution in the as-HIPped RR 1000 with different HIPping temperatures (a) 1107℃, (b) 1125 ℃, (c) 1160 ℃, (d) 1180 ℃.

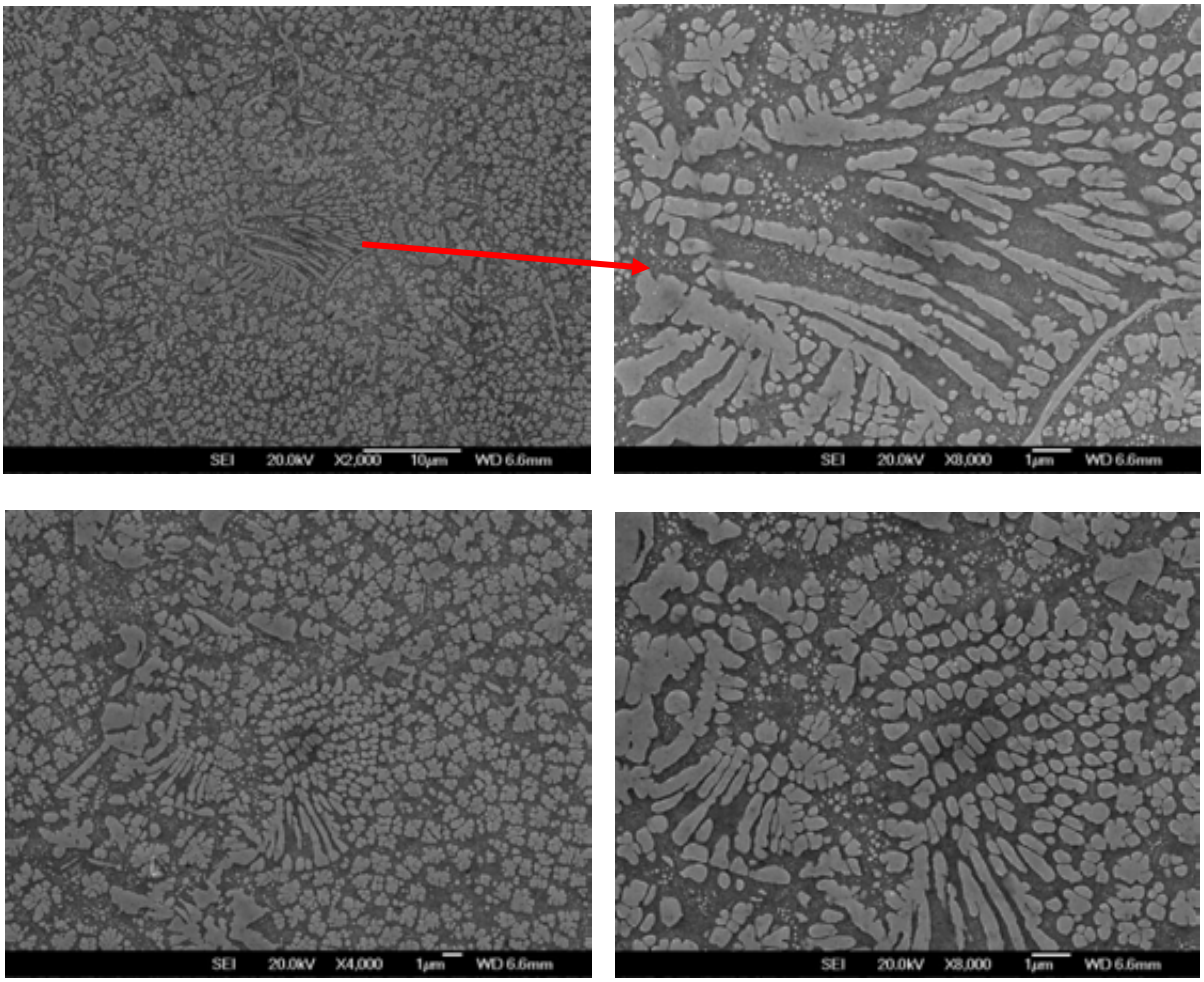

Figure 5.21 Secondary electron SEM micrographs showing the fan-type gamma prime structure in the as-HIPped RR 1000 after being HIPped at 1180℃/150MPa/4h and cooled at 5℃/min to room temperature.

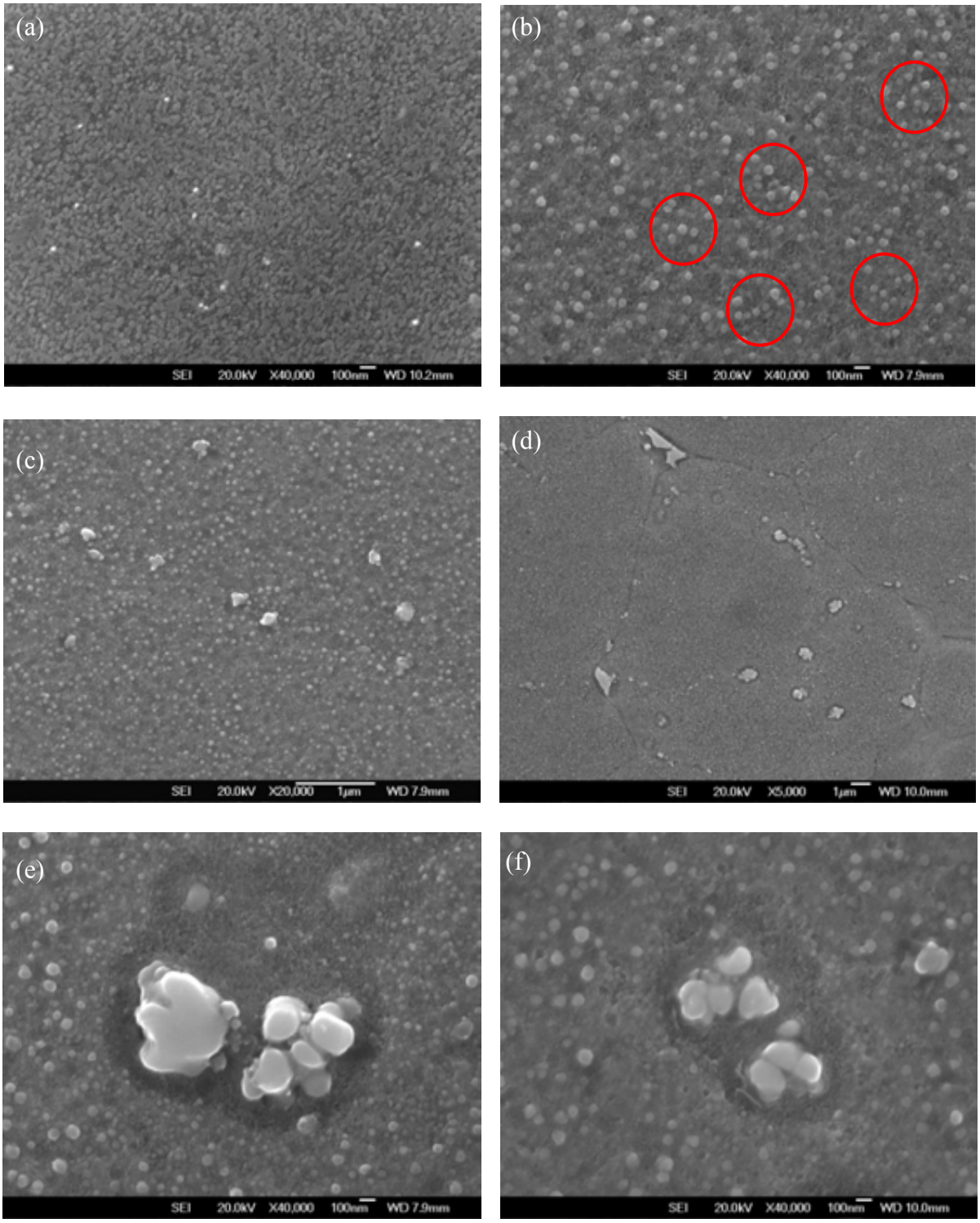
(a)
SEI 20.0kV X40,000 100nm WD 10.2mm
(b)
SEI 20.0kV X40,000 100nm WD 7.9mm
(c)
SEI 20.0kV X20,000 1μm WD 7.9mm
(d)
SEI 20.0kV X5,000 1μm WD 10.0mm
(e)
SEI 20.0kV X40,000 100nm WD 7.9mm
(f)
SEI 20.0kV X40,000 100nm WD 10.0mm

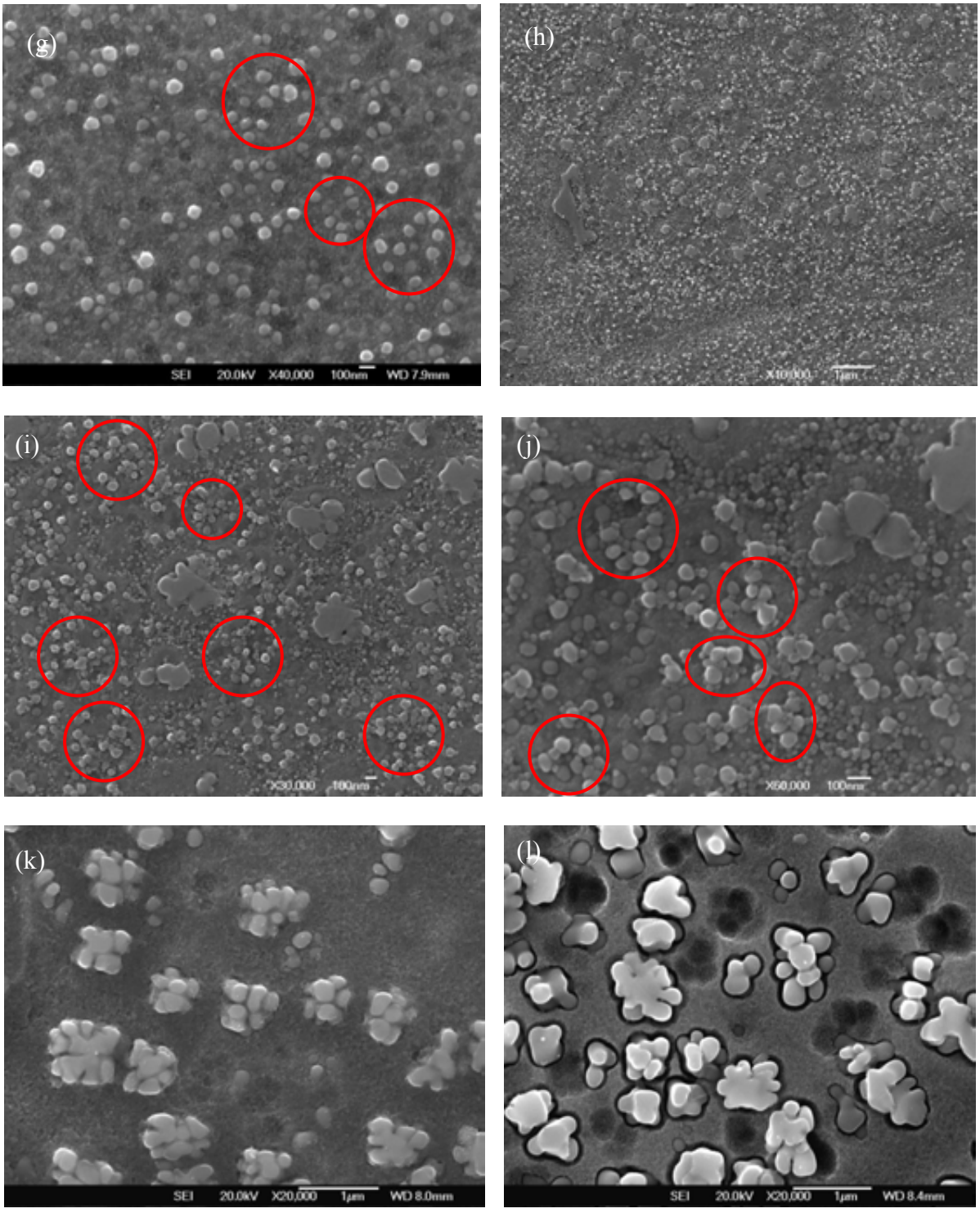

Figure 5.22 Secondary electron SEM micrographs showing the evolution of γ′ during slow cooling (at 5℃/min) from 1180℃ to (a) 1160℃; (b,c) 1130℃; (d-g) 1110℃; (h-j) 1095℃; (k) 1080℃; (l) 1050℃, followed by immediate water quench

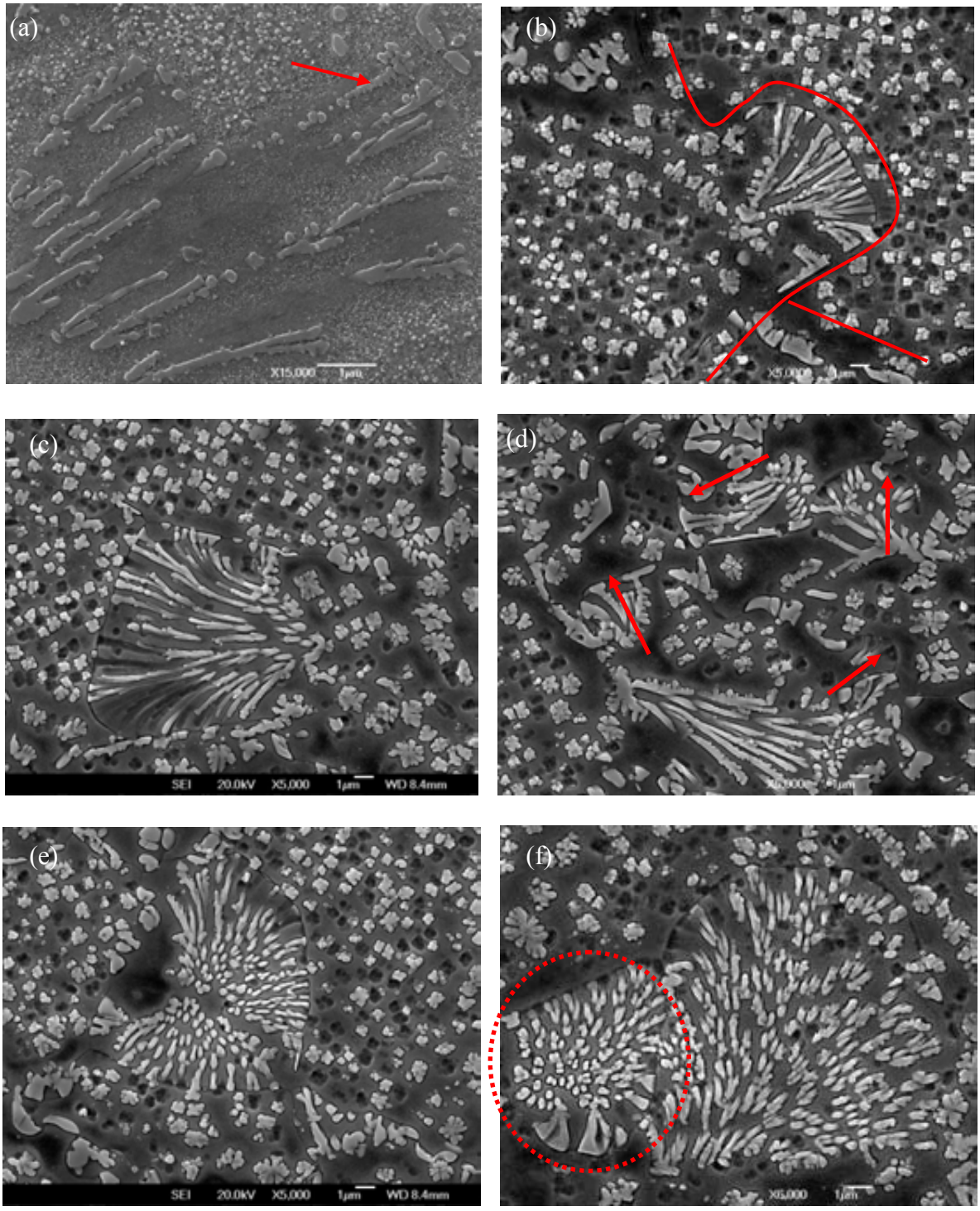

Figure 5.23 Secondary electron SEM micrographs showing the formation and evolution of fan-type γ′ structure during slow cooling from 1180℃ to the temperatures, (a)1095℃, (c)-(f)1050℃, followed by immediate water quench. The arrow in (a) shows the formation of a single γ′ rod while the rest arrows and curves show the curved or serrated grain boundaries caused by the discontinuous precipitation. The loop in (f) shows the discontinuous precipitation in a grain along all outward directions

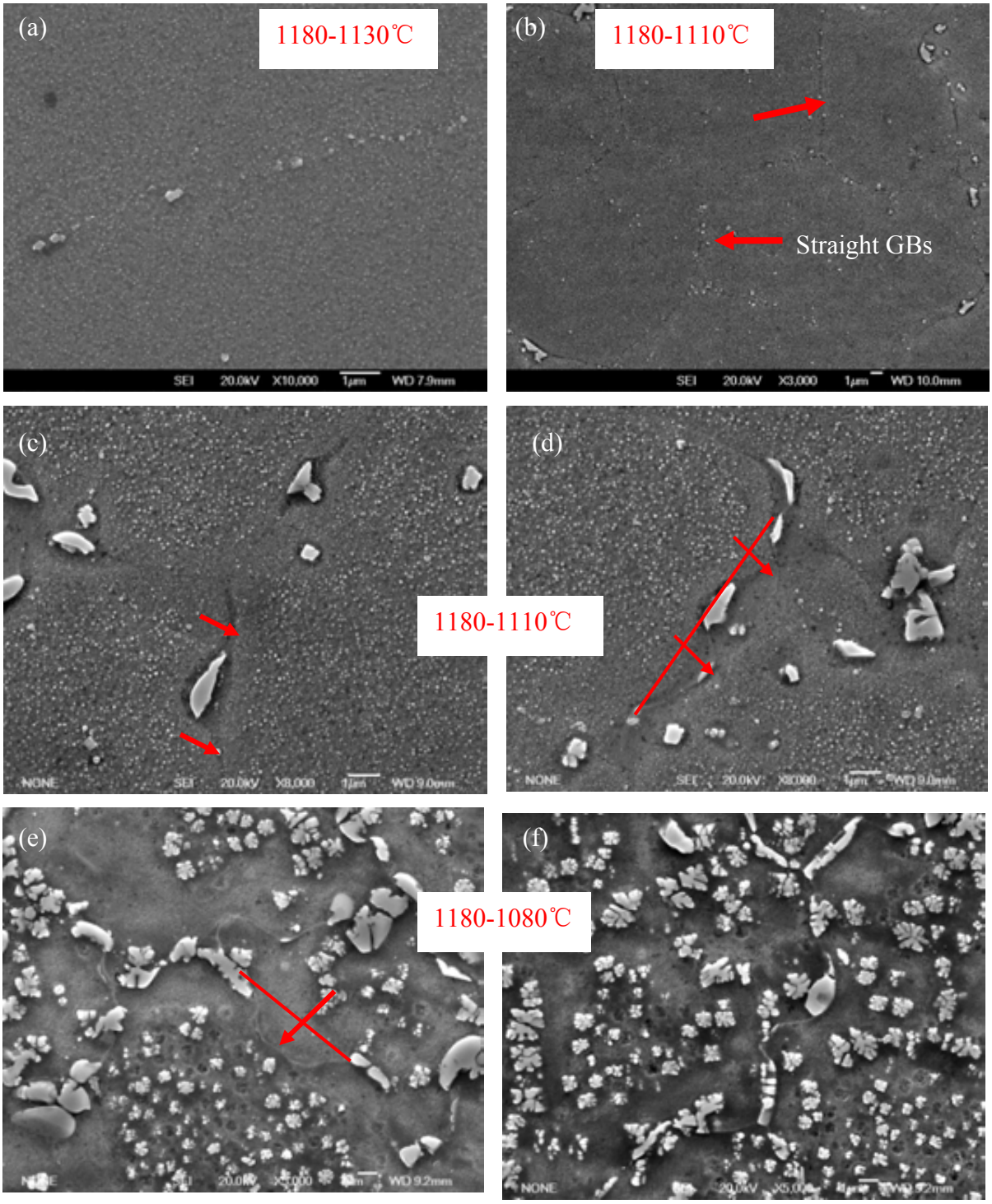
(a)
1180-1130℃
(b)
1180-1110℃
Straight GBs
(c)
(d)
1180-1110℃
(e)
1180-1080℃
(f)

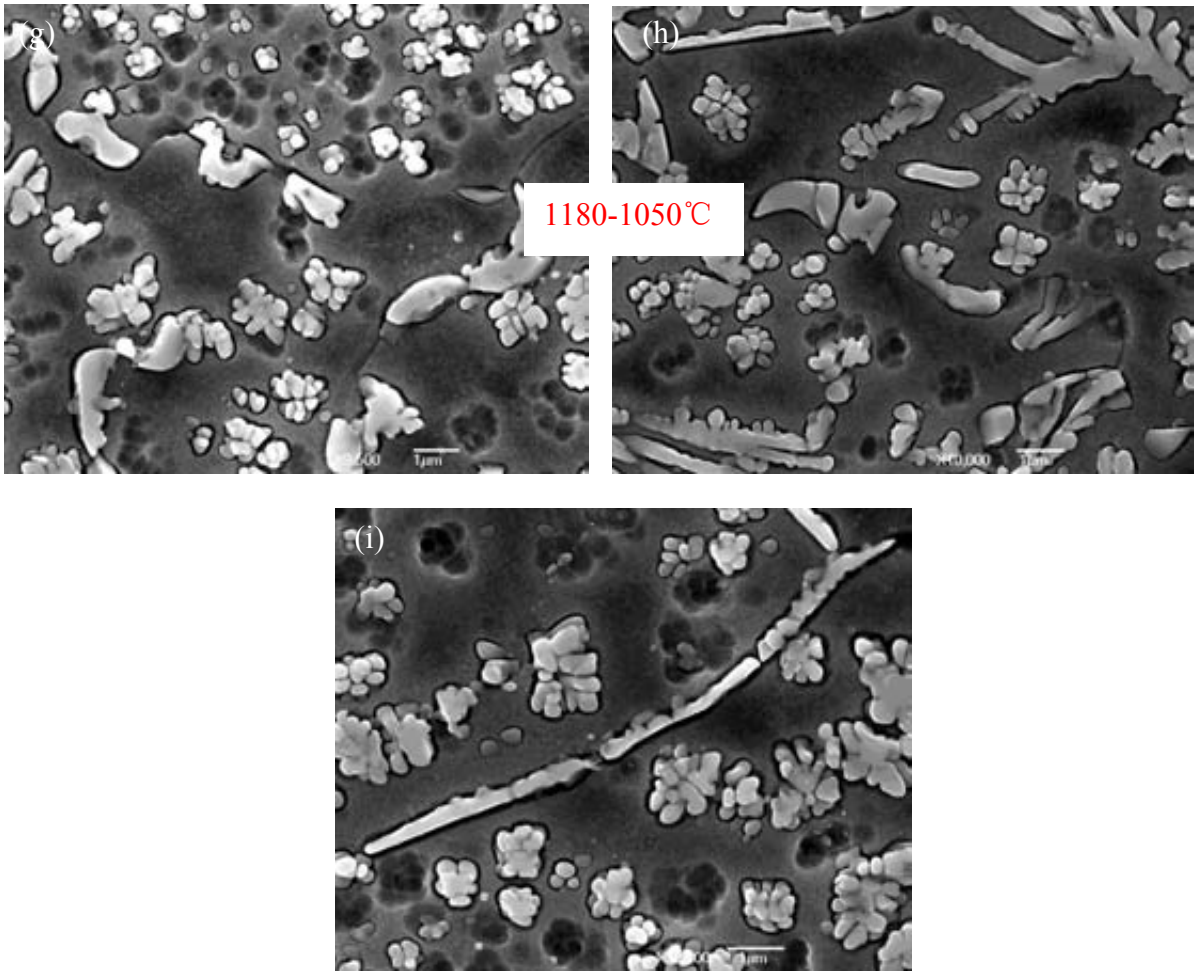

Figure 5.24 Secondary electron SEM micrographs showing the evolution of grain boundaries during slow cooling at 5℃/min from 1180℃ to temperatures, (a)1130℃; (b)-(d)1110℃;(e)-(f)1080℃; (g)-(i)1050℃, followed by immediate water quench. The arrows show the potential grain boundary migration direction.

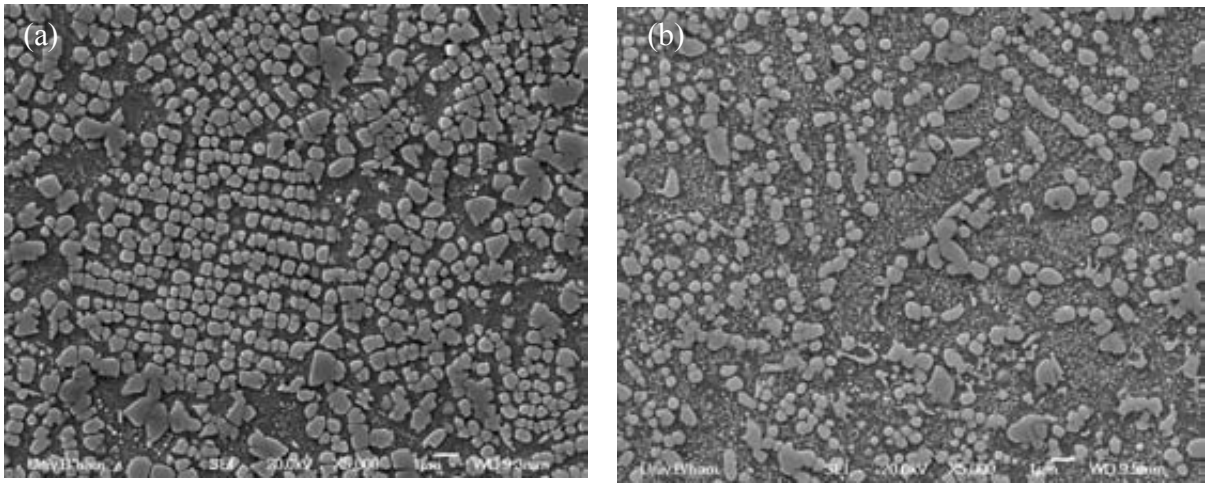

Figure 5.25 Secondary electron SEM micrographs showing the gamma prime distribution of the samples HIPped at 1107 ℃/100MPa/4h followed by cooling at (a)5℃/min; (b)132℃/min.

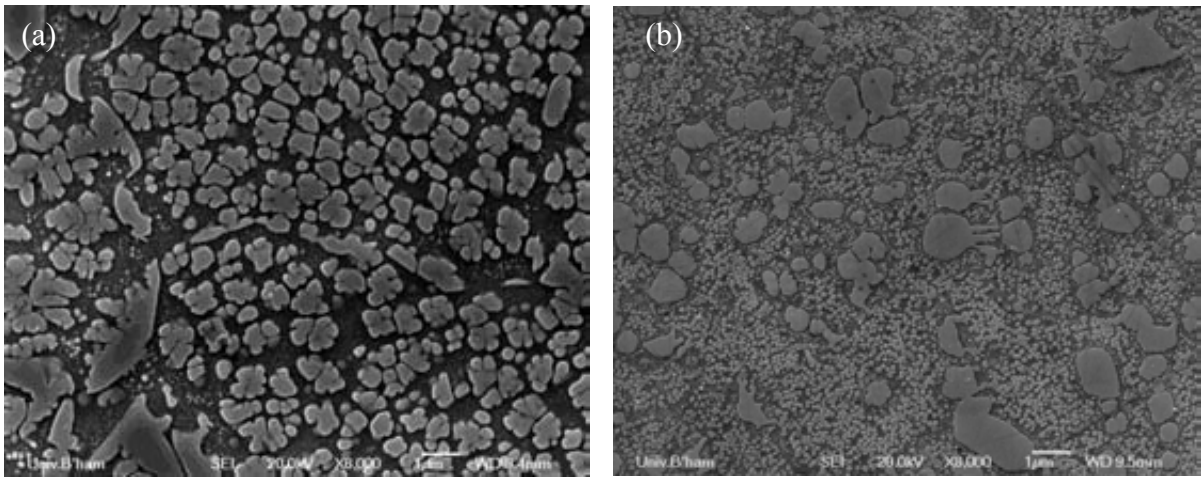

Figure 5.26 high magnification secondary electron SEM micrographs showing the gamma prime distribution of the samples HIPped at 1125 ℃/100MPa/4h followed by cooling at (a)5℃/min; (b) 132℃/min.

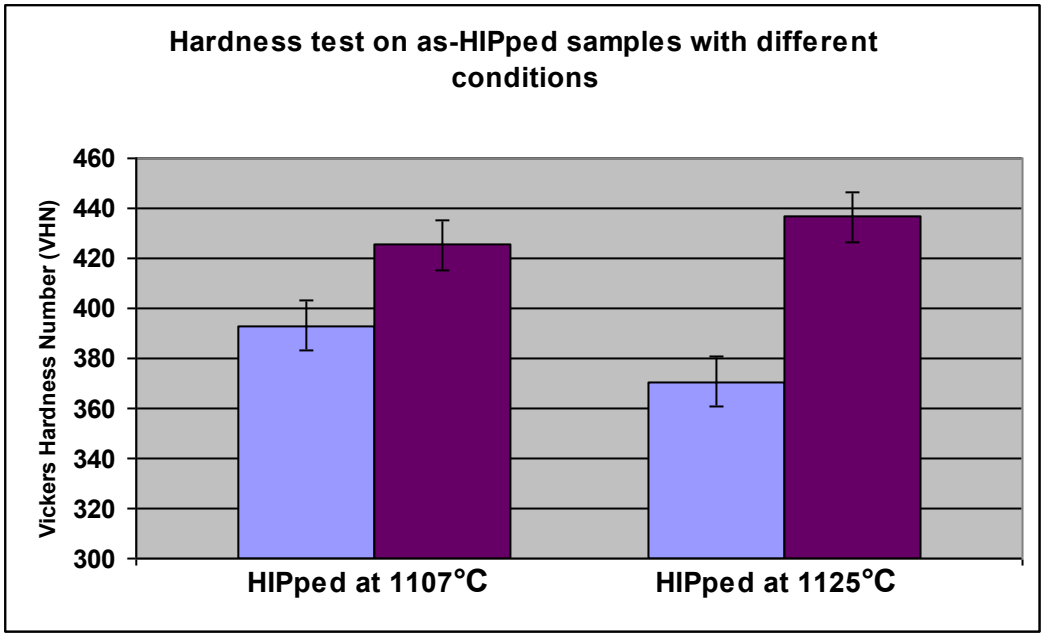

Figure 5.27 Diagram showing the dependence of hardness of samples on the cooling rate from HIPping temperature. The blue bars represent a cooling rate of 5℃/min; the purple bars represent a cooling rate of 132℃/min.

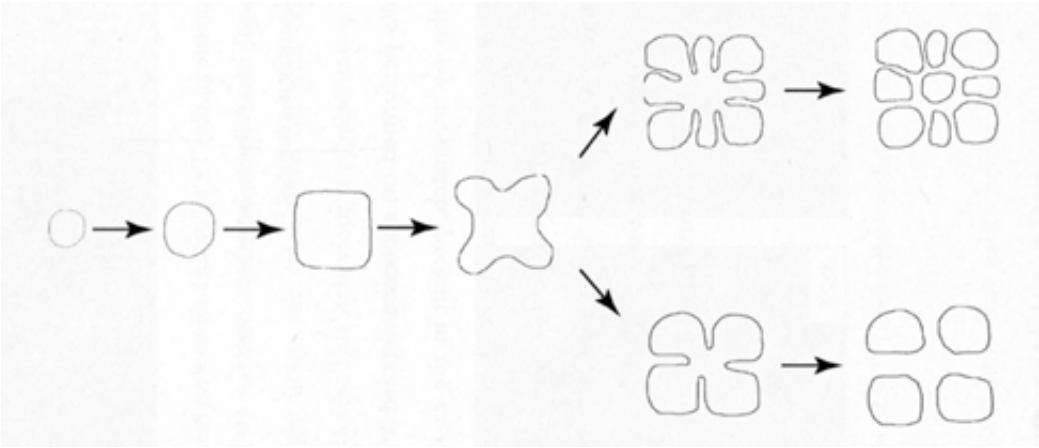

Figure 5.28 Schematic showing the coarsening and splitting of γ′ precipitates [4]

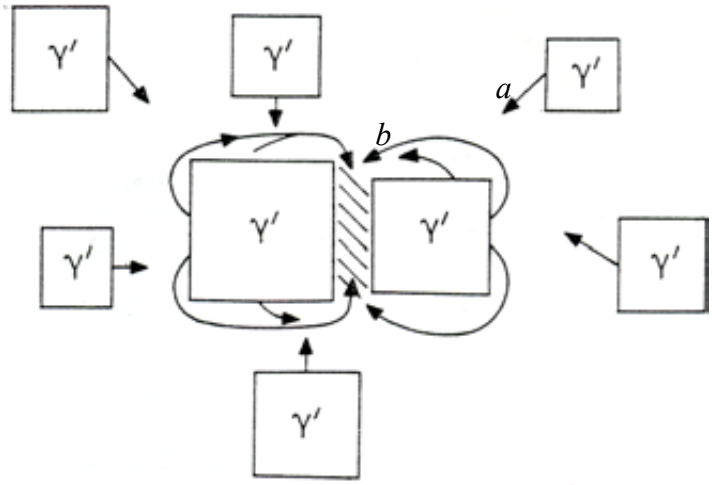

Figure 5.29 Schematic illustrating a stress-directed diffusion mechanism to bring largest γ′ into contact: *a* solute flux from smaller precipitates; *b* solute flux to remove elastically distorted matrix between cuboids [5]

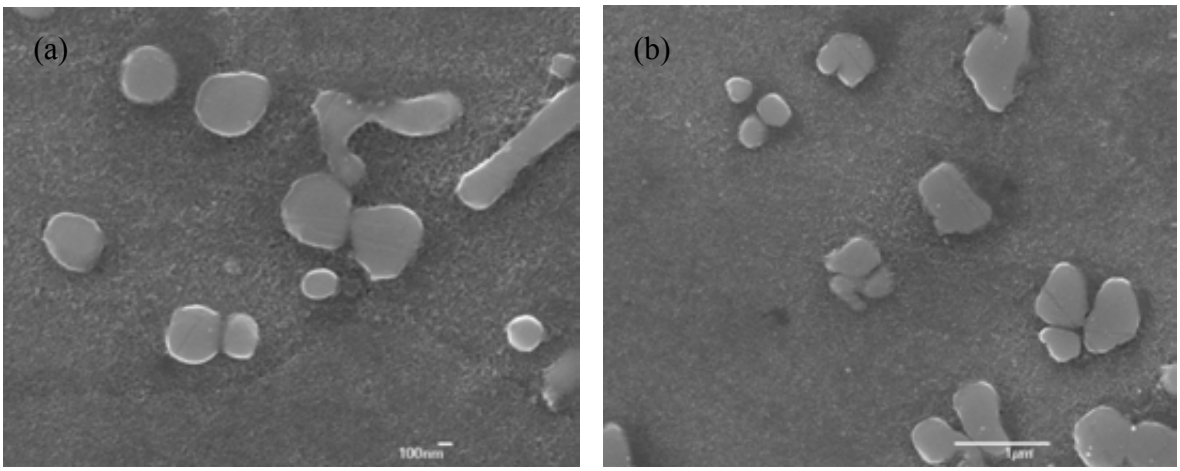

Figure 5.30 SEM micrographs showing the gamma prime structure in samples that were heated from room temperature to 1107℃, solution treated for 1h and then water quenched.

Chapter Six- Post-HIP Heat treatment and microstructure

6.1. Introduction

To achieve desired mechanical properties, various microstructural features such as grain size, γ′ size and distribution can be altered by using different heat treatments. In powder HIPping process, heat treatment may further influence the PPB precipitate size and distribution and the formation of thermally-induced pores.

This chapter focuses on the study of the microstructural changes that occur during heat treatment. Alloy response to solution treatment and cooling rate is presented in terms of grain growth, primary and secondary γ′ size and distribution and area fraction. Potential changes in PPB precipitate size and distribution and the formation of thermally-induced pores by solution treatment are also investigated. The response of intragranular γ′ to ageing treatment is presented in terms of the size and fraction of tertiary γ′.

6.2 Results

Figure 6.1 shows the large thermally induced pores after solution treatment at a temperature above or equivalent to a HIPping temperature 1107℃. The size of the pores ranges from 1μm to 10μm and they usually show an irregular morphology, see Figure 6.1(a). These pores are believed to be caused by the reopening of gas bubbles which remained in as-received powders before HIPping. When the solution temperature is lower than but very close to the HIPping temperature 1180℃, small thermally induced pores with size of 1~3μm were observed and generally show a spherical morphology, see Figure 6.2(a)(b). At a lower solution treatment temperature, like 1120℃, such microvoids could be hardly observed even though dwell duration was increased, see Figure 6.2(c). That the thermally induced porosity

level could be reduced by decreasing solution treatment has been well recognized in previous reports [1].

Figure 6.3 shows the PPB precipitate distribution in samples with different heat treatment conditions. It can be seen that both solution treatment and ageing treatment show no obvious change to the PPB precipitate size and distribution. However, solution treatment at 1120℃ seems to increase grain size slightly, see Figure 6.4, although this sub-solvus temperature is not able to dissolve all γ′, see Figure 6.5. As compared with the themomechanically processed samples, the current net-shape HIPped samples all showed bigger grain sizes. The most pronounced influence of heat treatment on microstructure was found in the γ′ size and distribution. Ageing made no great difference to primary and secondary γ′ but seemed to increase the precipitation of very fine γ′ and lead to slight growth, see Figures 6.6-6.7. Solution treatment showed a profound influence on γ′ size, distribution and morphology. It is clear from the figures that solution treatment at 1120℃ followed by air cooling considerably decreased the volume fraction of large secondary γ′ and changed the irregularly-shaped γ′ into cuboidal or near-triangular morphology. The particle size range of secondary γ′ also decreased from 600nm~1.2μm to 350~750nm. Moreover, a large volume fraction of much finer near-cuboidal tertiary γ′ with medium particle sizes of 100~200nm were produced after solution treatment, see Figures 6.7(c) and (d). Very fine γ′ precipitates, smaller than 50nm in diameter, are associated with the large secondary γ′ and medium-sized γ′, leading to a multi-modal γ′ distribution, see Figure 6.7 (c). Solution treatment at 1160℃ followed by air cooling could even eliminate the coarse primary and secondary γ′ and form a much finer secondary γ′ (around 300nm) microstructure, see Figure 6.6(d). However, these refined secondary γ′ showed an irregular morphology, see Figure 6.7(d). After deep etching, the detailed microstructure of secondary γ′ could be further revealed, as shown in Figure 6.8. The irregular-shaped secondary γ′ showed a cauliflower-like morphology and were composed of

many γ′ particles with size range from 200nm to 500nm. The cuboidal secondary γ′ were composed of numerous microzones or small particles with size of around 50nm. Fan-type γ-γ′ structure could be still observed in the samples that were heat treated, see Figure 6.9. In the HIPped and aged samples, the volume fraction of this type of structure is around 3% while in the samples which were solution treated at 1120℃ followed by air cooling, this structure could be only observed occasionally and sporadically. In the samples solution treated at 1160 ℃ followed by air cooling, no such structure was observed. It is noted that these finger-like γ′ dendrites in the samples that were solution treated were also composed of considerable superfine particles or microzones, see Figures 6.9(d)-(f).

6.3 Discussion

The experimental results demonstrate that solution treatment temperature shows significant influence on the formation of thermally induced porosity (TIP). When the temperature is above or equivalent to HIPping temperature, gas bubbles were observed (see Figure 6.1). This is consistent with previous work which suggested that during high temperature post-HIP heat treatment without pressure, swelling can occur as gas establishes an equilibrium pressure dependent on the surface energy and consequently lead to the reopening of gas bubbles [2]. TIP formed during high temperature post-HIP solution treatment was also reported by Huron et al [3-4] who suggested that the addition of boron could increase the amount of incipient melting and thus weaken the grain boundaries, which would promote TIP formation, especially at high temperature. The presence of pores in nickel-based superalloys has been widely reported to be very harmful for fatigue properties [5-8]. They were usually found to act as fatigue crack nucleation sites [5-8]. Their presence at grain boundaries may further promote grain boundary sliding at elevated temperature and thus accelerate creep rate. Decreasing solution treatment temperature was found to be able to

decrease or avoid the formation of TIP. This is also consistent with Hyzak et al's report [1] that by slightly decreasing the solution treatment temperature from 1190℃ to 1182℃ for a HIPped (HIPping temperature at 1190℃) AF-115 P/M superalloy, the thermal induced porosity level reduced from 0.42% to 0.16% in volume fraction, which led to an improvement in the fatigue lifetimes by two to five times. However, too low solution treatment temperature may show reduced influence on controlling the microstructure such as grain size and gamma prime size and distribution, which are also very important for mechanical properties. Therefore, it is essential to find out the most appropriate temperature for solution treatment to achieve a desired microstructure without too many TIP defects.

Solution treatment at 1120℃ followed by air cooling was found not only to be able to avoid the formation of TIP for HIPped RR 1000 samples, which would be beneficial for fatigue and creep properties, but also to produce a high population of much finer γ′, which would be good for tensile and creep properties. Although a sub-solvus heat treatment at this temperature was unable to increase grain size significantly (which is not good for creep) because a sub-solvus temperature is unable to dissolve γ′ at GBs completely for grain growth; the use of a super-solvus HIPping temperature which already maximized grain size, does not allow a large window for solution treatment to achieve much increase in grain size without minimizing the population of gas bubbles and TIP.

In spite of a sub-solvus temperature, the solution treatment at 1120℃ followed by air cooling shows great influence on the as-HIPped microstructure, especially γ′ size, morphology and distribution. A large population of coarse and irregular-shaped primary and secondary γ′ in as-HIPped samples was replaced with a large volume fraction of finer cuboidal secondary γ′ and tertiary γ′. The cuboidal secondary γ′ was found to be made up of many superfine γ′ particles (see Figure 6.8). This structure suggests that even cuboidal secondary γ′ may be formed by coalescence of even smaller γ′ particles, analogous to the

formation mechanism of irregular-shaped secondary γ′ precipitates in the as-HIPped samples (see Chapter 5). However, due to the use of a rapid cooling rate (air cooling) here in contrast to the slow cooling after HIPping, the diffusion-induced outbound coarsening of particulate branches in coalesced structure may be to a large extent suppressed and thus the integration of γ′ clusters would dominate during the whole cooling process which led to the formation of cuboidal secondary γ′ rather than irregular-shaped γ′.

Samples that were solution treated at 1160℃ and then air cooled showed a much finer secondary γ′ microstructure. This may be because higher solution treatment temperature could dissolve more γ′ and during subsequent fast cooling, γ′ need to nucleate from the solid solution matrix first and it also took time to form γ′ clusters. Therefore, coarse γ′ could be prevented during fast cooling. Although air cooling from higher solution temperature (like 1160℃) led to an even more homogeneous γ′ microstructure, the absence of an appropriate number of coarse primary γ′ at grain boundaries may reduce crack propagation resistance and ability to impede grain boundary sliding. Pang et al. [6] suggested that a higher volume fraction of coarse and discrete primary γ′ provides crack growth barrier effects and thus better short crack growth resistance, beneficial for overall fatigue lifetime. Moreover, as mentioned in Chapter 5, the presence of coarse primary γ′ at grain boundaries usually led to the formation of grain boundary serrations, which could impede grain boundary sliding and crack growth and thus are beneficial for both creep and fatigue crack propagation properties. Removal of these coarse precipitates at grain boundaries means removal of grain boundary serrations and thus the corresponding benefits. Even worse, solution treatment at 1160℃ gave rise to TIPs, which are obviously a disadvantage. It is clear that from the microstructural point of view, solution treatment at 1120℃ is suggested.

Ageing treatment was found to further increase the number of superfine γ′ and make them coarsen. Given that increased ageing temperature and dwell duration would lead to

coarsening and splitting of secondary γ′ [9-10], an ageing temperature at 760℃ for 16 hours was selected, which has been proved to show no significant effect on secondary γ′ in both the current study and previous studies [9-11].

6.4 Conclusions

The influence of solution treatment and ageing treatment on microstructures of HIPped samples was studied. It was found that solution treatment near the HIPping temperature led to thermally induced pores (TIP) but lower temperature like 1120℃ avoided TIP and changed significantly the γ′ size, distribution and morphology during subsequent air cooling. The dominant coarse and irregular-shaped primary and secondary γ′ in as-HIPped samples were replaced with a large volume fraction of finer cuboidal secondary γ′ and medium-sized tertiary γ′ after solution treatment. The cuboidal secondary γ′ was made up of many superfine γ′ particles, which suggests that even the cuboidal secondary γ′ may be formed by coalescence of even smaller γ′ particles. However, the sub-solvus solution treatment showed no significant increase in grain size.

Ageing treatment at 760℃ was found to increase the precipitation of superfine γ′ and make them coarsen but show no observable influence on primary and secondary γ′.

The influence of the different microstructures developed on mechanical properties has been studied and is discussed in Chapters 7 and 8.

References

[1] Hyzak JM, Bernstein IM. The effect of defects on the fatigue crack initiation process in two P/M superalloys: Part2, surface-subsurface transition. Metallurgical Transactions A 1982; 13: 45-52.

[2] Atkinson HV, Davies S. Fundamental aspects of hot isostatic pressing: An overview. Metallurgical and Materials Transactions A 2000; 31: 2981-3000.

[3] Huron ES, Casey RL, Henry MF, Mourer DP. The influence of alloy chemistry and powder production methods on porosity in a P/M nickel-base superalloy. In: Kissinger RD, Deye DJ, Anton DL, Nathal MV, Pollock TM, Woodford DA editors. Superalloys 1996. Warrendale, Pennsylvania, USA: The Minerals, Metals and Materials Society;1996. p. 645-652.

[4] Huron ES, Bain KR, Mourer DP, Schirra JJ, Reynolds PL, Montero EE. The influence of grain boundary elements on properties and microstructures of P/M nickel base superalloys. In: Green KA, Pollock TM, Harada H, editors: Superalloys 2004. Warrendale, PA: The Minerals, Metals and Materials Society (TMS); 2004. p. 381-390.

[5] Davidson DL, Chan KS. Crystallography of fatigue crack initiation in astrology at ambient temperature. Acta Metallurgica 1989;37(4):1089–1097.

[6] Pang HT, Reed PAS. Fatigue crack initiation and short crack growth in nickel-base turbine disc alloys—the effects of microstructure and operating parameters. International Journal of Fatigue 2003;25: 1089–1099.

[7] Luo J, Bowen P. Small and long fatigue crack growth behaviour of a PM Ni-based superalloy, Udimet 720. International Journal of Fatigue 2004; 26: 113–124.

[8] Chang DR, Krueger DD, Sprague RA. Superalloy Powder Processing, Properties and Turbine Disk Applications. In: Sunerallovs 1984, Proceedings of the Fifth International Symposium on Superalloys. Warrendale, PA: TMS-AIME; 1984. p. 245-273.

[9] Mitchell RJ. Development of a new powder processed Ni-base superalloy for rotor disc application, PhD thesis, 2004.

[10] Mitchell RJ, Preuss M. Inter-relationships between composition, γ′ morphology, hardness, and γ-γ′ mismatch in advanced polycrystalline nickel-base superalloys during aging at 800 ℃. Metallurgical and Materials Transactions A, 2007;38:615-627.

[11] Hardy MC, Zirbel B, Shen G, Shankar R. Developing damage tolerance and creep resistance in a high strength nickel alloy for disc applications. In: Green KA, Pollock TM,

Harada H, editors: Superalloys 2004. Warrendale, PA: The Minerals, Metals and Materials Society (TMS); 2004. p. 83-90.

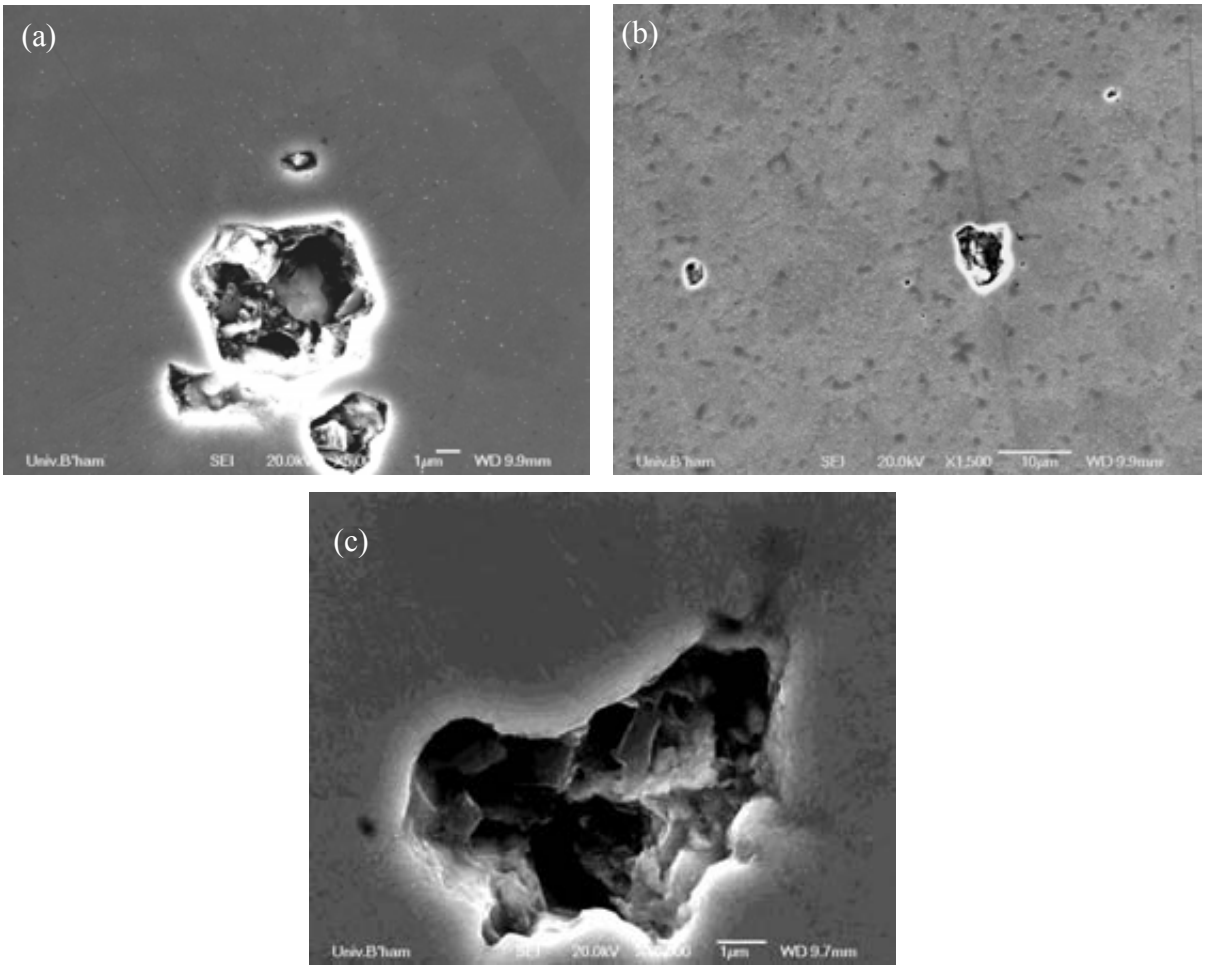

Figure 6.1 Secondary electron SEM micrographs showing the reopening of gas bubbles in samples after solution treatment at a temperature above or equivalent to HIPping temperature, (a)HIP 1107℃/100MPa/4h +ST 1125℃/2h/AC; (b) HIP 1125℃/100MPa/4h +ST 1125℃/2h/AC; (c) HIP 1125℃/100MPa/4h +ST 1160℃/2h/AC.

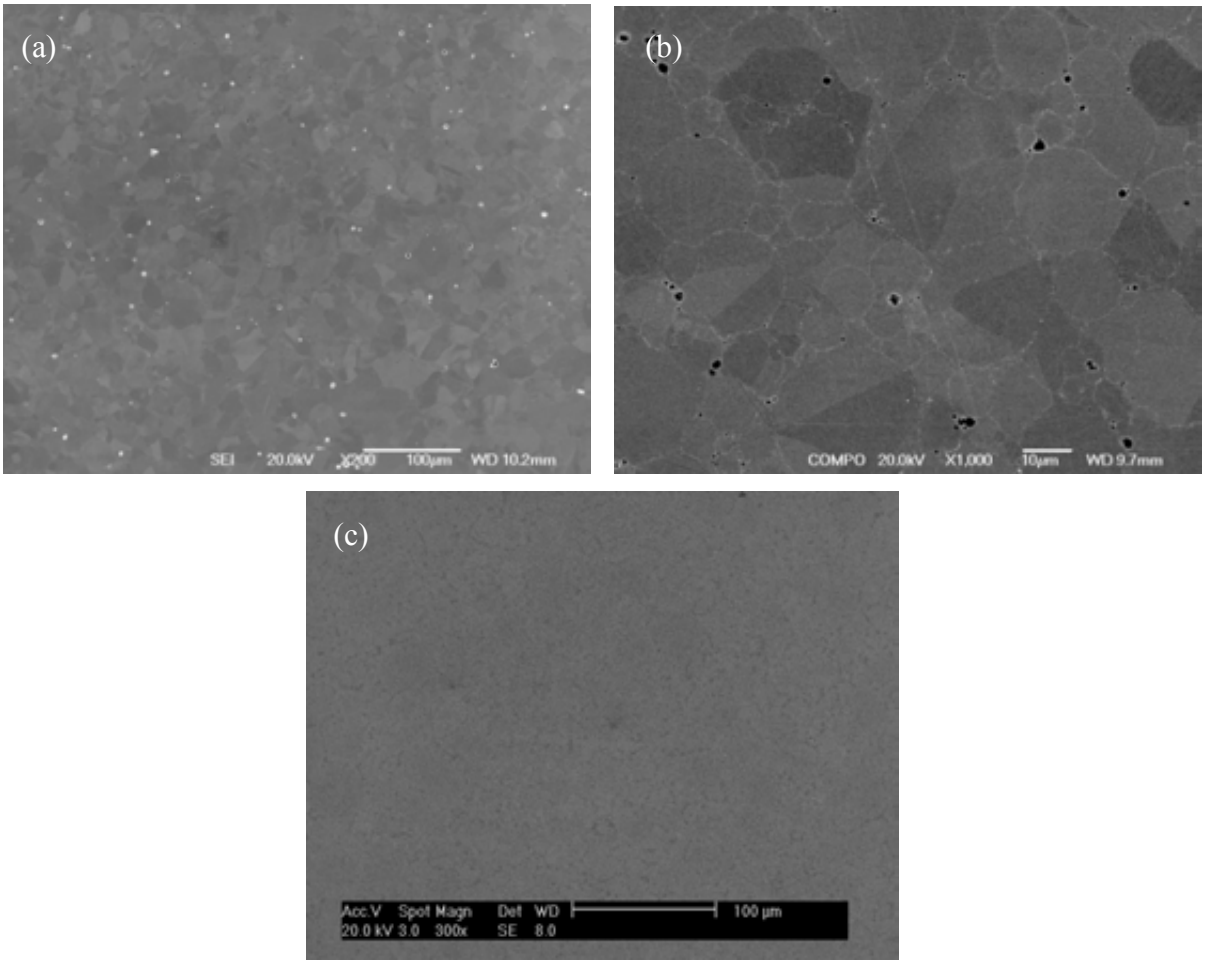

Figure 6.2 Secondary electron SEM micrographs showing the presence of porosities in the samples (a)(b) HIP1180℃/150MPa/4h + ST 1160℃/2h/AC; and the absence of voids in the samples (c) HIP1180℃/150MPa/4h + ST 1120℃/48h/AC.

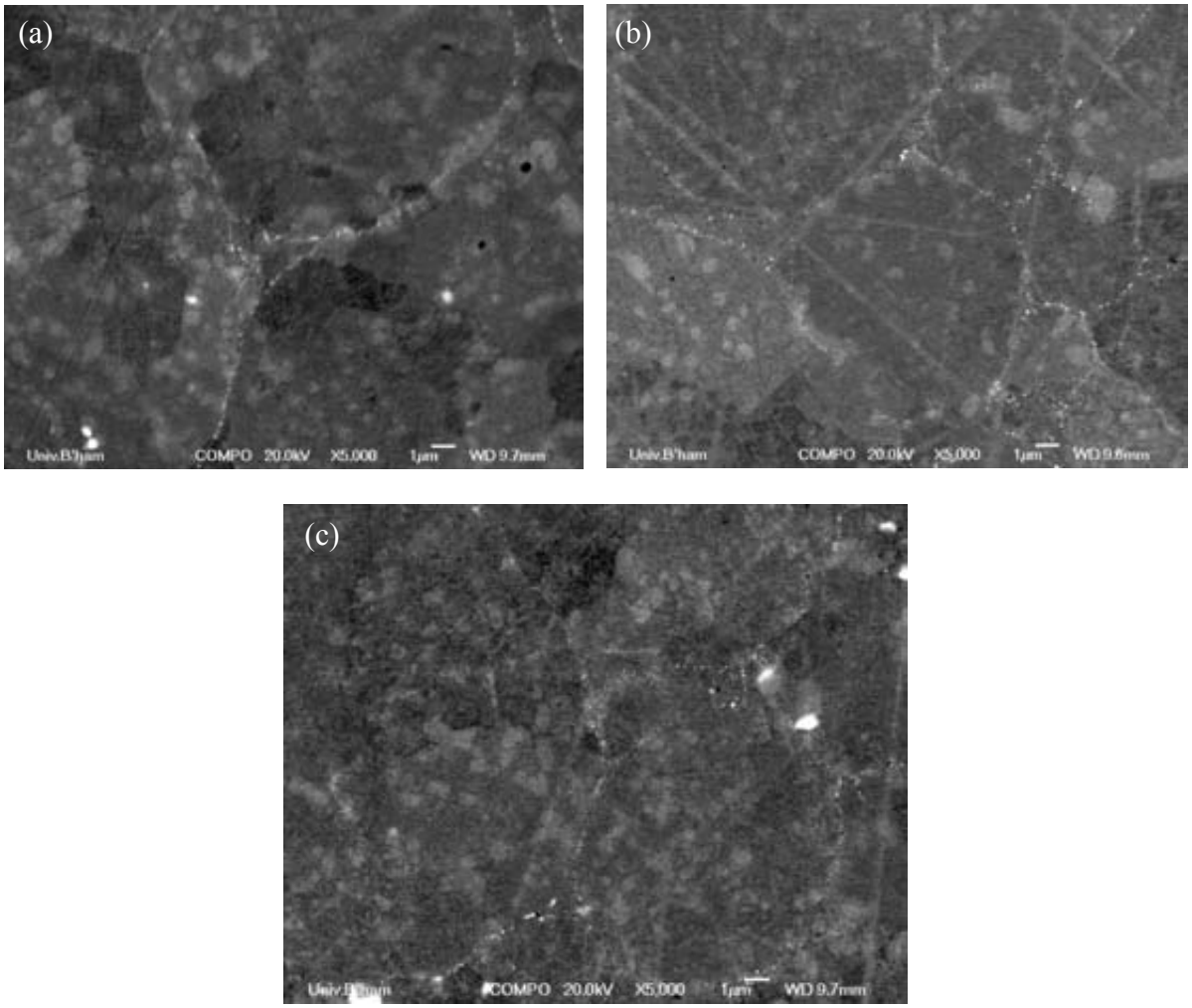

Figure 6.3 Back scattered SEM images showing the PPB precipitate distribution in the samples (a) HIP 1180℃/150MPa/4h; (b) HIP 1180℃/150MPa/4h+ ST 1120℃/2h/AC; (c) HIP 1180℃/150MPa/4h+ Aged at 760℃/16h/AC

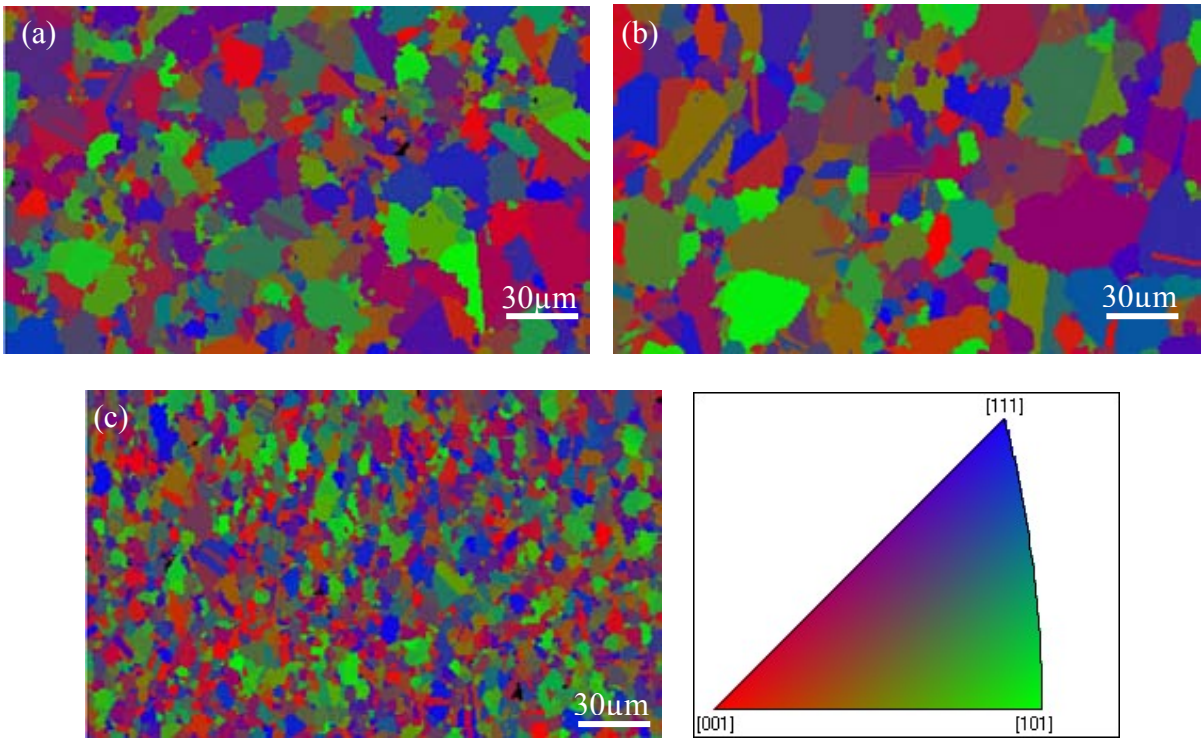

Figure 6.4 EBSD micrographs showing the grain structures of RR 1000 samples with different processing conditions (a) HIP 1180℃/150MPa/4h and aged at 760℃/16h/AC, average grain diameter *d*=12μm; (b) HIP 1180℃/150MPa/4h, and Solution treated at 1120℃/2h/AC and aged at 760℃/16h/AC, *d*=15μm; (c) HIP 1107℃/100MPa/4h + Extruded+ Solution treated at 1125℃/2h/AC and aged at 760℃/16h/AC, *d*=7μm

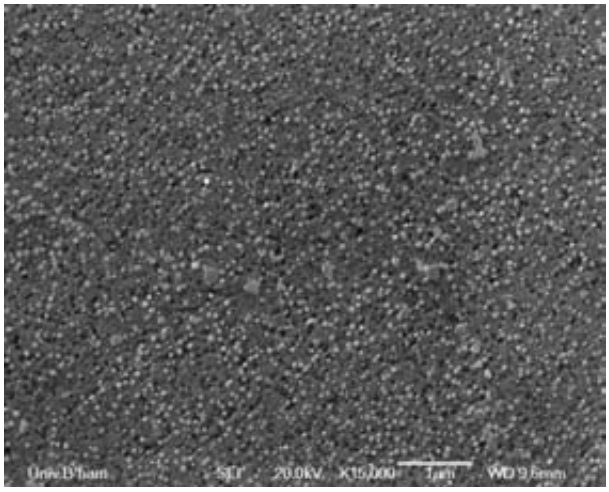

Figure 6.5 Secondary electron SEM micrograph showing many retained gamma prime at 1120℃/1h, the microstructure was 'frozen' by water quench from 1120℃

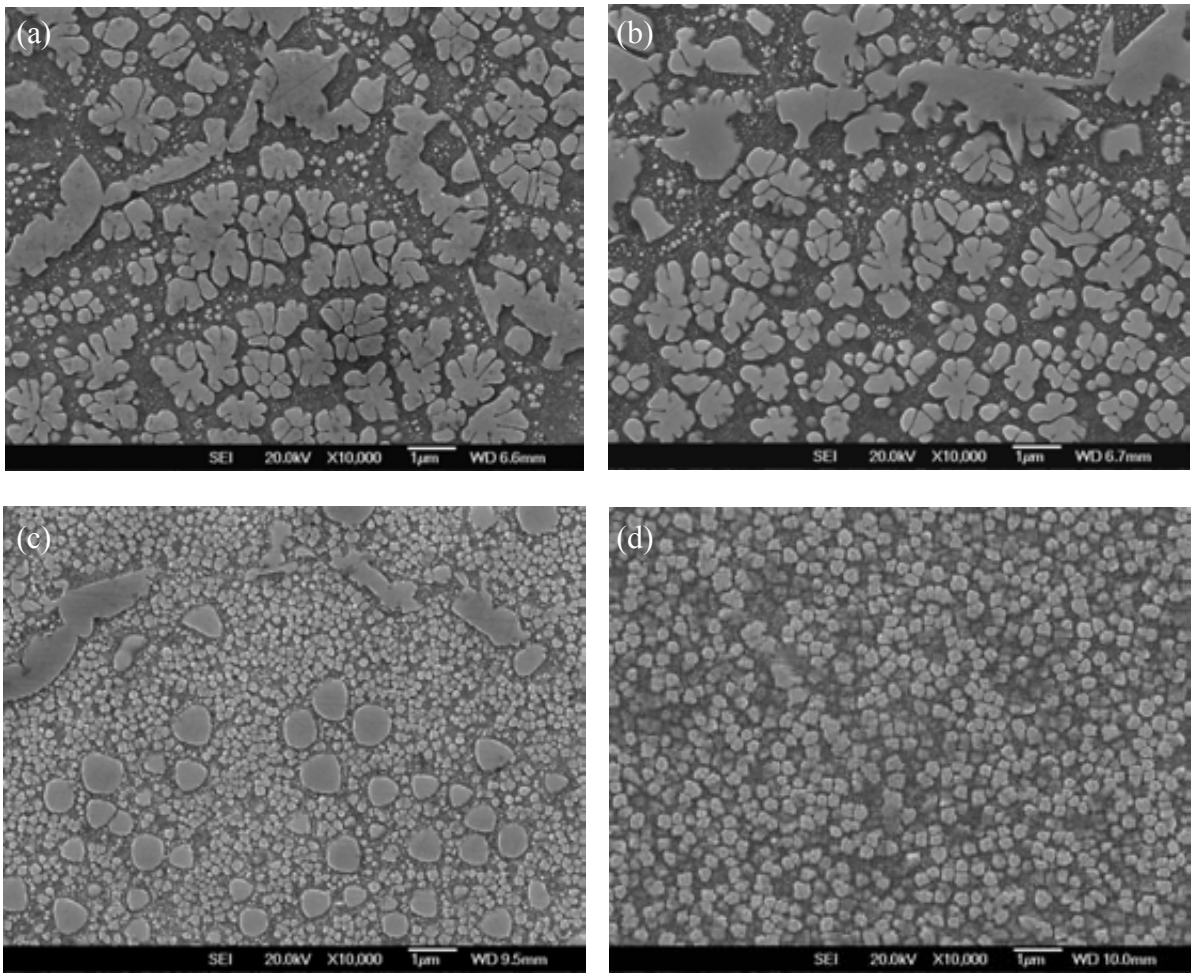

Figure 6.6 Secondary electron SEM micrographs showing the change in γ′ size, distribution and morphology in RR 1000 samples with different heat treatments (a) HIP 1180 ℃ /150MPa/4h; (b) HIP 1180℃/150MPa/4h and aged at 760℃/16h/AC; (c) HIP 1180℃ /150MPa/4h, and Solution treated at 1120℃/2h/AC and aged at 760℃/16h/AC; (d) HIP 1180 ℃/150MPa/4h, and Solution treated at 1160℃/2h/AC and aged at 760℃/16h/AC

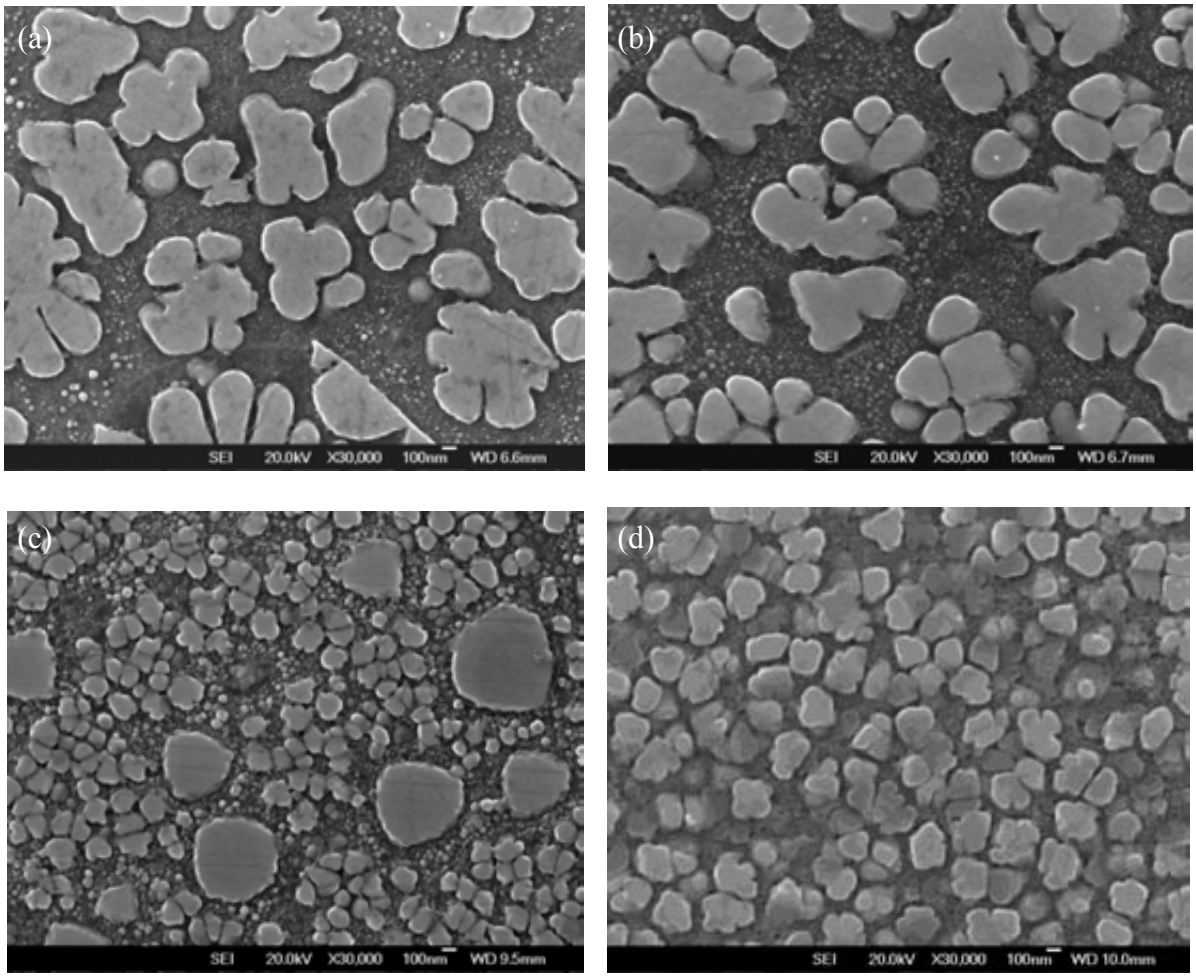

Figure 6.7 high magnification secondary electron SEM micrographs showing the change in γ′ size, distribution and morphology in RR 1000 samples with different heat treatments, (a) HIP 1180℃/150MPa/4h; (b) HIP 1180℃/150MPa/4h and aged at 760℃/16h/AC; (c) HIP 1180℃/150MPa/4h, and Solution treated at 1120℃/2h/AC and aged at 760℃/16h/AC; (d) HIP 1180℃/150MPa/4h, and Solution treated at 1160℃/2h/AC and aged at 760℃/16h/AC

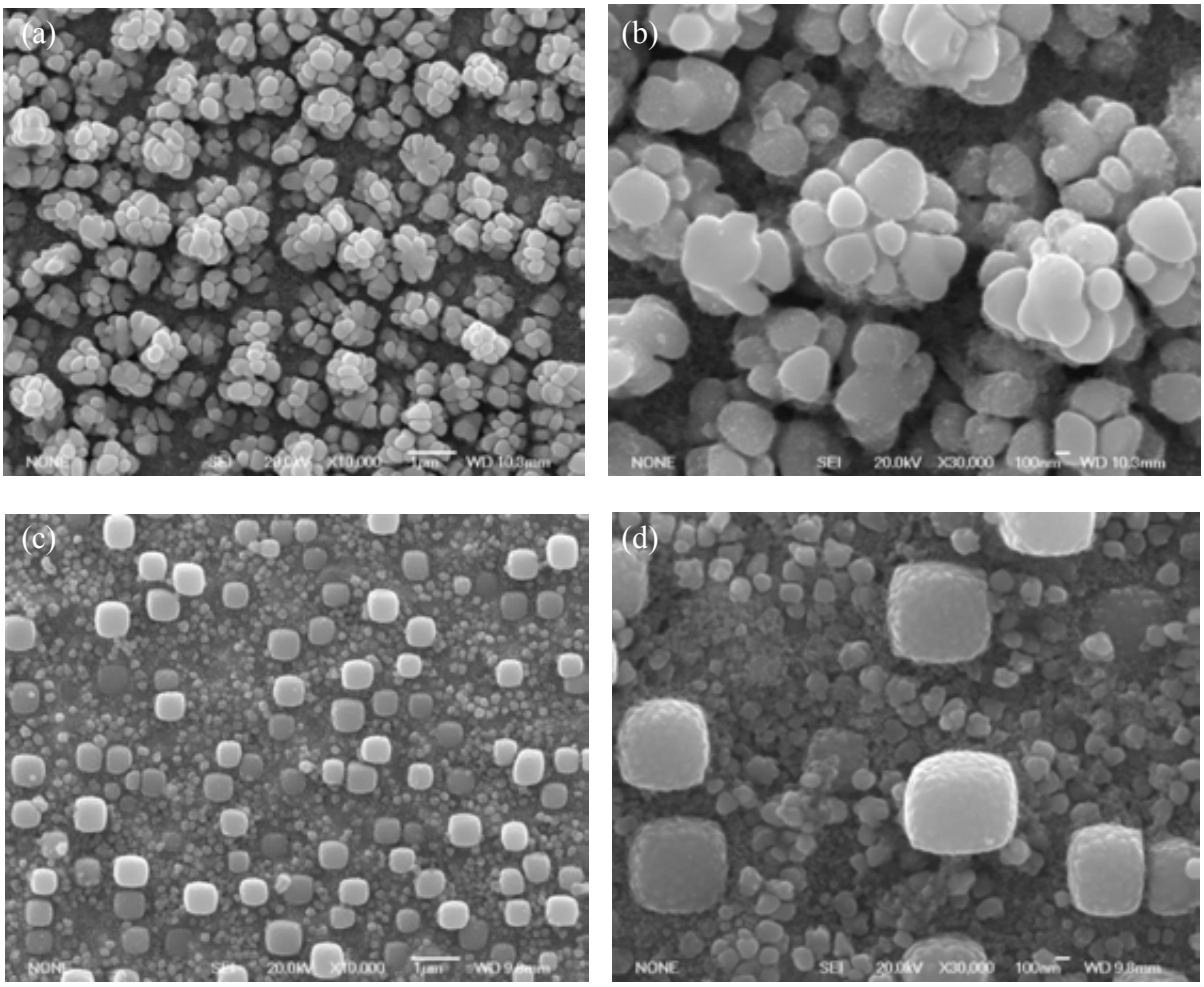

Figure 6.8 high magnification secondary electron SEM micrographs showing the details of secondary γ′ in the samples, (a)(b) HIP 1180℃/150MPa/4h and aged at 760℃/16h/AC, a cauliflower-like secondary γ′ could be observed; (c)(d) HIP 1180 ℃ /150MPa/4h, and Solution treated at 1120℃/2h/AC and aged at 760℃/16h/AC, the cuboidal secondary γ′ were found to be composed of many fine particles. The samples had been subject to full etching.

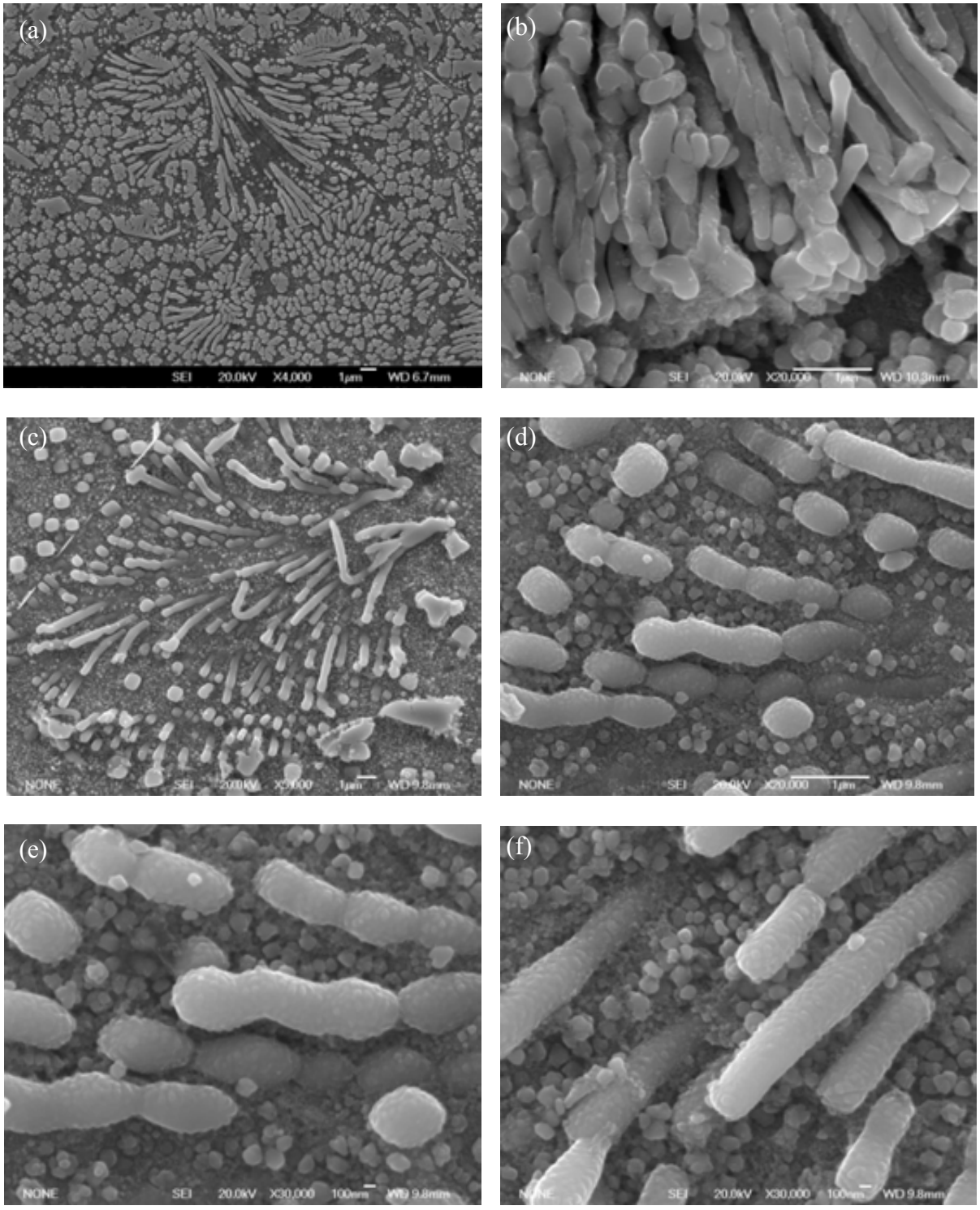

Figure 6.9 Secondary electron SEM micrographs showing the details of γ′ fan-type structure in the samples (a)(b) HIP 1180℃/150MPa/4h + aged 760℃/16h/AC; (c)-(f) HIP 1180℃/150MPa/4h + ST 1120℃/2h/AC + aged 760℃/16h/AC, the γ′ rods were found to contain many very fine particles.

Chapter Seven-Tensile Behaviour

7.1 Introduction

In the last two chapters, the influence of HIPping and heat treatment parameters on microstructure has been extensively studied. However, their influence on mechanical properties needs to be fully understood. This chapter will mainly focus on the investigation of influence of processing condition on tensile properties. The influence of processing condition on fatigue and creep properties is reported in Chapter 8.

Moreover, it was found that both HIPping and post-HIP heat treatment led to the formation of multi-modal γ′ with different size ranges and morphologies. The deformation and strengthening mechanisms of different colonies of γ′ with varied sizes and morphologies will be studied and discussed in this chapter. The fracture behaviour of different samples will be examined as well.

7.2 Results

7.2.1 Effect of HIPping Temperature or Procedure

Figure 7.1 and Table 7.1 show the tensile properties of RR 1000 samples HIPped at different HIPping temperatures or using different procedures. These samples were tested at both room temperature and intermediate temperature, 700℃ or 750℃. It can be seen that changing the HIPping procedure generally did not make a significant difference to tensile properties except that ramping up the temperature first and then pressure seemed to marginally improve elongation. HIPping temperature obviously shows a more significant influence on the tensile properties of RR 1000. When tested at room temperature, the samples HIPped at 1180℃, which had a much coarser grain size (see Chapter 5), showed a reduction of the 0.2% yield strength by around 100MPa but showed similar ultimate tensile strength

(UTS) and elongation, as compared with the samples HIPped at 1107℃. When tested at 700℃, the samples HIPped at 1180℃ showed even lower 0.2% yield strength but their UTS and elongation are much higher than the samples HIPped at 1107℃, around 250MPa and above 20% increase in magnitude, respectively.

Figures 7.2 and 7.3 show the fracture surfaces of samples obtained from different HIPping processes after tensile testing at room temperature and 700℃, respectively. It can be seen that the samples HIPped at 1107℃, irrespective of HIPping procedure, all showed an inter-particle debonding failure mode whereas those HIPped at 1180℃ generally showed a ductile trans-granular fracture mode.

7.2.2 Effect of Heat Treatment

Figure 7.4 summarises the room temperature tensile properties of as-HIPped RR 1000 samples (HIPped at 1180℃) and those that were HIPped and heat treated. As can be seen, for plain samples, ageing treatment led to slight increase in both 0.2% yield strength and UTS, typically by 50MPa. Solution treatment followed by air cooling led to a marked improvement of 0.2% yield strength and UTS by around 200MPa and 150MPa, respectively, as compared with those simply HIPped samples. Notched samples obviously showed much higher UTS than the plain ones (by around 200 MPa for the HIPped+aged samples and about 300 MPa for samples that were solution treated and aged), which suggests that the RR 1000 samples prepared should be fairly notch-insensitive. Solution treatment followed by air cooling also led to improvement of UTS of notched samples by 200MPa relative to that of HIPped and aged notched samples. It is therefore clear that the solution treatment followed by air cooling can cause remarkable improvement in strength. However, increasing solution treatment temperature from 1120℃ to 1160℃ showed no great change to the tensile properties, see Table 7.2.

The tensile properties of RR 1000 samples at 700℃ are shown in Figure 7.5. Again the samples that were solution-treated and aged showed more significant increases in 0.2% yield stress and in UTS over the values of as-HIPped samples. Thus the directly aged sample showed no obvious increase in UTS but the sample that was solution treated and aged showed an increase of 170MPa. Notched samples again showed much higher UTS than the plain ones and solution treatment led to around 100MPa improvement in UTS.

The increase in testing temperature led to a decrease of 100MPa in both 0.2% yield strength and UTS in all samples but the elongation was almost unchanged.

Also, according to Table 7.2, the net-shape HIPped RR 1000 samples that were solution treated at either 1120 ℃ or 1160 ℃ show comparable tensile properties to the thermomechanically processed (extruded) RR 1000 materials which are currently used as disc materials in Rolls-Royce's advanced turbine engine.

7.2.3 Deformation Behaviour

7.2.3.1 Deformation at Room Temperature

Figure 7.6 shows a photograph of RR 1000 samples after tensile testing. It can be seen that these samples actually show no necking and instead show almost identical cross section areas in the parallel part. This appears inconsistent with the general concept that ductile materials usually show necking after tensile fracture (here RR 1000 shows an elongation around 30% and should be considered ductile). Figure 7.7 shows a typical room temperature tensile stress-strain curve for these samples. It can be seen that the stress increased rapidly to a yield point and then steadily increased until failure. Considering the cross section area of specimens always decreased in the progress of tensile testing, the true stress for RR 1000 samples actually continuously increased until failure where the stress reaches the maximum. This suggests the whole deformation process occurred in a very uniform mode and work

hardening should have continued to build up. Obviously, the large elongation for RR 1000 samples was mainly due to this homogeneous deformation and continued work hardening.

To find out the deformation mechanism for these samples, the microstructure of longitudinal section of tested samples was investigated. Figure 7.8 shows the γ′ morphological change after tensile testing. It can be seen that all the secondary γ′ have been elongated to some extent along the tensile loading direction. Moreover, pronounced localized shearing of secondary and tertiary γ′ was observed in all samples irrespective of processing condition or γ′ morphology, see Figure 7.9. For irregular-shaped γ′, slip seemed to occur mainly by cutting through their branches. The slip steps show offsets of tens of nms showing that many dislocations had sheared through the precipitates and that within the resolution of these images the dislocations have slipped on the same plane.

Figure 7.10 and Figure 7.11 show the bright-field images and weak-beam dark-field images of dislocations in the samples tested at room temperature. Appreciable densities of dislocations were found inside the secondary γ′, see Figures 7.10(a) and (c). Weak-beam images show stacking faults inside the precipitates, see Figures 7.10(b) and (d). For irregularly-shaped secondary γ′, well extended stacking faults were often observed while for cuboidal secondary γ′, a mixture of stacking faults and unextended dislocations were observed, see Figures 7.10 (d) and (f). Around these secondary γ′, a significant density of dislocations and stacking fault ribbons were observed in the γ channels. For medium-sized tertiary γ′, 100-150nm in diameter in the samples that were solution treated, most were found to be free of dislocations and only a few contained stacking faults, as shown in Figure 7.11. Also, many stacking fault ribbons were seen in the channels between these large or medium-sized γ′ precipitates. Given the presence of numerous even finer γ′ in the channels between large secondary or tertiary γ′ (see Figure 6.7), the stacking faults in the channels may be the

result of slip of dislocations through these fine precipitates. Actually, the spacing of these ribbons is usually equivalent to the size of the fine precipitates (around 50nm).

7.2.3.2 Deformation at 700℃

RR 1000 samples showed basically similar stress-strain trend at 700℃ to that at room temperature, see Figure 7.12. When the continuous decrease in cross section area during testing is taken into account, it is clear that the true stress again increased steadily. Similarly, this led to uniform deformation, which can also be evidenced by the absence of necking in the tested samples, see Figure 7.13.

Again, pronounced shearing of γ′ with slip planes inclined to tensile loading direction was observed in the tested samples, especially in the area close to the slant fracture surface where this pronounced shearing was widespread, see Figure 7.14 (d). Slip passed through fan-type γ′ precipitates by shearing the finger-like γ′, see Figure 7.15.

The samples tested at 700°C, were found to show an even higher density of stacking fault ribbons, see Figure 7.16. In the large secondary γ′, extended stacking faults were widespread through the precipitates. Most of the medium-sized γ′ were cut through by dislocations leaving stacking faults in contrast to the observations at room temperature where these were not cut by dislocations (see Figure 7.11). Some of the stacking faults even extended across the γ channel into the adjacent tertiary γ′ precipitates. Some of the stacking fault ribbons overlapped and intertwined with each other, see Figure 7.16(f). It is obvious that increasing temperature led to a more planar but more complicated deformation mechanism.

7.2.4 Fracture Analysis

7.2.4.1 Fracture after Room Temperature Tensile Testing

It is noted from Figure 7.6 that the samples tested at room temperature all show a flat fracture surface normal to the applied tensile loading direction. This fracture feature is

usually believed to be dominated by plane strain conditions and usually suggests poor fracture toughness [2]. SEM observation in Figure 7.17 (a) reveals chevron-shaped markings with ridges and valleys, radiating from a site of the fracture surface. Crack initiation of samples investigated all occurred in a cleavage mode from sample surface (Figure 7.17(b)) while crack propagation basically followed a transgranular fracture mode, see Figure 7.17(c). A few facets and voids were observed on the fracture surface. Some of the voids formed apparently because of the crack propagation along PPBs (see Figure 7.17(e)) while others may be due to the presence of inclusion clusters (see Figure 7.18).

Figure 7.19 shows the section surface of the tested samples with different heat treatments. A few secondary cracks were observed throughout the tested samples. These secondary cracks could be initiated at either PPBs or big spherical hafnium oxide precipitates or inclusion clusters, see Figure 7.19(a)-(c). Occasionally, secondary cracks were also observed at script precipitates which were rich of Mo and Cr, see Figure 7.19(d). The results suggest those sites, such as PPBs, oxides and carbides, are still the weak points for crack initiation.

7.2.4.2 Fracture after tensile testing at 700℃

Samples tested at 700℃ exhibited mixed fracture features, i.e., flat fracture in the centre and slant fracture at the edges, see Figures 7.20 (a-b) and Figure 7.21. The flat fracture could be due to plane strain conditions while the slant fracture is because of plane stress conditions [2]. This fracture feature usually suggests intermediate fracture toughness. The slant fracture surface is at about 45° to the tensile stress axis, where the shear stress dominates. Cracking was shown to initiate at the area near sample surface in a cleavage mode and then propagated to form many chevron-shaped markings on the flat fracture surface, see Figure 7.20(a) and (b). The crack propagated mainly in the form of faceted fracture but occasionally via inter-particle fracture; see Figure 7.20(e). As compared with room temperature fracture, fracture at 700℃ is more faceted and crystallographic, consistent with the more planar deformation at

elevated temperature described above. In contrast to flat fracture, slant fracture gave rise to a much more ductile fracture pattern characterized by massive dimples, see Figure 7.20(f). Appreciable secondary cracks were also observed in the section of tested samples, see Figure 7.22.

7.2.4.3 Notch fracture

The notched samples, irrespective of processing condition or testing temperature, were all found to fail at the notch root due to the nucleation and coalescence of big holes induced by the presence of inclusion clusters. Figures 7.23 and 7.24 show such a typical fracture feature. Several holes in the middle with radiating chevron-shaped markings could be observed. These holes have actually coalesced with one another and are always associated with clusters of inclusions. It seems that the notch fracture is quite sensitive to the presence of inclusions.

7.3 Discussion

7.3.1 Effect of HIPping Temperature or Procedure

The 0.2% yield strength has been shown to decrease with increased HIPping temperature for tests at both room temperature and 700℃. This is obviously caused by the increased grain size with increased HIPping temperature, see Figure 5.18. The finer secondary γ′ in the samples HIPped at lower temperature (see Figure 5.20) may also contribute to the increase of 0.2% yield strength to some extent. However, the room temperature UTS and elongation showed no obvious decrease with increased HIPping temperature but high temperature (700℃) UTS and elongation increased remarkably with increased HIPping temperature. On the other hand, it is noted that samples HIPped at a sub-solvus temperature (1107℃) which contained considerable PPBs failed in a PPBs' de-bonding mode while those that were HIPped at a super-solvus temperature (1180℃) and showed significantly reduced PPBs failed in a much more ductile fracture mode (basically trans-granular fracture). It seemed that

the presence of PPBs did not affect the room temperature UTS and elongation, although failure occurred at PPBs for the samples HIPped at lower temperature. At elevated temperature (700℃), PPBs seemed to become weakened and cracks could relatively easily initiate at PPBs, which led to earlier failure and dramatic decrease in UTS and ductility for the samples HIPped at 1107℃. The weakening of PPBs at high temperature may be caused by mass or void diffusion at PPBs, which promoted the PPB sliding and crack initiation. The current results are consistent with previous reports which also suggested that PPBs did not affect room temperature tensile properties greatly but led to significant degradation of high temperature tensile properties [3-7]. Increasing HIPping temperature to a supersolvus, which led to significant reduction in PPBs and promoted the formation of serrated grain boundaries, is obviously favourable for grain boundary strengthening at high temperature by impeding grain boundary sliding and crack initiation. Therefore, the prolonged deformation and work hardening are possible, which may account for the improved high temperature UTS and elongation.

Changing HIPping procedure (HIPped at 1107℃) did not effectively improve the tensile properties at either room temperature or 750℃. All the samples failed in an inter-particle de-bonding mode due to fracture along PPBs.

7.3.2 Effect of Heat Treatment

Ageing treatment was found to improve 0.2% yield strength at both room temperature and 700 ℃ by around 50MPa. Microstructural investigation indicated that ageing treatment increased the precipitation of fine γ′ and made these precipitates slightly coarsened, see Figure 6.7. Ageing treatment shows no significant change to the size and morphology of secondary γ′. The results are consistent with previous reports about the role of aging treatment [8-12]. It is generally believed that when the very fine precipitates are usually

smaller than the critical size that offers maximum resistance to dislocation motion, the strength increases with the increase in the size of the very fine γ′ precipitates. These fine γ′ precipitates were usually smaller than the critical size after solution treatment [8-12]. Ageing treatment, which could lead to minor growth of these precipitates, then is believed to promote strength improvement. In the current work, massive dislocations and stacking faults were believed to pass through or develop inside these fine γ′ (see Figures 7.10 and 7.11), which may be responsible for the slight improvement in 0.2% yield strength.

Solution treatment at 1120℃ followed by air cooling was found to cause significant improvement in both 0.2% yield strength and UTS while maintaining a good ductility. As indicated in Chapter 6, solution treatment led to slight increase in grain size and a significant change in γ' size, distribution and morphology. The dominant coarse and irregular-shaped primary and secondary γ′ in as-HIPped samples were replaced with a large volume fraction of finer cuboidal secondary γ′ and spherical tertiary γ′ and superfine γ′ precipitates after solution treatment. Obviously, the improved strength should not be caused by increased grain size but instead by the refined γ′. TEM study on dislocation structure of the samples deformed in tension indicated that irrespective of difference in γ′ morphology, dislocations passed through both irregular-shaped and cuboidal secondary γ′ and led to the formation of stacking faults inside them. Dislocations were also found to cut through numerous superfine γ′ embedded in the γ channels. It seemed that solution treatment showed no significant influence on the deformation behaviour of large secondary γ′ and superfine γ′ even though the morphology of secondary γ′ was changed. However, most of the medium-sized tertiary γ′ in samples that were solution treated were found not to be cut through by dislocations. Instead, they were mainly surrounded by many dislocations. It seems that it is these precipitates that may have been responsible for the marked improvement of strength after solution treatment by effectively blocking and impeding dislocation motion. The detailed

strengthening mechanisms of the microstructures developed will be discussed in the following sections.

Also, it is noted that the samples prepared under the current processing conditions all showed much better 0.2% yield strength and UTS at both room temperature and 700℃ than the property requirements (see Appendix A). For example, the samples that were HIPped at 1180℃+aged showed a proof stress around 830MPa and a UTS around 1300MPa at 700℃, which are far better than the tensile property requirements (proof stress>410MPa, UTS>560MPa). Solution treatment at 1120℃ followed by air cooling and aging treatment led to further improvement in 0.2% yield strength and UTS. The ratio of UTS of the notched samples to that of the un-notched samples is always bigger than 1.0, which thus also meets the requirement (>1.0).

7.3.3 Deformation Mechanisms

The TEM study of the deformed samples generally showed behaviour very similar to that reported in many papers of deformed Ni superalloys, with shearing and looping of γ′ precipitates. However some of the observations are inconsistent with previous reports. Thus in samples that were solution treated, most of the medium-sized tertiary γ′ (100~150nm) were found not to be cut through by dislocations whereas those much larger cuboidal secondary γ′ (350~750nm) were always sheared by dislocations. Increased precipitate size usually causes increased difficulty for dislocations to pass through the precipitates and instead Orowan loops form around them [13-17]. Deep etching of the large cuboidal secondary γ′ together with high magnification observations revealed that these precipitates actually consisted of many superfine microzones or particles with size of around 50nm (see Figure 6.8), which are smaller than the medium-sized tertiary γ′ precipitates (100~150nm). The presence of these superfine microzones or particles may be much easier for dislocations

to cut through them since the distance that a ½<110> partial dislocation would have to traverse is limited to the size of these particles rather than the size of the secondary γ′.

Another difference between current results and previous reports lies in the nature of the dislocations in deformed samples. It is generally observed that at lower temperatures, deformation is dominated by coupled a/2<110> unit dislocations shearing the γ′ precipitates, with an APB in between the coupled dislocations [13-16]. However, in the current study, coupled dislocations associated with APB were not seen and instead stacking faults were observed within the γ′ precipitates. The most obvious explanation for this observation is that the alloy has a lower stacking fault energy than other polycrystalline nickel-based superalloys. This is possible since RR 1000 was designed to produce a minimum value of stacking fault energy to promote planar slip and to inhibit cross slip which are beneficial for both crack growth rates and creep behaviour [18]. This actually can be envisaged by the highest addition of Co (which is believed to be able to reduce stacking fault energy) in RR1000, among all of the current advanced P/M superalloys; see Table 2.3. If the stacking fault energy is not significantly reduced some other factor is stabilizing the observed separation of the relevant partial dislocations. The stacking faults were observed in samples deformed to stresses above the UTS so that the partial dislocations associated with the faults were gliding under very high imposed stresses and this could lead to widely separated partials; the question is what is the factor causing the separation to be maintained when the applied stress is no longer operative? This question could perhaps be answered if detailed observations were made of the dislocations associated with the faults; it is possible that at the high stresses the operating partials interacted with other dislocations locking them so that they were unable to glide and eliminate the stacking faults.

At 700℃, deformation was mainly dominated by shearing of γ′ precipitates which led to the formation of stacking faults. Even those medium-sized tertiary γ′ in the samples that were

solution treated, which were rarely cut through by dislocations at room temperature, were found to be easily cut at 700℃ leading to well extended stacking faults. This result is consistent with many previous observations on the deformation of nickel-based superalloys at intermediate temperatures [19-23].

7.3.4 Strengthening Mechanisms

In terms of work hardening of a polycrystalline nickel-based superalloy, several strengthening mechanisms have been recognized. These include solid-solution strengthening, γ′ precipitate strengthening and grain size hardening, each of which makes different contributions to the work hardening of a material [12]. γ′ precipitate strengthening, however, usually outweighs other strengthening mechanisms for nickel-based superalloys. In the current work, since no obvious coupled dislocations associated with APB were observed, the main strengthening effect is considered to come from the shearing of γ′ by dislocations and the formation of stacking fault ribbons at this stage. When dislocations move through these stacking faults, complex interactions between dislocations and stacking faults may occur, which will further contribute to strengthening of the material. Accumulation of a/2<110> dislocations in γ channels and any process impeding the movement of these dislocations will delay deformation and thus provide another source of work hardening [24]. This is especially noticeable for the large volume fraction of medium-sized tertiary γ′ in the samples which were solution treated.

At 700℃, the strengthening mechanism could become more complex since the deformation was more planar. The presence of well extended stacking fault ribbons may cause cross slip to be more difficult. If one partial slips onto a {111} plane and then back to a plane parallel to the original slip plane the two partials are now stuck since each of them is now forced to drag out fault behind it. This leads to an increase in strengthening of the

material at elevated temperature. The motion of the partials would not happen unless the second partial also manages to cross slip to exactly the same plane. Besides, potential interactions between stacking faults may also contribute to the high temperature strengthening [24].

7.4 Conclusions

Increasing HIPping temperature was found to decrease the 0.2% yield strength at both room temperature and 700℃, which may be due to the coarsened grain size. However, the room temperature UTS and elongation show no obvious decrease with increased HIPping temperature. Moreover, increased HIPping temperature improved high temperature UTS and elongation. Samples HIPped at a sub-solvus temperature (1107℃) were found to fail in a particle-debonding mode whereas samples HIPped at a supersolvus (1180℃) failed in a dominant transgranular mode.

Changing HIPping procedure (samples HIPped at 1107℃) did not change tensile properties and fracture behaviour significantly. All the samples that were HIPped at 1107℃, irrespective of HIPping procedure, failed due to particle debonding along PPBs.

Ageing treatment was found to improve yield strength at both room temperature and 700℃ by around 50MPa, which may be due to the increased number and size of very fine γ′. Solution treatment at 1120℃ followed by air cooling and ageing treatment led to considerable improvement in both 0.2% yield strength and UTS while maintaining a good ductility. This is believed to be due to the formation of medium-sized tertiary γ′ which could effectively impede dislocation motion. Increasing solution temperature from 1120℃ to 1160℃ was found to show no great change in tensile properties. The samples prepared under the current processing conditions were all shown to meet the tensile property requirements.

Deformation of samples at room temperature mainly occurred via slip of dislocations through both secondary γ′ and the very fine γ′ and the formation of stacking faults in these precipitates. Deformation at 700℃ was due to the formation of extended stacking faults across both γ and γ′. Plain samples (those HIPped at 1180℃ and then heat treated) mainly failed in a cleavage mode while notched samples were often found to fail at the sites of large inclusion clusters. Crack propagation basically followed a transgranular fracture mode.

References

[1] Mitchell RJ. Development of a new powder processed Ni-base superalloy for rotor disc application, PhD thesis, University of Cambridge, 2004.

[2] Hertzberg RW. Deformation and fracture mechanics of engineering materials, second edition. USA: John Willey & Sons, Inc; 1983.p. 248-300

[3] Rao GA, Srinivas M, Sarma DS. Effect of oxygen content of powder on microstructure and mechanical properties of hot isostatically pressed superalloy Inconel 718. Materials Science and Engineering A 2006; 435-436: 84-89.

[4] Williams DL. Hot isostatically pressed alloy APK1, a nickel-based superalloy. Powder Metallurgy 1977; 2: 84-89

[5] Rao GA, Kumar M, Sarma DS. Effect of solution treatment temperature on microstructure and mechanical properties of hot isostatically pressed superalloy Inconel 718. Materials Science and Technology 2004;20:1161-1170.

[6] Radavich J, Furrer D. Assessment of Russian P/M superalloy EP741NP. In: Green KA, Pollock TM, Harada H, editors: Superalloys 2004. Warrendale, PA: The Minerals, Metals and Materials Society (TMS); 2004. p. 381-390.

[7] Rao GA, Kumar M, Srinivas M, Sarma DS. Effect of standard heat treatment on the microstructure and mechanical properties of hot isostatically pressed superalloy inconel 718. Materials Science and Engineering A 2003;355:114-125.

[8] Pope DP, Ezz SS. Mechanical properties of Ni_3Al and nickel-base alloys with high volume fraction of gamma-prime. International Metals Review 1984; 29:136-167.

[9] Mao J, Chang KM, Yang W, Ray K, Vaze SP, Furrer DU. Cooling precipitation and strengthening study in powder metallurgy superalloy U720LI. Metallurgical and Materials Transactions A 2001;32: 2441–2452.

[10] Mao J, Chang KM, Yang W, Furrer DU, Ray K, Vaze SP. Cooling precipitation and strengthening study in powder metallurgy superalloy Rene88DT. Materials Science and Engineering A 2002;332: 318–329.

[11] Jackson MP, Reed RC. Heat treatment of UDIMET 720Li: the effect of microstructure on properties. Materials Science and Engineering A 1999;259:85–97

[12] Kozar RW, Suzuki A, Milligan WW, Schirra JJ, Savage MF, Pollock TM. Strengthening mechanisms in polycrystalline multimodal nickel-base superalloys. Metallurgical and Materials Transactions A 2009; 40: 1588-1603.

[13] Reppich B. Some new aspects concerning particle hardening mechanisms in γ′ precipitating Ni-base alloys-I Theoretical concept. Acta Metallurgica 1982;30:87-94.
[14] Reppich B, Schepp P, Wehner G. Some new aspects concerning particle hardening mechanisms in γ′ precipitating Ni-base alloys-II Experiments. Acta Metallurgica 1982;30: 95-104.
[15] Nembach E, Suzuki K, Ichihara M, Takeuchi S. In-situ deformation of the gamma prime hardened superalloy Nimonic PE 16 in high-voltage electron microscopes. Philosophical Magazine A 1985;51:607-618.
[16] Sun YQ, Hazzledine PM. A TEM weak-beam study of dislocations in γ' in a deformed Ni-based superalloy. Philosophical Magazine A 1988;58:603-617.
[17] Sims CT, Stoloff NS, Hagel WC, editors. Superalloys, 2nd. New York, USA: John Wiley & Sons; 1987. p.69-78.
[18] Hardy MC, Zirbel B, Shen G, Shankar R. Developing damage tolerance and creep resistance in a high strength nickel alloy for disc applications. In: Green KA, Pollock TM, Harada H, editors: Superalloys 2004. Warrendale, PA: The Minerals, Metals and Materials Society (TMS); 2004. p. 83-90.
[19] Leverant GR, Kear BH. The mechanism of creep in gamma prime precipitation hardened nickel-base alloys at intermediate temperatures. Metallurgical Transactions A 1973;1: 491-498.
[20] Decamps B, Rajoul S, Coujou A, Pettinari-Sturmel F, Clement N, Locq D, Caron P. On the shearing mechanism of γ′ precipitates by a single (a/6)<112> Shockley partial in Ni-based superalloys. Philosophical Magazine A 2004;84:91-107.
[21] Chen QZ, Knowles DM. Mechanism of <112>/3 slip initiation and anisotropy of γ' phase in CMSX-4 during creep at 750 °C and 750 MPa**.** Materials Science and Engineering A 2003;356:352-367.
[22] Milligan WW, Antolovich SD. The mechanisms and temperature dependence of superlattice stacking fault formation in the single-crystal superalloy PWA 1480. Metallurgical and Materials Transactions A 1991;22:2309-2318.
[23] Viswanathan GB, Sarosi PM, Henry MF, Whitis DD, Milligan WW, Mills MJ. Investigation of creep deformation mechanisms at intermediate temperatures in René 88 DT. Acta Materialia 2005;53:3041-3057.
[24] Rae CMF, Reed RC. Primary creep in single crystal superalloys: origins, mechanisms and effects. Acta Materialia 2007; 55: 1067–1081.

Table 7.1 The tensile properties of samples obtained from different processing conditions and tested at different temperatures

Testing temperatures	Processing Conditions	$\sigma_{0.2}$ (MPa)	UTS (MPa)	Elongation (%)
Room temperature	HIP 1107℃/100MPa/4h	968 971	1463 1448	28 25
	Temperature first, pressure later + HIP 1107℃/100MPa/2h	947 936 944	1449 1421 1448	29 25 30
	HIP 1180℃/150MPa/4h	871 873	1429 1430	31 29
750℃	HIP 1107℃/100MPa/4h Tested at 750℃	1030 1072	1180 1207	6.7 7.8
	Temperature first, pressure later Tested at 750℃	1062 1050	1191 1230	10 13.4
700℃	HIP 1107℃/100MPa/4h Tested at 700℃	960 957	1060 1065	8.7 9.0
	HIP 1180℃/150MPa/4h Tested at 700℃	772 775	1305 1310	34 30

Table 7.2 The tensile properties of the samples obtained under different processing conditions after testing at room temperature and 700℃

Type of testpiece	Conditions	Room Temperature			700°C		
		$\sigma_{0.2}$ (MPa)	UTS (MPa)	Elongation (%)	$\sigma_{0.2}$ (MPa)	UTS (MPa)	Elongation (%)
Plain	HIP1180℃/150MPa/4h	871 873	1429 1430	31 29	772 775	1305 1310	34 30
	HIP1180℃/150MPa/4h + Aged 760℃/16h/AC	925 922	1474 1470	24 25	827 835	1304 1308	35 30
	HIP 1180℃/150MPa/4h + ST 1120℃/2h/AC + Aged 760℃/16h/AC	1070 1072	1580 1589	25 24	975 982	1473 1476	25 24
	HIP 1180℃/150MPa/4h + ST 1160℃/2h/AC + Aged 760℃/16h/AC	1072 1075	1567 1573	20 22	972 963	1466 1453	17.5 22
	HIP 1107℃/100MPa/4h + Extruded + ST 1125℃/4h/AC+ Aged 760℃/16h/AC [1]	1075	1575	≥10	980	1300	≥10
Notched (Kt=3.1)	HIP1180℃/150MPa/4h + Aged 760℃/16h/AC		1652 1658 1665			1668 1633 1613	
	HIP1180℃/150MPa/4h + ST 1120℃/2h/AC + Aged 760℃/16h/AC		1872 1856 1874			1766 1797 1711	

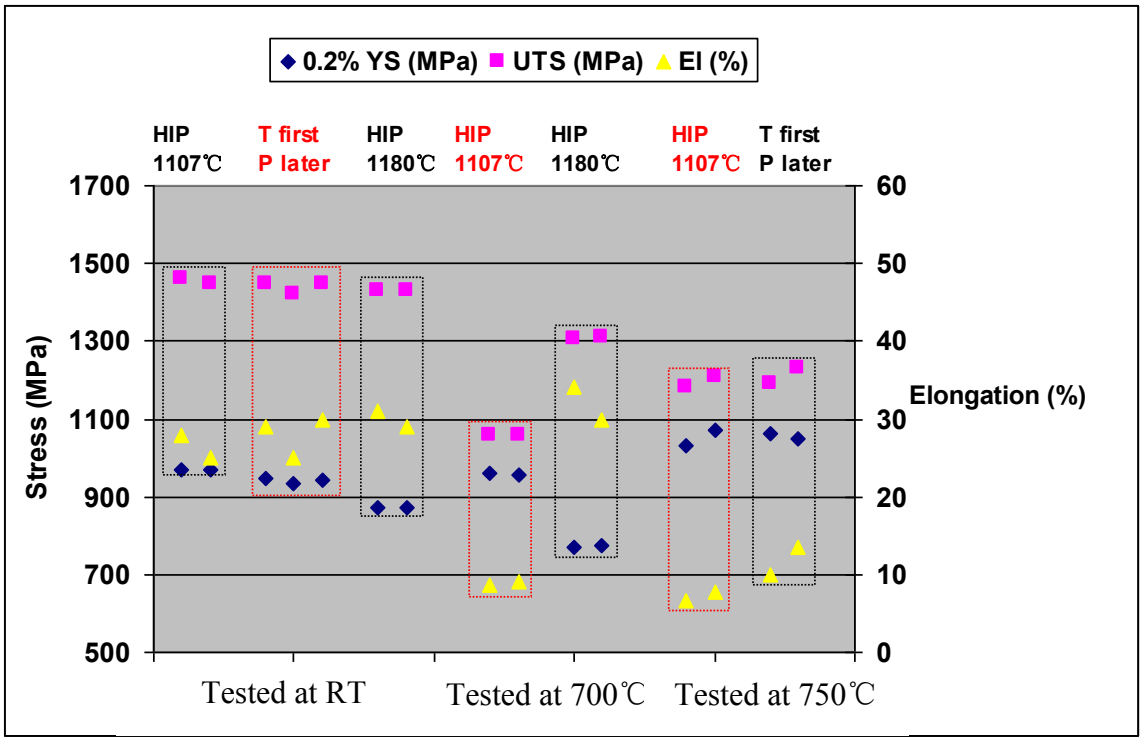

Figure 7.1 Tensile properties of RR 1000 samples HIPped at different temperatures and procedures and tested at different temperatures, YS referring to yield strength, UTS to ultimate tensile strength and El to elongation. RT represents room temperature and T first P later means that temperature was ramped first and pressure later followed by holding at 1107℃/100MPa/2h. For the other two HIPping conditions, temperature and pressure were ramped up together to designated levels, e.g., HIP 1107℃-HIP 1107℃/100MPa/4h; HIP 1180℃-HIP 1180℃/150MPa/4h.

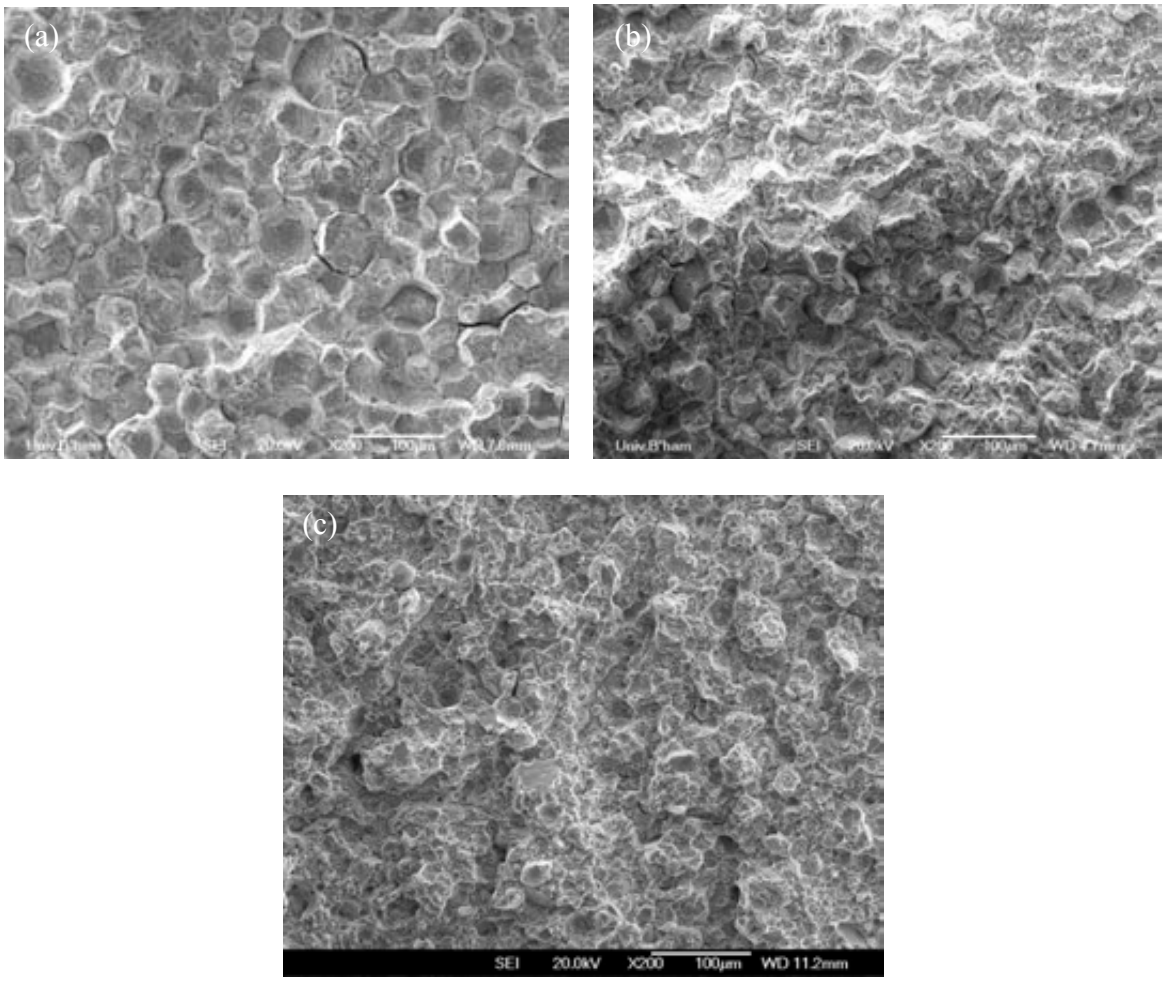

Figure 7.2 Secondary electron SEM micrographs showing the fracture surfaces of RR 1000 samples after room temperature tensile testing (a) HIP 1107℃/100MPa/4h; (b) ramping temperature first and then pressure, to 1107℃/100MPa/2h; (c) HIP 1180℃/150MPa/4h.

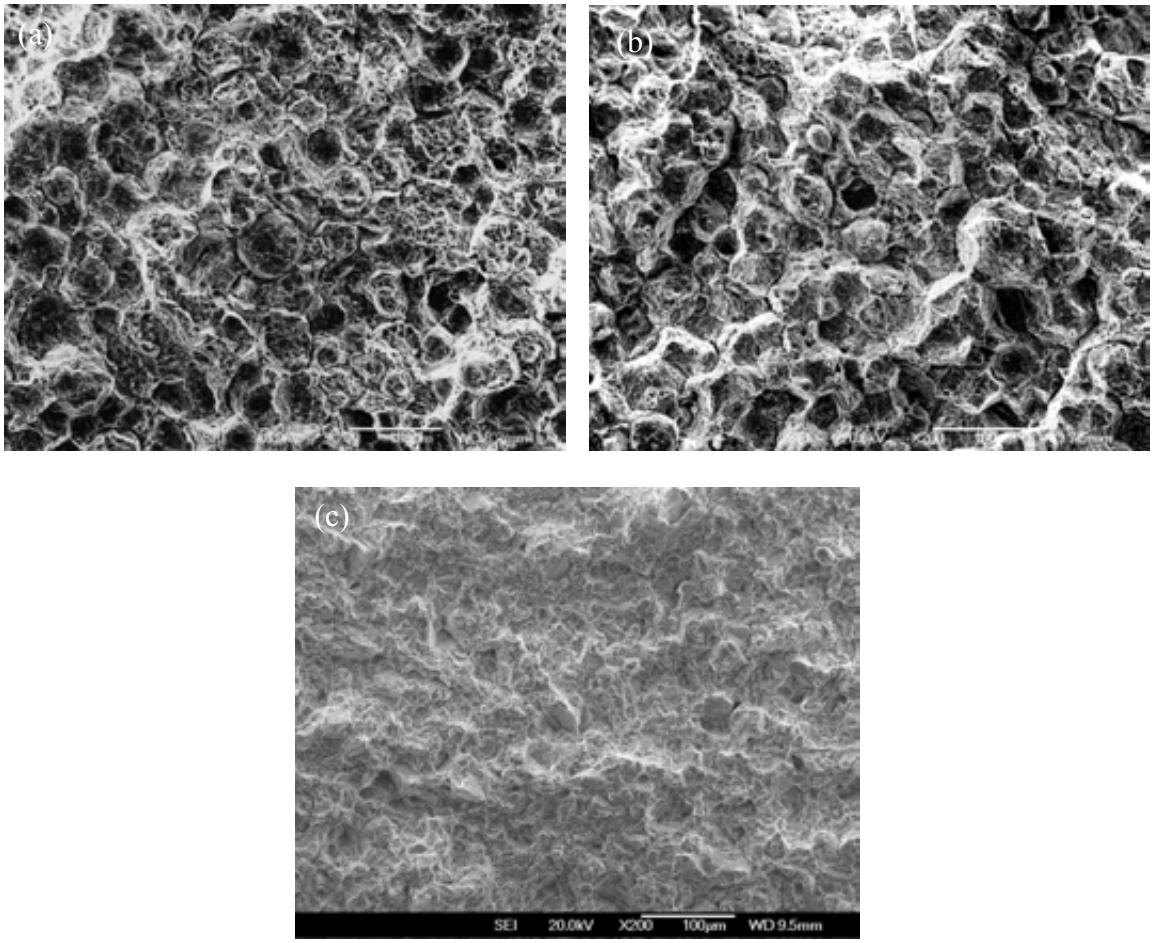

Figure 7.3 Secondary electron SEM micrographs showing the fracture surfaces of RR 1000 samples after testing at 700℃, (a) HIP 1107℃/100MPa/4h; (b) ramping temperature first and then pressure, to 1107℃/100MPa/2h; (c) HIP 1180℃/150MPa/4h.

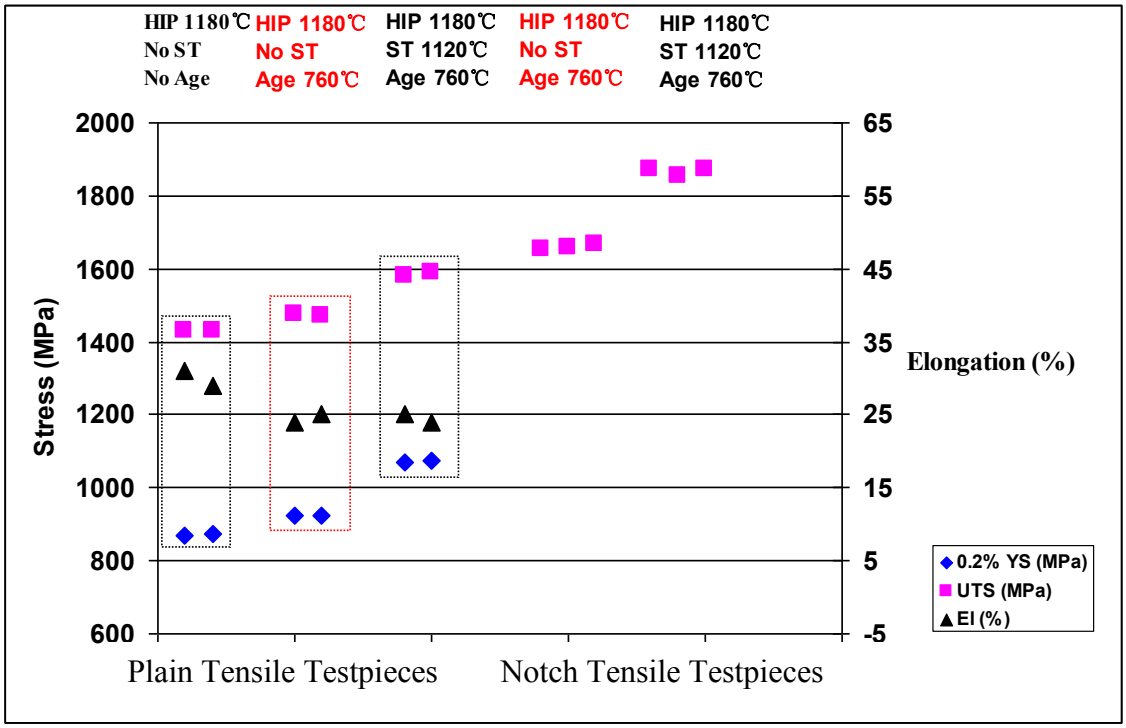

Figure 7.4 Room temperature tensile properties of plain and notched RR 1000 samples with or without heat treatment, YS referring to yield strength, UTS to ultimate tensile strength and El to elongation.

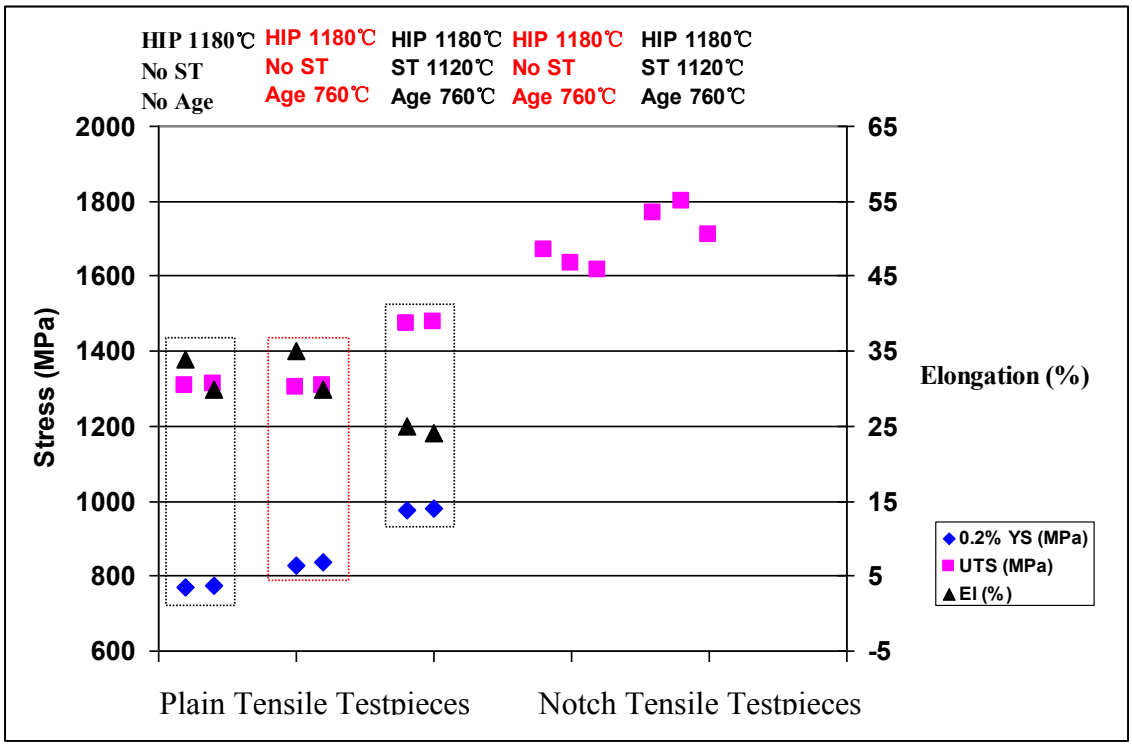

Figure 7.5 Tensile properties of RR 1000 samples with or without heat treatment, tested at 700℃, YS referring to yield strength, UTS to ultimate tensile strength and El to elongation.

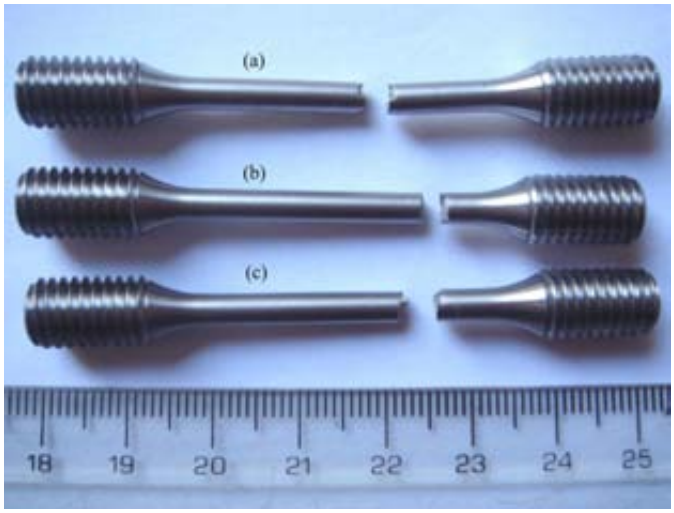

Figure 7.6 Photograph showing the geometry of the failed RR 1000 tensile test pieces after room temperature tensile testing, (a) HIPped at 1180℃/150MPa/4h; (b) HIPped at 1180℃/150MPa/4h + aged at 760℃/16h/AC; (c) HIP1180℃/150MPa/4h + Solution treated at 1120℃/2h/AC+ Aged at 760℃/16h/AC

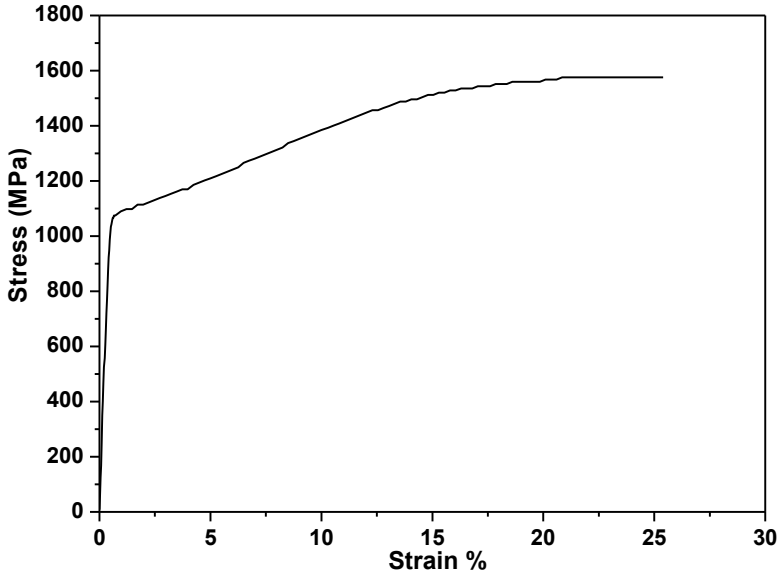

Figure 7.7 A typical room temperature tensile stress-strain curve for RR 1000 as-HIPped and heat treated samples.

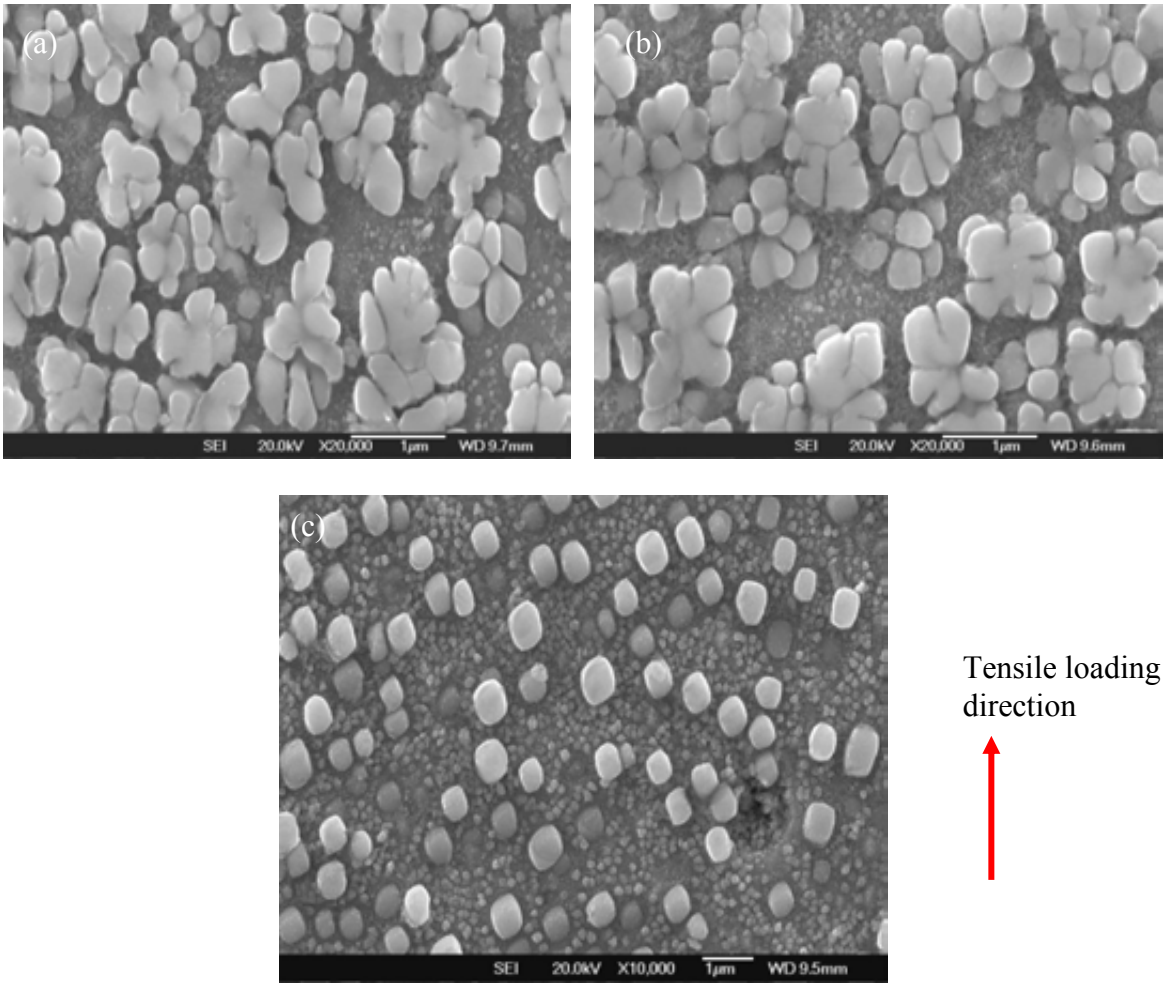

Figure 7.8 Secondary electron SEM micrographs showing that secondary γ′ irrespective of morphologies have been uniformly elongated along axial tensile direction, (a) HIPped at 1180℃/150MPa/4h; (b) HIPped at 1180℃/150MPa/4h + aged at 760℃/16h/AC; (c) HIP1180℃/150MPa/4h + Solution treated at 1120℃/2h/AC+ Aged at 760℃/16h/AC

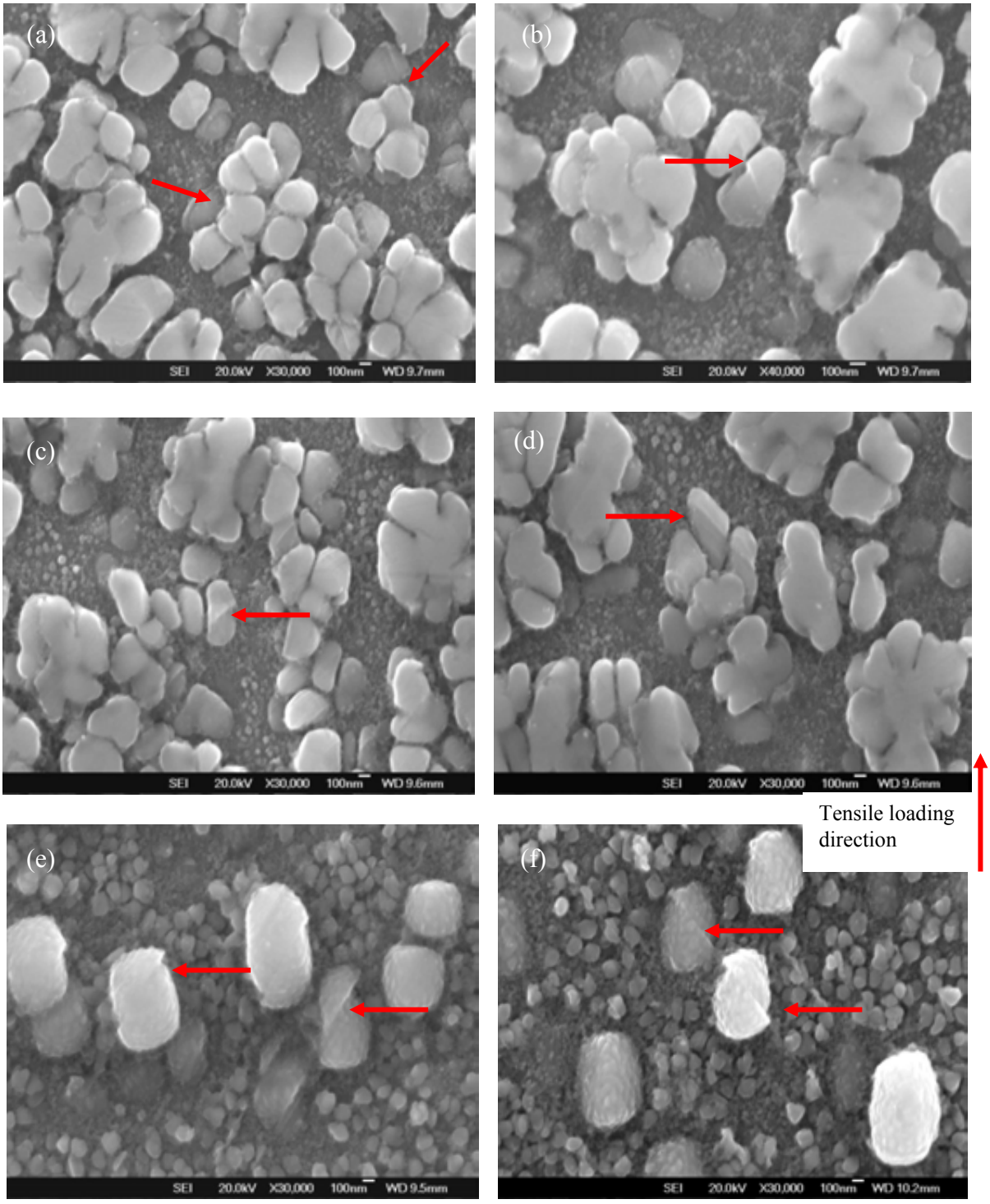

Figure 7.9 Secondary electron SEM micrographs showing the pronounced shearing of secondary γ′ precipitates in RR 1000, see arrows, (a)(b) HIPped at 1180℃/150MPa/4h/FC (see red arrows); (c)(d) HIPped at 1180℃/150MPa/4h/FC + aged at 760℃/16h/AC (see red arrows); (e)(f) HIPped at 1180℃/150MPa/4h/FC + Solution treated at 1120℃/2h/AC+ Aged at 760℃/16h/AC.

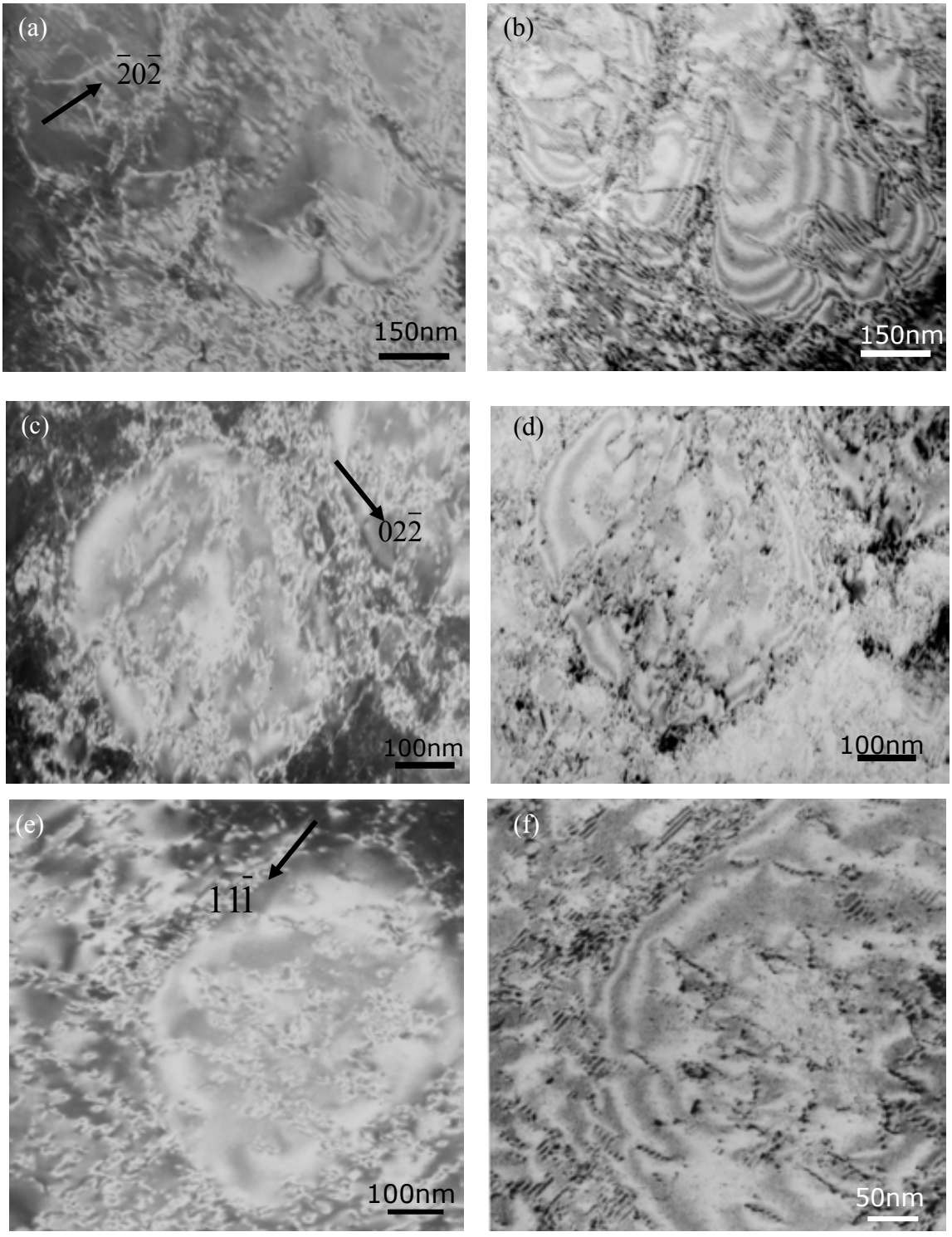

Figure 7.10 TEM bright-field images and weak-beam dark-field images showing the dislocation structures and stacking faults in secondary γ′ in the room temperature tensile tested samples, (a)(b) HIPped at 1180℃/150MPa/4h/FC + aged at 760℃/16h/AC; (c)-(f) HIPped at 1180℃/150MPa/4h/FC + Solution treated at 1120℃/2h/AC+ Aged at 760℃/16h/AC.

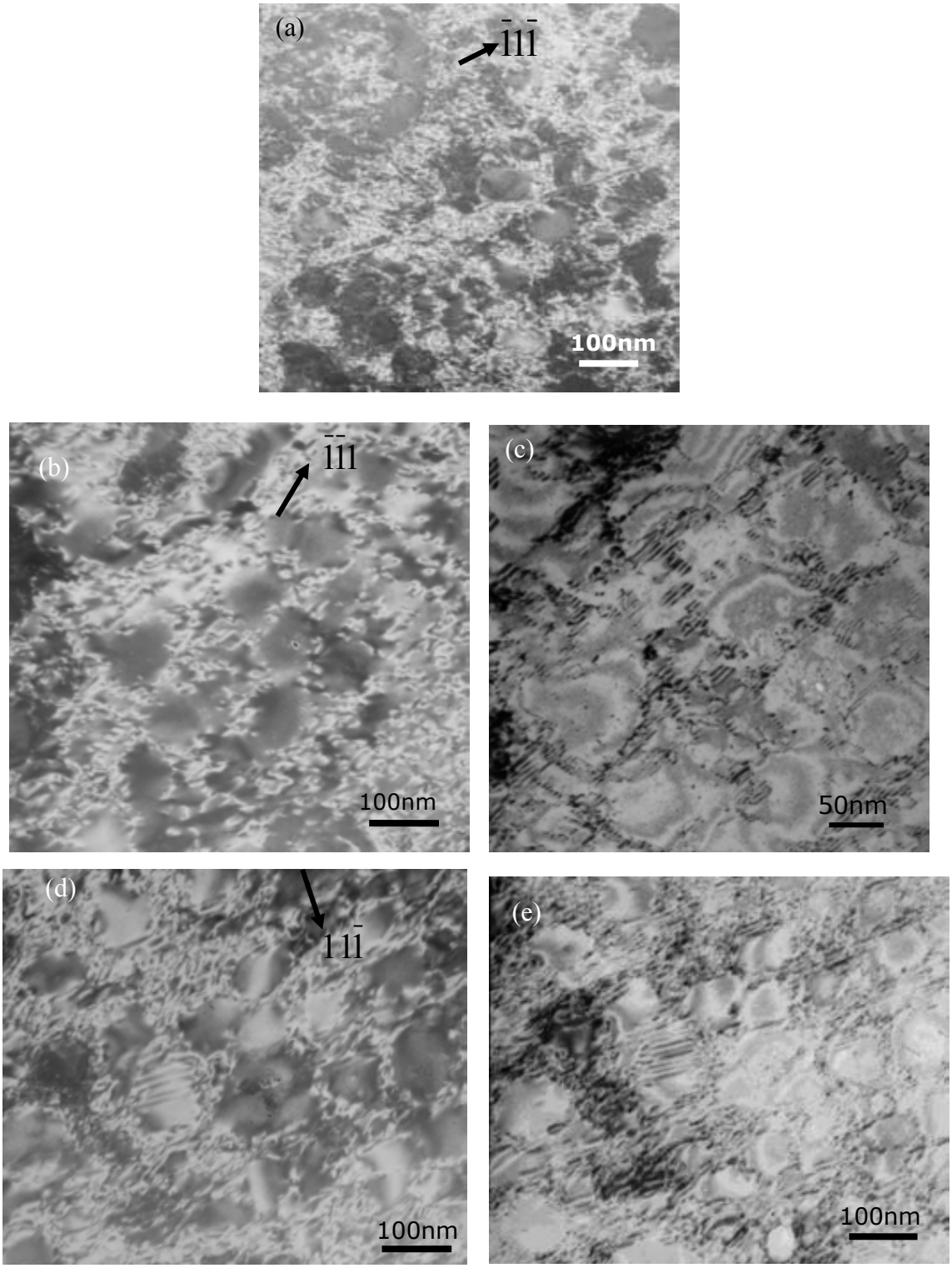

Figure 7.11 (a)(b)(d)TEM bright-field images under two-beam condition and (c)(e)weak-beam dark-field images showing dislocation structures of medium-sized tertiary γ′ in samples that were HIPped at 1180℃/150MPa/4h/FC + Solution treated at 1120℃/2h/AC+ Aged at 760℃/16h/AC, and tensile tested at tested at room temperature.

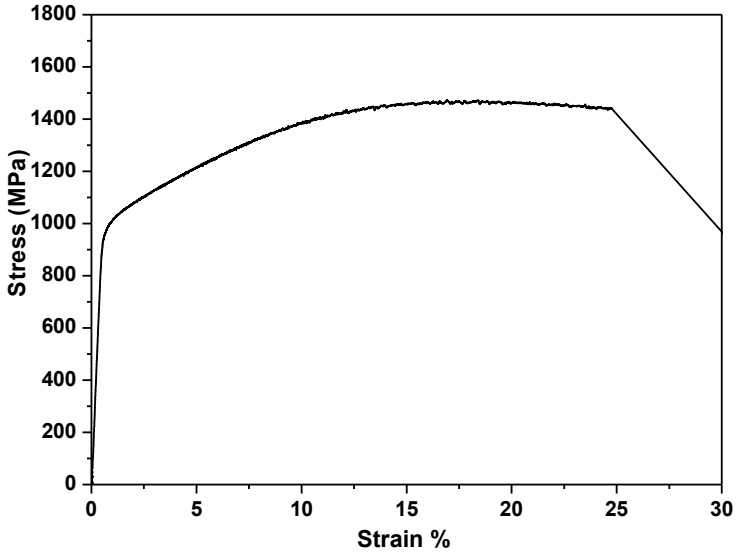

Figure 7.12 A typical tensile stress-strain curve for as-HIPped and heat treated RR 1000 samples after tensile testing at 700℃

Figure 7.13 Photograph showing the geometry of the failed RR 1000 tensile test pieces after tensile testing at 700℃, (a) HIPped at 1180℃/150MPa/4h; (b) HIPped at 1180℃/150MPa/4h + aged at 760℃/16h/AC; (c) HIP1180℃/150MPa/4h + Solution treated at 1120℃/2h/AC+ Aged at 760℃/16h/AC

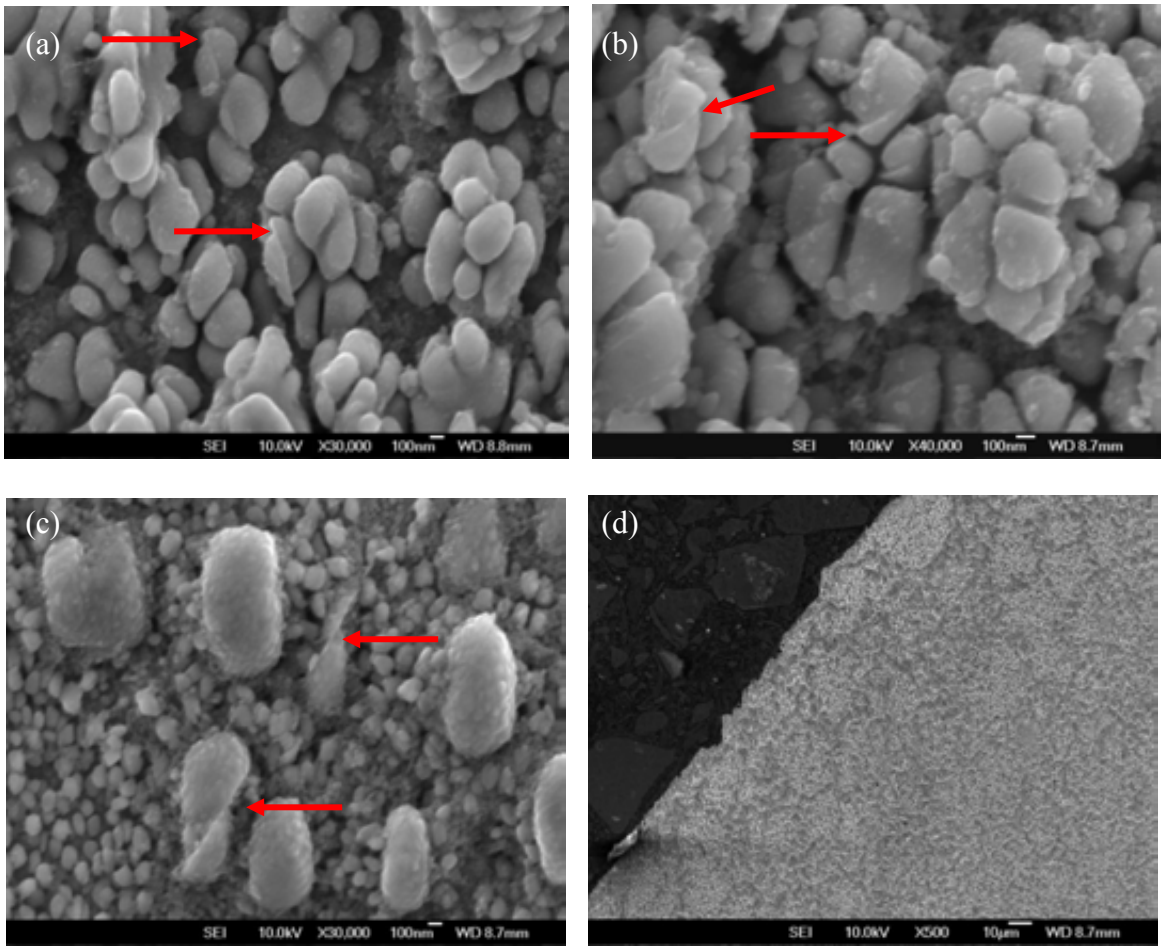

Figure 7.14 Secondary electron SEM micrographs showing the pronounced shearing (see red arrows) of secondary γ′ precipitates in RR 1000 samples after tensile testing at 700℃, (a) HIPped at 1180℃/150MPa/4h/FC; (b)HIPped at 1180℃/150MPa/4h/FC+aged at 760℃/16h/AC; (c)HIPped at 1180℃/150MPa/4h/FC + Solution treated at 1120℃/2h/AC+ Aged at 760℃/16h/AC; (d)widespread pronounced shearing of γ′ could be observed especially at the area adjacent to the slant fracture surface.

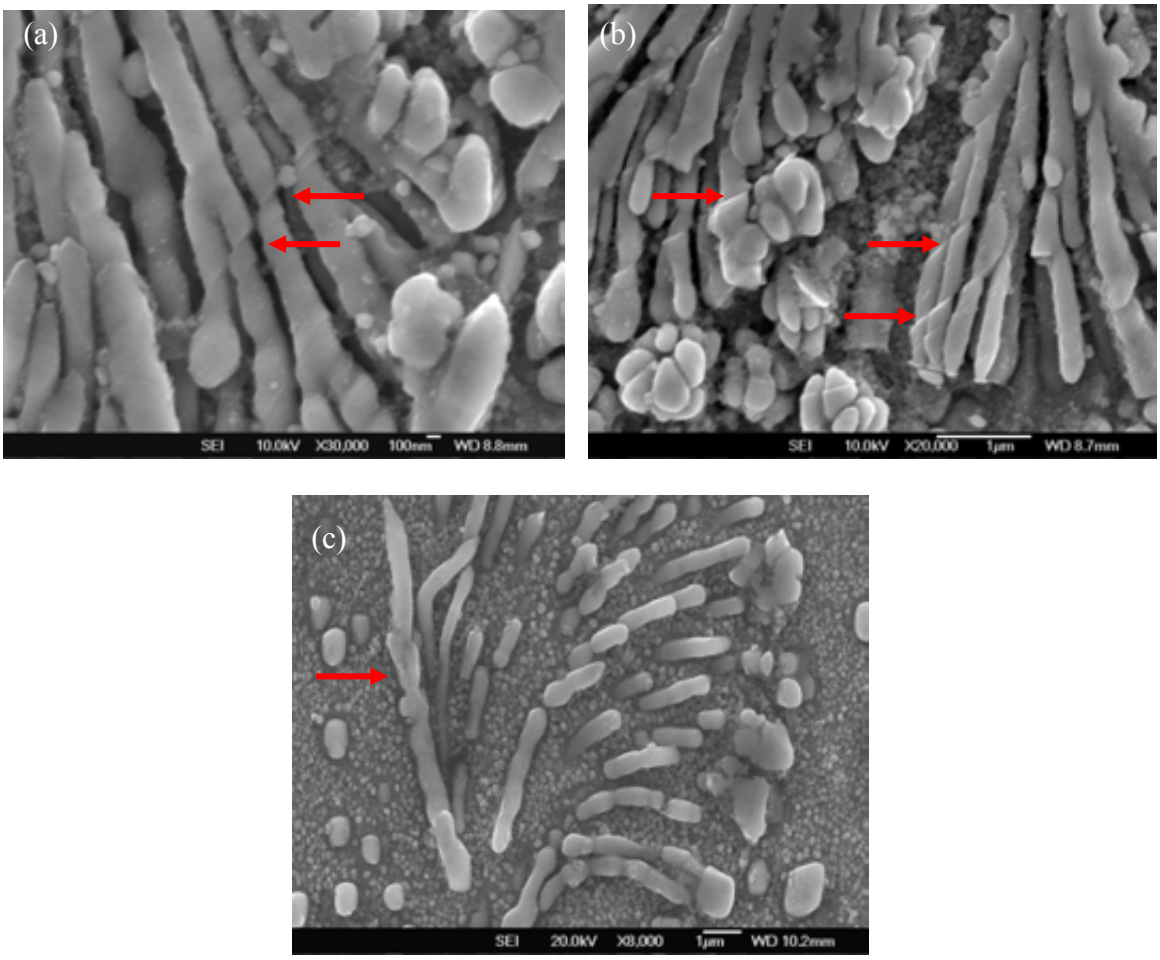

Figure 7.15 Secondary electron SEM micrographs showing the pronounced shearing (see red arrows) of γ′ rods in the fan-type γ′ structure in RR 1000 samples after tensile testing at 700℃, (a) HIPped at 1180℃/150MPa/4h/FC; (b) HIPped at 1180℃/150MPa/4h/FC + aged at 760℃/16h/AC; (c) HIPped at 1180℃/150MPa/4h/FC + Solution treated at 1120℃/2h/AC+ Aged at 760℃/16h/AC.

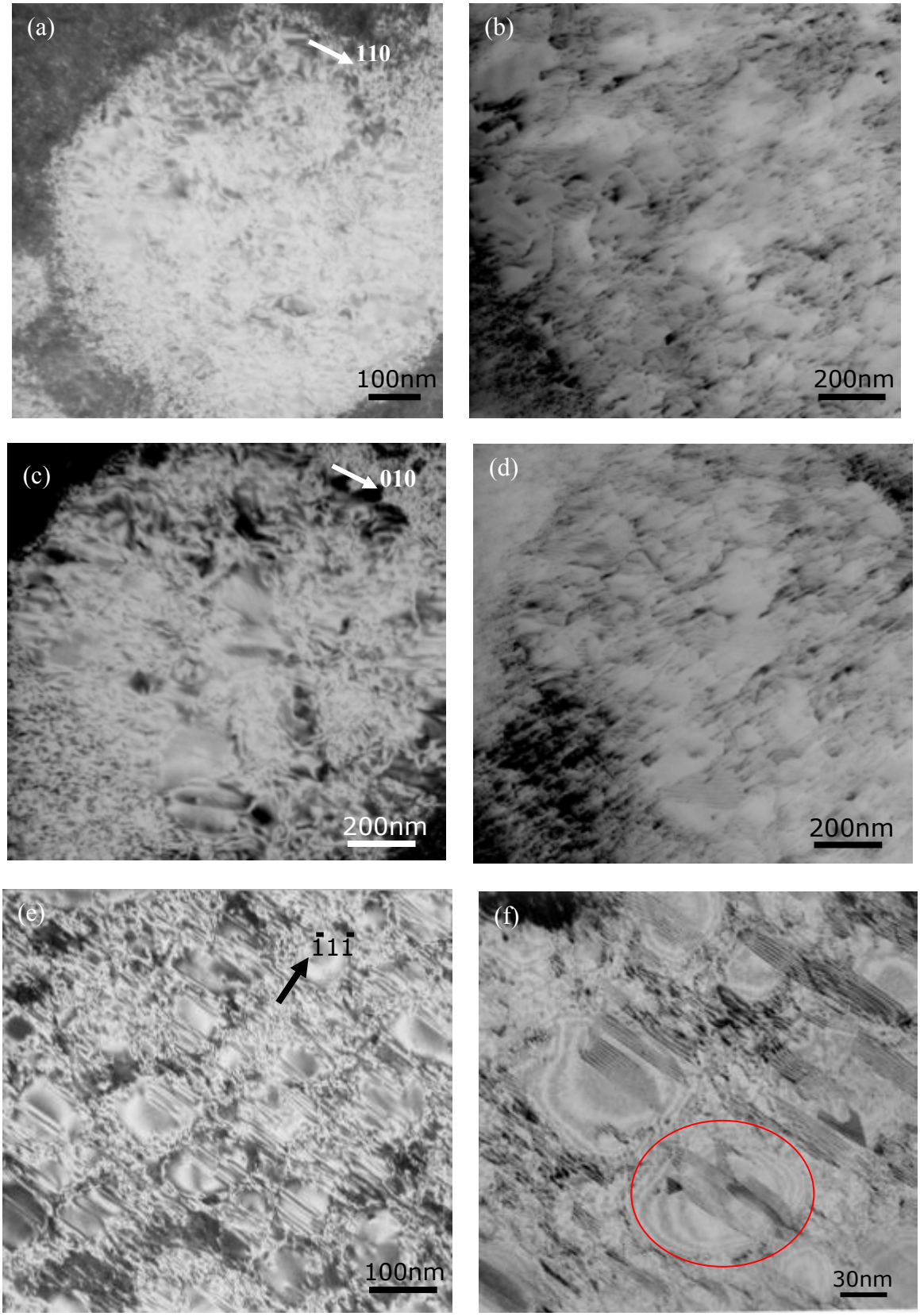

Figure 7.16 (a)(c)(e)TEM bright-field images and (b)(d)(f)weak-beam dark-field images showing the dislocation structures in (a-d) secondary γ′ and (e-f) tertiary γ′ in the samples that were HIPped at 1180℃/150MPa/4h/FC + Solution treated at 1120℃/2h/AC+ Aged at 760℃/16h/AC, and tensile tested at 700℃.

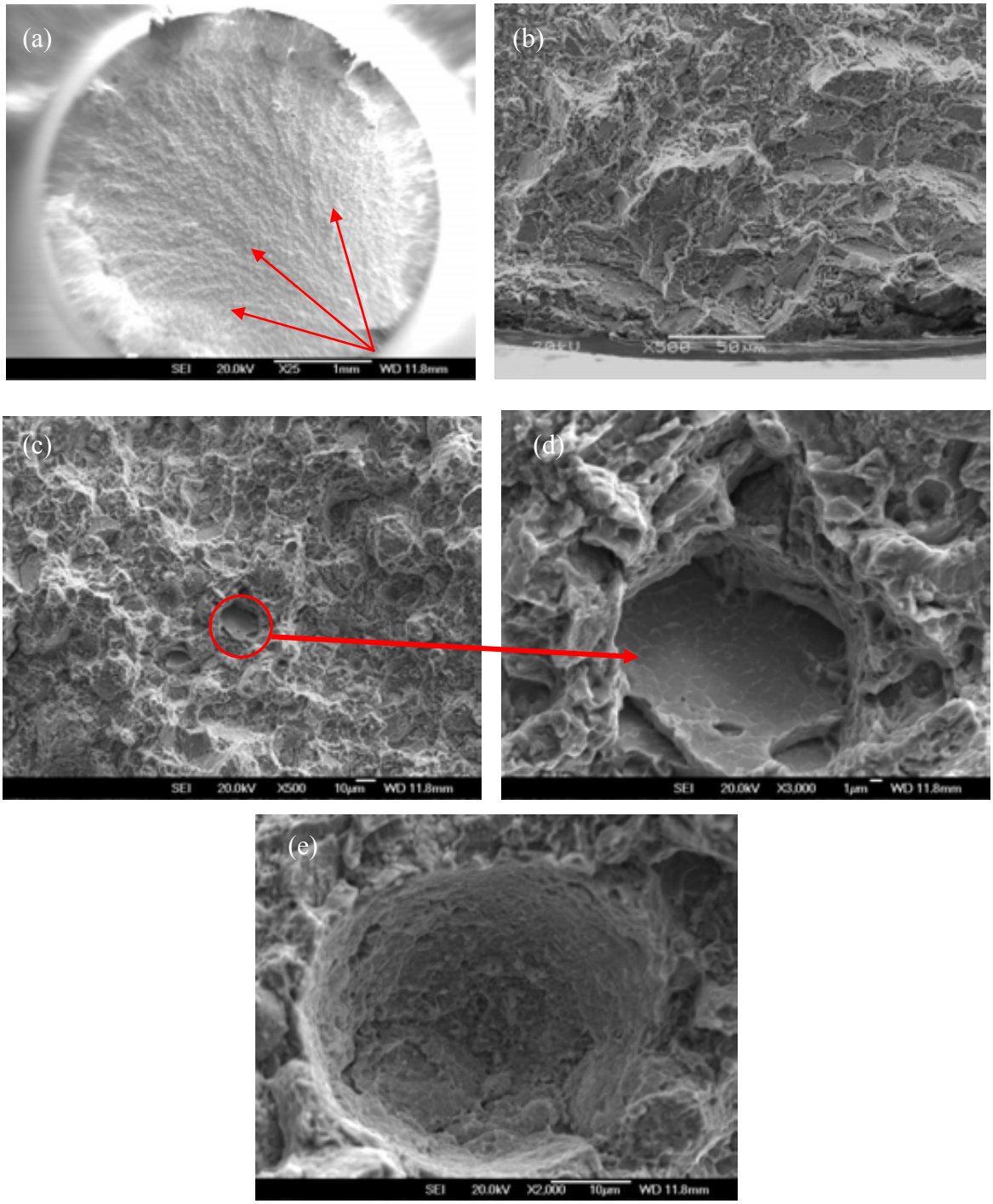

Figure 7.17 Secondary electron SEM micrographs showing the fracture surface of RR 1000 samples after tensile testing at room temperature, (a) chevron-shaped markings disperse from the sample surface; (b)crack initiation by cleavage of the matrix alloy from the sample surface; (c)crack propagation generally in a transgranular fracture mode; (d) a few facets observed; (e) voids due to crack propagation along PPBs. The sample shown here was HIPped at 1180℃/150MPa/4h + aged at 760℃/16h/AC.

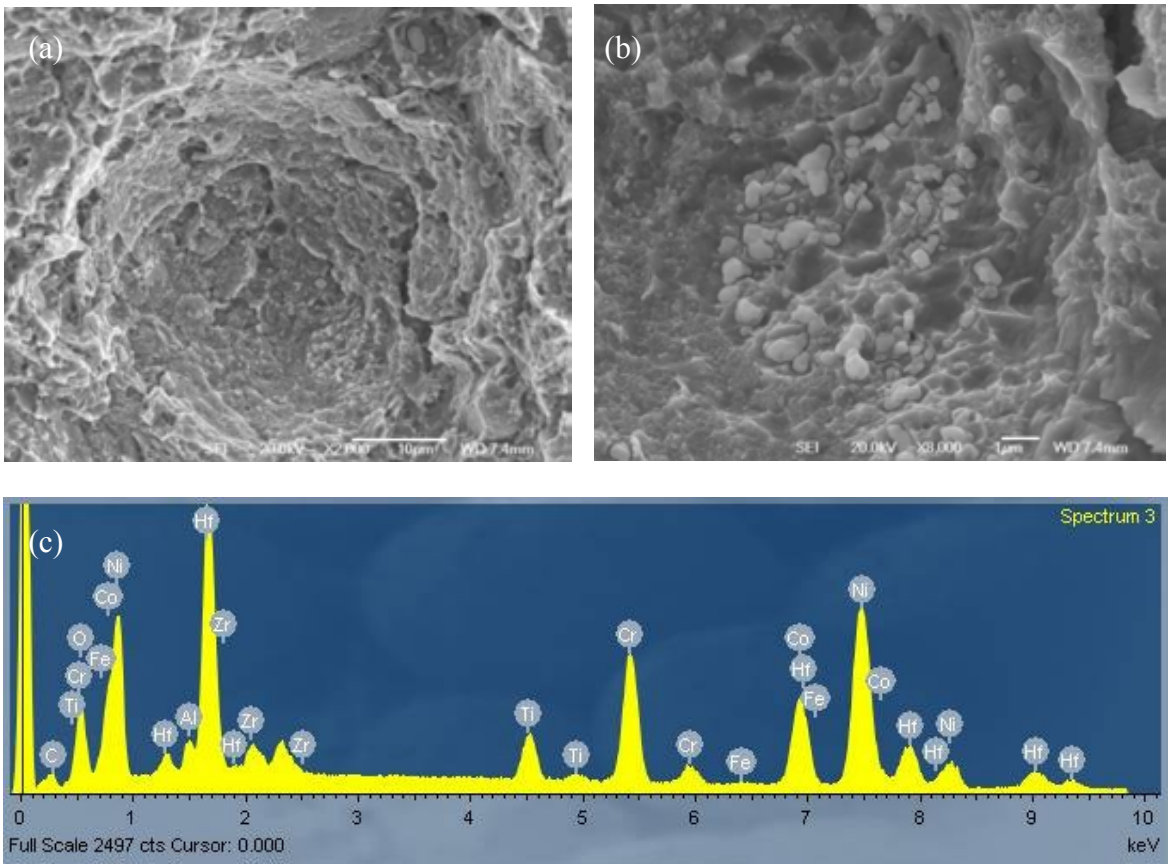

Figure 7.18 (a, b) Secondary electron SEM micrographs showing the inclusions-induced holes after room temperature tensile testing and (c) the EDX analysis showing the compositions of the inclusions, basically indentified to be (Hf, Zr)-rich oxides. The sample shown here was HIPped at 1180℃/150MPa/4h/FC + Solution treated at 1120℃/2h/AC+ Aged at 760℃/16h/AC.

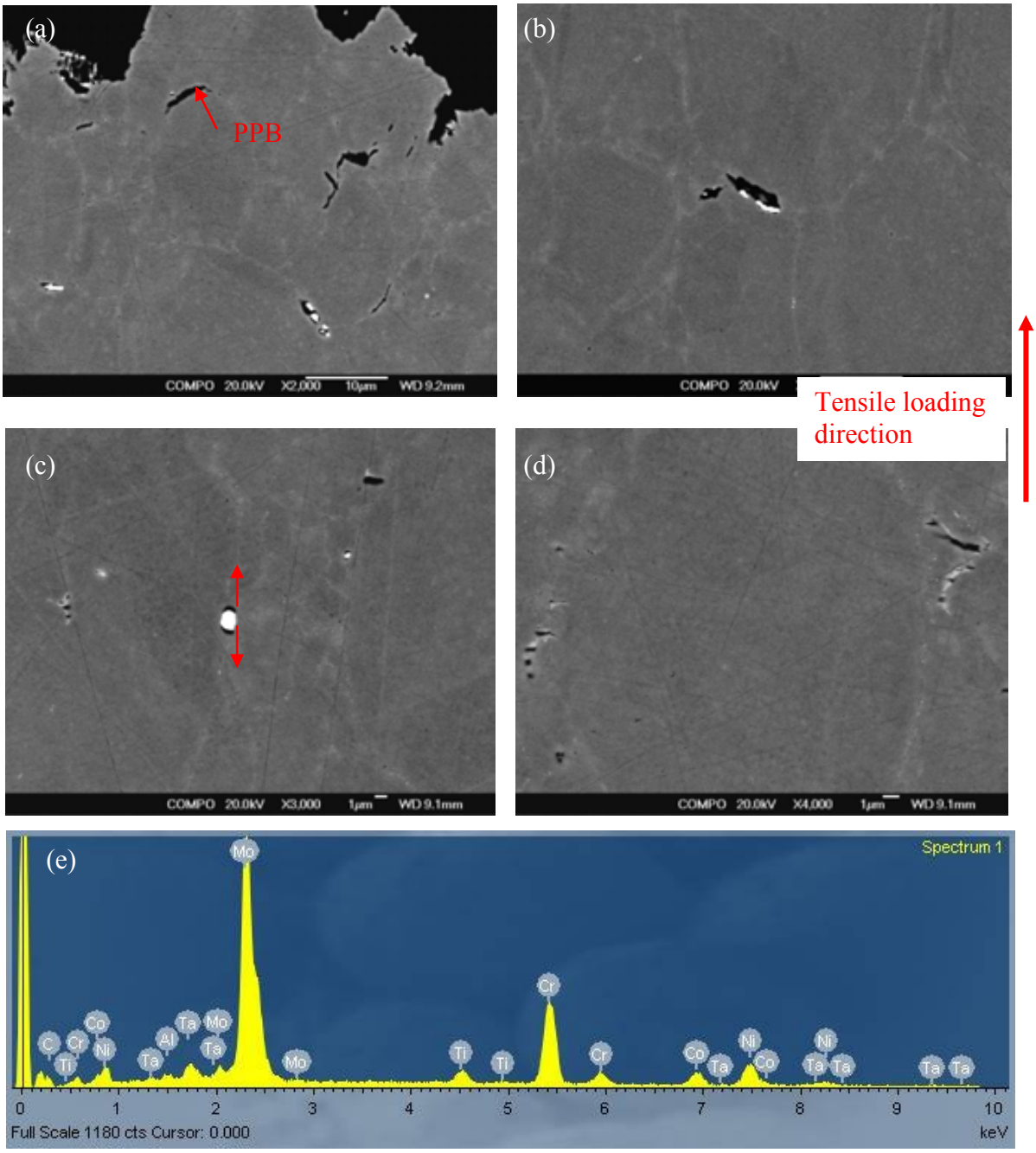

Figure 7.19 (a)-(d) Back scattered SEM micrographs showing secondary cracks initiating at inclusion particles in the section of RR 1000 samples after room temperature tensile testing; (e) EDX analysis showing the composition of script precipitates in Figure 7.19 (d) to be rich of Mo and Cr. The sample tested here was HIPped at 1180℃/150MPa/4h/FC + Solution treated at 1120℃/2h/AC+ Aged at 760℃/16h/AC. This sort of section feature after room temperature tensile testing was also observed in other samples, irrespective of processing condition.

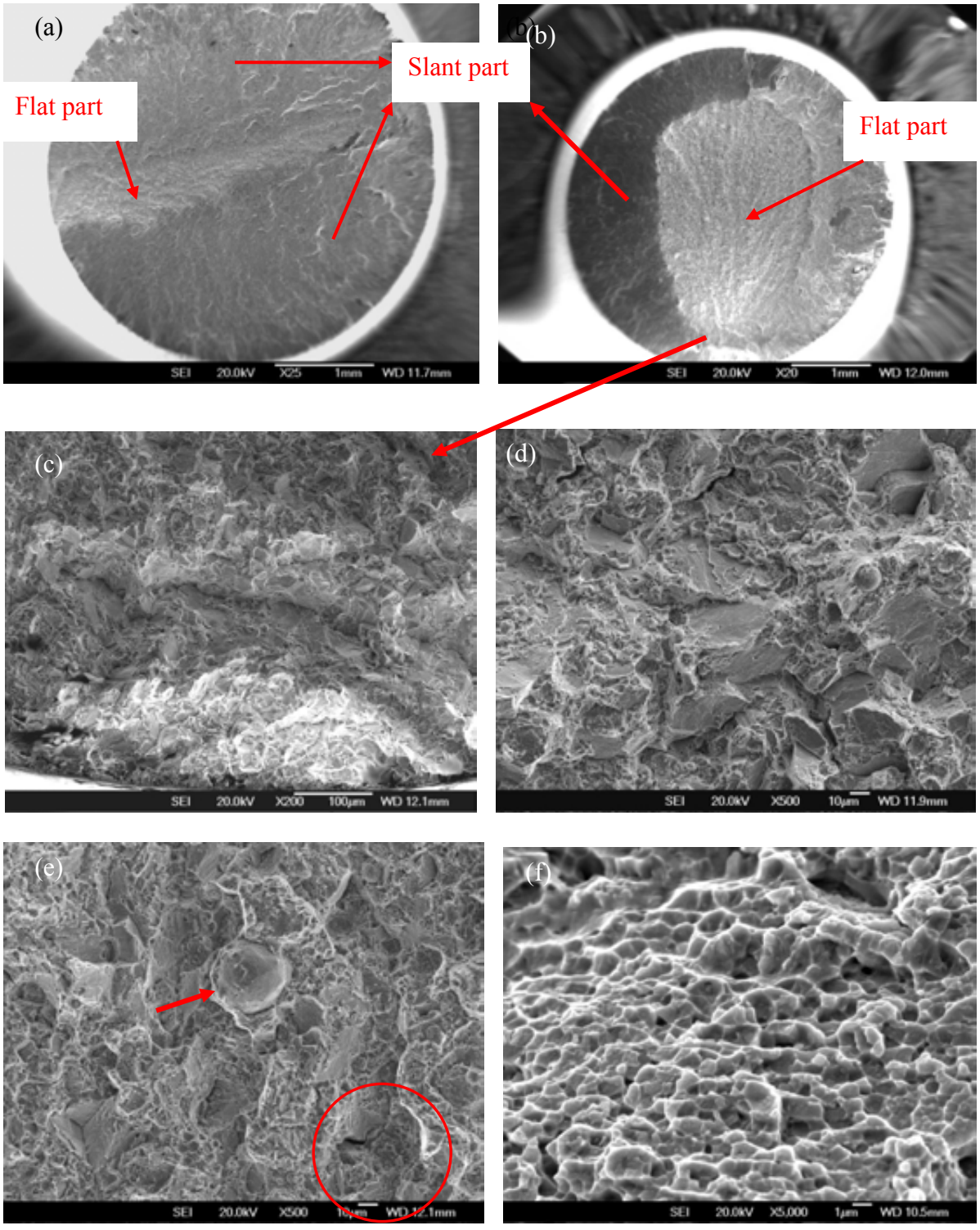

Figure 7.20 Secondary electron SEM micrographs showing fracture surface of RR 1000 sample after tensile testing at 700℃, (a)(b)slant part and flat part on the fracture surface; (c) crack initiation in a cleavage mode; (d) crack propagation in a highly crystallographic and faceted mode; (e) occasional inter-particle debonding along PPBs; (f) ductile dimple fracture on the slant part, the sample shown here was HIPped at 1180℃/150MPa/4h + Solution treated at 1120℃/2h/AC+ Aged at 760℃/16h/AC

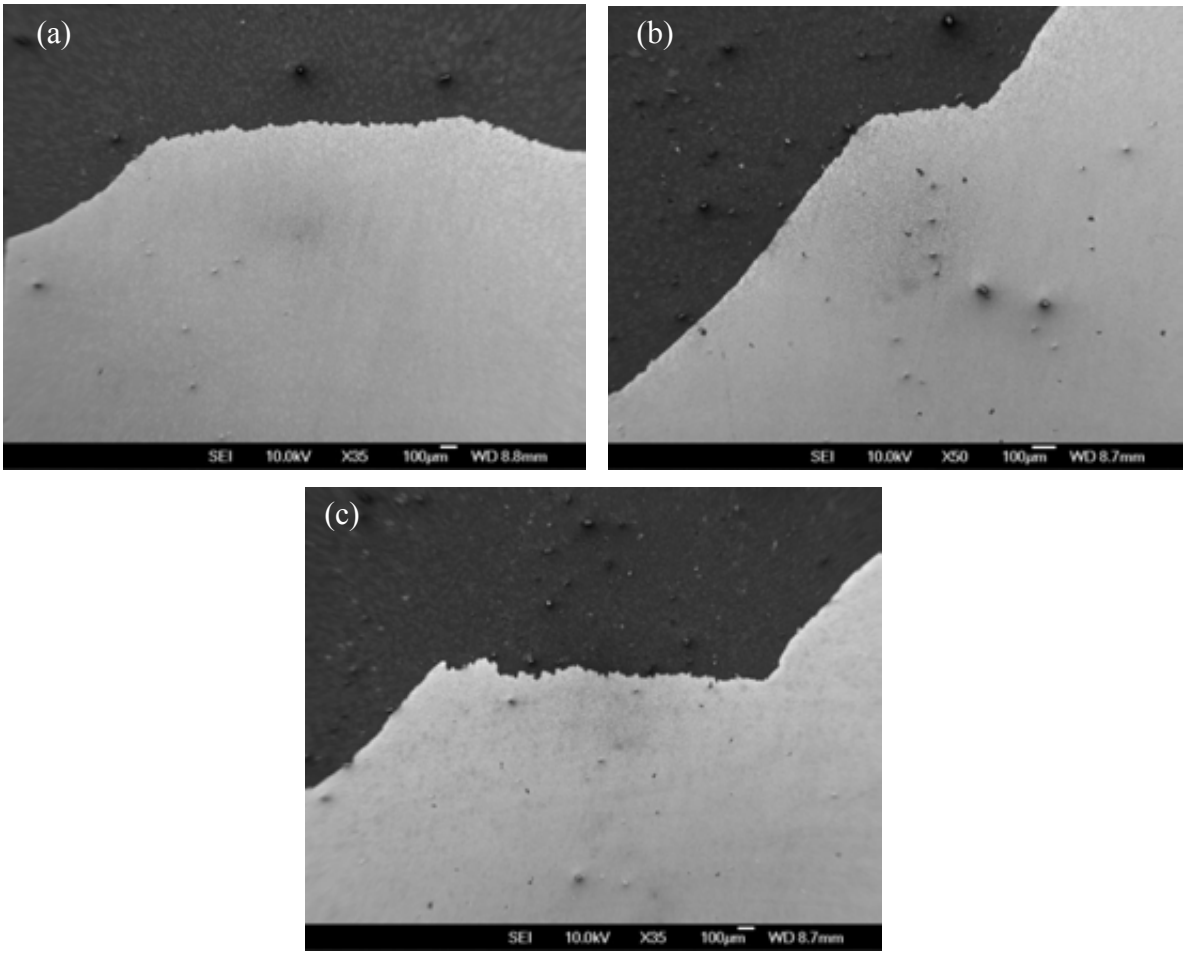

Figure 7.21 Secondary electron SEM micrographs showing the section of samples after tensile testing at 700℃which reveals a combination of flat and slant fracture features, (a) HIPped at 1180℃/150MPa/4h; (b) HIPped at 1180℃/150MPa/4h + Aged at 760℃/16h/AC; (c) HIPped at 1180℃/150MPa/4h + Solution treated at 1120℃/2h/AC+ Aged at 760℃/16h/AC

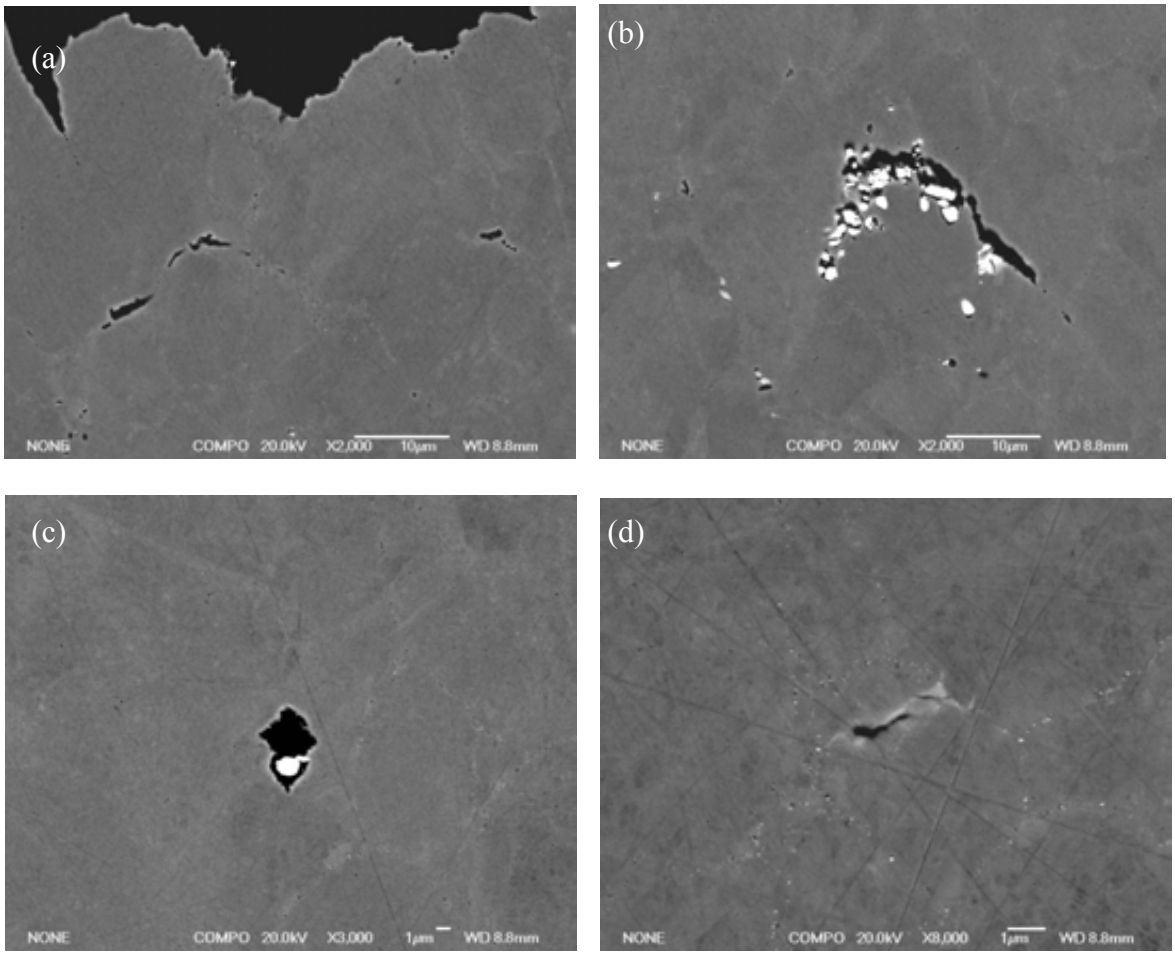

Figure 7.22 Secondary electron SEM micrographs showing the secondary cracks on the section of tested samples after tensile testing at 700℃. The sample shown here was HIPped at 1180℃/150MPa/4h + Solution treated at 1120℃/2h/AC+ Aged at 760℃/16h/AC

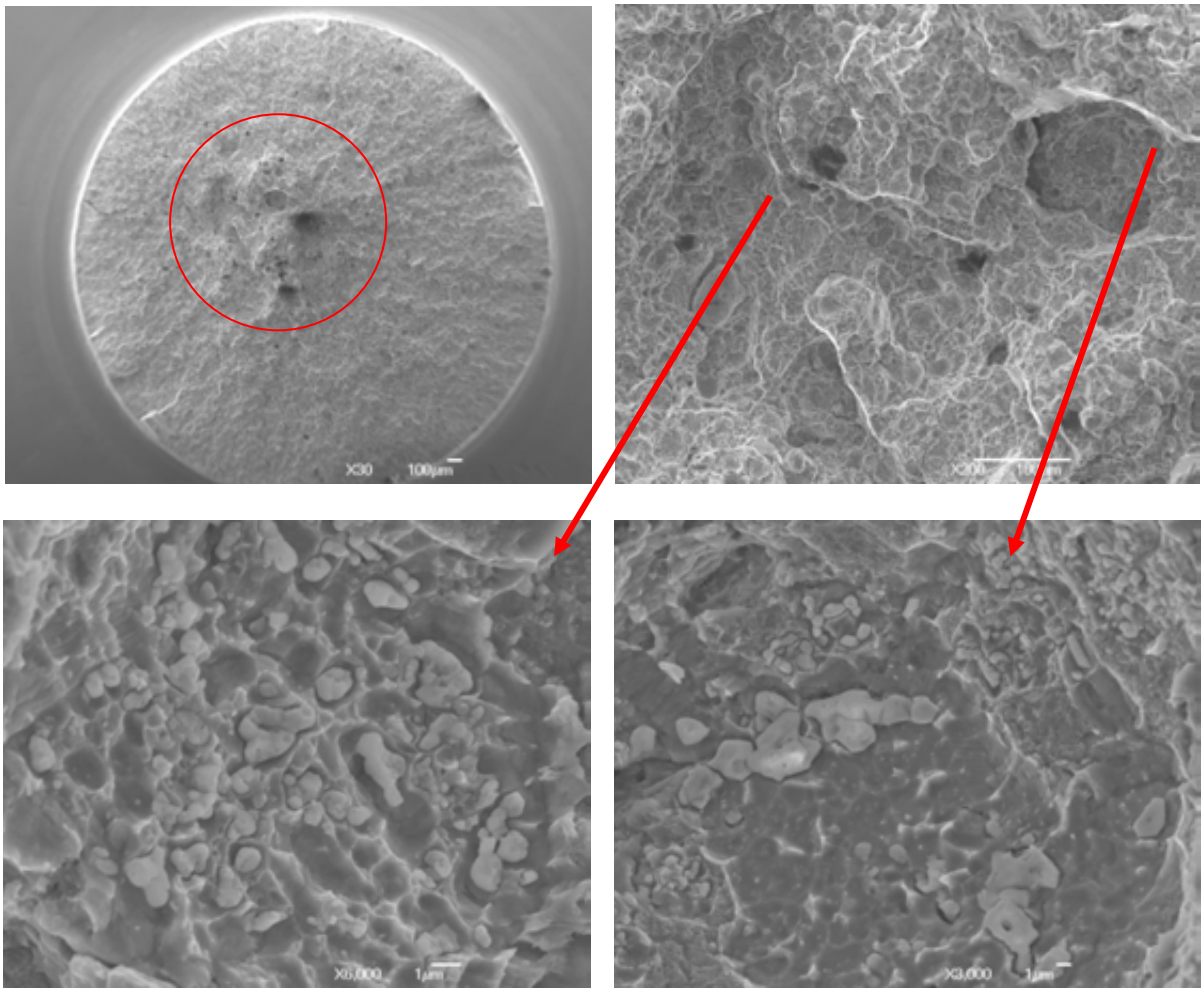

Figure 7.23 SEM micrographs showing the inclusions-induced fracture of a notched sample which was HIPped 1180℃/150MPa/4h + Aged at 760℃/16h/AC after room temperature tensile testing.

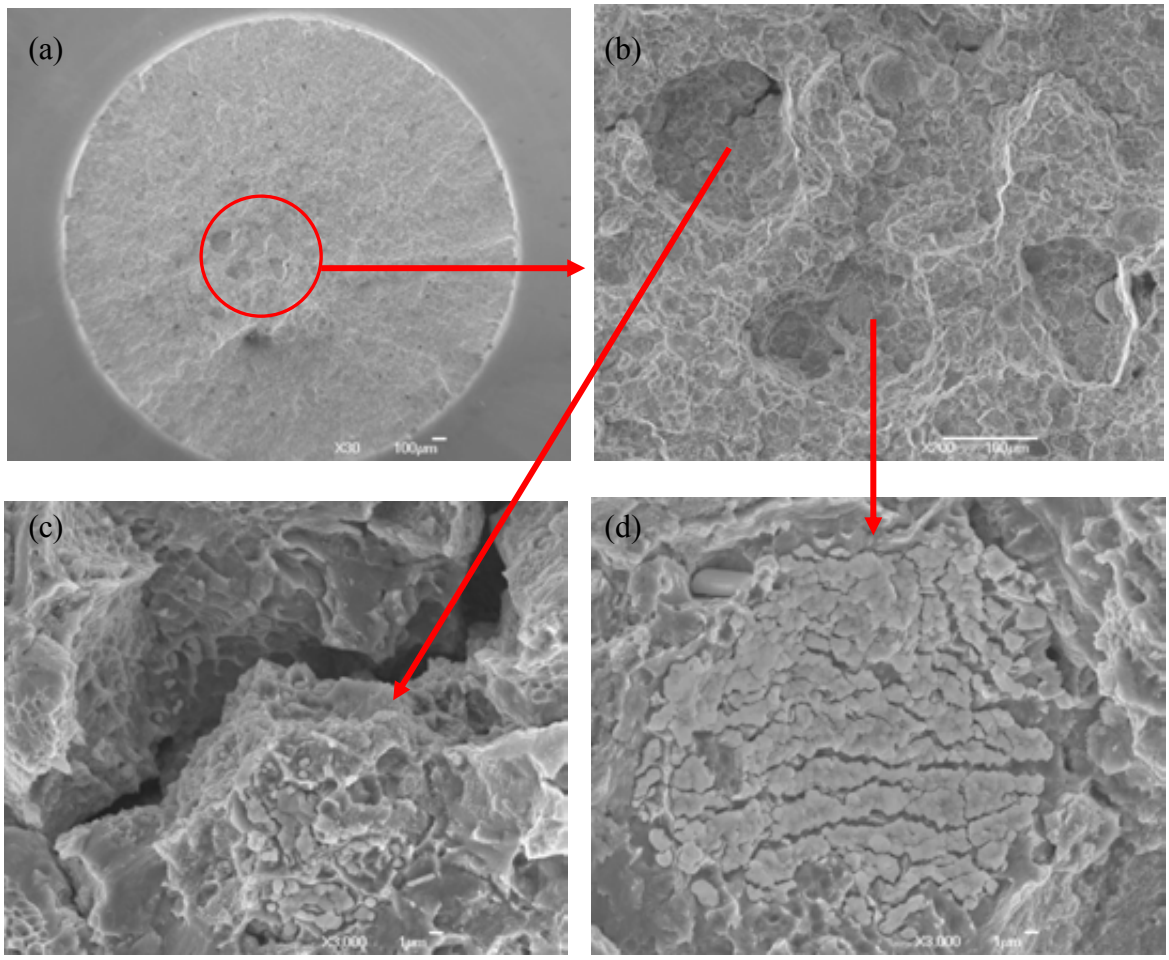

Figure 7.24 Secondary electron SEM micrographs showing the inclusions-induced fracture of a notched sample which was HIPped 1180℃/150MPa/4h + Solution treated at 1120℃/2h/AC+ Aged at 760℃/16h/AC, after room temperature tensile testing.

Chapter Eight-Fatigue and Creep Behaviour

8.1 Introduction

It is well recognised that fatigue is one of the critical properties for materials used in turbine engines. In fact, it is generally considered that over 80 percent of all service failures can be traced to mechanical fatigue, whether in association with cyclic plasticity, sliding or physical contact (fretting and rolling contact fatigue), environmental damage (corrosion fatigue), or elevated temperatures (creep fatigue) [1]. In engine applications, there are often two components to this problem: (1) low-cycle fatigue, which results from relatively large cycles associated with the stopping and starting of the turbine, and (2) high-cycle fatigue (HCF), associated with vibrational loading during service. The HCF, in particular, has been recognised as one of the largest causes of engine failures in civilian and particularly military aircraft [2-4]. It results in rapid and often unpredictable failures due to the propagation of fatigue cracks in engine components (like blades and disks) under high-frequency loading, where the cracking initiates from small defects, in many instances resulting from fretting or foreign-object damage [3]. Due to the high vibrational frequencies involved (>1kHz), even cracks growing at slow per-cycle rates can propagate to failure in short time periods, possibly within a single flight segment. Consequently, HCF-critical turbine-engine components must be operated below the fatigue-crack initiation or growth thresholds, such that cracking cannot occur within 10^9 cycles [2]. In this chapter, both four-point bending fatigue tests and tension-tension fatigue tests at both room temperature and high temperature have been carried out to evaluate the HCF properties of RR 1000 materials with different processing conditions and microstructures. Surface-sensitiveness and notch-sensitiveness, which are critical to component design and materials application, are also examined by using different types of test specimens and testing methods.

Since in the HCF regime, the vast majority of the life is spent in the initiation and early propagation of small cracks (typically of a size in the range of few to hundreds of micrometers), in this chapter, both fatigue crack initiation origins and micromechanism of the fatigue crack propagation of the as-HIPped and heat treated RR 1000 samples will be investigated. Besides, since creep properties are also significant for turbine engine components, the creep behaviour of the RR 1000 samples prepared under different processing conditions was also studied.

8.2 Results

8.2.1 Effect of HIPping Temperature and Procedure on Four-point Bending Fatigue Behaviour

Figure 8.1 shows the four-point bending fatigue properties of RR 1000 samples HIPped at different temperatures or using different procedures. All the tests were carried out at room temperature. It can be seen that changing HIPping condition did not change the fatigue properties significantly. At the same stress levels, samples HIPped under different conditions generally showed comparable fatigue lifetime although the samples that were HIPped at a super-solvus temperature 1180℃ were found to have slightly improved fatigue lives at the same stress levels (especially at higher stress ≥ 900MPa) as compared with those that were HIPped at 1107℃.

The fracture surfaces of all failed samples were examined in order to understand the factors which lead to initiation of fatigue failure. A summary of the location and nature of the fatigue crack initiators is listed in Table 8.1. All the fatigue crack initiations occurred from the sample surface where high tension-tension stress was expected. At the lower stress levels ($\sigma_{max} \leq 850$MPa), fatigue cracking initiated at inclusion clusters or they were characterised by large crystallographic facets, also see Figure 8.2. In view of the fact that the addition of Hf

into the melt during atomisation has been related (see Chapter 3 and 4) to the presence of clusters of hafnia inclusions it is necessary to consider if these inclusions influenced the fatigue life. The data in table 8.1 shows that, although the presence of such inclusion clusters at the fracture-initiation sites led to a small reduction in the fatigue properties, the reductions observed were within scatter. At higher stress levels (σ_{max}>850MPa) no inclusion clusters were observed and cleavage fracture was found to characterise the fatigue crack initiation sites, also see Figure 8.3.

Figure 8.4 shows a typical four-point bending fatigue crack propagation sequence for the as-HIPped samples. Fatigue crack initiation from sample surface was followed by a cleavage fracture and then a long-range striated fracture and finally a monotonic fracture. The detailed typical fracture surface feature of samples HIPped at 1180℃/150MPa/4h at each stage is shown in Figure 8.5. In the adjacent areas around crack initiators (usually called near-threshold regime and further lower portion of the Paris regime), the fracture appeared to be highly crystallographic and faceted, as evidenced by considerable sharp and angular facets which are usually believed to be equivalent to the size of grains. Fine fatigue striations and steps could be observed on some of the crystallographic facets, see Figure 8.5 (b), suggesting the occurrence of highly localized plastic deformation during fatigue crack growth in this region. At the further crack propagation region, usually called upper Paris regime which shows higher ΔK levels (ΔK, crack-tip intensity factor range) and the crack-tip opening displacement is usually bigger than grain size, a striated fatigue crack propagation feature dominated, see Figures 8.5 (c) and (d). At even higher ΔK levels where monotonic fracture is predominant, a ductile-dimpled fracture mode was observed, see Figures 8.5 (e) and (f). The current result is consistent with the normal fatigue crack propagation procedure for nickel-based superalloys [1,5-8]. For the samples HIPped at lower temperature, like 1107℃/100MPa/4h, they showed the same fatigue crack propagation sequence and almost similar

fracture mode at each stage to those HIPped at super-solvus except that in the final static fracture stage, they failed in a widespread particle-debonding mode, see Figure 8.6. This is consistent with the fracture observation after tensile testing.

8.2.2 Effect of Heat Treatment on Four-point Bending Fatigue Behaviour

Figure 8.7 shows the room temperature four-point bending fatigue properties of RR 1000 samples with or without heat treatment and it can be seen that at lower stress levels (σ_{max}< 850MPa), those samples which were HIPped and then aged showed the best fatigue life. In this stress range, the HIPped and aged samples all ran out, to greater than 10^7 cycles whereas most of the samples from other conditions failed at about 10^6 cycles. However, it is noted that at higher stress levels (σ_{max} ≥850MPa), the fatigue lives for samples prepared using different HIP or post-HIP conditions are generally comparable when they were tested at the same stress levels.

The fracture surfaces after fatigue test were analysed using SEM. The fatigue crack initiators together with fatigue life of the tested samples are summarised in Table 8.2. It can be seen that at lower stresses (σ_{max} <850MPa), the HIPped and aged samples all ran out whereas those samples that were solution treated failed earlier at the site of inclusion cluster or failed in a brittle manner as indicated by the large cleavage facets at the initiation sites, see Figure 8.8. This may account for the reduction of fatigue limit for the samples that were solution treated. Similar large cleavage facets were also observed in the samples which were not solution treated but failed at higher stress levels see Figure 8.9. EBSD image in Figure 8.9 (c) shows that these large cleavage facets were actually due to the presence of several large grains which would be a region where deformation would occur more easily and become localised under fatigue conditions. This is consistent with previous report which suggested coarse grains are favourable for fatigue crack initiation [9]. At higher stresses (σ_{max}

≥850MPa), samples failed either due to the presence of inclusion clusters or they failed in a cleavage fracture mode, see Table 8.2. In the previous section when considering tension it was noted that the presence of large inclusion clusters did not downgrade the fatigue properties significantly and similar results were obtained in four point bending fatigue. Thus for samples that were tested at the same stress level only slightly smaller fatigue lives are associated with failures which occur at inclusion clusters than are found when no inclusions are seen and large cleavage facets are seen at the initiation sites. Moreover, despite the fact that the fatigue life was impaired to some extent by the presence of inclusion clusters, the samples prepared all showed a fatigue limit well above the requirement (400Mpa, as indicated in Appendix A). Even the samples (that were solution treated) with lowest fatigue limit among the samples investigated, still showed a fatigue limit around 700MPa.

In terms of fatigue crack propagation, the samples that were aged or solution treated plus aged showed almost the same fracture modes at each crack growth stage as those simply HIPped, see Figure 8.10 and Figure 8.5. To be noted, on the fracture surface of last stage, some secondary cracks could be observed, which are found to be associated with failure at PPBs. Actually they usually initiated from PPBs and then propagated either intergranularly or transgranularly, see Figure 8.10(f). Moreover, some voids which may be due to the separation at remnant PPBs could be observed occasionally, see Figure 8.10(g). The bottom of these voids usually showed massive fine dimples (see Figure 8.10(h)), indicating a ductile separation.

Sections of the samples after fatigue fracture testing were examined and examples are shown in Figure 8.11. Throughout the section of each sample, inclusions (probably coarsened PPB precipitates) and voids could be observed and very often some inclusions were found exactly located in voids, See Figures 8.11 (c) and (d).

8.2.3 Tension-Tension Fatigue Behaviour

8.2.3.1 Testing at room temperature

Figure 8.12 shows the room temperature tension-tension fatigue life for variously processed plain and notched samples. Plain specimens, irrespective of processing conditions, all run out when the testing stress level is below 850MPa. Solution treatment seems to show no obvious influence on tension-tension HCF limit. However, compared with four-point bending fatigue tests, tension-tension fatigue tests led to much better fatigue limit, especially for the tension-tension samples that were solution treated. The ratio (notch stress concentration factor K_t × fatigue limit for notched samples)/(fatigue limit for plain samples) was shown to be 2.26×425/875 =1.1 which is higher than 1.0 (see the Appendix A), suggesting that tension-tension fatigue for this material is notch-insensitive.

Figure 8.13 shows a typical fracture surface of plain samples after tension-tension fatigue tests at room temperature. A summary of fatigue lives together with crack initiation origins of the un-notched samples tested at room temperature are shown in Table 8.3. In contrast to the observations made on samples tested in four point bending summarised in tables 8.1 and 8.2, all the samples tested, fatigue crack initiation was always associated with clusters of inclusions; see Figure 8.13 (c) and (d). These inclusions were found to be rich in Hf, Zr, O and C through EDX analysis, as shown in Figure 8.14. Basically, they could be reckoned as (Hf, Zr)O_2, as suggested by rough quantification in Table 8.5. For most of the samples, fatigue cracks initiated from the sub-surface inclusion clusters but in some cases, fatigue crack initiation was found to occur at clusters of inclusions present in the surface region, see Figures 8.13(e) and (f). Also, it seemed that the fatigue life is associated with the location of the crack initiation site. Actually, those subsurface crack initiators usually led to much longer fatigue life than surface crack initiators, see Figure 8.14. In another group's comparison under the same testing conditions, when the crack initiator is further from the sample surface,

the fatigue life is better, see Figure 8.15. These results are consistent with the previous reports on other powder-processed nickel-based superalloys [10-13].

Around the crack initiators, a radiating fracture surface could be observed. Depending on the distance from crack initiation site, several distinct crack propagation regions with different fracture modes could be seen. In the near-threshold and lower portion of Paris regimes, crystallographic cleavage mode dominates. With crack propagation, a faceted-striated transition could be observed on the fracture surface, see Figure 8.16 (c) and in the higher portion of Paris regimes, pronounced striations together with secondary cracking were present, see Figures 8.16 (c) and (d). In the high ΔK regime, the ductile-dimpled static fracture mode was observed to be active. Moreover, in this regime, whenever clusters of inclusions were encountered, cracks were developed and pores were formed due to material separation at these sites, see Figures 8.16(e) and (f). In general, samples for tension-tension fatigue tests showed the similar crack propagation micromechanism to those for four-point bending fatigue tests, irrespective of the difference in sample geometry.

Notched samples under tension-tension fatigue condition all failed from the surface of notch root and cracks could initiate in either trans-granular mode or due to separation at the γ/γ' interface or at sites of inclusions, which can be seen from Table 8.4 and Figures 8.17 and 8.18. However, inclusion clusters-induced crack initiation mode still dominated in many tests, see Figure 8.19. Once the fatigue cracks were initiated, the notched samples followed the same crack propagation procedure as those plain samples.

Figure 8.20 shows a typical section surface of the samples after room temperature tension-tension fatigue testing. Obvious secondary cracks were found in the tension-tension fatigue tested samples. The cracks were always developed at the inclusions/matrix interfaces. The results further suggest that inclusion clusters are very harmful for fatigue initiation and propagation of RR 1000 samples.

8.2.3.2 Testing at 700℃

Figure 8.21 shows the tension-tension fatigue life at 700℃ for differently processed samples. Solution treatment at 1120℃ seems to show no appreciable influence on the high temperature tension-tension fatigue properties of RR 1000. Samples with or without solution treatment both show a fatigue limit at 750MPa, which however, is 100MPa lower than the room temperature tension-tension fatigue limit (850MPa, see Figure 8.12). Moreover, those samples that failed at 700℃ usually show a relatively short lifetime as compared with those failing at room temperature, see Table 8.3. For notched samples at 700℃, a tension-tension fatigue limit of 500MPa (nominal stress) was observed, which is 100MPa higher than that at room temperature and thus the peak stress ($K_t\sigma$) at the notch root achieved even bigger improvement, 226MPa, suggesting that RR 1000 is less notch sensitive at 700℃ than at room temperature.

The high temperature tension-tension fatigue properties together with fatigue crack initiators have been summarized in Table 8.3 and Table 8.4. The fatigue crack initiation of those failed samples was also due to the presence of large inclusion clusters. To be mentioned, despite the fact that the tension-tension fatigue crack initiation at both room temperature and 700℃ was due to large inclusion clusters which may impair fatigue life to some extent, the several groups of samples investigated here all showed a much higher fatigue limit than the requirement (around 400MPa as indicated in Appendix A). Similar to the case at room temperature, the fatigue lifetime of samples (irrespective of processing condition) is highly dependent on the location of large inclusion cluster, i.e., the distance from the site of inclusion cluster to the sample surface. When a sample failed from the sample surface due to inclusion clusters, it suffered the lowest fatigue life; see Figure 8.21 and Figure 8.22(a)(b). Also the fatigue life of samples increased with the increased distance

between the fatigue crack initiation site and the sample surface, see Figure 8.23 and Figure 8.24. For the same type of inclusion clusters, the size of an inclusion cluster seems to be insignificant with the depth of inclusion cluster from the surface having a far larger effect. This is evidenced by both Figure 8.23 and 8.24 where the samples failed at larger inclusion clusters but showed even higher fatigue life, because of the larger distance between these inclusion clusters to the sample surface. In addition, the type of inclusion cluster may influence the fatigue properties. Figure 8.25 shows that samples that were obtained from the same processing condition failed at different types of inclusion clusters and consequently showed a large difference in fatigue lifetime. The compact Al_2O_3-type inclusion cluster, the composition of which is listed in Figure 8.25(e) and Table 8.6, led to a higher fatigue life than those dispersed and large hafnia-type inclusion clusters, even though the hafnia cluster was further from the surface than the Al_2O_3 cluster.

Somewhat different from room temperature tests (which failed from the notch root surface), the notched samples tested at 700℃ in the current study all failed from notch root sub-surface area due to the presence of inclusion clusters, see Figure 8.26.

Samples tested at 700℃ showed similar fatigue crack propagation behaviour to those tested at room temperature, that is, crack initiation followed by a cleavage fracture stage and then striation mode and finally transgranular fracture mode, see Figure 8.27. However, the final crack propagation stage seemed to be more faceted and crystallographic at 700℃ than at room temperature, see Figure 8.27(e) and (f), which is consistent with the observations on tensile deformation in Chapter 7 and obviously is due to the easier planar slip at elevated temperature. Besides, it is noted that RR 1000 samples tested at room temperature all show a very flat fracture surface while samples tested at 700℃ show part flat fracture surface and part slant fracture surface, see Figure 8.28 and 8.29. Given that the part slant fracture surface area actually corresponded to the final monotonic fracture, this slant fracture is obviously

dominated by the plain stress condition, which is also consistent with the previous tensile study.

8.2.4 Creep Behaviour

Figure 8.30 shows the temperature-dependence of creep rate of samples prepared from different processing conditions at 550MPa and 400MPa, respectively. At 550MPa, when the testing temperatures were below 750℃, all the samples showed no significant difference in creep rate whereas at higher testing temperatures, the samples that were HIPped at 1180℃ and then solution treated at 1120℃ plus aging showed better creep rate than the other samples, see Figure 8.30(a). The advantage of solution treatment became increasingly obvious with increased testing temperature. And, this was also observed for the tests at lower stress 400MPa but higher temperature conditions, see Figure 8.30(b). To be mentioned, testing at 400MPa but below 700℃ for several hours, no creep strain change could be detected based on the current detection resolution (10^{-7}). It is also noted that the net-shape HIPped samples (HIPped at 1180℃) with heat treatments all showed better creep rate than those HIPped at 1107℃ and thermomechanically processed samples.

Figure 8.31 shows the stress-dependence of creep rate of samples prepared using different processing procedures at 746℃ and 800℃. It can be seen that creep rate increased steadily with increased stress level. Among the three groups of samples, those that were HIPped at 1180℃ and then solution treated at 1120℃ plus aging treatment again showed the best creep properties, especially at higher stress levels. The net-shape HIPped samples (HIPped at 1180℃) with heat treatments also showed better creep rate than those that were HIPped at 1107℃ and thermo-mechanically processed. This became more pronounced with increased stress level.

The stress- and temperature-dependence of the steady-state creep rate for superalloys at various stress levels and temperatures can be described as

$$\dot{\varepsilon} = A\sigma^{n}\exp\left(-\frac{Q_c}{RT}\right) \qquad \text{Equation 8.1}$$

Where A is a structure sensitive constant, σ is the applied stress, n is the applied stress exponent, Q_c is the apparent activation energy for creep, R is the gas constant and T is the absolute temperature.

According to this equation, the values of Q_c and n at different temperature ranges and stress ranges for samples obtained from different processing conditions are shown in Figure 8.32 and Figure 8.33, respectively. It can be seen that at high temperatures (above 700℃) all the samples showed basically comparable Q_c at around 550 KJ/mol, which is similar to previous report on other nickel-based superalloys [14-16]. At lower temperatures, Q_c was significantly reduced to 160 KJ/mol. In terms of stress exponent, at 746℃, in the applied stress range between 348 MPa and 685MPa, the samples that were HIPped at 1180℃ and solution treated plus aging showed a relatively constant stress exponent of around 5.7. For the samples that were HIPped and aged, a stress exponent of 7.3 was observed at 278 ~ 482 MPa and 3.0 at higher stress regime. The samples that were HIPped at 1107℃ and thermomechaically processed showed very changeable stress exponent with stress range and the values were usually very high. When tested at higher temperature like 800℃, the stress exponent for all the samples varied greatly with stress range.

Examination of the crept samples revealed no obvious sign of cavitation or cracking at grain boundaries which would cause final creep rupture.

8.3 Discussion

8.3.1 Effect of HIPping Temperature or Procedure on Four-point Bending Fatigue Property

It was demonstrated that for four-point bending fatigue testing, fagitue cracking could initiate either at inclusion clusters or they were characterised by large crystallographic facets ($\sigma_{max} \leq 850$MPa), see Table 8.1. Although the presence of the inclusion clusters at the fracture-initiation sites led to a small reduction in the fatigue properties, the reductions observed were within scatter, See Figure 8.1. At higher stress levels ($\sigma_{max} > 850$MPa) where no inclusion clusters were observed and cleavage fracture dominated the fatigue crack initiation, samples HIPped under different conditions were found to show comparable fatigue lifetime at the same stress levels, see Table 8.1. This suggests that neither HIPping procedure nor HIPping temperature can change the four-point bending fatigue properties significantly. Also, it is noted that neither HIPping procedure nor HIPping temperature changed the fatigue crack initiation mode and early-stage crack propagation. However, in the final fatigue crack propagation stage, those samples HIPped at super-solvus showed a dimple-ductile transgranular fracture mode in contrast to the particle de-bonding mode (that is, cracking along PPBs) for the samples HIPped at sub-solvus. This is obviously due to the significant reduction of PPBs after super-solvus HIPping.

8.3.2 Effect of Heat Treatment on Fatigue Properties

In terms of four-point bending fatigue, those HIPped and aged samples appeared to show the best fatigue limit whereas samples which were solution treated showed the lowest fatigue limit resulting from early failure in the lower stress levels (below 800MPa) due to the presence of either large inclusion cluster or large grain clusters in surface area. The clusters of large grains on the sample surface seemed to be favourable for local stress/strain

concentration which then led to early crack initiation by slipping through grains. This is consistent with the previous report which suggested large grains were favourable for fatigue crack initiation although they are beneficial for crack propagation [9]. Uniform distributions of small and large grains in the surface are believed to promote release or relaxation of stress concentration whereas the large grain clusters on the sample surface are not good for easing stress concentration to surrounding regions due to the absence of many adjacent small grains and larger grain boundary area around. Given that the large grain crystallographic cracking at the surface was also observed in the samples free from solution treatment, although these samples failed at higher stress levels, more samples from different processing conditions are obviously needed for further investigation and in order to obtain a more comprehensive statistics to determine the true influence of heat treatment on four-point bending fatigue properties.

As for the plain tension-tension fatigue, the HIPped and aged sample group and the HIPped-solution treated-aged sample group both showed similar fatigue limits at both room temperature and 700℃. As compared with four-point bending fatigue tests, tension-tension fatigue tests showed improved fatigue limit, which was especially obvious for those samples which had been solution treated. This may be associated with the different stress conditions which the samples were subjected to. For four-point bending fatigue tests, the sample surface suffered not only high tension-tension stress but also large normal shear stress and thus was the most vulnerable area for stress-concentration for crack initiation whereas in tension-tension fatigue tests the whole volume of material experienced much more homogeneous stress distribution and the crack initiation could occur at either internal area or on the sample surface where inclusion clusters were present. The latter was thus less surface-sensitive and demonstrated better fatigue life under the same stress conditions.

8.3.3 Effect of Inclusion Cluster Characteristics on Fatigue Properties

In the current studies, none of the primary fatigue crack initiation was due to PPB defects, although during the later stage of fatigue crack propagation, primary or secondary cracks could grow along PPBs and led to the formation of pores on the fracture surface. Instead, most of the primary fatigue crack initiators, especially for tension-tension fatigue tests, were associated with large inclusion clusters. In this sense, inclusion clusters seemed to be more harmful for fatigue properties than PPB defects. The fact that all tension-tension fatigue samples failed at inclusion clusters may simply be associated with the fact that a small number of samples were tested for each condition and that if more samples had been tested some would have shown faceted failure sites as found in 4-point bending fatigue. Alternatively the fact that the whole sample is stressed in tension in tension-tension tests, rather than in the case of 4-point bending where only the region near the surface is subjected to the maximum tensile stress, may lead to a cluster of inclusions always being the failure initiation site in tension-tension tests. The fact that a significant number of failure initiators are characterised by faceted regions in four-point bending fatigue tests may suggest that these regions are also regions of weakness and the presence of regions which have a larger grain size (see figures 8.8 and 8.9) suggests that indeed these do cause failure if inclusions do not cause failure first.

It has been reported that fatigue lifetime of a P/M superalloy is closely related to the size, location and number of inclusions [10-13]. Fatigue lifetime generally decreases with increased number and size of inclusions. Internal crack initiation usually leads to improvement in fatigue lifetime as compared with surface initiation [10-13]. In the current work, most of the fatigue crack initiations were due to the presence of large inclusion clusters. The fatigue lifetime did not necessarily degrade with increased inclusion cluster size but did show improvement by internal initiation relative to surface initiation under the same stress

conditions, irrespective of test temperature (see Figure 8.13 and 8.22). Moreover, as the crack initiator was further away from the sample surface, the fatigue life was better (see Figures 8.15, 8.23 and 8.24). It is generally believed that the less constrained surface allows relatively easy slip [13, 17-18]. This, when interacting with surface inclusions that are usually subjected to stress concentration, would lead to accelerated localized strain concentration and consequently to earlier crack initiation. Internal inclusions, however, are subject to plastic constraint and thus more difficult to lead to crack initiation.

In addition, the current experimental results demonstrated that even the type of inclusions could show great influence on fatigue property. Actually, crack initiation at the compact Al_2O_3 inclusion cluster led to much higher fatigue life in contrast to the initiation due to the dispersed and large hafnia inclusion clusters along PPBs under the same stress condition, even though they were closer to sample surface (see Figure 8.25).

8.3.4 Effect of Temperature on Fatigue Properties

At high temperatures, oxidation and creep deformation may be involved, which could affect fatigue properties to some extent depending on the testing conditions, like loading frequency. The influence of oxidation on low cycle fatigue has been extensively investigated. It is generally believed that oxygen penetration at the crack tip leads to the formation of an oxide layer causing embrittlement, which is primarily responsible for increased fatigue crack growth and damage at elevated temperature in nickel based superalloys [19-24]. One of the common features of oxidation is intergranular fracture due to the preferential oxygen diffusion at grain boundaries [20,24]. However, on the other hand, it was reported that increasing loading frequency (like from 0.25Hz to 5.0Hz) could significantly reduce the oxidation effect [23, 25-27], which would also change the failure mode from intergranular to transgranular fracture. As for the high cycle fatigue tests, due to the use of much higher loading frequency (basically several tens of Hzs) relative to low cycle fatigue (around

0.25Hz), the influence of oxidation on HCF properties may be very limited. Unfortunately, there were only very few reports on the high temperature high cycle fatigue behaviour and the influence of oxidation on HCF properties was not well understood [28].

In the current study, increasing the testing temperature from room temperature to 700℃ was found to lead to the decrease of high cycle tension-tension fatigue limit (by 100MPa) and fatigue lifetime of plain samples. However, it is noted that the fracture modes of these samples remained almost the same with increased test temperature. Fatigue crack initiation also occurred at either surface or internal inclusion clusters. Fatigue crack propagation also followed a highly crystallographic and faceted mode firstly and then a striated mode and finally a transgranular mode. Transition of failure mode from transgranular fracture at room temperature to intergranular fracture at elevated temperature, which is commonly observed in low cycle fatigue tests due to oxidation along grain boundaries (as mentioned above), did not happen in this work. Instead, fracture in the final stage of crack propagation actually became even more crystallographic and faceted at 700℃ (see Figure 8.27). Moreover, the presence of striations usually indicated that cyclic fatigue deformation was the dominant fracture mechanism in fatigue [21]. All of these suggested that oxidation atmosphere may have a negligible effect on fatigue crack initiation and propagation and thus fatigue life, probably due to the use of a very high loading frequency (around 74Hz) which may suppress the diffusion and penetration of oxygen to grain boundary areas to induce intergranular fracture [21,29-30]. The widespread crystallographic or faceted fracture at the final crack propagation may be due to the easier and more planar deformation at 700℃, which is consistent with the study on tensile deformation and fracture mechanism of RR 1000 samples in Chapter 7. It is possible that this easier deformation around the stress concentrating large inclusion clusters would promote local plastic strain buildup and thus accelerated the separation of inclusions/matrix interface to induce earlier crack initiation. The easier deformation was also

favourable for crack propagation. Both of these could lead to the decrease of fatigue lifetime and thus fatigue limit for plain samples at elevated temperature.

8.3.5 Creep Behaviour

The creep results demonstrated that the current net-shape HIPped samples (HIPped at 1180℃) generally showed improved creep rate over those that were HIPped at 1107℃ and thermomechanically processed. This is especially obvious at higher temperature and higher load. It is noted that the net-shape HIPped samples showed much coarser grain size than those thermomechanically processed samples (see Figure 6.4). This is believed to cause the improvement in creep rate by reducing grain boundary sliding and diffusion. Samples that were HIPped (at 1180℃) and solution treated were found to show the best creep rate, especially at high temperature and load. It may be partly due to their largest grain size among the samples studied and partly due to their much finer and coherent γ′ which were beneficial for strengthening as evidenced in Chapter 7.

Besides, it is noted that all the samples showed high activation creep energy at intermediate and high temperatures (above 700℃), around 550 KJ/mol, which is much higher than that of the self-diffusion of pure Ni in the austenite (290 KJ/mol) and in the intermetallic Ni_3Al (about 300 KJ/mol) [15, 31-32]. This suggested that the creep process of the present samples above 700℃ was not mainly controlled by the diffusion of elements. The samples that were HIPped at 1180℃ and solution treated plus ageing were found to show a stress exponent of around 5.7 at a high temperature 745℃, which is close to the value of 5 for climb-controlled creep [33-34]. Climb-induced creep deformation at high temperature and increased load has been well recognized [35]. It is believed that at high temperature climb by-pass of γ′ precipitates occurs mainly through the motion and accumulation of individual, unpaired a/2<110> dislocations in the γ channels between γ′ particles. For other

samples or at higher temperature like 800℃, stress exponents were found to vary greatly with stress levels and the values were usually very high. The creep mechanism involved is not known at this stage. Obviously, more work should be done to reveal creep mechanisms operative in the different microstructures.

8.4 Conclusions

High cycle fatigue tests and creep tests have been carried out. In terms of the four-point bending fatigue tests, initiation of fatigue cracks was due to either inclusion clusters or to crystallographic cleavage fracture. Crack initiation due to inclusion clusters was shown to lead to a small reduction in the fatigue properties but the reductions observed were within scatter and at the same stress levels, crack initiation due to inclusion clusters or cleavage fracture generally showed comparable fatigue life. Therefore, the general trend for the influence of processing condition on four-point bending fatigue properties could still be determined. Thus, changing HIPping procedure was shown to have no significant influence on four-point bending fatigue properties while increasing HIPping temperature led to a slight improvement in fatigue life at higher stress levels. HIPped and aged samples showed the best four-point bending fatigue limit while solution-treated +aged samples had the lowest fatigue limit with failure occurring mainly by cleavage of the matrix alloy at lower stress levels. In spite of the slight influence from inclusion clusters, the fatigue limits for the several groups of samples investigated here are all well above the property requirement.

As for the plain tension-tension fatigue tests, samples failed mainly due to large inclusion clusters which may impair the fatigue properties of the samples to some extent and thus the influence of processing condition on the fatigue properties is masked. However, the fatigue limits for tension-tension fatigue tests were shown to be even better than those for four point bending fatigue tests and also are above the property requirement. It is also noted that

internal crack initiation was usually associated with improved fatigue life as compared with surface crack initiation. Moreover, it was shown that the samples that were solution treated at 1120℃ showed fairly good notch insensitiveness during the tension-tension fatigue testing.

Creep tests indicated that solution treatment at 1120°C improved creep rate of RR 1000 samples, especially at elevated temperatures and stress levels. Samples that were HIPped at higher temperature (like 1180℃) with heat treatments all showed better creep rate than those that were HIPped at lower temperature (1107℃) and thermomechanically processed. This became increasingly obvious with elevated temperature and loading levels. These observations and those reported in other chapters are used in the final chapter to identify the optimum HIP/heat treatment conditions for Net Shape HIPping of RR 1000 powder.

References

[1] Ritchie RO. Mechanisms of fatigue-crack propagation in ductile and brittle solids, International Journal of Fracture 1999; 100: 55–83.

[2] Gao Y, Kumar M, Nalla RK, Ritchie RO. High-cycle fatigue of Nickel-Based Superalloy ME3 at ambient and elevated temperatures: role of grain-boundary engineering, Metallurgical and Materials Transactions A 2005;36:3325-3333.

[3] Cowles BA. High cycle fatigue in aircraft gas turbine-an industry perspective. International Journal of Fracture 1996; 80: 147-163.

[4] Gao Y, Stolken JS, Kumar M, Ritchie RO. High-cycle fatigue of nickel-base superalloy Rene′ 104 (ME3): Interaction of microstructurally small cracks with grain boundaries of known character. Acta Materialia 2007; 55: 3155–3167

[5] Reed PAS, Gale WF, King JE. Intrinsic threshold in polycrystalline Udimet 720. Materials Science and Technology 1993;9:281–287.

[6] Luo J, Bowen P. Small and long fatigue crack growth behaviour of a PM Ni-based superalloy, Udimet 720. International Journal of Fatigue 2004; 26: 113–124.

[7] Mercer C, Shademan S, Soboyejo WO. An investigation of the micromechanisms of fatigue crack growth in structural gas turbine engine alloys. Journal of Materials Science 2003;38:291–305.

[8] King JE. Effects of grain size and microstructure on threshold value and near-threshold crack growth in powder-formed Ni-base superalloy. Metal Science 1982;16:345–355.

[9] Pang HT, Reed PAS. Effects of microstructure on room temperature crack initiation and short crack propagation in Udimet 720Li Ni-base superalloy. International Journal of Fatigue 2008;30:2009–2020.

[10] Chang DR, Krueger DD, Sprague RA. Superalloy powder processing, properties and turbine disk applications. In: Sunerallovs 1984, Proceedings of the Fifth International Symposium on Superalloys. Warrendale, PA: TMS-AIME; 1984. p. 245-273.

[11] Hyzak JM, Bernstein IM. The effect of defects on the fatigue crack initiation process in two P/M superalloys: Part I. Fatigue Origins. Metallurgical Transactions A 1982; 13:33-43.

[12] Hyzak JM, Bernstein IM. The Effect of Defects on the Fatigue Crack Initiation Process in Two P/M Superalloys: Part II. Surface-Subsurface Transition. Metallurgical Transactions A 1982; 13: 45-52.

[13] Huron ES, Roth PG. The Influence of Inclusion on Low Cycle Fatigue Life in a P/M Nickel-Base Disc Superalloy. In: Kissinger RD, Deye DJ, Anton DL, Nathal MV, Pollock

TM, Woodford DA editors. Superalloys 1996. Warrendale, Pennsylvania, USA: The Minerals, Metals and Materials Society; 1996.p. 359-368.

[14] Dennison JP, Holmes PD, Wilshire B. The creep and fracture behaviour of a nickel based Superalloy, IN100. Materials Science and Engineering 1978; 33: 35-47.

[15] Stevens RA, Flewitt PEJ. The dependence of creep rate on microstructure in a γ' strengthened superalloy. Acta Metallurgica 1981; 29: 867-882.

[16] Guo JT, Ranucci D, Picco E, Strocchi PM. An investigation on the creep and fracture behaviour of cast nickel-base superalloy IN 738LC. Metallurgical Transactions A 1983; 14: 2329-2335.

[17] Harkegard G. An experimental study of the influence of inclusions on the fatigue properties of steel. Engineering Fracture Mechanics 1974;6:795-803.

[18] Eylon D, Hyzak JM. An investigation of fatigue origins in superalloy powder compacts. Metallurgical Transactions A 1978; 9:127-129.

[19] Andrieu E, Molins R, Ghonem H, Pineau A. Intergranular crack tip oxidation mechanism in a nickel-based superalloy. Materials Science and Engineering A 1992;154:21-28.

[20] Molins R, Hochstetter G, Chassaigne JC, Andrieu E. Oxidation effects on the fatigue crack growth behaviour of alloy 718 at high temperature. Acta materialia 1997; 45: 663-674,.

[21] Tong J, Dalby S, Byrne J, Henderson MB, Hardy MC. Creep, fatigue and oxidation in crack growth in advanced nickel base superalloys. International Journal of Fatigue 2001;23: 897–902.

[22] Hide NJ, Henderson MB, Tucker A, Reed PAS. The effects of microstructure and environment on high temperature fatigue and creep-fatigue mechanisms in a nickel base superalloy. In: F. Ellyin, J.W. Provan, editors. Progress in mechanical behaviour of materials. Victoria, Canada: ICM 8;1999. P. 429–434.

[23] Onofrio G, Osinkolu GA, Marchionni M. Fatigue crack growth of UDIMET 720 Li superalloy at elevated temperature. International Journal of Fatigue 2001; 23: 887–895.

[24] Everitt S, Starink MJ, Pang HT, Wilcock IM, Henderson MB, Reed PAS. A comparison of high temperature fatigue crack propagation in various subsolvus heat treated turbine disc alloys. Materials Science and Technology 2007; 23: 1419-1423

[25] Tong J, Byrne J. Effects of frequency on fatigue crack growth at elevated temperature. Fatigue Fracture Engineering Materials Structure 1999; 22: 185–193

[26] Andersson H, Persson C, Hansson T. Crack growth in IN718 at high temperature. International Journal of Fatigue 2001; 23: 817–827

[27] Evans WJ, Jones JP, Williams S. The interactions between fatigue, creep and environmental damage in Ti 6246 and Udimet 720Li. International Journal of Fatigue 2005; 27: 1473–1484.

[28] Gao Y, Kumar M, Nalla RK, Ritchie RO. High-cycle fatigue of Nickel-based superalloy ME3 at ambient and elevated temperatures: role of grain-boundary engineering. Metallurgical and Materials Transactions A 2005; 36:3325-3333

[29] Pineau A. Fatigue and creep-fatigue behaviour of Ni-base superalloys: microstructural and environmental effects. In: Branco CM et al, editors. Mechanical Behaviour of Materials at Temperature. Kluwer Academic;1996. p. 135–154.

[30] Moulin G, Arevalo P, Salleo A. Influence of external mechanical loadings (creep, fatigue) on oxygen diffusion during nickel oxidation. Oxidation Metals 1996; 45: 153–181.

[31] Burton B, Crossland IG, Greenwood GW. Creep of nickel at low stresses. Metal Science 1980; 14: 134-136.

[32] Yuan C, Guo J, Wang S. High temperature creep and fracture behavior of a directionally solidified Ni-base superalloy**.** Journal of Materials Sciences and Technology 1998; 14: 219-225.

[33] Blum W, Reppich B. Creep of particle-strengthened alloys. In: Whilshire B, Evans RW. Creep behaviour of crystalline solids; 1985.p. 83-136.

[34] Koul AK, Wallace W. A note on the microstructural dependence of creep strength in Inconel 700. Metallurgical Transactions A 1982;13A: 673-675.

[35] Manonukul A, Dunne FPE, Knowles D. Physically based model for creep in Ni-base superalloy C263 both above and below the gamma solvus. Acta materialia 2002;50:2917-2931.

Table 8.1 Summary of four-point bending fatigue crack initiation sites of the samples with different HIPping conditions

Conditions / Stress (MPa)	HIP 1107℃/100MPa/4h	Temperature first and pressure later, dwelt 1107℃/100MPa/2h	HIP 1180℃/150MPa/4h
700	Run out	-	-
750	1.99×10^6, Inclusions	Run out	Run out for 2 times
775	-	Run out	-
800	Run out 2 times	1.60×10^6, Cleavage	1.35×10^6,or 1.67×10^6 Inclusions
850	0.95×10^6, Inclusions	1.42×10^6, Cleavage, or run out	0.74×10^6, Inclusions
900	1.63×10^6, Cleavage	0.93×10^6, Cleavage	0.99×10^6, Cleavage
950	0.40×10^6, Cleavage	0.46×10^6, Cleavage	0.91×10^6, Cleavage
1000	0.31×10^6, Cleavage	0.30×10^6, Cleavage	0.62×10^6, Cleavage
1050	0.26×10^6, Cleavage	0.33×10^6, Cleavage	-
1100	0.24×10^6, Cleavage	0.25×10^6, Cleavage	-

Table 8.2 Summary of four-point bending fatigue crack initiation sites of the samples with different heat treatments

Conditions / σ_{max} (MPa)	HIP 1180℃/150MPa/4h	HIP 1180℃/150MPa/4h + Aged 760℃/16h/AC	HIP1180℃/150MPa/4h, ST 1120℃/2h/AC, Aged 760℃/16h/AC
700		Run out	Run out or 2.8×10^6, Inclusions
750	Run out for 2 times	Run out	2.2×10^6 Large cleavage facets
800	1.35×10^6,or 1.67×10^6 Inclusions	Run out	1.85×10^6, Large cleavage facets
825			1.25×10^6, Large cleavage facets
850	0.74×10^6, Inclusions	Run out or 1.29×10^6, Large cleavage facets	0.61×10^6, Inclusions
900	0.99×10^6, Large cleavage facets	0.68×10^6, Inclusions	0.81×10^6, Inclusions
950	0.91×10^6, Large cleavage facets	0.61×10^6, Inclusions	
1000	0.62×10^6, Large cleavage facets		

Table 8.3 Summary of tension-tension fatigue properties and crack initiation sites of the un-notched samples subject to different heat treatments

Testing conditions	Processing conditions	750 (MPa)	800 (MPa)	850 (MPa)	900 (MPa)	925 (MPa)	950 (MPa)
Room Temperature	HIP+Age	Run out	Run out	Run out	Run out twice	Run out	0.2648×10^6, or 9.2189×10^6, inclusion clusters
	HIP+ST+Age	Run out	Run out	Run out	Run out, or 4.9240×10^6, Inclusion clusters	-	2.7886×10^6, or 6.9034×10^6, inclusion clusters
700℃	HIP+Age	Run out twice	0.7898×10^6, 0.6634×10^6, 0.8499×10^6, 9.3996×10^6, inclusion clusters	0.0243×10^6, 0.9667×10^6 inclusion clusters	-	-	-
	HIP+ST+Age	Run out	Run out, 1.1947×10^6, 0.9933×10^6, Inclusion clusters	1.5393×10^6, 1.7901×10^6, Inclusion clusters	-	-	-

HIP+Age-HIP1180℃/150MPa/4h+ Aged 760℃/16h/AC; HIP+ST+Age-HIP1180℃/150MPa/4h +ST 1120℃/2h/AC+Aged 760℃/16h/AC.

Table 8.4 Summary of tension-tension fatigue properties and crack initiation sites of the notched samples which were HIPped1180℃/150MPa/4h+ ST 1120℃/2h/AC + Aged 760℃/16h/AC (the stress concentration factor at the notch Kt=2.26).

Testing condition	**400 (MPa)**	**450 (MPa)**	**500 (MPa)**	**550 (MPa)**	**600 (MPa)**	**650 (MPa)**	**700 (MPa)**	**800 (MPa)**
Room Temperature, All failed from the surface of notch root	Run out	8.4088×10^6, γ-γ′ Interface	0.3482×10^6 Inclusion clusters	-	0.2074×10^6 Inclusion clusters	0.3424×10^6, transgranular and inclusion clusters	0.1342×10^6 Cleavage and Inclusion clusters	0.0776×10^6, Inclusion clusters
700℃ All failed from the sub-surface of notch root	-	-	Run out twice	0.1458×10^6, 1.0721×10^6, 1.0541×10^6, Inclusion clusters	0.4083×10^6, 0.4619×10^6, Inclusion clusters	-	-	-

Table 8.5 compositions of particles in the inclusion cluster (at.%) analyzed using EDX

Element	1	2	3	4	5	6	7	8	Average
C	18.90	16.86	18.68	18.99	22.92	17.47	19.28	16.83	18.74
O	51.66	57.17	49.45	47.90	38.85	38.28	45.49	49.57	47.30
Ti	1.23	0.87	0.94	1.03	1.90	2.14	0.83	0.39	1.17
Cr	1.25	1.37	1.60	1.60	1.98	2.57	1.72	1.66	1.72
Co	1.74	1.72	2.03	1.98	2.30	2.97	1.98	2.24	2.12
Ni	4.79	5.27	5.51	5.75	7.58	8.37	5.94	5.39	6.07
Zr	4.23	4.05	3.89	4.33	3.06	5.03	3.73	1.87	3.77
Hf	16.20	12.68	17.90	18.41	21.41	23.18	21.00	22.06	19.10

Table 8.6 Chemical composition in at.% of the inclusion in Figure 8.25 (d) using EDX analysis

Element	O	Al	Ti	Cr	Co	Ni
Concentration, at.%	59.83	37.64	0.19	0.70	0.35	1.29

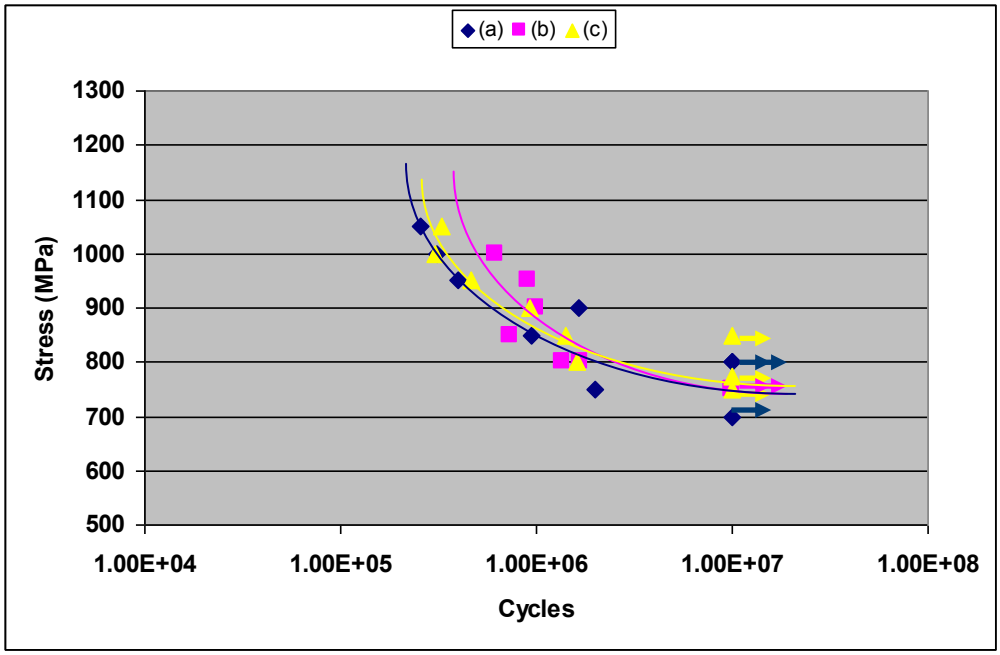

Figure 8.1 Four-point bending fatigue properties of RR 1000 samples (a) HIPped at 1107℃ /100MPa/4h; (b) HIPped at 1180℃/150MPa/4h; (c) Ramping up temperature first and then pressure during HIPping, and dwelt 1107℃/100MPa/2h. The lines were drawn based on the general trend of fatigue lifetime with stress level

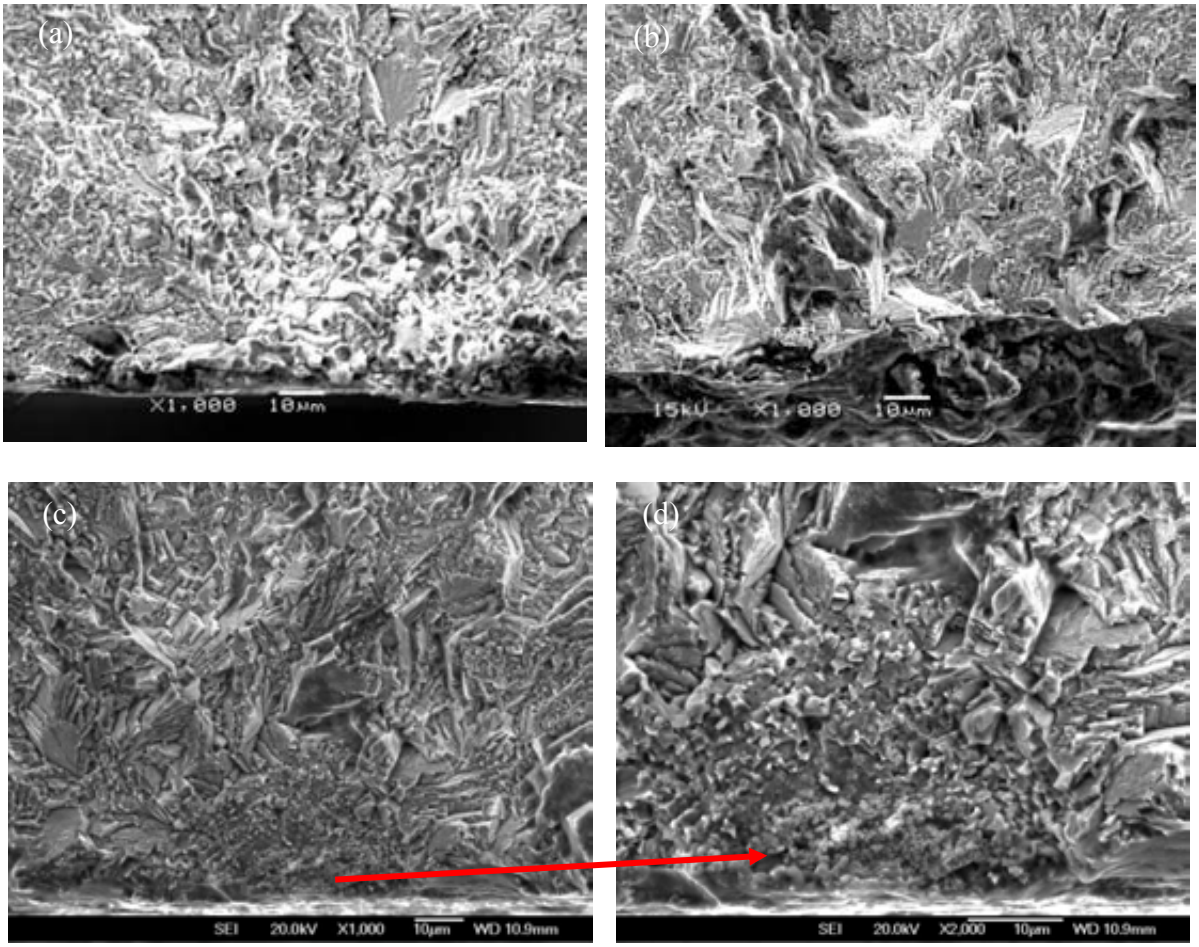

Figure 8.2 Secondary electron SEM micrographs showing the four-point bending fatigue crack initiation sites of the RR 1000 samples which were HIPped following the procedures (a) normal (e.g. ramping up temperature and pressure together) HIPping at 1107℃/100MPa/4h, tested at the stress range 85-850MPa and failed at 0.9520×10^6 cycles; (b) ramping up temperature first and pressure later, dwelt at 1107℃/100MPa/2h, tested at the stress range 85-850MPa and failed at 1.4151×10^6 cycles; (c)(d) normal HIPping at 1180℃/150MPa/4h, tested at 85-850MPa and failed at 0.7365×10^6 cycles

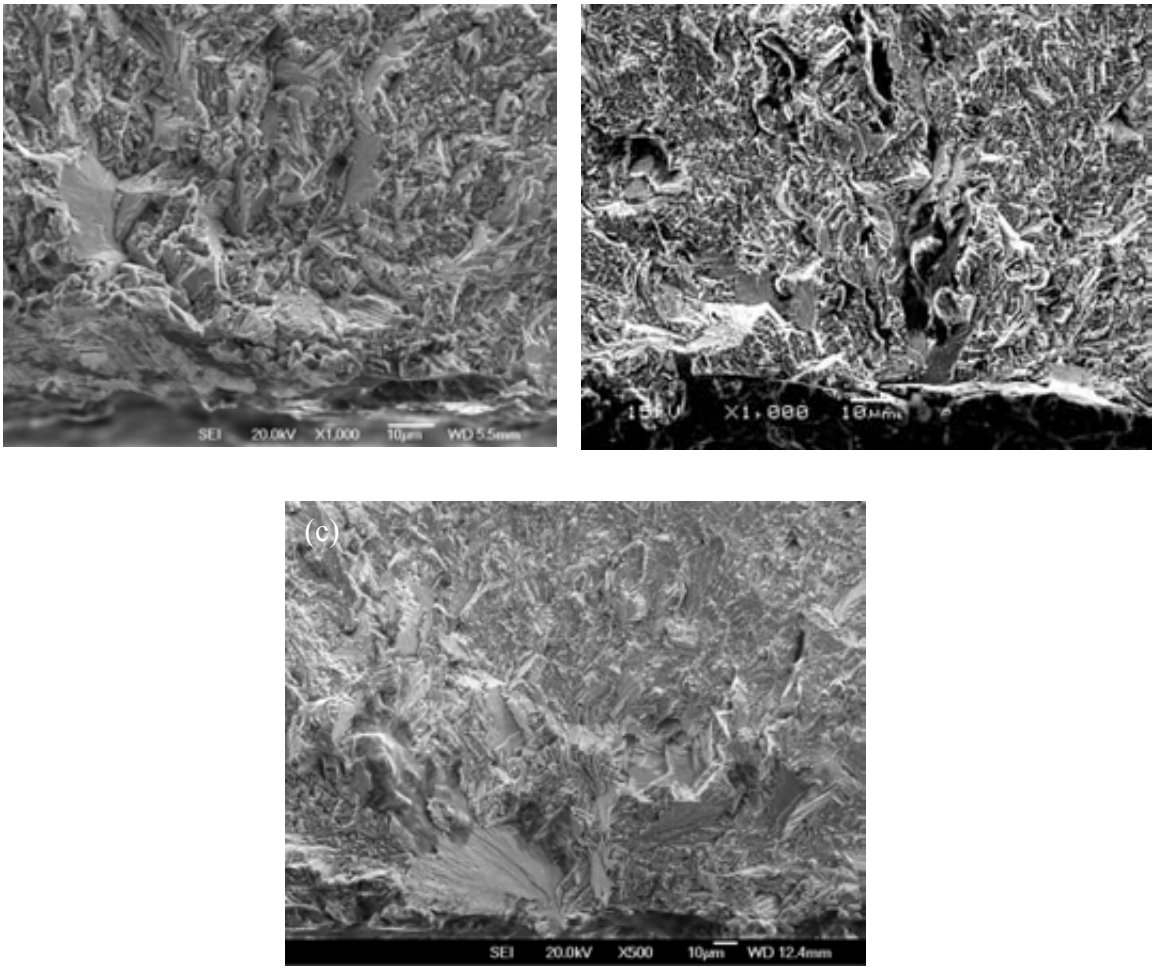

Figure 8.3 Secondary electron SEM micrographs showing the four-point bending fatigue crack initiation sites of the RR 1000 samples which were HIPped following the procedures (a) normal HIPping at 1107℃/100MPa/4h, tested at the stress range 90-900MPa and failed at 1.6336×10^6 cycles; (b) ramping up temperature first and pressure later, dwelt at 1107℃ /100MPa/2h, tested at the stress range 90-900MPa and failed at 0.9303×10^6 cycles; (c) normal HIPping at 1180℃/150MPa/4h, tested at 90~900MPa and failed at 0.99×10^6 cycles

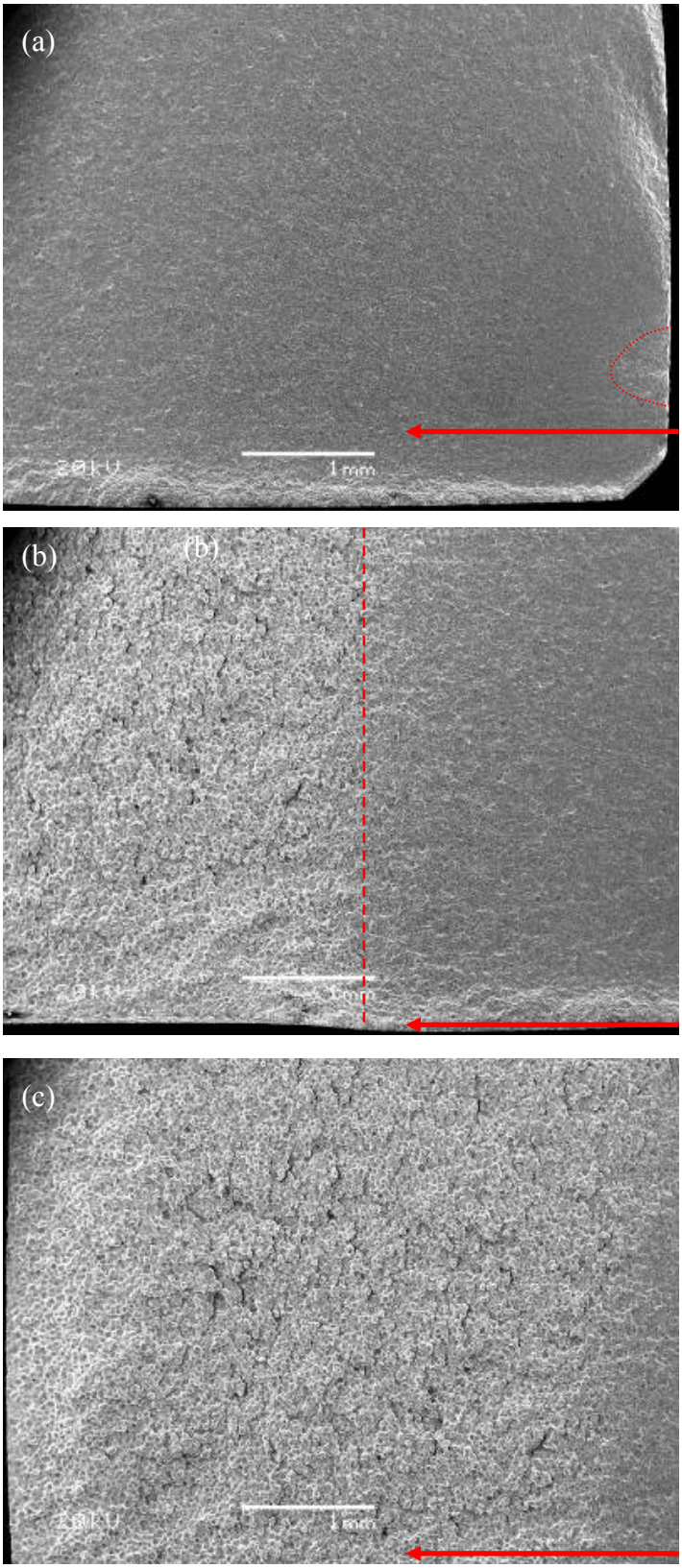

Figure 8.4 Secondary electron SEM micrographs showing the typical four-point bending fatigue fracture sequence: (a) fatigue crack initiation to striated propagation; (b) striated propagation to monotonic fracture; (c) monotonic fracture, the arrow showing the crack growth direction. Fatigue crack propagation followed a sequence: from (a) to (b) to (c)

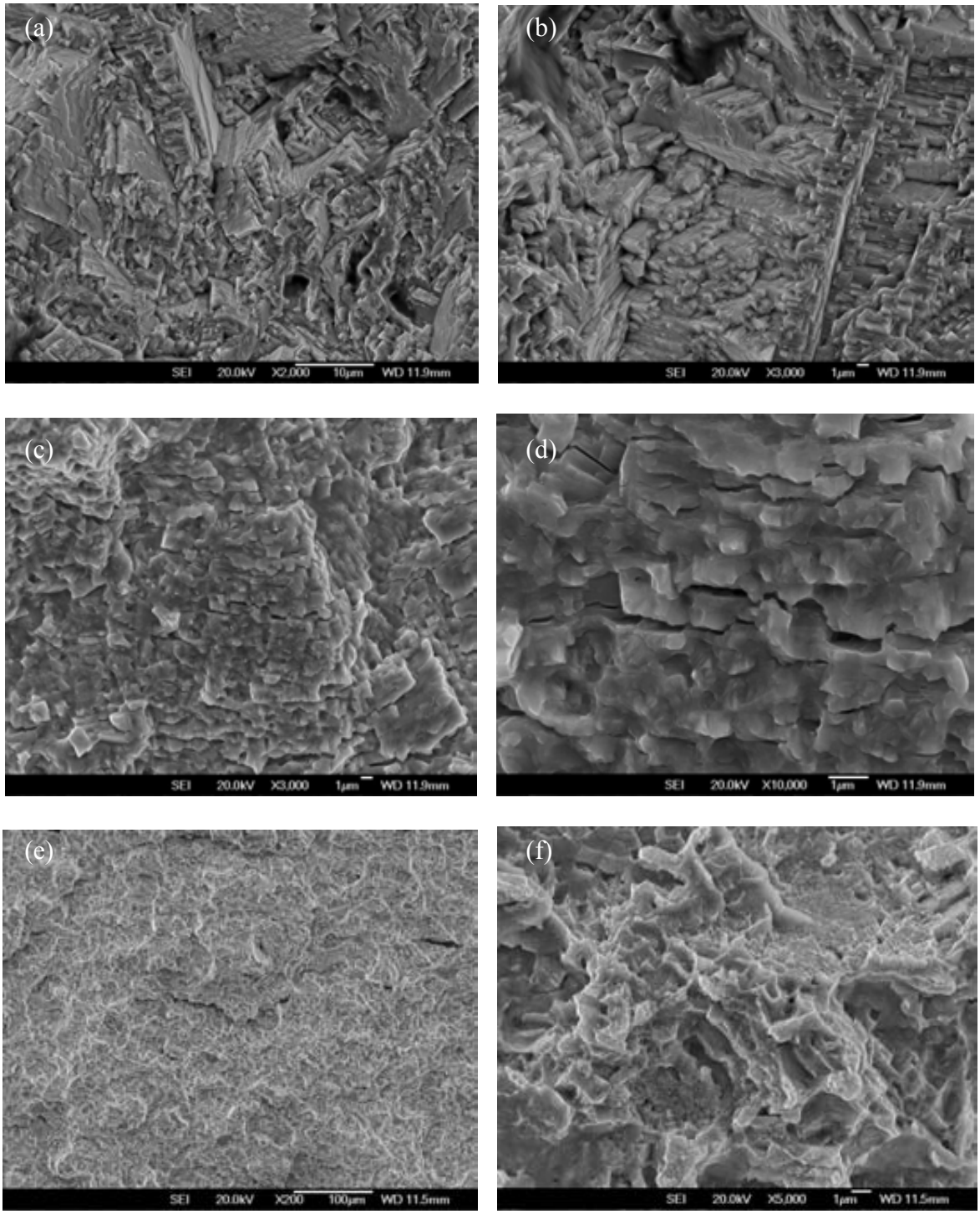

Figure 8.5 Secondary electron SEM micrographs showing the four-point bending fatigue crack propagation sequence and fracture feature of RR1000 samples at each stage, (a)(b)highly crystallographic and faceted crack propagation after crack initiation, in the near-threshold area and lower Paris regime; (c)(d)striated crack propagation in higher Paris regime; (e)(f)dimple-ductile crack propagation in the final monotonic/static fracture stage. The sample shown here was HIPped at 1180℃/150MPa/4h and tested at the stress range 95-950MPa and failed at 0.9086×10^{6} cycles.

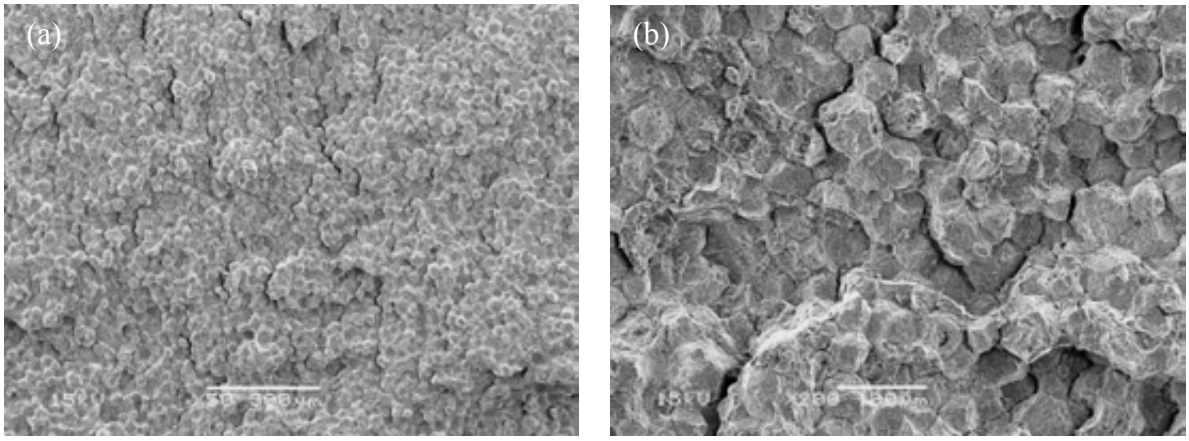

Figure 8.6 Secondary electron SEM micrographs showing the particle-debonding in the final monotonic fatigue crack propagation stage of the RR 1000 samples which were HIPped at 1107℃/100MPa/4h and tested at the stress range 90-900MPa and failed at 0.9303×10^6 cycles

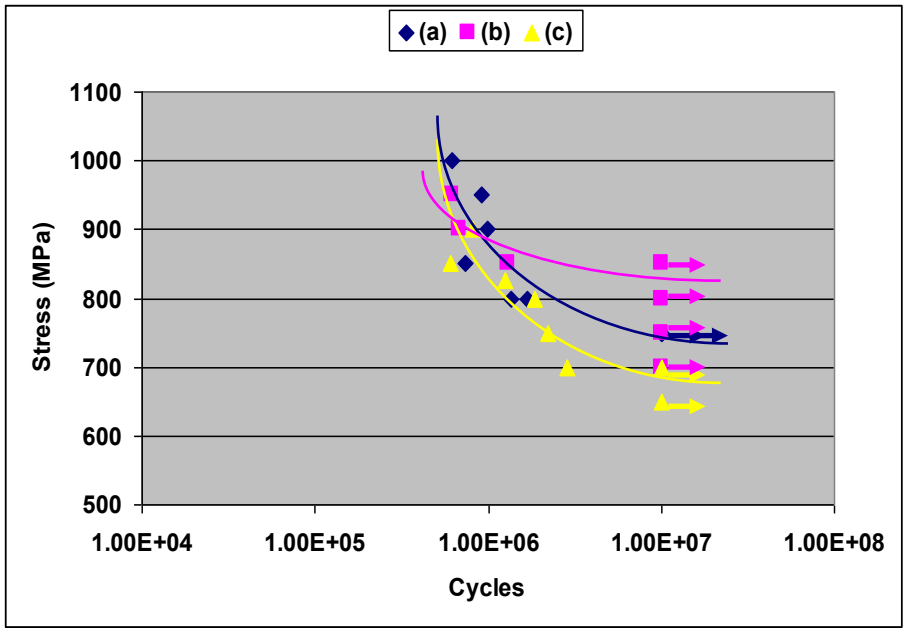

Figure 8.7 Room temperature four-point bending fatigue properties of RR 1000 samples (a) HIPped at 1180℃/150MPa/4h; (b)HIPped at 1180℃/150MPa/4h and then aged at 760℃/16h/AC; (c) HIPped at 1180℃/150MPa/4h, solution treated at 1120℃/2h/AC and then aged at 760℃/16h/AC. The lines were drawn based on the general trend of fatigue lifetime with stress level

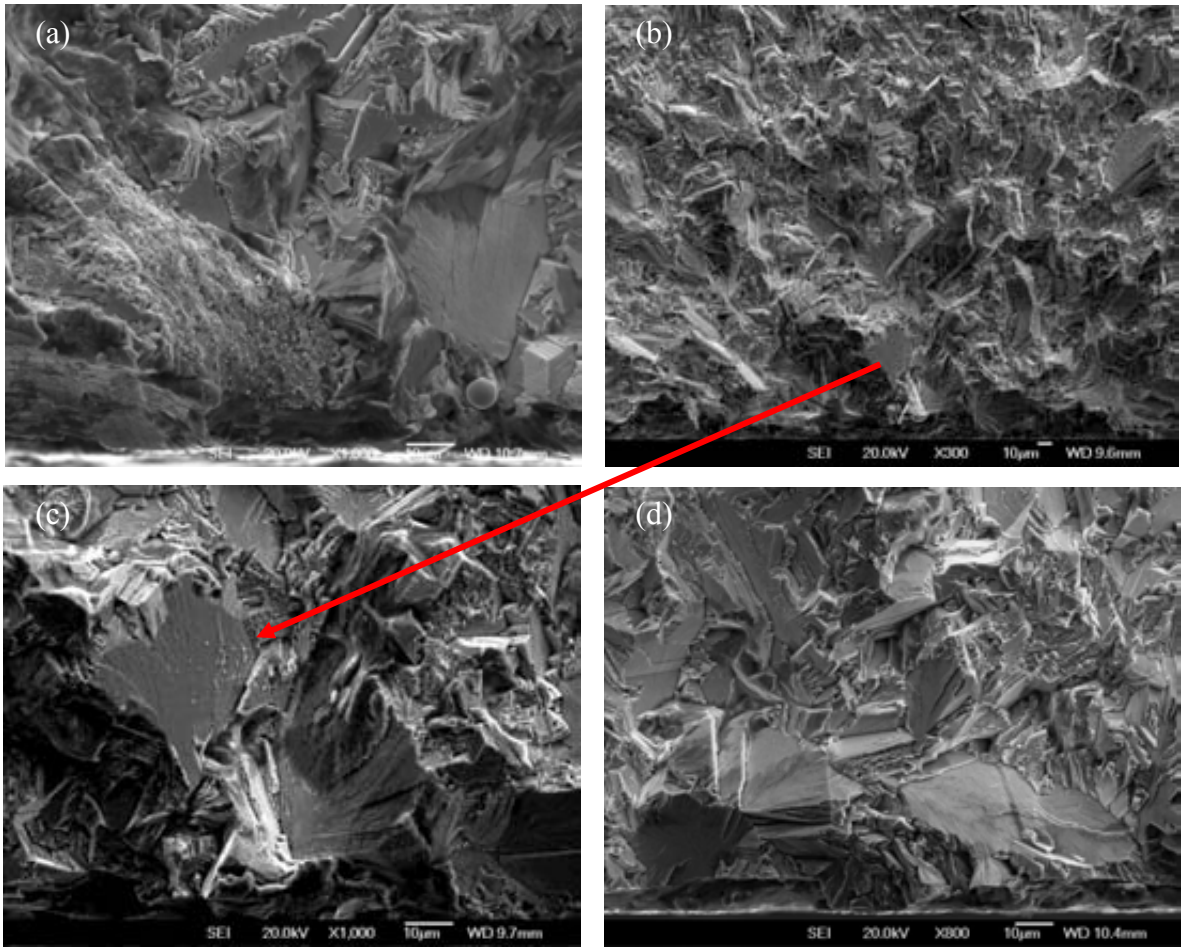

Figure 8.8 Secondary electron SEM micrographs showing the four-point bending fatigue crack initiators for the RR1000 samples HIPped at 1180℃/150MPa/4h, solution treated at 1120 ℃/2h/AC and then aged at 760℃/16h/AC, (a) tested at 70~700MPa, failed at 2.8397×10^6 cycles; (b)(c) tested at 75~750MPa, failed at 2.2087×10^6 cycles; (d) tested at 80~800MPa, failed at 1.8467×10^6 cycles.

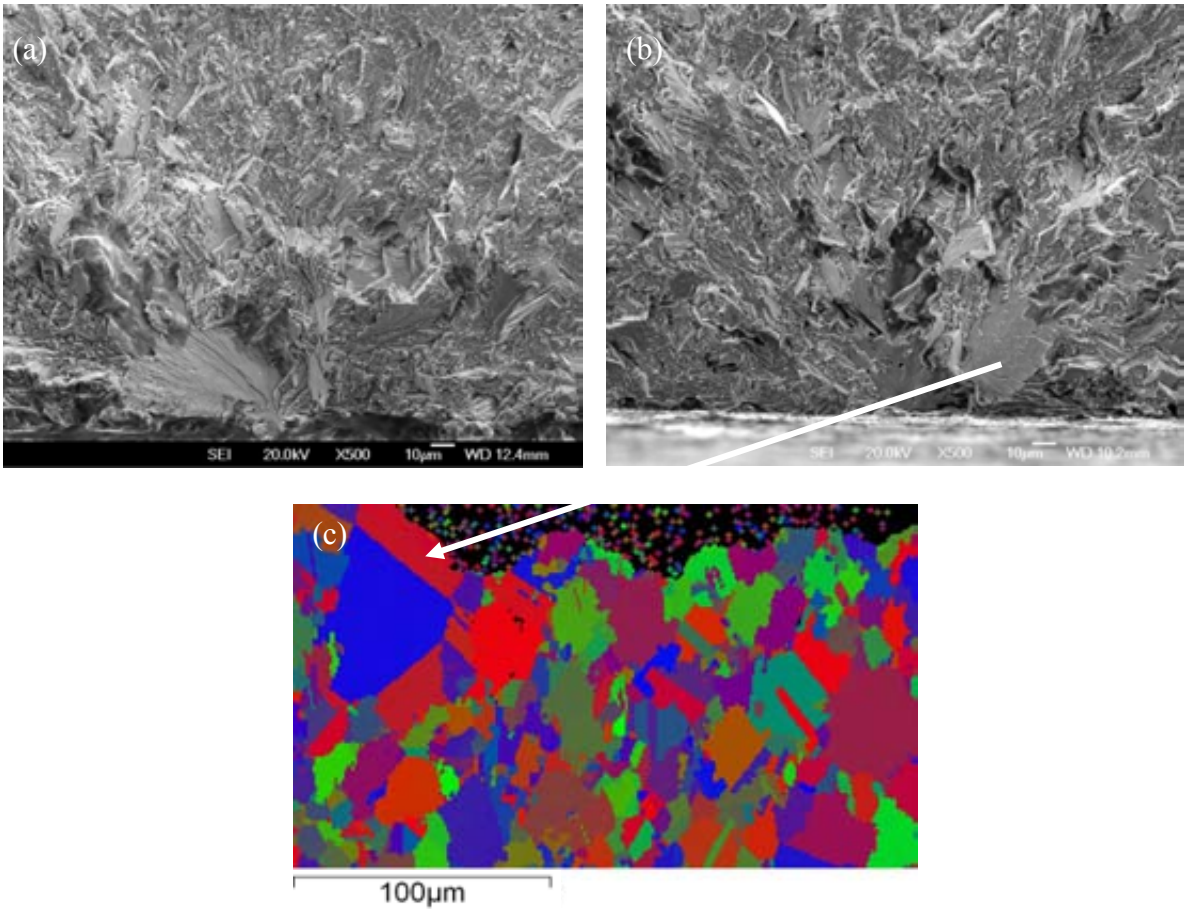

Figure 8.9 Secondary electron SEM micrographs showing the crack initiation at the large cleavage facets for the RR1000 samples after four-point bending fatigue testing, (a) HIPped at 1180℃/150MPa/4h, tested at 90~900MPa and failed at 0.99×10^6 cycles; (b) HIPped at 1180℃/150MPa/4h and then aged at 760℃/16h/AC, tested at 85~850MPa and failed at 1.29×10^6 cycles; (c) EBSD image showing the clustering of servarl large grains at the section of the fatigue crack initiation facets

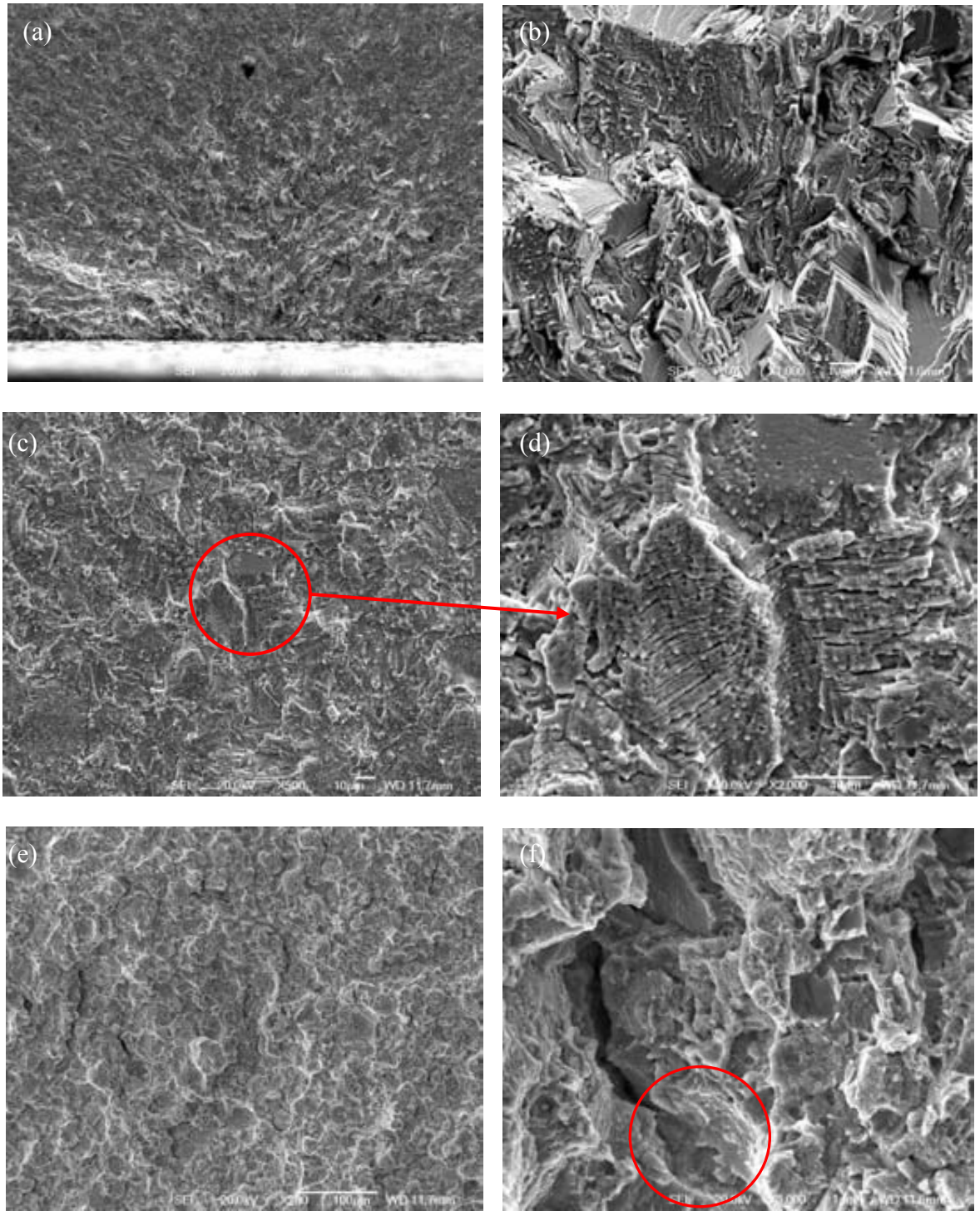
(a)
(b)
(c)
(d)
(e)
(f)

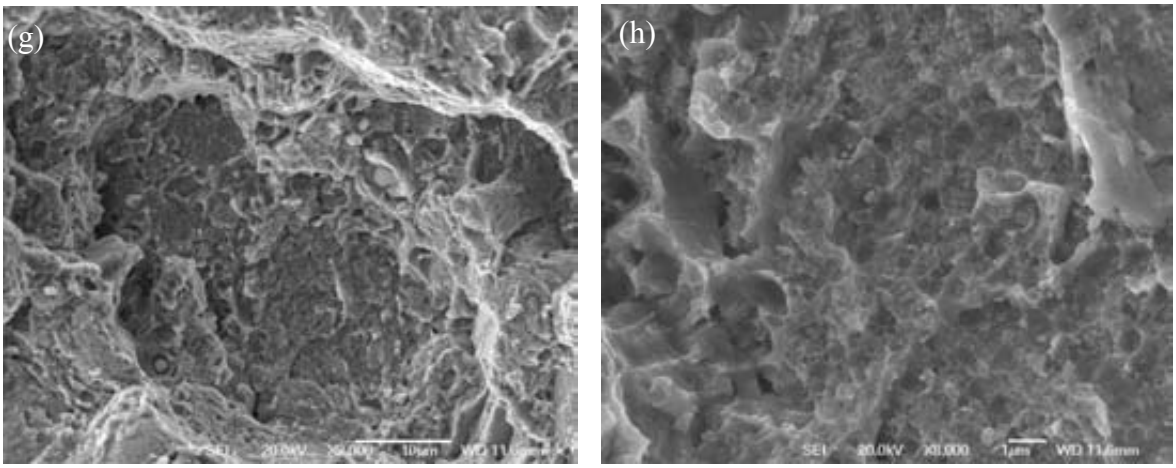

Figure 8.10 Secondary electron SEM micrographs showing the four-point bending fatigue crack propagation of a RR1000 sample that was HIPped at 1180℃/150MPa/4h, solution treated at 1120 ℃/2h/AC and then aged at 760℃/16h/AC, the sample failing at 0.6083×10^6 cycles at 85-850MPa stress range, (a)fatigue crack nucleation and progation at the early stage; (b)highly crystallographic and faceted crack propagation after crack initiation, in the near-threshold area and lower Paris regime; (c)(d)striated crack propagation in higher Paris regime; (e) generally dimple-ductile crack propagation in the final monotonic fracture stage; (f)-(h)crack propagation along remenant PPBs in in the final monotonic fracture stage

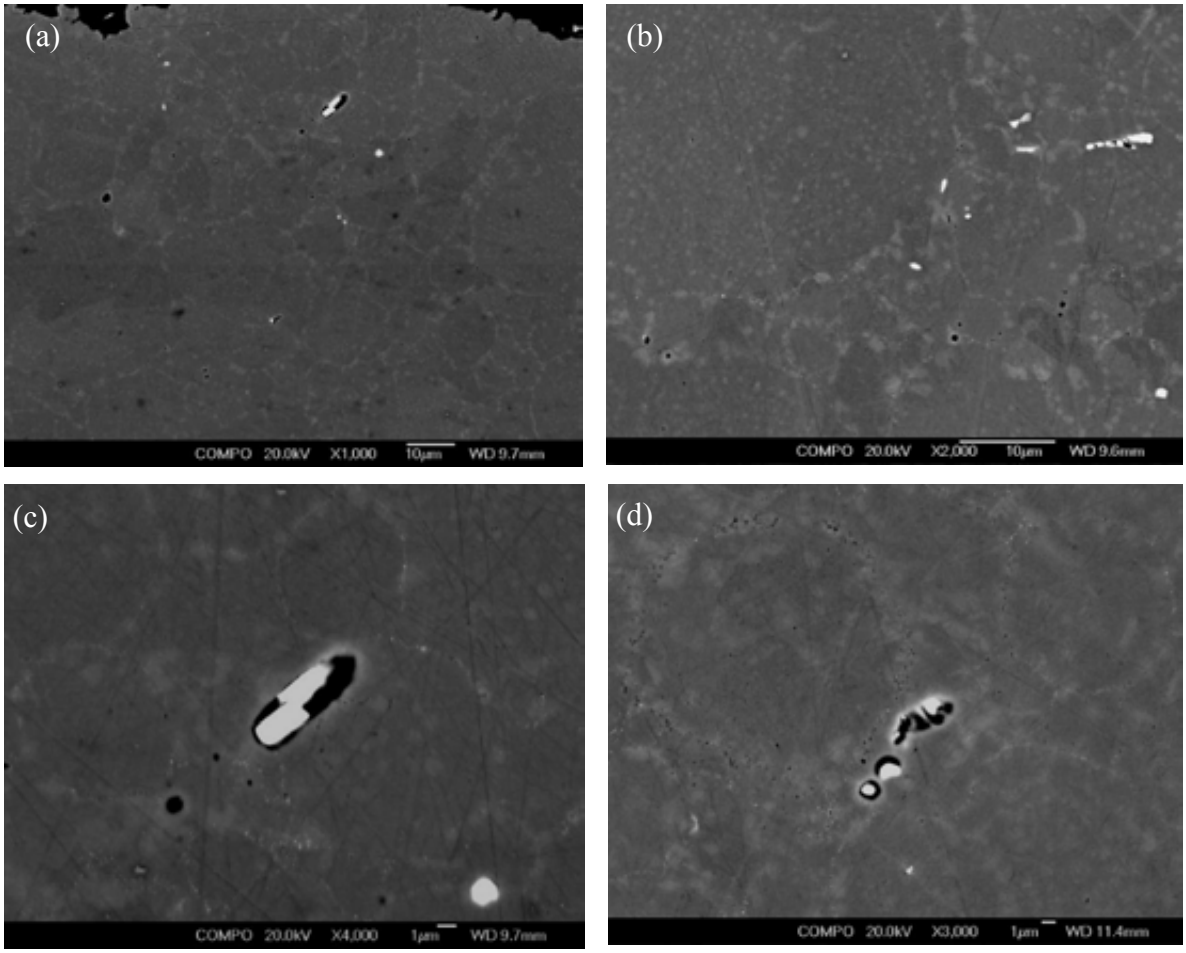

Figure 8.11 Back scattered SEM micrographs showing the voids and inclusions in the section of a RR 1000 sample after four-point bending fatigue testing. Some voids and secondary cracks are clearly associated with inclusion particles, see (c) and (d). The sample shown here was HIPped at 1180℃/150MPa/4h, solution treated at 1120℃/2h/AC and then aged at 760℃/16h/AC, failing at 0.6083×10^6 cycles at 85-850MPa stress range. The voids and inclusions-induced secondary cracks were also observed in other four-point bending fatigue tested samples irrespective of processing condition.

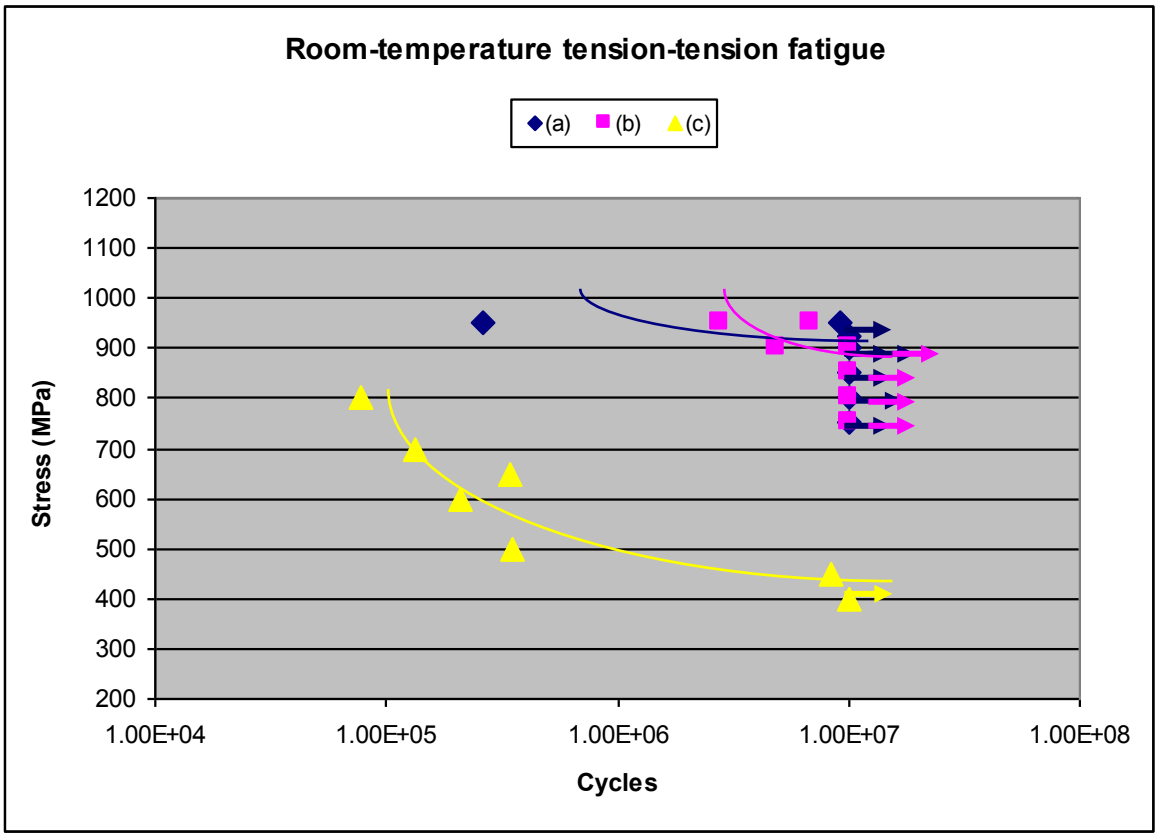

Figure 8.12 Room temperature tension-tension fatigue life of the samples, (a) HIP 1180℃ /150MPa/4h/FC + Aged 760℃/16h/AC; (b) HIP1180℃/150MPa/4h/FC+ ST1120℃/2h/AC+ Aged 760℃/16h/AC; (c) notched fatigue for samples processed under condition (b), Kt=2.26. The lines were drawn based on the general trend of fatigue lifetime with stress level.

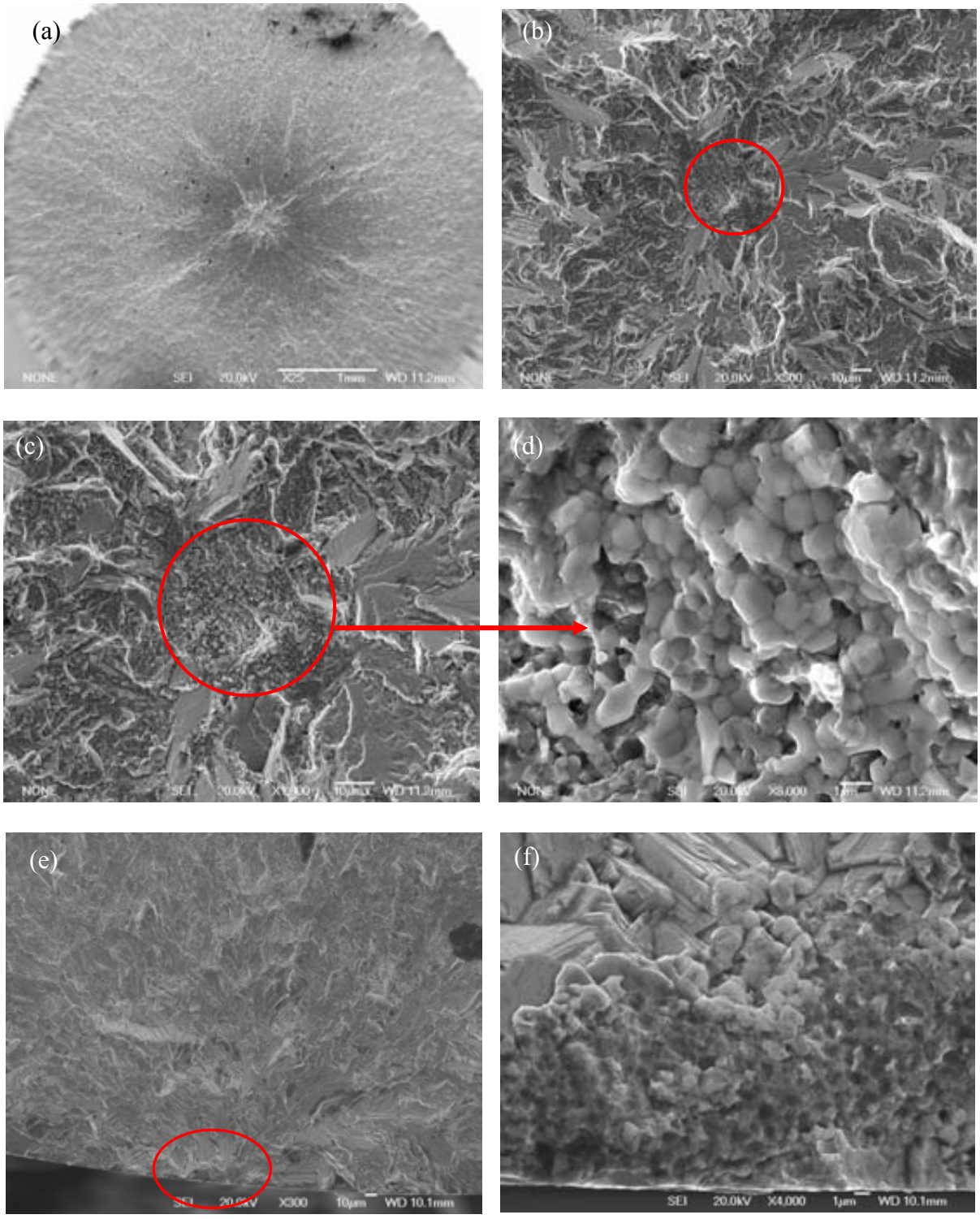

Figure 8.13 Secondary electron SEM micrographs showing the fatigue crack initiation at clusters of inclusions (a)-(d) either in the interior of a sample, failed at 9.2189×10^6 cycles; or (e)-(f) in the surface region, failed at 0.2648×10^6 cycles. The two samples were HIPped at 1180℃/150MPa/4h and then aged at 760℃/16h/AC and tested at the same stress range (95-950MPa).

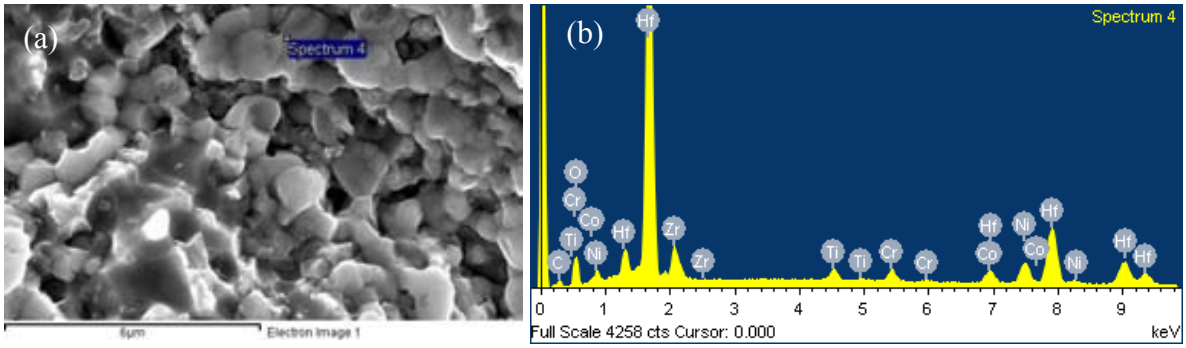

Figure 8.14 (a) secondary electron SEM micrograph showing inclusion particles (also shown in Figure 8.13(d)) for EDX analysis; (b) EDX analysis showing the composition of one of the inclusion particles which was shown to be rich of Hf, Zr and O.

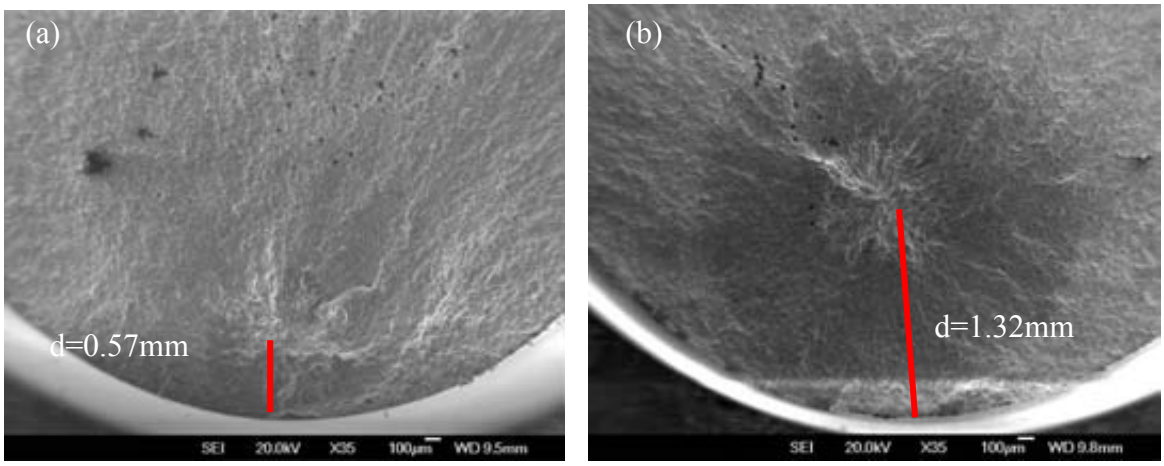

Figure 8.15 Secondary electron SEM micrographs showing the distance, d, from fatigue crack initiator to the sample surface after room temperature tension-tension fatigue test (tested at a stress range of 95~ 950MPa): (a) failed at 2.7886×10^6 cycles, d=0.57mm; (b) failed at 6.9034×10^6 cycles, d=1.32mm. The samples were HIPped at 1180℃/150MPa/4h, solution treated at 1120 ℃/2h/AC and then aged at 760℃/16h/AC

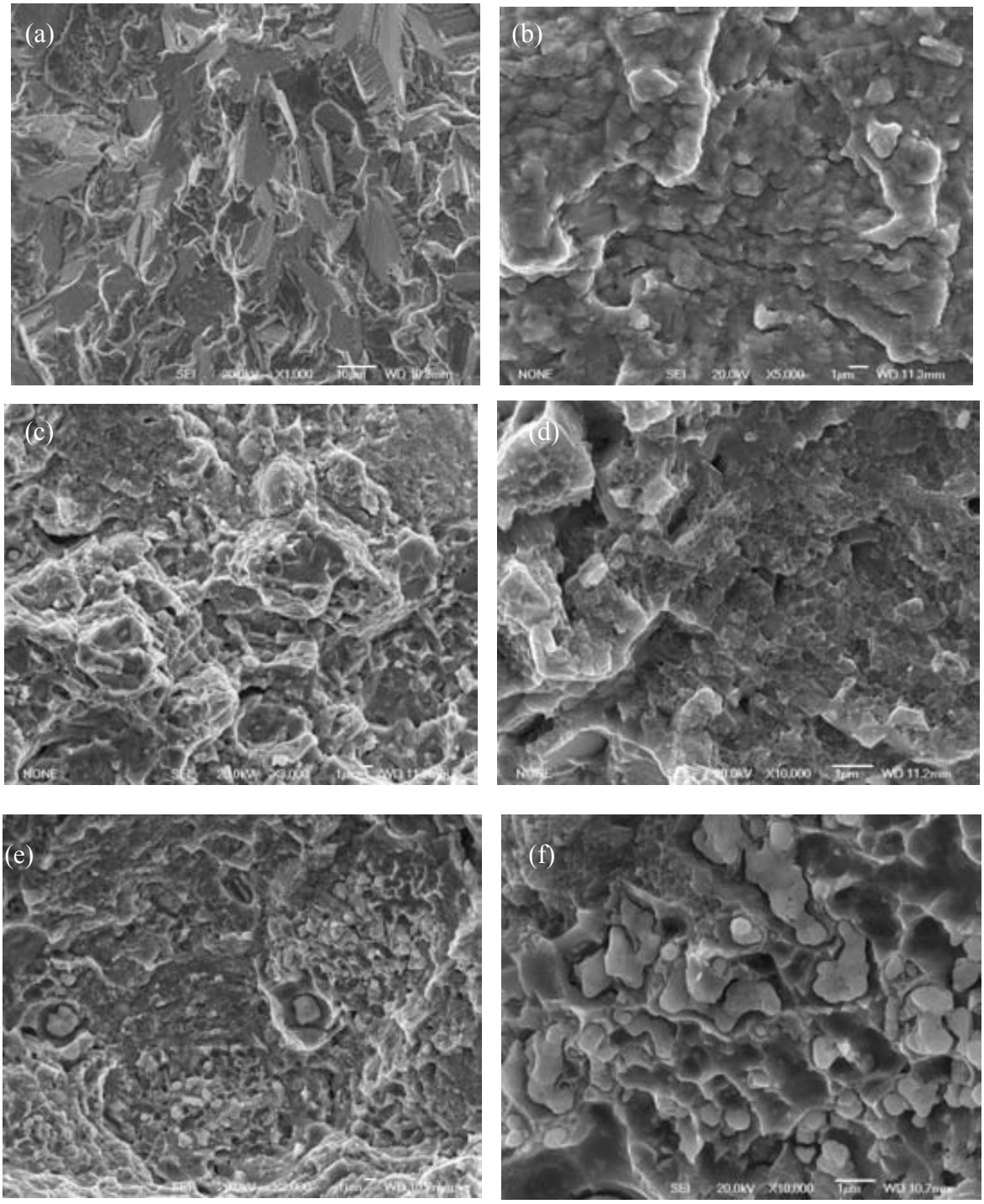

Figure 8.16 Secondary electron SEM micrographs showing the room temperature tension-tension fatigue fracture surfaces of a RR1000 sample, (a) cleavage facets at the lower Paris regime; (b) fatigue striations at the upper Paris regime; (c)(d) dimple-fracture at the high ΔK regime of the fatigue crack growth, and (e)(f) crack propagation at the sites of inclusion clusters. The sample shown here was HIPped at 1180℃/150MPa/4h, solution treated at 1120℃/2h/AC and then aged at 760℃/16h/AC, and tested at the stress range 95-950MPa and failed at 6.9034×10^6 cycles

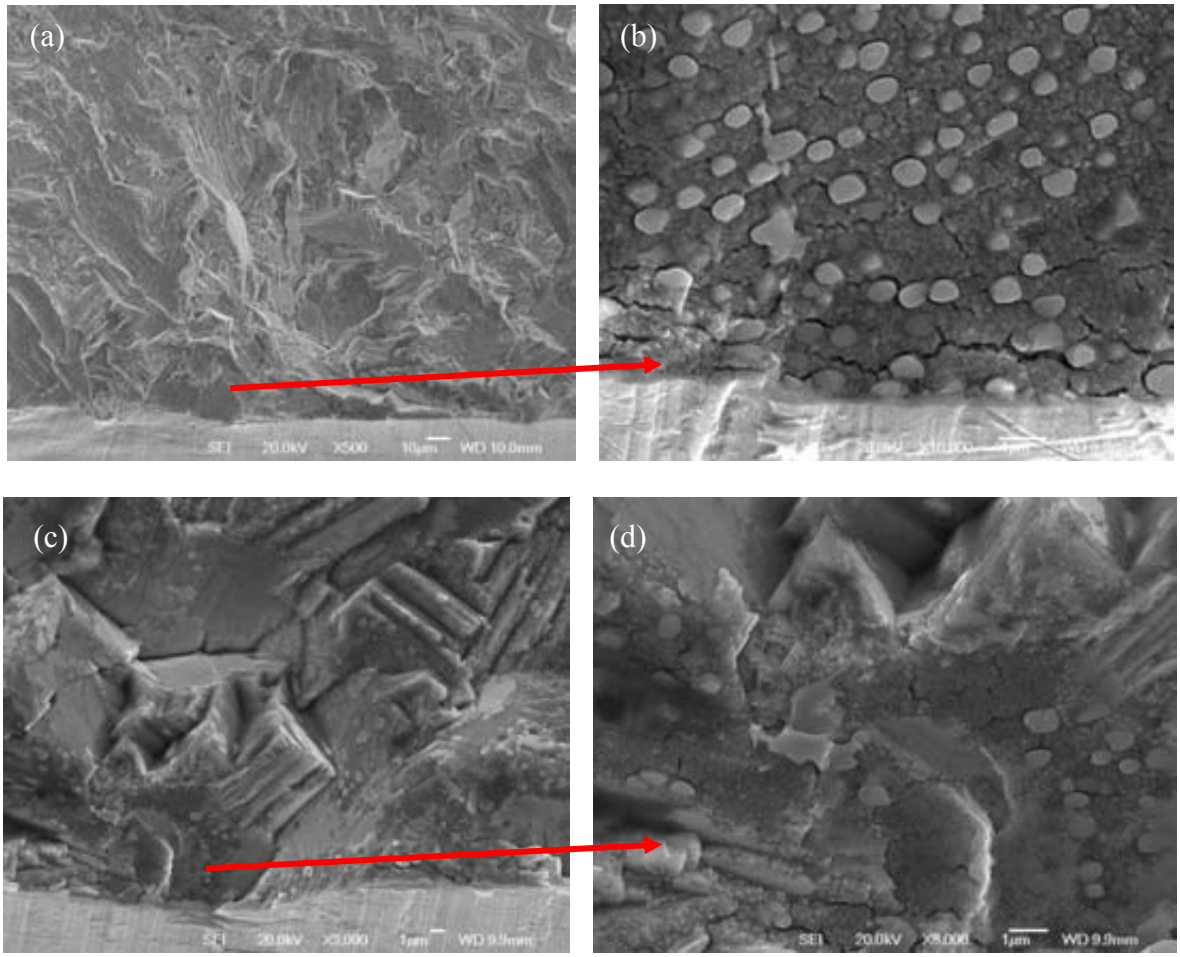

Figure 8.17 Secondary electron SEM micrographs showing the fatigue crack initiation sites for a notched sample after room temperature tension-tension fatigue test at 45-450MPa, failing at 8.4088×10^6 cycles. The sample shown here was HIPped at 1180℃/150MPa/4h, solution treated at 1120 ℃/2h/AC and then aged at 760℃/16h/AC.

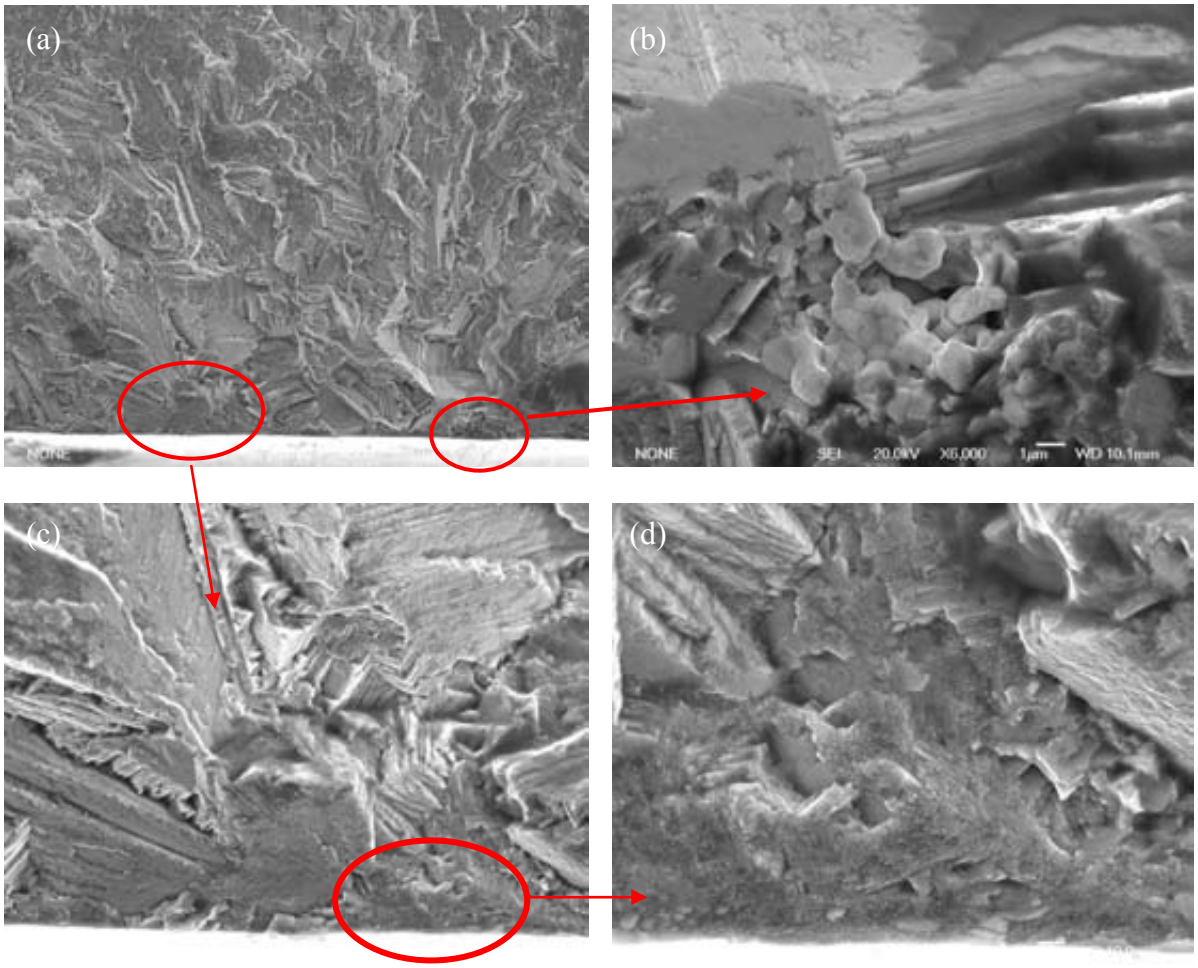

Figure 8.18 Secondary electron SEM micrographs showing the fracture crack initiation sites for a notched sample after room temperature tension-tension fatigue test at 65-650MPa, failing at 0.3424×10^6 cycles. The sample was HIPped at 1180℃/150MPa/4h, solution treated at 1120 ℃/2h/AC and then aged at 760℃/16h/AC

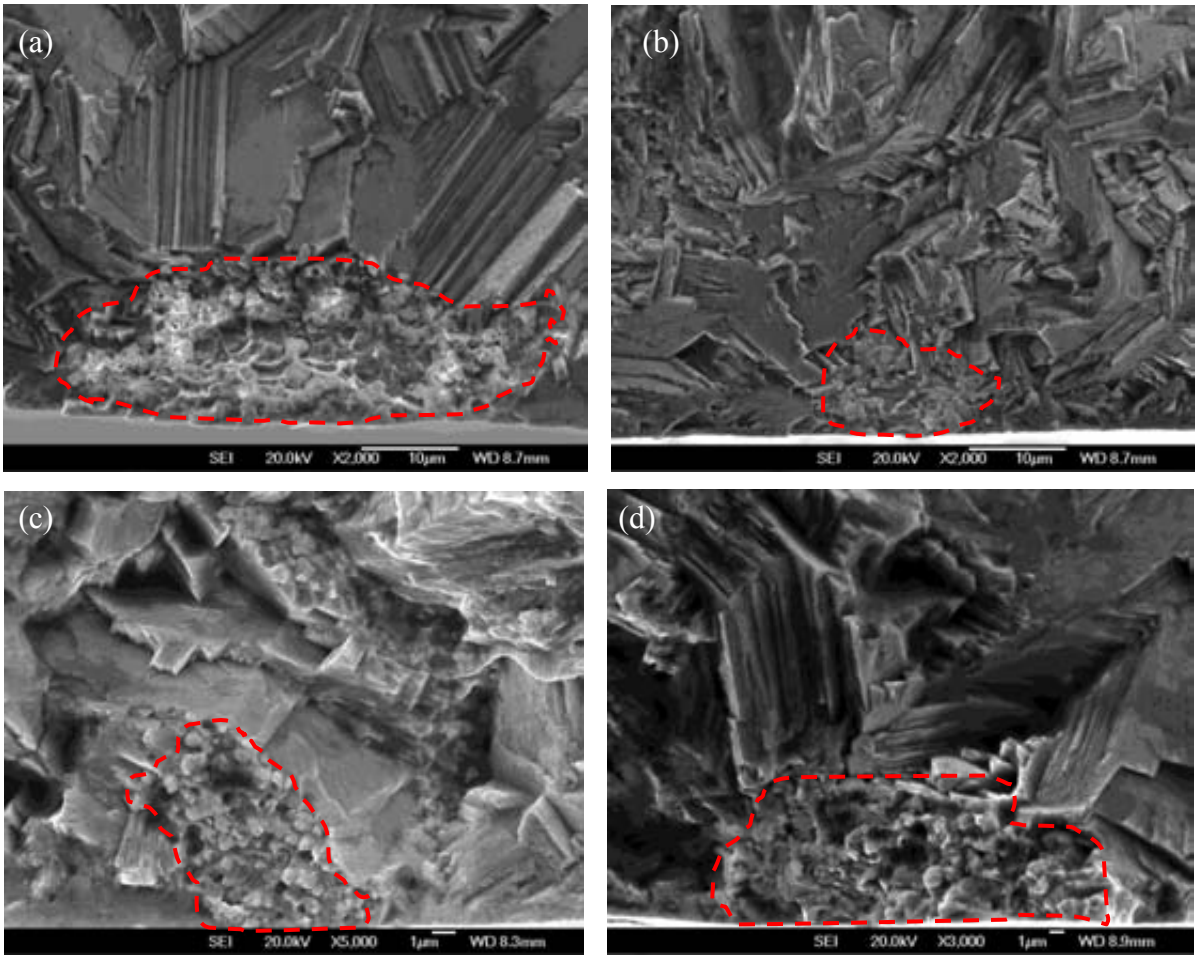

Figure 8.19 Secondary electron SEM micrographs showing the fatigue crack initiation site of notched samples after room temperature tension-tension fatigue test at (a) 50-500MPa, failed at 0.3482×10^{6} cycles; (b)60-600MPa, failed at 0.2074×10^{6} cycles; (c)70-700MPa, failed at 0.1342×10^{6} cycles; (d)80-800MPa, failed at 0.0776×10^{6} cycles. The samples were HIPped at 1180℃/150MPa/4h, solution treated at 1120 ℃/2h/AC and then aged at 760℃/16h/AC

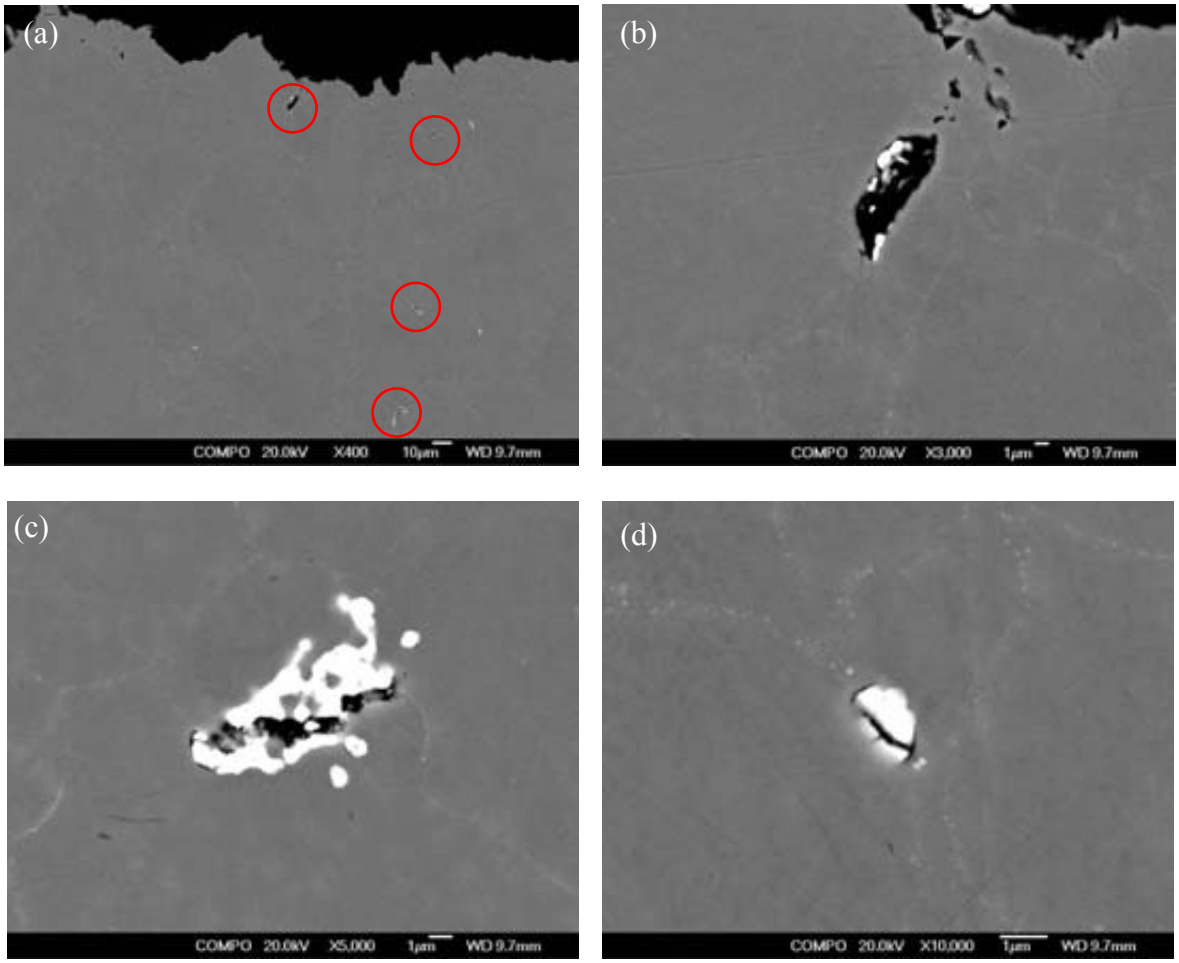

Figure 8.20 Back scattered SEM micrographs showing the inclusions and secondary cracks on the section of RR 1000 plain samples after room temperature tension-tension fatigue test. The sample shown here was HIPped at 1180℃/150MPa/4h, solution treated at 1120 ℃ /2h/AC and then aged at 760℃/16h/AC, and tested at the stress range 95-950MPa and failed at 2.7886×10^{6} cycles

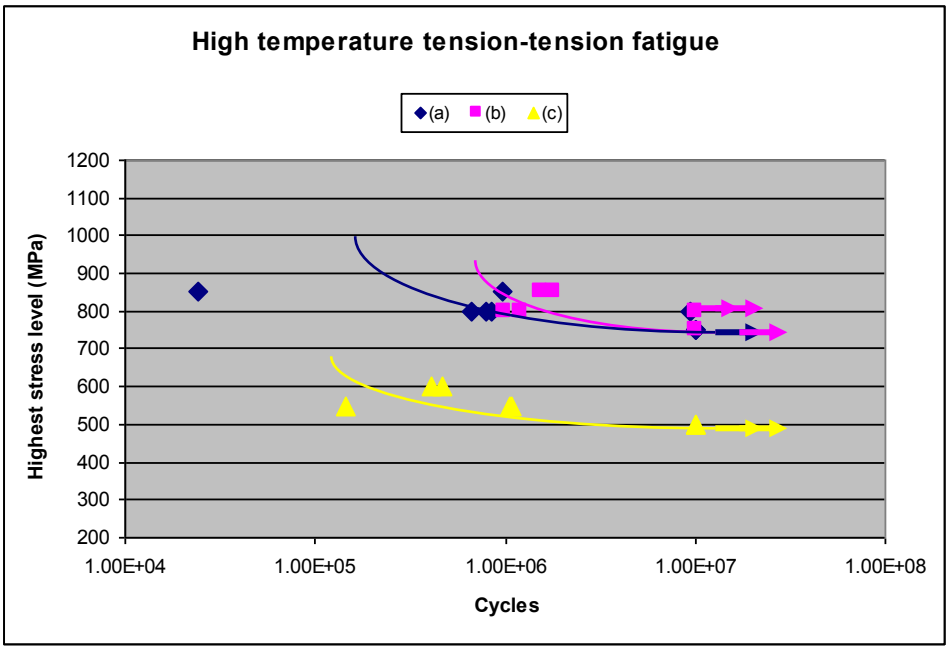

Figure 8.21 Tension-tension fatigue properties of samples tested at 700℃, (a) HIP 1180℃ /150MPa/4h/FC + Aged 760℃/16h/AC; (b) HIP1180℃/150MPa/4h/FC+ ST1120℃/2h/AC+ Aged 760 ℃ /16h/AC; (c) tension-tension fatigue for notched samples prepared using processing condition (b), the stress concentration factor at the notch is K_t=2.26. The lines were drawn based on the general trend of fatigue lifetime with stress level

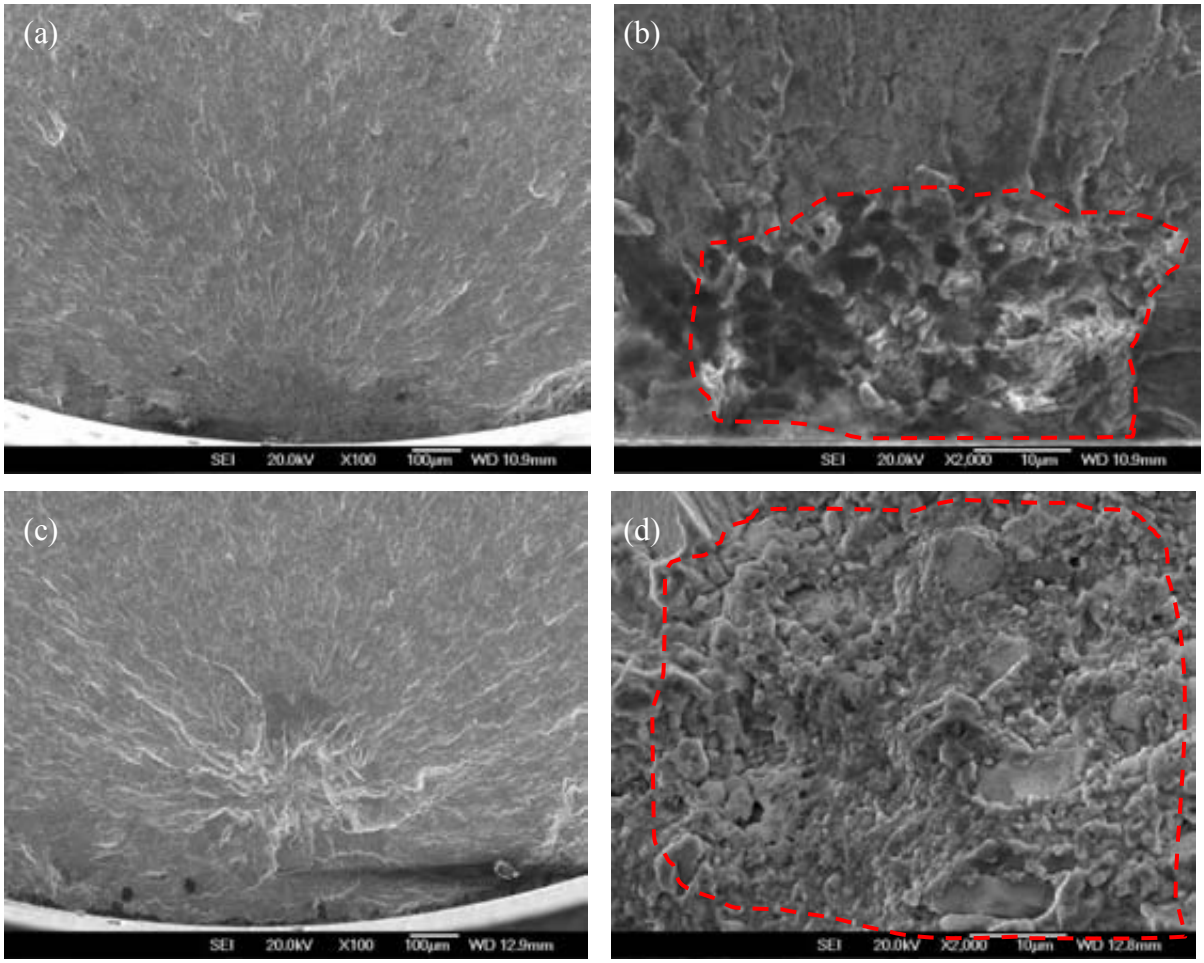

Figure 8.22 Secondary electron SEM micrographs showing the crack initiation sites and origins of samples after tension-tension fatigue test at 700℃. The samples investigated were all HIPped at 1180℃/150MPa/4h+Aged 760℃/16h/AC and tested at 85~850MPa. (a)(b) failed at 0.0246×10^6 cycles; (c)(d) failed at 0.9667×10^6 cycles.

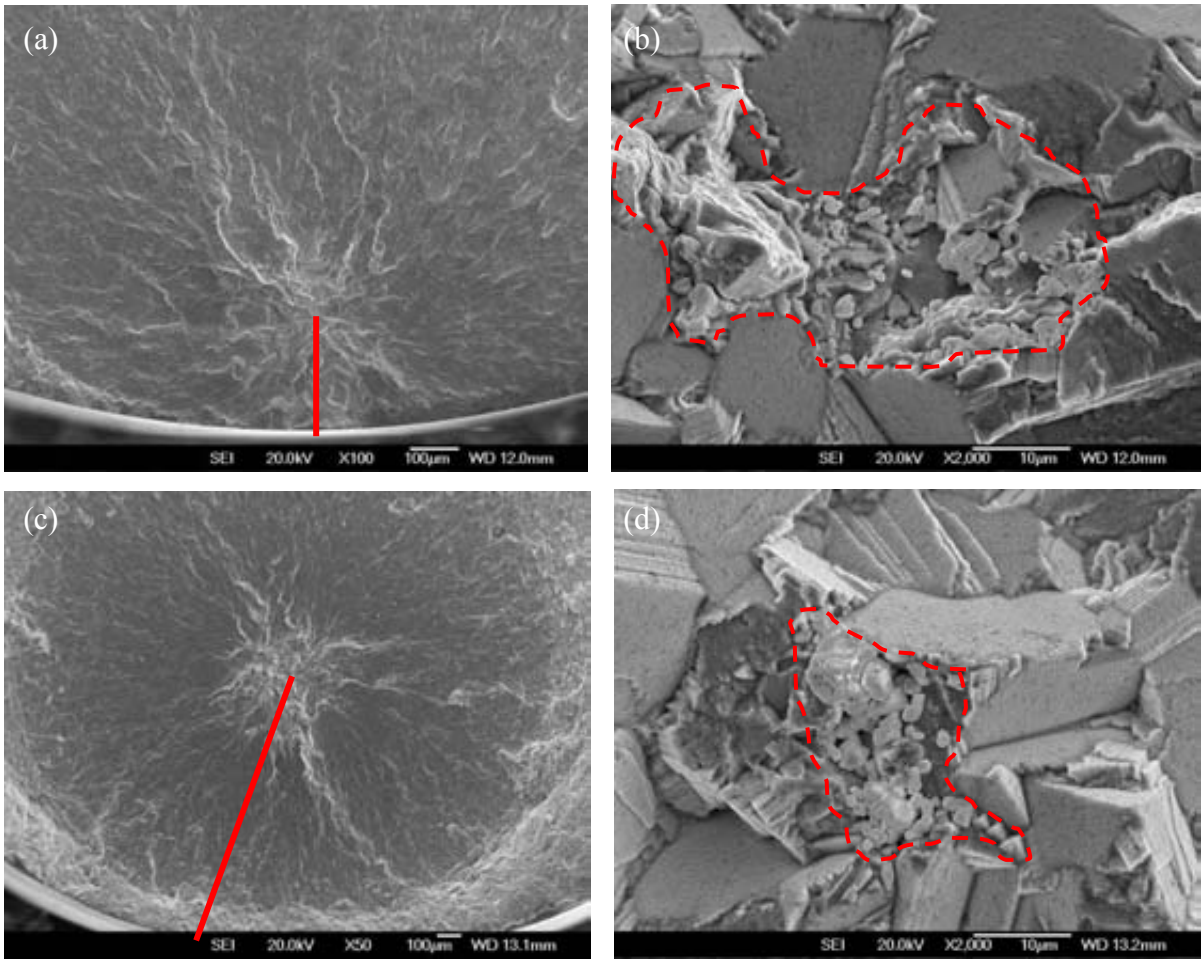

Figure 8.23 Secondary electron SEM micrographs showing the crack initiation sites and origins of samples after tension-tension fatigue test at 700℃. The samples investigated were all HIPped at 1180℃/150MPa/4h+Solution treated at 1120℃/2h/AC+Aged 760℃/16h/AC and tested at 80~800MPa. (a)(b) failed at 0.9933×10^6 cycles; (c)(d) failed at 1.1947×10^6 cycles.

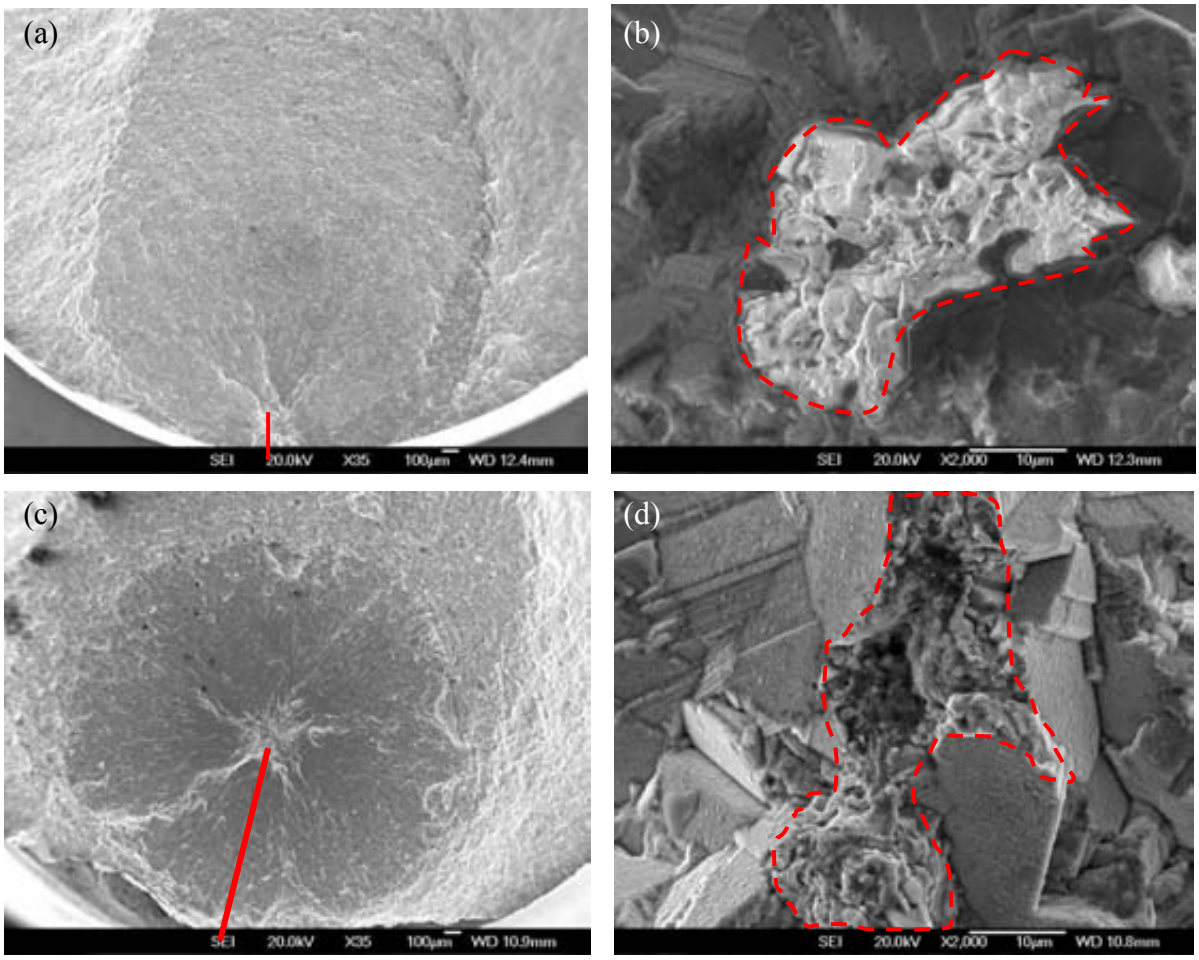

Figure 8.24 Secondary electron SEM micrographs showing the crack initiation sites and origins of samples after tension-tension fatigue test at 700℃. The samples investigated were all HIPped at 1180℃/150MPa/4h+Solution treated at 1120℃/4h/AC+Aged 760℃/16h/AC and tested at 85~850MPa. (a)(b) failed at 1.5393×10^6 cycles; (c)(d) failed at 1.7901×10^6 cycles.

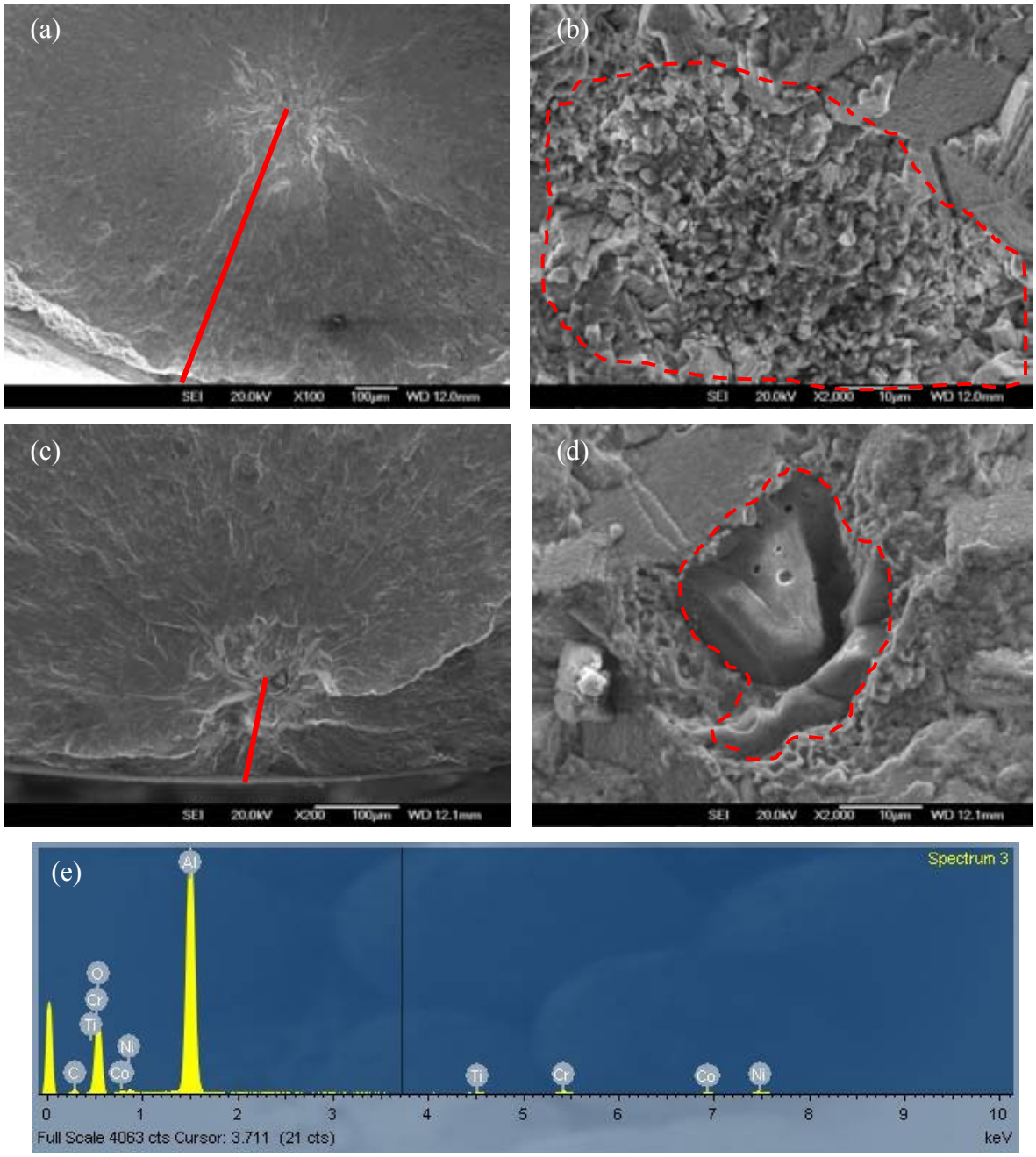

Figure 8.25 Secondary electron SEM micrographs showing the crack initiation sites and origins of samples after tension-tension fatigue test at 700℃. The samples investigated were all HIPped at 1180℃/150MPa/4h+Aged 760℃/16h/AC and tested at 80~800MPa. (a)(b) failed at 0.7898×10^6 cycles; (c)(d) failed at 9.3996×10^6 cycles; (e)EDX analysis showing the composition of the inclusion in Figure 8.25(d), suggesting that this inclusion should be Al_2O_3.

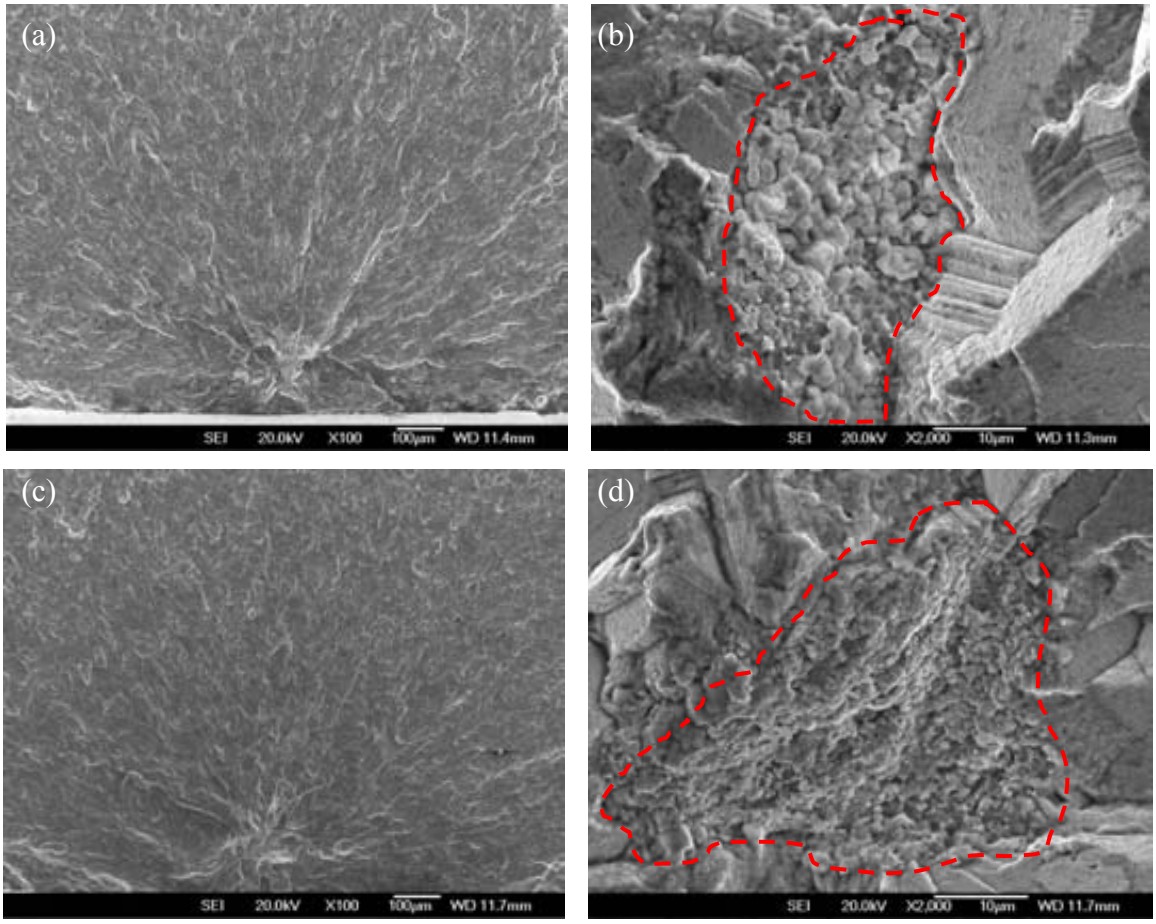

Figure 8.26 Secondary electron SEM micrographs showing the crack initiation sites and origins of notched samples after tension-tension fatigue test at 700℃. The samples investigated were all HIPped at 1180℃/150MPa/4h+Solution treated at 1120℃/4h/AC+Aged 760℃/16h/AC and tested at 60~600MPa. (a)(b) failed at 0.4083×10^6 cycles; (c)(d) failed at 0.4619×10^6 cycles.

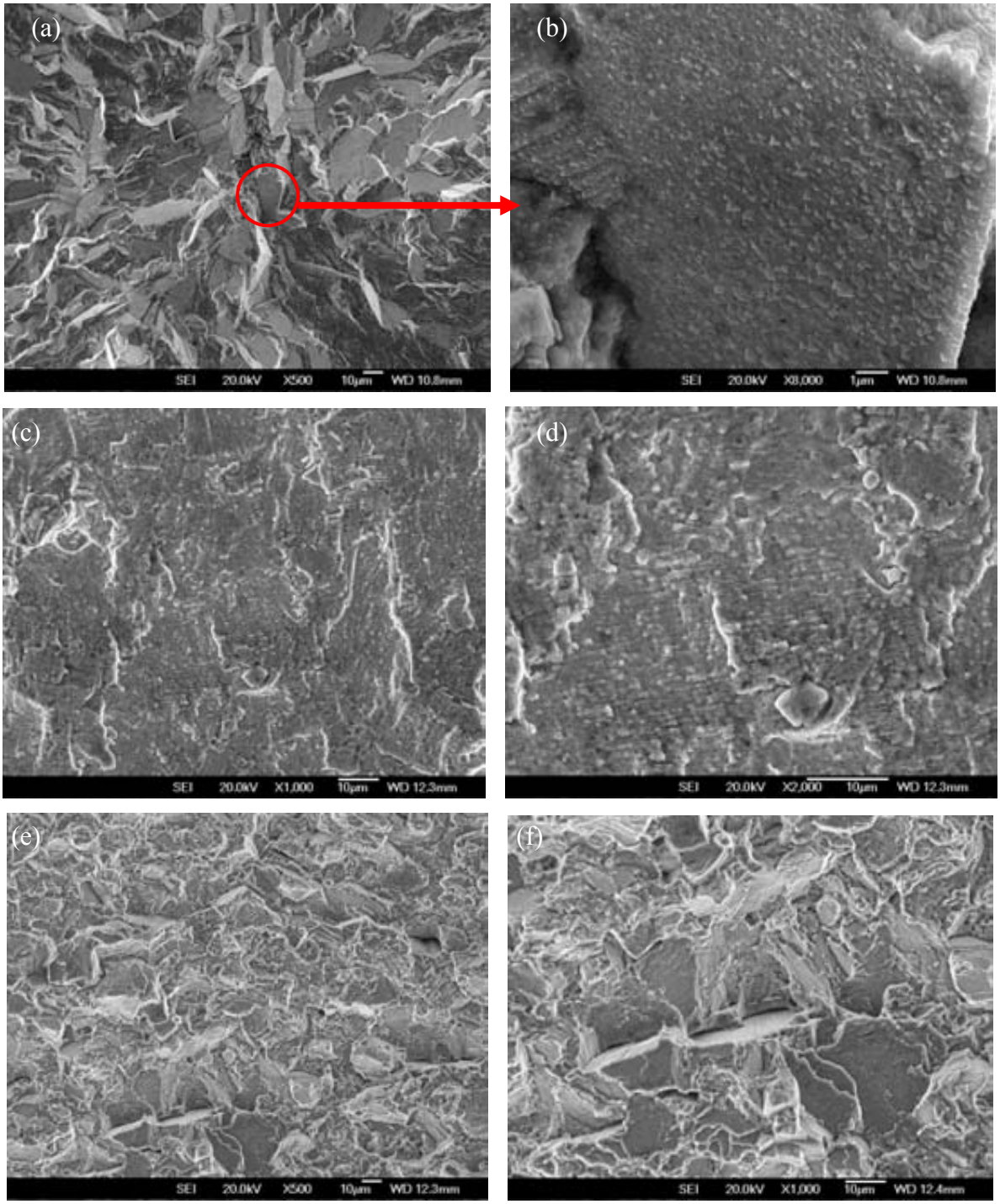

Figure 8.27 Secondary Electron SEM micrographs showing the fracture surface of samples after tension-tension fatigue test at 700℃, (a)(b)crystallographic and faceted fracture after crack initiation; (c)(d)fracture in a ductile striation mode; (e)(f)transgranular fracture in the final crack propagation stage. The samples shown here was HIPped at 1180 ℃ /150MPa/4h+Solution treated at 1120 ℃ /2h/AC+Aged 760 ℃ /16h/AC and tested at 80~800MPa, failed at 1.1947×10^{6} cycles.

Figure 8.28 Photographs showing the samples after tension-tension fatigue testing, (a) tested at room temperature; (b) tested at 700℃. I, HIP1180℃/150MPa/4h+Aged760℃/16h/AC, plain samples; II, HIP1180℃/150MPa/4h+Solution treated 1120℃/2h/AC+Aged 760℃/16h/AC, plain samples; III, HIP1180℃/150MPa/4h+Solution treated 1120℃/2h/AC+Aged 760℃/16h/AC, notched samples.

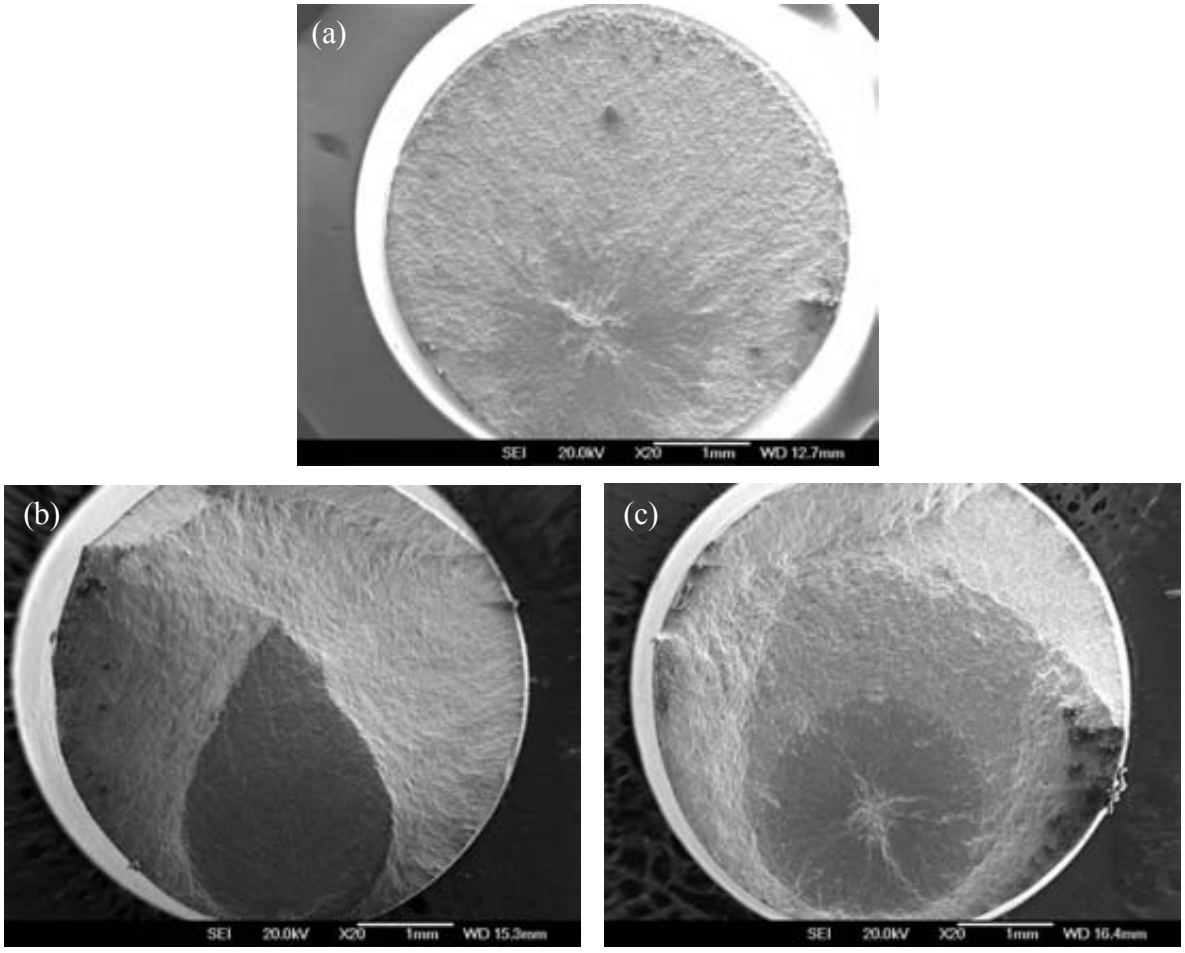

Figure 8.29 Secondary Electron SEM micrographs showing the typical general fracture surface of plain samples after tension-tension fatigue test (a) at room temperature, very flat fracture surface; (b)-(c) at 700℃, mixed fracture surfaces including both flat and slant fracture parts.

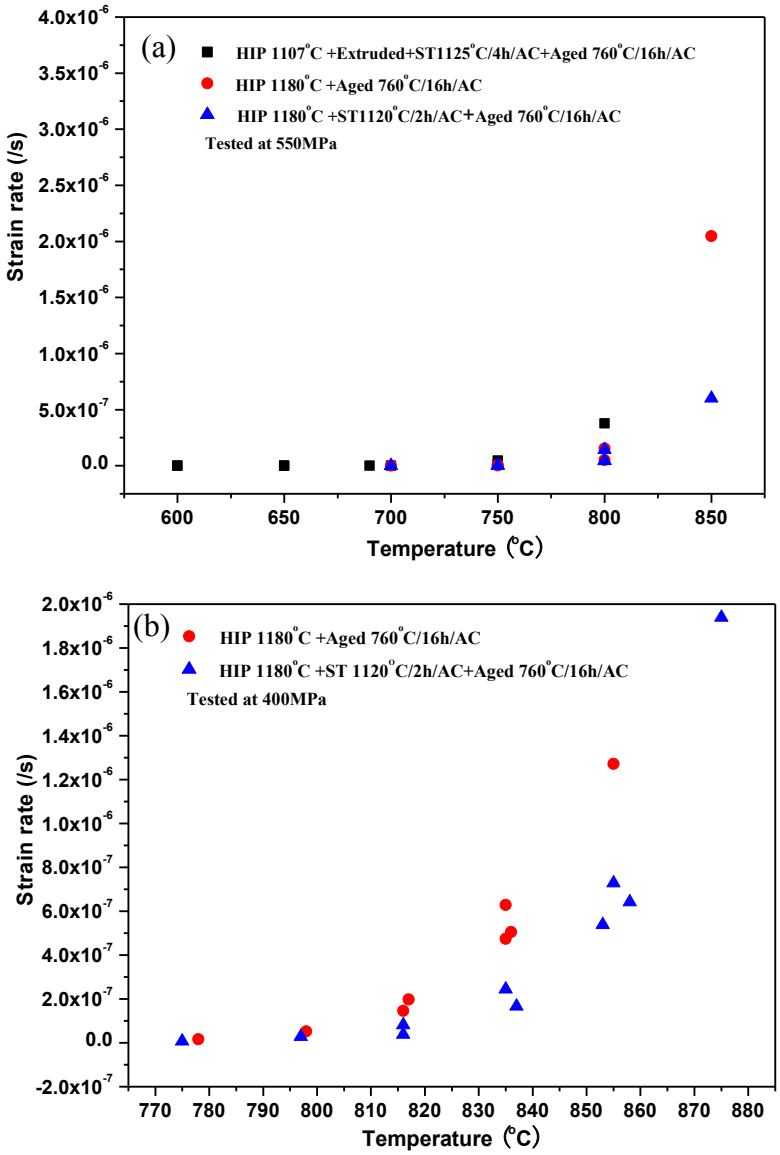

Figure 8.30 Dependence of the creep rate on temperature for RR 1000 samples obtained from different processing conditions, (a) tested at 550MPa; (b) tested at 400MPa.

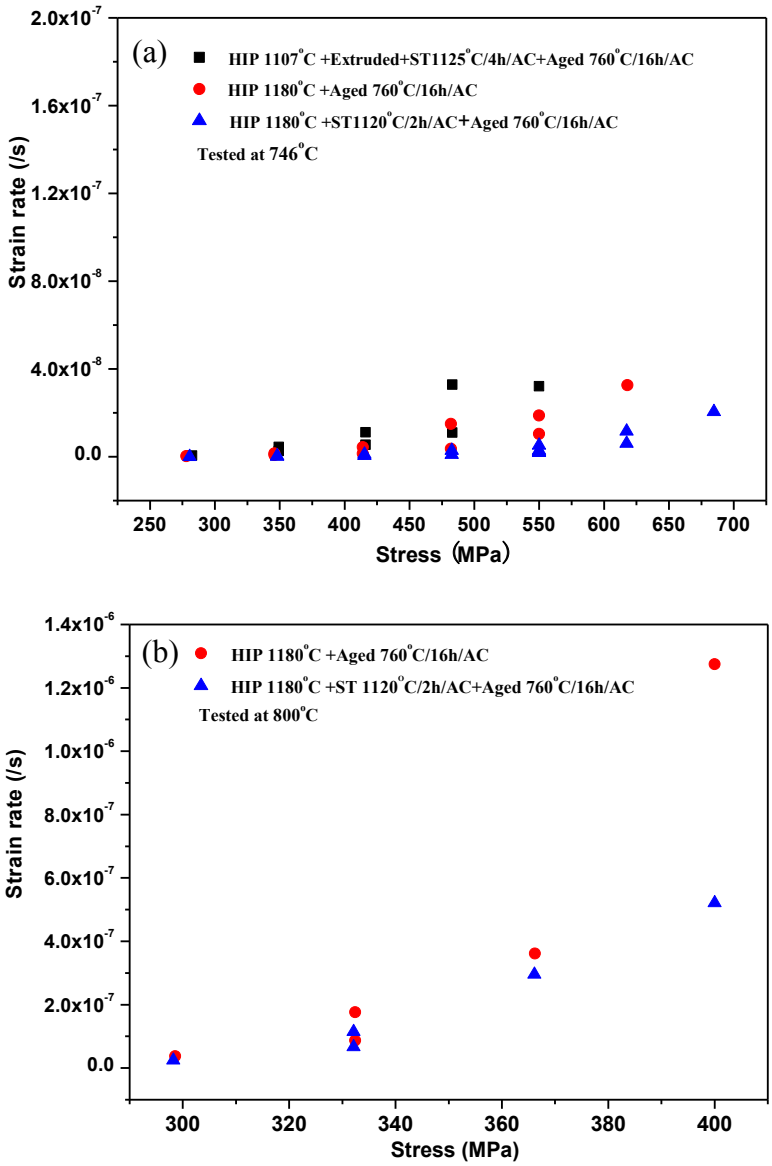

Figure 8.31 Dependence of the creep rate on applied stress for RR 1000 samples obtained from different processing conditions, (a) tested at 746℃; (b) tested at 800℃

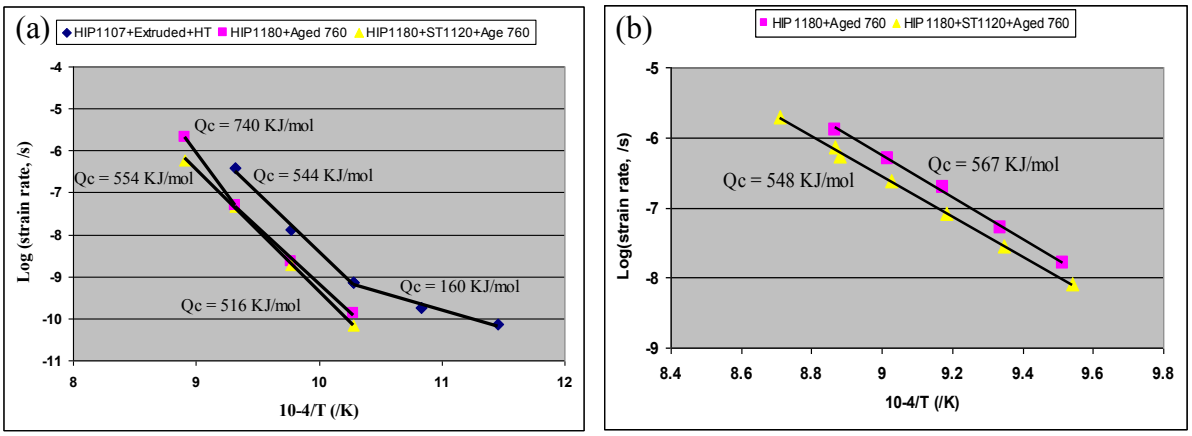

Figure 8.32 Dependence of the creep rate on temperature for RR 1000 samples prepared from different processing conditions, (a) tested at 550MPa; (b) tested at 400MPa.

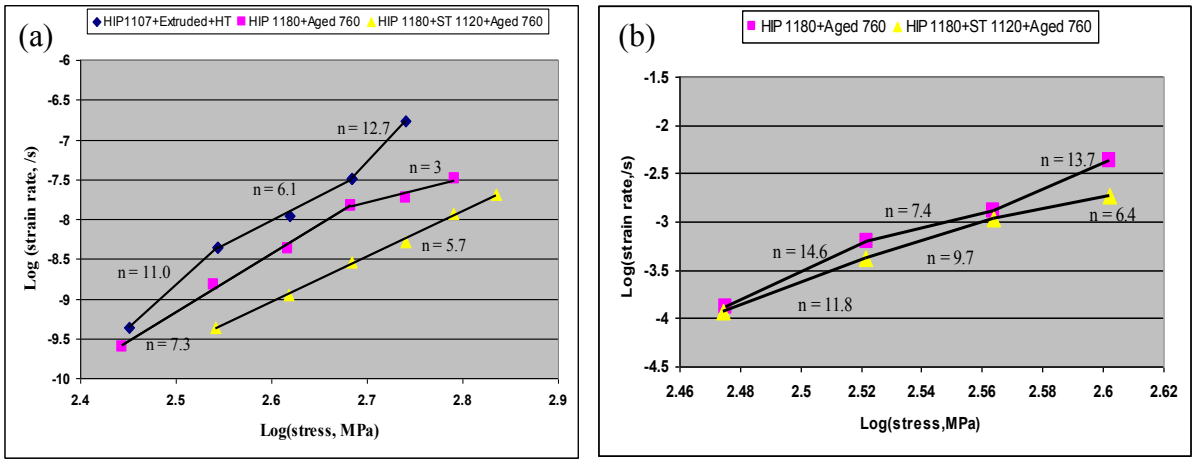

Figure 8.33 Dependence of the creep rate on applied stress for RR 1000 samples prepared through different processing conditions, (a) tested at 746℃; (b) tested at 800℃

Chapter 9 General Discussion, Conclusions and Future work

9.1 General Discussion

The work presented in Chapters 3-8 has involved a detailed study of the influence of HIPping conditions and subsequent heat treatments on the resultant microstructure and properties of RR1000. The aim of the work has been to understand the relationship between processing conditions, microstructure and properties and thus to develop a process-route which optimises the properties. Before discussing the influence of processing route on properties, the role of the large inclusion clusters in influencing properties, will be summarised. These clusters do not appear to influence the tensile properties. In the case of tension-tension fatigue all samples failed at inclusion clusters and it must be concluded that in this case the fatigue properties were probably downgraded. In the case of 4-point bending fatigue the clusters reduced the fatigue limit slightly compared with samples that failed via cleavage of the matrix alloy. These general observations should be borne in mind when assessing the influence of processing on properties. The important observations which have been made and which will form the basis for the subsequent discussion where optimum HIP/heat treatment conditions are identified are as follows:

(A) Influence of HIP conditions and heat treatments on microstructure

1 Heat treatment of powders prior to HIPping at high temperatures led to coarsening of PPB precipitates and thus more discrete distribution of precipitates.

2 Increasing HIPping temperature to super-solvus (>1170℃) led to grain growth and subsequent slow cooling led to very coarse and irregular-shaped secondary γ′ and fan-type γ′-γ structure and to serrated grain boundaries.

3 Solution treatment at 1120°C followed by air cooling changed the γ′ in as-HIPped samples to finer cuboidal secondary γ′ and even finer spherical tertiary γ′.

4 Solution treatment at 1160°C followed by air cooling eliminated the coarse primary and secondary γ′ and produced a very uniform irregular-shaped γ′ size and distribution.

5 Solution treatment at temperatures around the HIPping temperature led to opening of gas bubbles but using a lower solution temperature avoided these problems.

(B) Influence of HIP and heat treatment on tensile, fatigue and creep properties

(i) Influence of HIP procedure

1 Samples HIPped at lower temperature failed in a particle-debonding mode while those HIPped at higher temperature failure occurred in a transgranular mode in tensile tests.

2 Samples HIPped at lower temperature suffered a significant loss in UTS and elongation when the testing temperature was increased from room temperature to 700°C.

3 Increasing HIPping temperature decreases the 0.2% yield strength at room temperature and 700°C. However, the room temperature UTS and elongation show no obvious decrease with increase of HIPping temperature. Changing HIPping procedure was shown to show no significant influence on tensile properties.

4 Although the presence of inclusion clusters at the fracture-initiation sites led to a small reduction in the fatigue properties, the general trend for the influence of HIPping condition on four-point bending fatigue properties could still be determined. Thus, changing HIPping procedure was shown to show no significant influence on four-point bending fatigue properties while increasing HIPping temperature led to a slight improvement in fatigue life at higher stress levels.

(ii) Influence of heat treatments on the properties of HIPped samples.

1 Solution treatment at 1120°C followed by air cooling and aging treatment led to considerable improvement in 0.2% yield strength and UTS while maintaining good elongation.

2 Aging improved the 0.2% yield strength by 50MPa at both room temperature and 700°C.

3 HIPped and aged samples showed the best four-point bending fatigue limit while solution-treated +aged samples had the lowest fatigue limit with failure occurring mainly in cleavage of the matrix alloy in lower stress levels.

4 Solution treatment at 1120℃ followed by air cooling and aging improved creep.

5 Samples HIPped above the gamma prime solvus showed the best creep properties

C Deformation and failure mechanisms in HIPped/heat treated samples

1 Four-point bending fatigue cracks were all initiated from the sample surface but tension-tension fatigue cracks all initiated at the sites of large inclusion clusters in either surface or subsurface area.

2 Increasing testing temperature from room temperature to 700℃ was found to considerably decrease the tension-tension fatigue limit of plain samples but elevate that of notched samples.

These observations show that by altering the HIP conditions (including pre HIP treatments) and post-HIP heat treatments it is possible to influence the microstructure and thus many properties of HIPped powder RR1000. The above summary allows the optimum HIP and heat treatment conditions to be preliminarily identified.

HIPping at super-solvus temperature (like 1180℃) enabled grain growth to occur leaving precipitates that were at prior particle boundaries within grains. This led to a change in the fracture surfaces of samples where a ductile trans-granular fracture mode was observed for the samples HIPped at 1180℃ while for the samples HIPped at a sub-solvus temperature inter-particle debonding was observed. In addition serrated grain boundaries, which are believed to be beneficial for both creep and fatigue crack propagation resistance, were produced through slow cooling from super-solvus HIPping. The grain growth also improved creep properties. Tensile tests showed that although the grain growth associated with the increase of HIPping temperature resulted in a decrease in both room temperature and high temperature 0.2% yield strength the high temperature UTS and ductility were increased. The loss in 0.2% yield strength could be compensated through use of appropriate heat treatment as discussed below. At this stage it is concluded that the optimum HIPping conditions of those investigated in this work are 1180℃/150MPa/4h.

Post HIP heat treatments were shown to have a significant influence on properties. The experimental work showed that solution treatment at temperatures around the HIPping temperature led to formation of thermally induced pores (or gas bubbles). Use of a lower solution temperature (like 1120℃) was found to avoid this problem and furthermore solution treatment at 1120℃ followed by air cooling allowed the distribution of gamma prime to be controlled. Thus a high proportion of different colonies of γ′, with a small fraction of coarse primary γ′ pinning grain boundaries, a reasonable volume fraction of intermediate coherent cuboidal secondary γ′, and a large volume fraction of finer tertiary γ′ were formed. Although a more homogeneous γ′ microstructure could be obtained by air cooling from higher solution temperature the absence of an appropriate number of coarse primary γ′ at grain boundaries may reduce crack propagation resistance and ability to impede grain boundary sliding. Also,

this results in removal of the coarse primary γ′-associated grain boundary serrations which are believed to be beneficial for both creep and fatigue crack propagation resistance.

Tensile testing indicated that solution treatment at 1120°C followed by air cooling and aging treatment led to considerable improvement in 0.2% yield strength and UTS (because of the presence of both cuboidal secondary γ′ and the large volume fraction of fine tertiary γ′) while maintaining reasonable ductility. Creep testing indicates that solution treatment at 1120°C followed by air cooling and aging treatment improved creep performance especially at elevated temperatures and stress levels.

For the two most investigated processing routes in the current study: (i) HIPping at 1180℃/150MPa/4h + solution treatment at 1120℃/2h/AC + aged at 760℃/16h/AC (HIPped + ST + Aged), and (ii) HIPping at 1180 ℃/150MPa/4h + aged at 760 ℃/16h/AC (HIPped+aged), the mechanical data of the two groups of samples are compared with the general property requirements for a future combustion casing, as shown below:

1. A future combustion casing requires a temperature capability above 700℃
2. A proof stress greater than 410MPa and an ultimate tensile stress higher than 560MPa up to 700℃. In the current study, both groups of samples were shown to meet these requirements. The HIPped+aged samples showed a proof stress around 830MPa and a UTS around 1300MPa at 700℃, which are far better than the required tensile properties. Solution treatment at 1120℃ followed by air cooling and ageing treatment led to considerable improvement in 0.2% yield strength and UTS (because of the presence of both cuboidal secondary γ′ and the large volume fraction of medium-sized tertiary γ′) while maintaining reasonable ductility. Actually, the HIPped + ST + Aged samples showed a proof stress around 970MPa and a UTS around 1470MPa at

700℃. The room temperature proof stress and UTS were even better for both groups of samples.

3. A creep requirement for the skins. An estimate is to accommodate 400MPa without exceeding 0.5% Total Plastic Strain (TPS) over the life of the engine. This cannot be easily related to the current experimental data but it was found that when tested at 400MPa and 700℃, both groups of samples showed no detectable change in creep strain after several hours′ testing (the detection resolution for the current facility is a strain of 10^{-7}) and even at higher stresses or temperatures (e.g. 550MPa and 700℃), the creep strain detected was shown to be very low, suggesting that the current samples were highly creep resistant. Moreover, the two groups of samples generally showed better creep resistance than the thermo-mechanically processed materials which have been used as turbine disc materials operating under even more critical conditions. Also, the samples that were solution treated at 1120℃/2h/AC were shown to be more creep resistant than those samples without solution treatment. For a combustor, a better creep resistance is obviously preferred. However, a long term creep test is needed to fully evaluate the creep properties for the current materials for this application.

4. High cycle fatigue limit or strength (at 10^7 cycles) should be larger than 400MPa; Fatigue requirement based on modulus-greater than 170GPa; fatigue requirement based on the Smith–Watson–Topper (SWT) equivalent strain – greater than 0.004. The current high cycle fatigue testing indicates that despite the fact that fatigue properties were impaired to some extent by the presence of large inclusion clusters, the fatigue limit (or fatigue strength at 10^7 cycles) for the HIPped+ST+Aged samples

for four-point bending fatigue test still reached around 700MPa (or 65% of the proof stress) which is much higher than 400MPa. The HIPped+Aged samples showed an even higher four-point bending fatigue limit reaching around 800MPa (87% of the proof stress for these samples). As for the tension-tension fatigue tests, the fatigue limits for the two groups of samples were even better than those for four-point bending fatigue tests, both reaching 850MPa at room temperature and 750MPa at 700℃, even though most of the samples failed at sites of inclusion clusters. However, the last two fatigue requirements mentioned above (modulus-greater than 170GPa; SWT equivalent strain – greater than 0.004) cannot be obtained based on the current experimental data.

5. Notch insensitive. Both groups of samples were shown to have good notch sensitivity, as evidenced by the fact that the UTS for the notched samples were larger than those for the plain samples. The HIPped+ST+Aged samples showed superior notch strengthening to the HIPped+Aged samples. The former group of notched samples showed a UTS around 1850MPa at room temperature and 1750MPa at 700℃, both higher than the latter group of notched samples which showed a UTS around 1650MPa at both room temperature and 700℃. The notched HIPped+ST+Aged samples were also shown to have good notch sensitivity during tension-tension fatigue tests. The ratio (notch stress concentration factor K_t × fatigue limit for notched samples)/(fatigue limit for plain samples) was shown to be >1.0 at both room temperature and 700℃.

In general, the HIPped+ST+Aged samples were superior to the HIPped+Aged samples in terms of tensile properties, creep and notch strengthening. Although their four-point bending

fatigue limit was somewhat lower than the HIPped+Aged samples, their fatigue limit could still be considered good. Moreover, the optimized γ′ size and morphology were actually preferred in terms of microstructural stability and mechanical properties. Therefore, at this stage a post-HIP heat treatment of (i)1120℃/2h followed by air cooling and (ii) an aging treatment at 760℃/16h again followed by air cooling is preferred for Net Shape HIPping.

9.2 Conclusions

On the basis of the above considerations a HIP treatment of 1180℃/150MPa/4h followed by a post-HIP heat treatment of (i)1120℃/2h followed by air cooling and (ii) an aging treatment at 760℃/16h again followed by air cooling is suggested as the HIPping procedure to be used for Net Shape HIPping. All measured properties obtained using these procedures exceed the target properties.

9.3 Future Work

Work up to date has been focused on the study on the relationship between HIPping conditions and subsequent heat treatments and the resultant microstructures and mechanical properties such as tensile, fatigue and creep properties. It was found that most of the primary fatigue crack initiations were due to the presence of large (Hf, Zr)O_2 inclusion clusters. The PPB defects were also associated with the formation of fine (Hf, Zr)-rich oxides or carbides through an elemental diffusion mechanism, which led to a particle debonding failure during tensile tests. Although PPBs could be considerably reduced by using a super-solvus HIPping temperature, the remnant PPBs were still found to lead to formation of secondary cracks and promote primary crack propagation, as evidenced by the pull-out of particles during both tensile and fatigue tests. Therefore, it is suggested that control of inclusion and PPB precipitate sizes and densities by compositional changes (for example, removing Hf and Zr to

avoid the formation of (Hf, Zr)-rich oxides or carbides) and by improved process control are the areas where furture work should focus. C and O levels should be also minimized in alloy composition and powder preparation and handling processes. It would be of great interest to produce the optimized microstructure with greatly reduced numbers of inclusions and elimination of large inclusions and then to examine its mechanical properties.

The current creep tests showed an indication that solution treatment at 1120℃ seemed to improve creep rate at elevated temperatures and stresses. However, the creep rupture properties and creep mechanisms of the microstructures developed are not known due to the use of relatively short-term test (from several hours up to 25h). It would be more helpful to conduct some long-term (such as 100h, 1000h) creep tests to evaluate creep lifetime and rupture properties. Investigation on creep deformation mechanisms using TEM is also needed.

Extensive study on low cycle fatigue properties and fatigue crack propagation rates is also necessary to build up a comprehensive understanding of the microstructure-mechanical properties relationship, which is obviously beneficial for determining the best processing condition for net-shape manufacturing of turbine engine components.

Appendix A

Property requirements for an alloy for a future combustion casing (according to the information Rolls-Royce plc offered):

1. Temperature capability up to 700℃
2. A proof stress greater than 410MPa and an ultimate tensile stress (UTS) higher than 560MPa up to 700℃.
3. A creep requirement, an estimate is to accommodate 400MPa without exceeding 0.5% Total Plastic Strain (TPS) over the life of the engine. Creep strain requirement also specified as < 0.5%TPS at stress greater than 360 MPa for 1000 hours.
4. A fatigue requirement, high cycle fatigue limit or strength (at 10^7 cycles) larger than 400MPa; Fatigue requirement based on modulus – greater than 170 GPa; fatigue requirement based on the Smith-Watson-Topper (SWT) equivalent strain – greater than 0.004.
5. Notch sensitivity. The UTS for notched samples must be larger than that for plain samples, e.g. the ratio of the UTS for notched samples to that of plain samples should be larger than 1.0. For fatigue tests, the ratio (notch stress concentration factor K_t × fatigue limit for notched samples)/(fatigue limit for plain samples) is required to be ≥ 1.0.
6. Machinability. No specifications given and these properties have not been assessed during this work
7. Oxidation resistance. No detailed requirement specified but the as-HIPped alloy may have similar oxidation properties to those of thermomechanically processed material which is satisfactory
8. Other factors, such as crack propagation, fracture toughness and blade containment will also be important for combustion and turbine casings, but no design limits have been specified

Appendix B

B.1 The seven crystal systems

The axial lengths and angles and the symmetries exhibited in the seven crystal systems are shown in Table A.1.

Table A.1 The axial relationships and symmetries of the seven crystal systems [1].

Crystal	Axial length and angles	Minimum symmetry elements
Cubic	a=b=c, α=β=γ=90°	Four, threefold rotation axes
Hexagonal	a=b≠c, α=β=90°, γ=120°	One, sixfold rotation axis
Trigonal (or Rhombohedral)	a=b=c, α=β=γ≠90°	One, threefold rotation axis
Tetragonal	a=b≠c, α=β=γ=90°	One, fourfold rotation axis
Orthorhombic	a≠b≠c, α=β=γ=90°	Three, perpendicular twofold axis
Monoclinic	a≠b≠c, α=γ=90°≠β	One, two fold rotation axis
Triclinic	a≠b≠c, α≠β≠γ≠90°	None

B.2 Interplanar spacing

The value of d, the distance between adjacent planes in the set (*hkl*), may be obtained from the following equations [1].

Cubic: $$\frac{1}{d^2}=\frac{h^2+k^2+l^2}{a^2}$$

Tetragonal: $$\frac{1}{d^2}=\frac{h^2+k^2}{a^2}+\frac{l^2}{c^2}$$

Hexagonal: $$\frac{1}{d^2}=\frac{4}{3}\left(\frac{h^2+hk+k^2}{a^2}\right)+\frac{l^2}{c^2}$$

Rhombohedral: $\frac{1}{d^2}=\frac{(h^2+k^2+l^2)\sin^2\alpha+2(hk+kl+hl)(\cos^2\alpha-\cos\alpha)}{a^2(1-3\cos^2\alpha+2\cos^3\alpha)}$

Orthorhombic: $\frac{1}{d^2}=\frac{h^2}{a^2}+\frac{k^2}{b^2}+\frac{l^2}{c^2}$

Monoclinic: $\frac{1}{d^2}=\frac{1}{\sin^2\beta}\left(\frac{h^2}{a^2}+\frac{k^2\sin^2\beta}{b^2}+\frac{l^2}{c^2}-\frac{2hl\cos\beta}{ac}\right)$

Triclinic: $\frac{1}{d^2}=\frac{1}{V^2}\left(S_{11}h^2+S_{22}k^2+S_{33}l^2+2S_{12}hk+2S_{23}kl+2S_{13}hl\right)$

In the equation for triclinic crystals,

V = volume of unit cell

$S_{11}=b^2c^2\sin^2\alpha$

$S_{22}=a^2c^2\sin^2\beta$

$S_{33}=a^2b^2\sin^2\gamma$

$S_{12}=abc^2(\cos\alpha\cos\beta-\cos\gamma)$

$S_{23}=a^2bc(\cos\beta\cos\gamma-\cos\alpha)$

$S_{13}=ab^2c(\cos\gamma\cos\alpha-\cos\beta)$

B.3 Interplanar angles

The angles ϕ between the plane $(h_1k_1l_1)$, of spacing d_1, and the plane $(h_2k_2l_2)$, of spacing d_2, may be found from the following equations (V is the volume of the unit cell) [1].

Cubic: $\cos\phi=\frac{h_1h_2+k_1k_2+l_1l_2}{\left[\left(h_1^2+k_1^2+l_1^2\right)\left(h_2^2+k_2^2+l_2^2\right)\right]^{1/2}}$

Tetragonal: $\cos\phi=\left(\frac{h_1h_2+k_1k_2}{a^2}+\frac{l_1l_2}{c^2}\right)\times\left[\left(\frac{h_1^2+k_1^2}{a^2}+\frac{l_1^2}{c^2}\right)\left(\frac{h_2^2+k_2^2}{a^2}+\frac{l_2^2}{c^2}\right)\right]^{-1/2}$

Hexagonal: $$\cos\phi = \frac{h_1h_2 + k_1k_2 + \frac{1}{2}(h_1k_2 + h_2k_1) + \frac{3a^2}{4c^2}l_1l_2}{\left[\left(h_1^2 + k_1^2 + h_1k_1 + \frac{3a^2}{4c^2}l_1^2\right)\times\left(h_2^2 + k_2^2 + h_2k_2 + \frac{3a^2}{4c^2}l_2^2\right)\right]^{1/2}}$$

Rhombohedral: $$\cos\phi = \frac{a^4d_1d_2}{V^2}\begin{bmatrix}\sin^2\alpha(h_1h_2 + k_1k_2 + l_1l_2) + (\cos^2\alpha - \cos\alpha)\\ \times(k_1l_2 + k_2l_1 + l_1h_2 + l_2h_1 + h_1k_2 + h_2k_1)\end{bmatrix}$$

Orthorhombic: $$\cos\phi = \left(\frac{h_1h_2}{a^2} + \frac{k_1k_2}{b^2} + \frac{l_1l_2}{c^2}\right)\times\left[\left(\frac{h_1^2}{a^2} + \frac{k_1^2}{b^2} + \frac{l_1^2}{c^2}\right)\left(\frac{h_2^2}{a^2} + \frac{k_2^2}{b^2} + \frac{l_2^2}{c^2}\right)\right]^{-1/2}$$

Monoclinic: $$\cos\phi = \frac{d_1d_2}{\sin^2\beta}\left[\frac{h_1h_2}{a^2} + \frac{k_1k_2\sin^2\beta}{b^2} + \frac{l_1l_2}{c^2} - \frac{(l_1h_2 + l_2h_1)\cos\beta}{ac}\right]$$

Triclinic: $$\cos\phi = \frac{d_1d_2}{V^2}\begin{bmatrix}S_{11}h_1h_2 + S_{22}k_1k_2 + S_{33}l_1l_2 + S_{23}(k_1l_2 + k_2l_1)\\ +S_{13}(l_1h_2 + l_2h_1) + S_{12}(h_1k_2 + h_2k_1)\end{bmatrix}$$

B.4 Angles between poles

The angle ρ between two crystal directions $[u_1v_1w_1]$ and $[u_2v_2w_2]$ may be found from the following equations [2].

Cubic: $$\cos\rho = \frac{u_1u_2 + v_1v_2 + w_1w_2}{\left[(u_1^2 + v_1^2 + w_1^2)(u_2^2 + v_2^2 + w_2^2)\right]^{1/2}}$$

Tetragonal: $$\cos\rho = \frac{a^2(u_1u_2 + v_1v_2) + c^2w_1w_2}{\left[a^2(u_1^2 + v_1^2) + c^2w_1^2\right]^{1/2}\left[a^2(u_2^2 + v_2^2) + c^2w_2^2\right]^{1/2}}$$

Orthorhombic: $$\cos\rho = \frac{a^2u_1u_2 + b^2v_1v_2 + c^2w_1w_2}{\left(a^2u_1^2 + b^2v_1^2 + c^2w_1^2\right)^{1/2}\left(a^2u_2^2 + b^2v_2^2 + c^2w_2^2\right)^{1/2}}$$

Hexagonal: $$\cos\rho = \frac{u_1u_2 + v_1v_2 - \frac{1}{2}(u_1v_2 + v_1u_2) + \frac{c^2}{a^2}w_1w_2}{\left[\left(u_1^2 + v_1^2 - uv + \frac{c^2}{a^2}w_1^2\right)\times\left(u_2^2 + v_2^2 + w_2^2 + \frac{c^2}{a^2}w_2^2\right)\right]^{1/2}}$$

Monoclinic:

$$\cos\rho = \frac{a^2u_1u_2 + b^2v_1v_2 + c^2w_1w_2 + ac(w_1u_2 + u_1w_2)\cos\beta}{\left(a^2u_1^2 + b^2v_1^2 + c^2w_1^2 + 2acu_1w_1\cos\beta\right)^{1/2}\left(a^2u_2^2 + b^2v_2^2 + c^2w_2^2 + 2acu_2w_2\cos\beta\right)^{1/2}}$$

Triclinic: $\cos\rho = \dfrac{L}{I_{u_1v_1w_1} \times I_{u_2v_2w_2}}$

Where $L = a^2u_1u_2 + b^2v_1v_2 + c^2w_1w_2 + bc(v_1w_2 + w_1v_2)\cos\alpha$
$+ac(w_1u_2 + u_1w_2)\cos\beta + ab(u_1v_2 + v_1u_2)\cos\gamma$ and

$$L = a^2u^2 + b^2v^2 + c^2w^2 + 2bcvw\cos\alpha + 2acwu\cos\beta + 2abuv\cos\gamma$$

B.5 Acquisition of several diffraction patterns and useful measurement

Diffraction patterns offer much information for analysis of characteristic lattice parameters for a crystal structure. For comprehensive analysis, several diffraction patterns from the same spacing are usually needed. This could be realized by conducting tilting about a pole. Figure 1 shows the procedure to obtain such diffraction patterns, which starts with g_1 and g_2 strongly excited at pole 1 and then tilts to pole 2 keeping g_1 strongly excited. Similarly, tilting from pole 1 to pole 3 by keeping g_2 strongly excited will yield another set of diffraction patterns. This process usually could be easily operated by taking advantage of Kikuchi lines, as shown in Figure 2. To avoid considerable deviation of beam from the area of interest during tilting, an alternate operation between imaging (to get back to the area for analysis) and diffraction is significantly helpful to get to the desired pole.

Once several desired diffraction patterns are obtained, measurement on the diffraction patterns is very useful for identification of a crystal system. For example, By considering the relationship between the spacing R of diffraction maxima and the camera length L (illustrated in Figure 3) could one obtain

$$R/L = \tan 2\theta \approx 2\theta$$

From the Bragg equation we know that $\lambda/d = 2\sin\theta \approx 2\theta$, and so an equation could be obtained shown as follows:

$$Rd = \lambda L \text{ or } d = \frac{\lambda L}{R}$$

Where λ is the wavelength of the incident beam which is known and the camera length L is known as well. This indicates the measurement of R will lead to the acquisition of crystal spacing d.

Moreover, it is noted that the angles between diffraction maxima are angles between planes in the real crystal and the angles between beam directions (or poles) are angles between directions in the real crystal [1]. Therefore, by measuring the angles between two maxima ϕ, then the angles between two planes will be known and by recording α, β tilting readings at two poles and taking advantage of the following equation:

$$\cos\rho = \cos(\alpha_2 - \alpha_1)\cos(\beta_2 - \beta_1),$$

Then the angles between two beam directions ρ will be known.

It is suggested that in order to determine the crystal system of the samples from these diffraction patterns some trial assumption must be made, using information from just one of the patterns, and then testing the deductions using the information from the other two patterns [1]. Obviously, comparing these measured crystal spacing d, measured angles ϕ, and the measured orientation angle ρ between two beam directions with those theoretically calculated values using equations shown in A.2-A.5 sections will validate whether the assumption is right or wrong. Also, the measured information could be integrated to the above equations in A.2-A.5 sections so that the lattice parameters could be obtained.

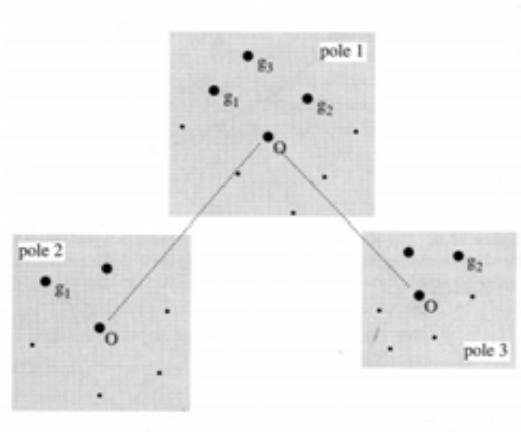

Figure 1 Indexing of reflections and poles by tilting to other poles in the same spacing: start with g_1 and g_2 strongly excited at pole 1. Tilting to pole 2 keeping g_1 strongly leads to achievement of a diffraction pattern, and then going back to pole 1 and tilting to pole 3 keeping g_2 strongly excited yields another diffraction pattern from the same spacing [3].

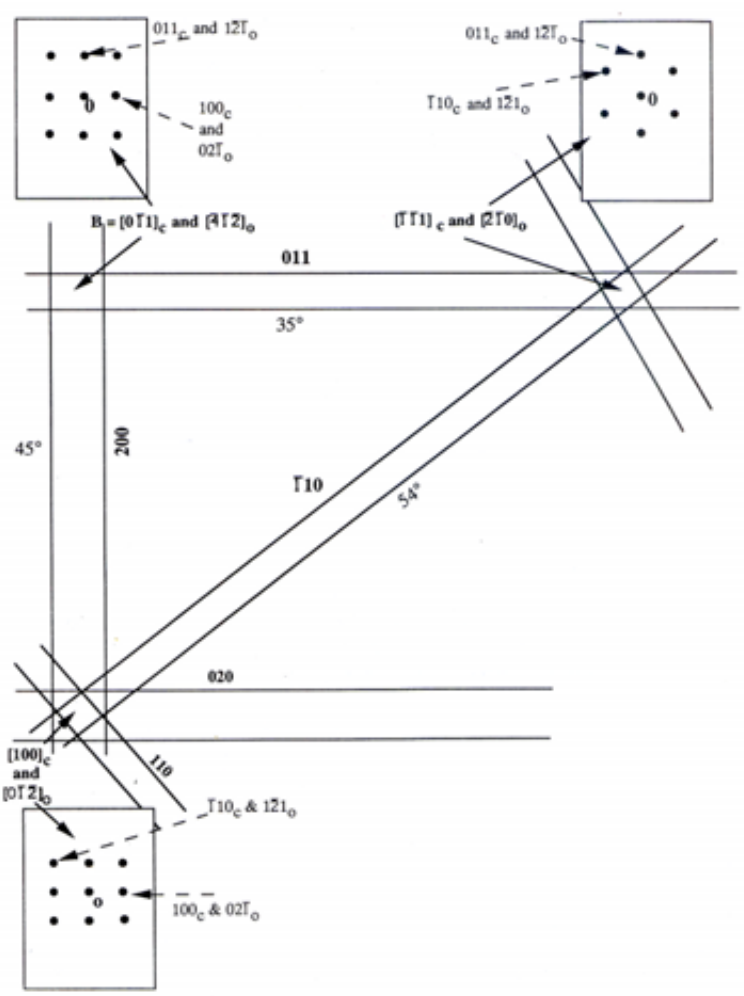

Figure 2 Schematic Kikuchi map and indexed diffraction patterns taken from the same area of a second phase particle which was formed in a matrix that was cubic. The tilt axis and angles between the various patterns are indicated. The beam directions in the three poles for each of the crystals are shown and the indices of a pair of reflections in each pole are shown to allow calculation of the beam directions. (The subscripts o and B refer to orthorhombic and cubic phases respectively) [1]

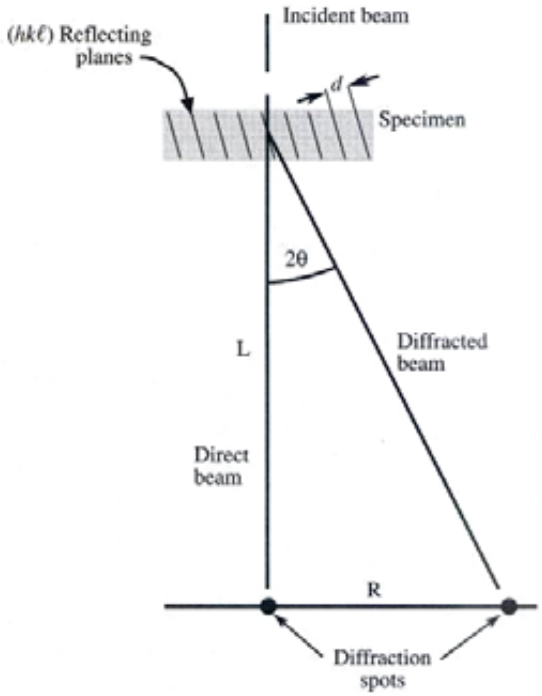

Figure 3 The relationship between the spacing R of diffraction maxima and the camera length , L [3].

References

[1] Loretto MH. Electron beam analysis of materials, second edition. London: Chapman & Hall Press;1994.

[2] Andrews KW, Keown SR. Interpretation of electron diffraction patterns, second edition. London: ADAM HILGER Ltd; 1971.

[3] Williams DB, Carter CB. Transmission electron microscopy, I-II. New York: Plenum, c Press; 1996.